Multi-modal registration of T1 brain image and geometric descriptors of white matter tracts

Viviana Siless

UNIVERSITÉ PARIS-SUD

ÉCOLE DOCTORALE 427 :
INFORMATIQUE PARIS SUD

Laboratoire: Parietal Team, INRIA Saclay, CEA, Neurospin

THÈSE

INFORMATIQUE

par
Viviana Siless

Multi-modal registration of T_1 brain image and geometric descriptors of white matter tracts

Date de soutenance: 08/07/2014

Composition du jury:

Directeur de thèse:	Dr Bertrand Thirion	INRIA Saclay – Parietal team, Saclay, France Neurospin/CEA, Saclay, France
Conseiller:	Dr Fillard Pierre	INRIA Saclay – Parietal team, Saclay, France
Rapporteurs:	Dr Christian Barillot	IRISA, Campus Universitaire de Beaulieu, Rennes, France
	Dr Natasha Lepore	Children's Hospital Los Angeles, Los Angeles, USA
Examinateurs:	Pr. Joan Glaunes	MAP5, Université Paris Descartes , Paris, France
	Dr. Marc Baboulin, HDR	Inria/University Paris-Sud, Orsay, France
	Demian Wassermann	IINRIA Sophia-Antipolis – Athena team Sophia-Antipolis—Méditerranée, France

Contents

Chapter 1

Abstrait

Le recalage des images obtenues par résonance magnétique (IRM) est un défi central pour le domaine de l'imagerie cérébrale. Le recalage nous permet d'analyser des groupes de sujets. Une fois tous les sujets alignés, il est possible de construire un atlas statistique représentatif du groupe; un tel atlas est utilisé pour comparer une image à une population présentant une pathologie neuro-dégénérative comme Alzheimer et trouver des biomarqueurs.

La forme et la configuration de chaque cerveau change en fonction de l'individu et elle peut être modulée par une pathologie. Le recalage des images tente d'aligner les structures d'un sujet avec les structures correspondantes d'un autre sujet ou d'une référence commune (atlas). Cet alignement est basé sur la recherche d'une transformation menant d'une image vers une autre tout en conservant les propriétés et structures originelles de cette première. Le principal défi du recalage consiste donc en l'identification des structures correspondantes a travers les sujets.

Généralement les algorithmes du recalage utilisent des images anatomiques du type T_1, qui montrent un contraste élevé pour la matière grise. Par contre la matière blanche est presque uniformément blanche et ne fournit aucune information pour le recalage. En complément, l'imagerie par diffusion (IRMd) aide à caractériser la structure de la matière blanche, qui est composée de fibres qui connectent les différentes régions du cerveau. Ces fibres peuvent aider à caractériser la matière grise car elles caractérisent la connectivité et donc la fonction cérébrale. Pour cette raison, nous exploitons la complémentarité de ces deux modalités pour améliorer le recalage des structures du cerveau.

Nous utilisons un algorithme connu pour le recalage des images, nommé *algorithme des démons*, et en étendons le principe pour recaler conjointement la matière grise et la matière blanche. L'information de diffusion peut être représentée par des valeurs scalaires de la quantité de diffusion (par ex. FA, anisotropie fractionnelle), par des image de tenseurs (une représentation 3D de la diffusion dans chaque voxel) ou géométriquement lorsque l'on tente de reconstruire les faisceaux axonaux de la matière blanche. Nous nous sommes concentré sur la géométrie de la matière blanche.

Il y a des milliards de fibres axonales dans le cerveau, qui sont représentées par des dizaines de milliers de tracts à partir d'IRM de diffusion. L'analyse de cette quantité de fibres, et surtout le recalage des images, est un travail lourd et coûteux en calcul. Ainsi nous utilisons, analysons et développons des algorithmes de *clustering* pour simplifier la représentation de la matière blanche. Ces algorithmes sont définis dans un espace métrique afin de comparer les éléments. Quand on utilise des métriques plus adaptées à des courbes, nous montrons que la simplification de la matière blanche est de meilleure qualité.

Notre algorithme de recalage minimise conjointement les distances entre les images T_1 et les

tracts les plus représentatifs de chaque sujet. Les tracts sont comparés par des métriques de courbes: le point le plus proche, les Courants et les Mesures. La première métrique requiert une correspondance explicite entre fibres, le deuxième une correspondance entre faisceaux, et la dernière aucune correspondance a priori. Chaque métrique a ses avantages et inconvénients, qui ont étés analysés pendant cette thèse.

Nous avons validé notre algorithme de recalage d'image conjointement à la géométrie dans une base de donnée de sujets contrôles. Les résultats ont montré qu'en utilisant l'information de diffusion en complément de l'information anatomique, on améliore systématiquement le recalage qui utilise seulement de information anatomique de contraste T_1, mais aussi le recalage des images de tenseur ou le recalage de T_1 avec FA. En conclusion, on peut affirmer que la structure de la matière blanche, après simplification, permet de diminuer les erreurs dans le processus de recalage, et par conséquent améliore les résultats finaux des analyses de groupe.

Chapter 2

Resumé

Je ferai le Bien : c'est encore la meilleure manière d'être seul.

— de Jean-Paul Sartre Extrait de Le diable et le bon dieu

2.1 Motivation

Depuis le début des années 90, de nombreuses méthodes d'analyse statistique des populations adaptée à l'imagerie par résonance magnétique ont été proposées afin de mieux comprendre le développement normal de cerveau et aussi trouver des biomarqueurs des maladies neurodégénératives à un stade précoce.

Le recalage des images du cerveau consiste à aligner les structures correspondantes pour faciliter la comparaison entre les différentes sujets. Une fois que tout les images sont alignées, elles partagent le même système de coordonnées, ce qui signifie que les structures sont alignées par voxels. Ainsi, les méthodes morphométriques niveau voxel sont utilisées pour détecter des changements dans différentes études Leporé et al. [2010], Lepore et al. [2008a], Mani et al. [2010a]. L'alignement est obtenu en appliquant une déformation qui peut être analysée afin de mesurer la quantité de déformation entre une image donnée et un modèle. Ceci est utile dans les études longitudinales de maladies neurodégénératives telles que la maladie d'Alzheimer, notamment pour caractériser des changements de structure cérébrale au cours du temps; par exemple, la

diminution du volume de la matière blanche et l'augmentation de liquide céphalo-rachidien dans ventricules.

L'IRM anatomique (T_1) est la référence dans le domaine de recherche de l'imagerie médicale et de la radiologie, mais depuis la fin des années 90 d'autres modalités d'imagerie telles que l'IRM de diffusion et l'IRM fonctionnelle sont devenues important Filler [2009], Bandettini [2012], Oishi et al. [2008]. L'IRM de diffusion donne des informations sur l'organisation interne de la matière blanche qui sont les connexions à l'intérieur du cerveau. Les fibres neurales sont les voies d'interaction du cerveau, mais elles constituent également la liaison avec le reste du corps, et sont utilisées par le cerveau pour transmettre des informations. Beaucoup d'efforts ont été appliqués pour dévoiler l'architecture de la matière blanche du cerveau, soit pour l'estimation de chaque fibre spécifiquement ou pour une analyse au niveau plus générale de l'ensemble. Lors de cette dernière, un haut niveau d'abstraction est demandé où les efforts ne partent pas sur la microstructure de la matière blanche, mais plutôt sur le niveau fonctionnel, de savoir quelles régions sont connectées pour certains groupe de fibres Faria et al. [2012], Oishi et al. [2008]. .

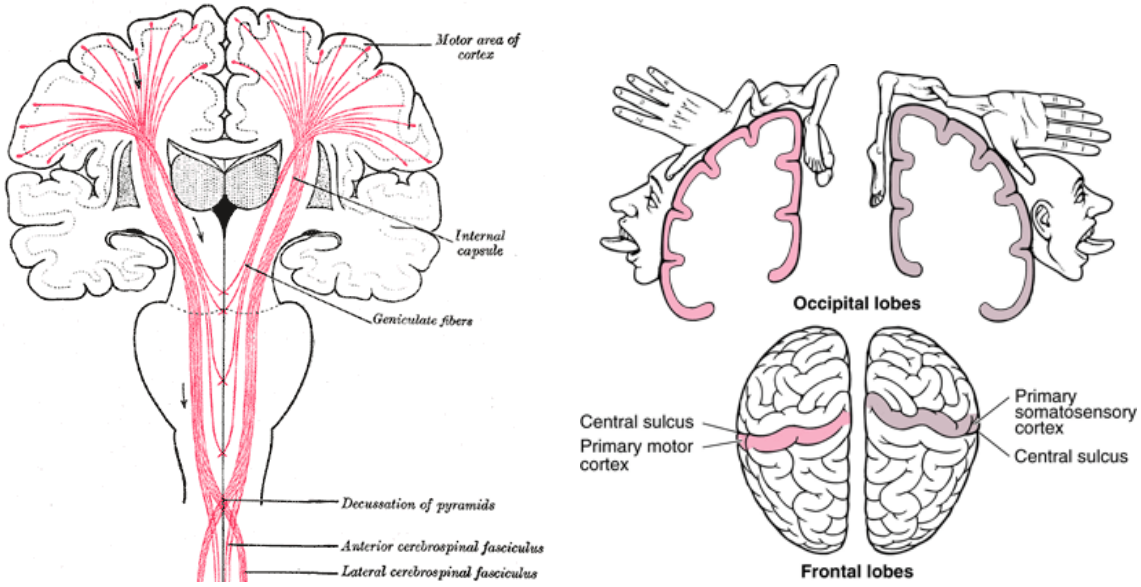

Figure 2.1: À droite une illustration somatosensorielle du cortex moteur primaire et sa topographie. À gauche, les connexions de la matière blanche impliquées dans le cortex moteur. Images prises de *teachmeanatomy.info* and *www.merckmanuals.com*.

Lorsque nous prenons un verre d'eau et le dirigeons vers notre bouche, de nombreuses régions du cerveau interagissent pour accomplir cette tâche : le lobe frontal postérieur par exemple est en charge des mouvements de motricité, le lobe pariétal postérieur d'analyser l'espace, et le lobe occipital de visualiser l'objet. Ces méta-rôles sont illustrés Fig. 4.1 . Afin de comprendre comment le cerveau est organisé et comment il fonctionne, nous avons besoin de comprendre comment il est connecté, et pour cette raison les fibres de la matière blanche sont généralement classées ensemble en fonction des les régions fonctionnelles qu'elles connectent. Ceci est crucial pour comprendre et suivre le développement normal du cerveau.

Par exemple, les premiers symptômes de la maladie d'Alzheimer (MA) sont la perte de mémoire

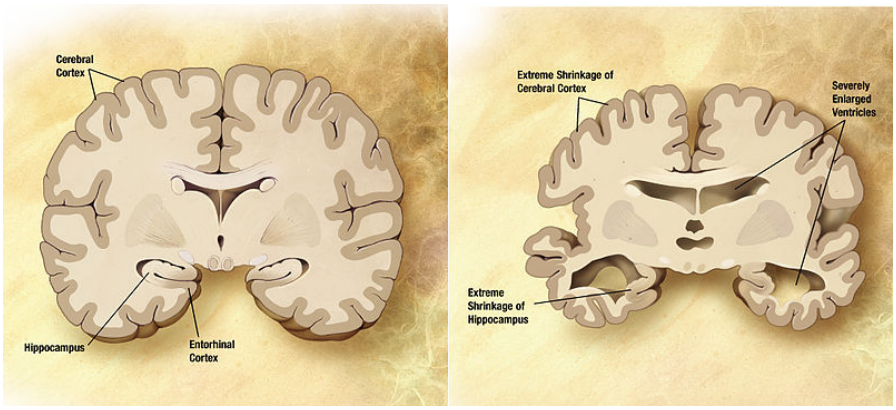

Figure 2.2: Combinaison de deux schémas de cerveau pour illustrer la variabilité entre un cerveau normal et un pathologique. Le cerveau de gauche est celui d'un sujet sain, tandis que le cerveau de droite est celui d'une personne atteint de la maladie d'Alzheimer. Image fournie par *The Alzheimer's Disease Education and Referral Center, a service of the National Institute on Aging.*

à court terme, et sont suivies progressivement par des problèmes de langage et la perte des fonctions du corps. On s'attend donc à ce que les régions du cerveau associées à ces tâches développent une grande atrophie physique comme représentée Fig. 4.2, où un sujet normal et un autre avec la maladie d'Alzheimer sont comparés. La recherche a montrée que la MA est associée dans ses premières étapes à des anomalies de la microstructure de la matière blanche (MB) Alves et al. [2012]. Cette dégénérescence peut être vue dans des images fonctionnelles et anatomiques Cash et al. [2012], Lorenzi et al. [2012], Li et al. [2012], Wagner [2000].

Néanmoins, l'étude de maladies telles que la dyslexie n'ont montré aucune différence entre les images T_1 de sujets avec problèmes de lecture et celles de sujets contrôles. A l'inverse, l'anisotropie des images de diffusion reflète une diminution de la microstructure des faisceaux de matière blanche comme indiqué dans Carter et al. [2009], Klingberg et al. [2000]. Dans une étude plus récente, des différences ont été trouvées dans les matières grise et blanche, ainsi qu'une corrélation potentielle avec des déficits de parole dans un environnement bruyant Dole et al. [2013]. Un autre exemple est le syndrome de Gerstmann, qui se caractérise par la tétrade de quatre facultés cognitives. Dans les années 1920, Gerstmann pensait qu'il y avait un dénominateur commun fonctionnel essentiel entre pour ces quatre régions. Toutefois, aucune preuve directe n'a encore été trouvée à partir de la perspective cognitive, mais une étude plus récente suggère une relation entre les structures interne de la matière blanche qui les connectent Rusconi et al. [2009].

Le recalage des images du cerveau est la base pour l'analyse d'une population, cependant la plupart des techniques d'enregistrement aujourd'hui utilisent uniquement les caractéristiques anatomiques telles que les lignes sulcales. Les lignes sulcales sont de bons points de référence pour des régions fonctionnelles et sont la principale information que on peut extraire des images anatomiques T_1 4.3 Goualher et al. [1997, 1998], Corouge and Barillot [2002]. Cependant, sauf pour les lignes les plus courantes, la détection et la classification

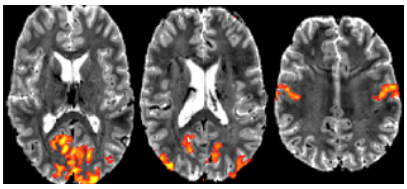

Figure 2.3: Images fonctionnelles de haute résolution montrant que les régions de détection d'activation sont clairement vers les lignes sulcales. Image fournie par *https://humanconnectome.org*

des lignes sulcales est difficile à effectuer sur toute la surface du cerveau, car ils varient beaucoup d'un sujet à l'autre, tant au niveau de leur taille que de leur emplacement. D'autres techniques de recalage utilisent l'IRM de diffusion et essaient d'aligner les régions de haute diffusion en utilisant différentes représentations telles que des images de Tenseur et des images d'anisotropie fractionnée. Même si cette technique est efficace pour détecter les régions avec des niveaux de diffusion anormaux dans une population, ce type d'étude ne contient pas d'informations sur les connections entre régions. Ces connections peuvent être estimées en suivant les chemins de haute diffusivité pour reconstruire les structures internes de la matière blanche, les faisceaux de fibres.

Cette thèse se base sur l'hypothèse que le recalage peut devenir plus efficace dans des contextes multi-modaux, afin d'améliorer la correspondance et la comparaison à travers des sujets Hellier et al. [2002], Lemoine et al. [1991]. Nous visons également à vérifier qu'en ajoutant des fibres nerveuses connues et fiables, on peut ainsi mieux guider le recalage, non seulement pour l'alignement des structures, mais aussi pour le reste de la matière blanche et des régions fonctionnelles. Les images anatomiques sont uniformément blanches dans les régions de la substance blanche et ne contiennent pas d'information de diffusion. Par conséquent, les déformations estimées ne garantissent pas l'alignement de la matière blanche. En plus, les images de diffusion ne sont pas adéquates pour l'analyse du cortex, car elles ne fournissent aucune information pertinente pour l'analyse des plissements du cortex, contrairement à la matière grise. Pour ces raisons, le recalage des images de diffusion est principalement utilisé pour l'analyse de la matière blanche.

Naturellement, les deux types d'images fournissent des informations utiles pour l'analyse du cerveau, si bien que dans cette thèse nous avons proposé une technique pour combiner les informations des images anatomiques et de diffusion pour améliorer le recalage. Nous proposons de représenter la matière blanche par des descripteurs géométriques tel que les courbes, ou des nuages de points, pour pouvoir les combiner avec l'image anatomique T_1.

Nous proposons d'abord des méthodes pour analyse les fibres obtenues para la tractographie, par les simplifier et faciliter après leur utilisation dans le recalage.

2.2 Représentation de la Matière Blanche

Grâce aux outils pour l'imagerie de diffusion actuels, nous pouvons estimer des millions de fibres nerveuses dans la matière blanche. Pour être efficace et précis, nous nous proposons d'extraire les fibres les plus pertinentes et de les intégrer ensuite dans le recalage. Nous analysons et proposons différentes techniques de regroupement des faisceaux de matière blanche en fonction de leur forme et de leur distance les uns des autres. Si bien la pertinence d'un faisceau peut être définie par exemple par son sens anatomique, nous nous concentrons plutôt sur les aspects techniques tels que notre capacité à les détecter dans différents sujets, ou leur importance au sein d'un seul sujet (i.e. la taille du faisceau).

Dans le chapitre **??** nous analysons trois algorithmes de classification différents utilisés pour regrouper les faisceaux de matière blanche:

1. KMeans: un algorithme simple mais largement utilisé et connu. Sa simplicité nous permet de tester différentes mesures plus adaptées aux courbes pour améliorer les caractéristiques intrinsèques des eux.

2. Two Level Average-linkage clustering: un algorithme de clustering agglomératif à deux niveaux développé par Guevara et al. [2012]. Il travaille sur une segmentation obtenue par le recalage du sujets sur l'espace de Tailaraich: Elle aide a séparer a priori les fibres par région avant qu'unalgorithme de classification soit appliqué à chacune. Le regroupement de second niveau est appliqué sur toutes les représentatives des classes obtenues dans chaque région de tous les sujets ensemble. Un faisceau a des correspondances à travers les sujets si dans la classe obtenue à la deuxième étape, il y des représentatives des différents sujets.

3. QuickBundles: un algorithme de clustering rapide développé par Garyfallidis et al. [2012], qui crée des groupes sur demande en fonction d'un seuil. Chaque fois qu'une nouvelle fibre est ajoutée, si aucun cluster n'est assez près de la fibre, un nouveau groupe est créé.

Chaque algorithme de clustering analysé a des caractéristiques et des objectifs différents. *Two Level Average-linkage clustering* est un pipeline multi-étapes qui aui necessite que les données soient recalées et segmentées au préalable, et qui implique de multiples étapes de classification. En conséquence, nous obtenons des faisceaux correspondants entre sujets. Néanmoins des erreurs peuvent être effectuées à chaque étape, et la fiabilité de la correspondance entre faisceaux peut être discutée. *Quickbundles* , au contraire, n'a pas besoin d'information ajoutée a priori et sert à une rapide compression de la représentation de la matière blanche de haut niveau. *KMeans* nous permet d'analyser l'impact de différentes métriques pour le regroupement des faisceaux de fibres.

Le plus fort pipeline pour l'analyse de la matière blanche a été développé par Guevara et al. [2012]. Il est basé sur une segmentation déjà définie sur les sujets, où la tractographie est d'abord divisée en fonction de segmentations précédemment effectuées sur le cortex, à partir des images T_1. Puis l'algorithme de classification est appliqué pour chaque sous-groupe. Un deuxième niveau de classement de fibres est appliqué sur l'ensemble des représentants de chaque cluster de tous le sujets, pour détecter les fibres correspondantes à travers les sujets. Cette méthodologie est robuste, et s'appuie sur de nombreuses étapes de prétraitement pour améliorer les résultats : la segmentation du cortex en fonction des images T_1 déjà alignées contre l'atlas de Tailaraich est utilisée pour construire une segmentation initiale des faisceaux de matière blanche, et ce dernier regroupement est effectuée dans l'espace du Tailaraich.

En contraste avec cette dernière technique, QuickBundles a été développé dans Garyfallidis et al. [2012]. Il s'agit d'un algorithme rapide, capable de traiter une base de données de tractographie massive en quelques secondes. Bien que QuickBundles n'a pas montré de meilleures performances que les autres métriques et les autres algorithmes, il est très pratique pour un traitement rapide, et nous avons constaté que dans le cas moyen, les principaux faisceaux de matière blanche sont finement détectés.

Pour comparer l'impact des différentes métriques sur l'analyse de la matière blanche, nous avons choisi l'algorithme K-Means et changé sa métrique pour mieux répondre à nos besoins. Nous montrons comment des mesures simples telles que la distance euclidienne qui est la plus largement utilisée avec les algorithmes de clustering, peut être améliorée. Plus précisément, nous nous intéressons à des métriques où aucune correspondance point à point n'est nécessaire. Ceci est pertinent dans l'analyse de la substance blanche non seulement parce que les fibres peuvent avoir des longueurs différentes, mais aussi, en raison de la mauvaise qualité de l'image, une fibre peut se terminer plus tôt, ou être divisée. Nos résultats montrent que la métrique de Measures (somme de Dirac deltas centrée a chaque point du fibre) donne de meilleurs resultats que les autres metriques. Nous avons également mis en place différentes métriques pour évaluer les résultats du regroupement largement connues dans la littérature de l'apprentissage automatique, mais très peu utilisée dans la communauté de l'IRM de diffusion en neuro-imagerie.

Nous sommes conscients que ces distances soit plus adaptées aux courbes et sans correspondance entre points sont plus coûteuses que les distance de point par point, comme la distance euclidienne. En raison de la grande dimension des données de diffusion, nous nous sommes retrouvés contraints d'explorer d'autres options. Nous présentons l'analyse multidimensionnelle qui incorpore les tracts dans une nouvelle espacées défini par la métrique désirée, pour après être analysée par l'algorithme K-Means. Ceci est réalisé en sélectionnant un pourcentage de tracts aléatoirement échantillonnées, et nous montrons que, bien que le temps de calcul change radicalement, la précision reste stable lorsque on varie le pourcentage de fibres a utilise.

2.3 Recalage Multi-modal: T_1 et Faisceaux de Fibres

Le cœur de cette thèse concerne sur le recalage multimodal d'images T_1 et des descripteurs géométriques de faisceaux de fibres. Nous explorons différentes représentations de l'architecture de la matière blanche, où chaque représentation exige différentes connaissances préalable au recalage. Nous nous appuyons sur un algorithme de recalage des image T_1 bien connu, le *Demons Algorithm*, qui cherche une déformation difféomorphe qui minimise la somme des distances carrés entre deux images. La nouvelle approche minimise conjointement la distance entre l'image et les descripteurs géométriques sur les images et des fibres respectivement des sujets.

Dans le Chapitre 9 nous développons et analysons un algorithme multi-modal avec les distances géométriques suivantes:

1. Le point le plus proche distance (PPD): les fibres sont représentés comme une séquence de points. Pour cette distance une correspondance un-à-un est utilisée comme a priori, et chaque point dans les fibres se déplace vers le point le plus proche sur la fibre fixe correspondant. Cette métrique est coûteuse, ainsi il est préférable d'avoir des fibres correspondantes. La déformation est également restreinte par les forces de l'image et des contraintes de régularisation pour obtenir des déformations difféomorphes.

2. Courants: Cette distance utilise la notion de tangentes dans les courbes (fibres). Les fibres sont représentées par l'intégrale des champs de vecteurs définis par les tangentes de chaque position de la fibre ou courbe. Ainsi, une orientation cohérente à travers les fibres est nécessaire pour une comparaison valable, puisque deux fibres en sens inverse peuvent induire en erreur le recalage. En conséquence, cette mesure nécessite des correspondances faisceau-à-faisceau, ou une segmentation de fibres orientées systématiquement entre les individus.

3. Mesures Pondérées: Cette approche s'appuie sur la notion de courants, néanmoins avec un sens géométrique plus léger. Dans ce cas, les tangentes sont remplacées par des poids représentant l'importance des faisceaux (par exemple, leur taille). Chaque faisceau est représenté par la somme du Dirac deltas centrées en chaque point, pondérée par son importance pour le sujet. Cet indicateur permet le recalage de deux sujets sans fort a priori et sans lourde étape de prétraitement.

Différentes approches ont été explorées au cours de cette thèse. La première preuve de concept a été effectuée en utilisant le point le plus proche. Les résultats ont montré que les recalages pourraient être largement améliorés, puisque l'alignement de l'image T_1 a été maintenue par le nouvel algorithme, mais l'alignement de la matière blanche a été grandement améliorée. Certains

sujets ont même montré des améliorations sur l'alignement de T_1 vérifiant que l'information en matière blanche peut en effet conduire à un meilleur recalage global d'un sujet.

Lors de l'utilisation de la métrique PPD, une correspondance fibre-à-fibre est pratique pour des raisons de calcul. Il a été obtenu en utilisant le pipeline de regroupement moyen de liaison 2 niveaux développé dans Guevara et al. [2012]. Les faisceaux résultants ont été encore simplifiés pour utiliser une seule fibre représentant le centre de gravité.

Pour éviter l'exigence d'une correspondance fibre-à-fibre qui est difficile à obtenir en pratique, nous améliorons l'algorithme de recalage en représentant des faisceaux de fibres avec des courants. Au lieu d'un nuage de points, chaque faisceau est représenté par une somme de Dirac deltas centrées aux points des fibres associées aux tangentes suivant la direction de la courbe. Bien que cette nouvelle représentation ne nécessite pas de correspondance fibre-à-fibre entre sujets, il nécessite un correspondance faisceau à faisceau parce que l'orientation doit être cohérente à travers les sujets pour une comparaison correct. Les résultats ont montré une conservation du niveau d'alignement de T_1 de tout en améliorant considérablement l'alignement de tractographie par rapport à l'algorithme original.

Dans une dernière étape, nous supprimons les exigences de correspondance faisceau-à-faisceau. La raison pour laquelle cette dépendance n'est pas souhaitable est la facilité d'utilisation. Tout d'abord, l'obtention de faisceaux correspondants entre sujets prend beaucoup de temps en prétraitement d'image, mais d'autre part, il n'est pas toujours possible de définir des correspondances à travers les sujets. Ceci arrive en particulier dans les maladies neurodégénérative, et les études longitudinales pour analyser le développement du cerveau. En revanche, nous souhaitons toujours simplifie la représentation de la matière blanc, et une nouvelle mesure a été définie sur cette base. Nous avons représenté l'ensemble des données de tractographie comme une somme de Dirac delta centrée à chaque point de chaque représentant de classe. Le regroupement peut être effectué avec n'importe quel procédé, mais nous avons utilisé QuickBundles. Chaque Dirac delta est pondérée par la quantité de fibres présent dans le groupe associée. Ce faisant, le recalage est dirigée principalement par les plus grandes classes, qui sont censées correspondre aux principaux faisceaux de matière blanche. Avec ce raisonnement, les faisceaux les plus petits sont considérés comme du bruit et ont un faible impact sur l'alignement. Une fois de plus, les résultats ont montré une amélioration spectaculaire de l'alignement de la substance blanche, tout en maintenant des résultats précis pour l'alignement des images T_1.

2.4 Conclusion

L'analyse de populations pour détecter les biomarqueurs de la maladie et pour comprendre la croissance normale est une technique standard motivée par la grande disponibilité des scanners dans les hôpitaux et l'intérêt de partage les bases de données à des fins de recherche. Le large éventail de techniques d'imagerie médical où chaque type d'image mesure des caractéristiques différentes du cerveau, nous amène sur un chemin d'évolution naturelle d'analyse. L'analyse multi-modale a commence a recevoir de plus en plus d'attention dans le domaine de la neuro-imagerie, et ce à chaque étape de l'analyse: le regroupement la matière blanche, la détection des régions d'activation fonctionnelle, la segmentation du cortex, le recalage, etc.

Dans cette thèse, nous avons principalement exploré la simplification de la structure de la substance blanche, et comment la matière blanche peut être incorporé dans un cadre de référence pour améliorer l'analyse inter-sujet.

Dans le Chapitre 8 nous avons effectué une analyse approfondie des techniques visant à simplifier l'analyse de la tractographie de fibres intra-sujet. Compte tenu de l'intérêt utiliser ces faisceaux pour le recalage entre sujets, nous nous concentrons sur les principaux faisceaux, c'est-a-dire ceuse qui sont grands et facilement détectables dans tous les sujets. Nous avons comparé différents algorithmes de clustering pour la simplification de la matière blanche, du plus célèbre comme K-Means, au plus récent, Quickbundles, en passant par un algorithme agglomératif hiérarchique. La suite a été spécialement conçu pour l'analyse rapide des données massives de la substance blanche.

Nous avons choisi K-Means pour l'analyse de différentes métriques, et nous avons montré que les métriques qui sont mieux adaptées aux courbes peuvent améliorer les résultats de classification. Toutefois les même analyses pourraient être faites a une échelle multi-dimensionnelle par Quick-Bundles ou avec le regroupement agglomératif hiérarchique, avec éventuallement des bénefices sur la précision de la classification.

Étant donné que les sorties de tractographie sont volumineuses, contenant quelques millions de tracts, et que les algorithmes de recalage sont coûteux, la simplifications de la matière blanche est obligatoire.

Dans le chapitre 9 nous avons étendu une méthode bien connue pour le recalage d'images T_1, les démons, et nous avons incorporé l'informations géométrique venant de fibres, en utilisant différentes métriques plus adaptées a l'analyse des courbes.

Nous avons comparé notre méthode de recalage avec des methodes de recalage avec tenseurs et muti-modal de $T_1 + FA$ (en utilisant le logiciel ANTS). Les résultats de recalage basés sur des image des tenseurs ont satisfait nos attentes: l'alignement de la matière blanche a été amélioré, mais le recalage était inutile pour l'analyse d'images anatomiques (T_1), et donc pour la plupart des approches multi-modales qui vont au-delà de l'analyse de la matière blanche. La comparaison avec le multi-modal $T_1 + FA$ était plus intéressant, et a montré que des améliorations de le recalage de la matiere blanche en utilisant la représentation des courant, mais ANT a montré des résultats légèrement meilleurs sur les critères d'image. D'autre part, pour la représentation des mesures pondérées, les résultats ont montré une amélioration dans la substance blanche mais également en ce qui concerne le critère d'imagerie. Comme nous pensions courants donnent une meilleure représentation de la forme de mesures, et nous concluons que l'amélioration est liée à l'application des correspondances entre faisceaux entre sujets.

En guise de travaux futurs sur le recalage, nous voudrions examiner l'utilisation de versions non-orientées de courants, comme le Varifold **?**.

En attendant, les méthodes de recalage proposées seront utilisées pour analyser l'impact de l'inclusion des connexions de la matière blanche dans le recalage pour analyser des images fonctionnel (IRMf), telles comme la détection des zones d'activation. Nous montrons des résultats préliminaires à la Fig. 10.1, où des informations de diffusion (telles que le FA) sont ajoutées au moment du recalage, pour améliorer ensuite la découverte de zones d'activation. Les résultats indiquent que les informations de connexion pourraient en effet améliorer la sensibilité. Ce premier résultat motive l'utilisation des méthodes développées dans cette thèse pour améliorer potentiellement la précision de la détection d'activation IRMf.

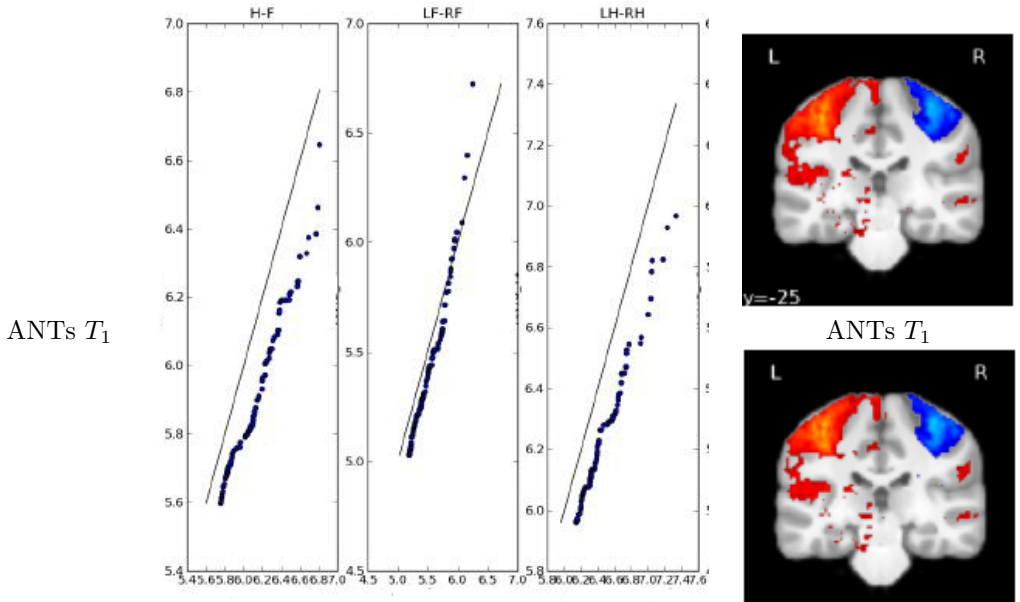

Figure 2.4: Comparaison des résultats d'une analyse de froupe de 20 sujets de la base de données HCP, en utilisant ANTs pour le recalage avec uniquement des image T_1 ; la conjonction de T_1+FA. Les résultats montrent que des valeurs les plus élevées sont obtenues avec l'incorporation de l'information venant des images de diffusion.

Chapter 3

Summary

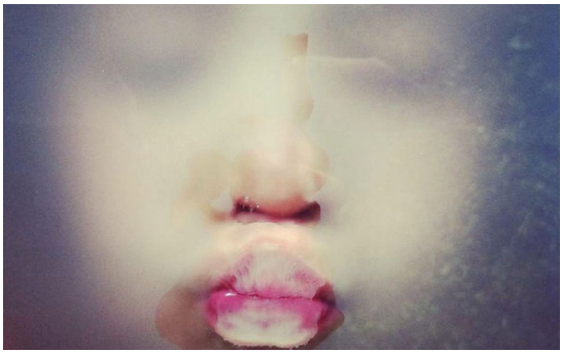

"... We have developed speed, but we have shut ourselves in. Machinery that gives abundance has left us in want. Our knowledge has made us cynical; our cleverness, hard and unkind. We think too much and feel too little. More than machinery, we need humanity. More than cleverness, we need kindness and gentleness. Without these qualities, life will be violent and all will be lost..."

—Charles Chaplin, The Barber's speech, The Great Dictator (1940)

3.1 Motivation

Since the late 90's many computational methods for the statistical analysis of brain Magnetic Resonance Imaging across populations have been proposed in order to better understand normal development as well as analysing diseases and finding biomarkers at early stage of neurodegenerative deseases.

Brain image registration consists in aligning corresponding structures to ease the comparison between different brain images. Once images are aligned, they share the same coordinate system, meaning that structures are aligned on a voxel basis. Voxel-based morphometric methods are

then used to detect changes across different studies Leporé et al. [2010], Lepore et al. [2008a], Mani et al. [2010a]. Alignment is achieved by warping the images; the deformation fields can in turn be analysed in order to quantify the shape difference between a given image and a template. The latter is useful in longitudinal studies of neurodegenerative deseases such as Alzheimer, where brain changes over time are characterized across subjects, such as decrease of white matter volume and the increase of cerebral-spinal fluid and ventricles size.

Anatomical MRI (T_1) is the reference modality in research and radiology, however since the late 90's other image modalities such as diffusion MRI and functional MRI have been gaining attention Filler [2009], Bandettini [2012], Oishi et al. [2008]. Diffusion MRI yields information on the underlying organization of the brain white matter, the connections inside the brain. Neural fibers are the pathways of brain interactions, but they also constitute the connection to the rest of the body, and are the medium used by the brain to transmit information. Lots of efforts have been spent to unveil the architecture of the brain white matter, from the estimation of each single fiber connection, to a bundle level analysis. At the latter, a higher level of abstraction is sought where the efforts are not on the microstructure of the white matter, but rather at a functional level Faria et al. [2012], Oishi et al. [2008].

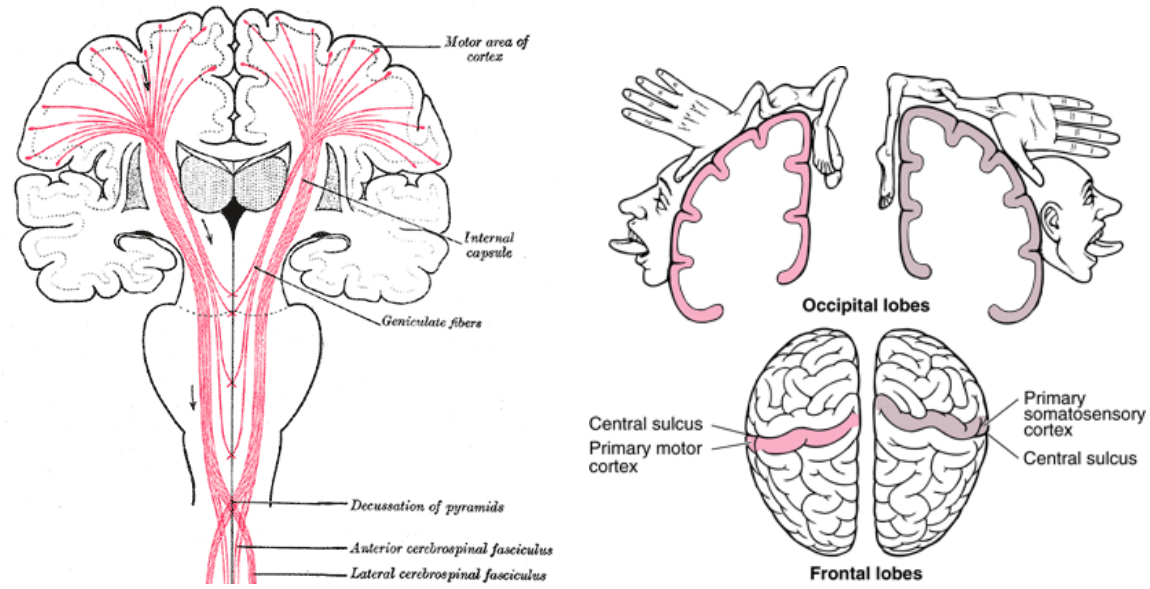

Figure 3.1: On the right the somatosensory illustration of the primary motor cortex and its topography, while on the left the white matter connections involved. Images taken from *teachmeanatomy.info* and *www.merckmanuals.com*

When we hold a glass of water and direct it to our mouth, many regions of the brain are interacting to fulfil this task: the posterior frontal lobe in charge of the motor movements, the posterior parietal lobe to analyse the space, and the occipital lobe to visualize the object, these meta-roles are illustrated in Fig. 4.1. In order to understand how the brain is organized and how it works, we need to understand how it is connected, and for this reason white matter fibers are generally classified together when connecting the same functional regions. This is crucial to understand and follow normal brain development.

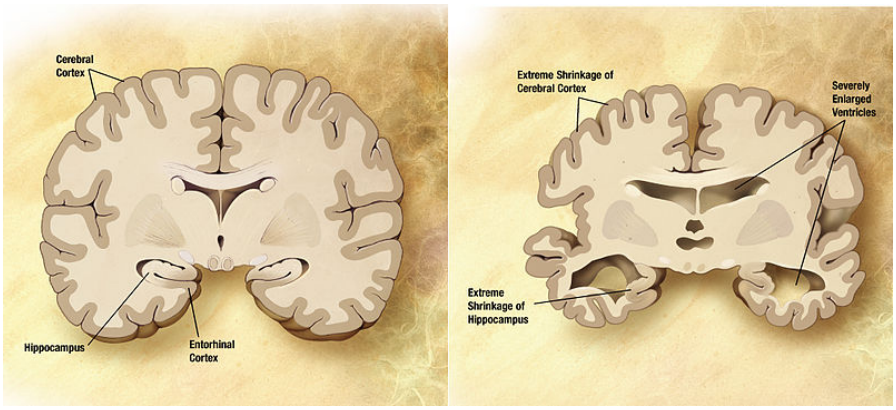

Figure 3.2: Combination of two brain diagrams to illustrate pathological brain variability. In the left normal brain, in the right brain of a person with Alzheimer's disease. Image provided by *The Alzheimer's Disease Education and Referral Center, a service of the National Institute on Aging.*

For example, early symptoms of Alzheimer (AD) are loss of short time memory, gradually followed up by language troubles and the loss of body functions. On the other hand, brain regions associated with those task are considered to develop high physical atrophy as shown in Fig. 4.2, where a comparison between a normal brain and an Alzheimer diseased brain are shown. Research has shown that in its early stages, AD is associated with microstructural abnormalities in white matter (WM) Alves et al. [2012], and these changes can also be observed in functional and anatomical images Cash et al. [2012], Lorenzi et al. [2012], Li et al. [2012], Wagner [2000]. Nevertheless, studies in diseases such as Dyslexia have shown no difference in T_1 images between poor readers and control subjects, while anisotropy in diffusion images reflected a decrease in the microstructure of the white matter tracts as shown in Carter et al. [2009], Klingberg et al. [2000]. In a later study, changes were found in both gray and white matter, and a potential correlation to defects in speech-in-noise deficits Dole et al. [2013]. Another example is the Gerstmann syndrome, that is characterized by the tetrad of four cognitive faculties. Gerstmann claimed in 1920s, that this resulted from the damage of a common functional denominator essential for those four regions. However no direct evidence has yet been found from the cognitive perspective, and a recent study suggests a detriment on the internal white matter structures connecting those four regions Rusconi et al. [2009].

Brain image registration is the basis of population comparison, nevertheless most registration techniques today rely purely on anatomical features such as sulcal lines, that are good landmarks for some functional regions and are the main information that can be extracted from anatomical T_1 images 4.3 Goualher et al. [1997, 1998], Corouge and Barillot [2002]. However, besides the most common sulci, sulci detection and classification is hard to perform on the whole brain surface, as they largely vary from one subject to another in size and location. Other registration techniques use diffusion MRI imaging, and try to map together the regions of high diffusion

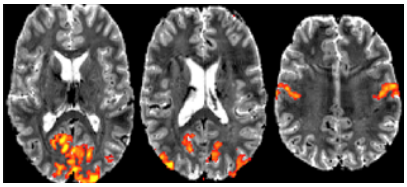

Figure 3.3: High resolution functional images show that functional activation is confined to grey matter. Image provided by *https://humanconnectome.org*

by using different diffusion representations such as Tensor based images and Fractional Anisotropy images. Although this technique can be good at detecting regions with an unexpected diffusion level in comparison to normal subjects, registration contains no information about connected regions. The later can be estimated following the paths of high diffusivity to obtain the underlying white matter structures, the fiber tracts.

This thesis is based on the hypothesis that registration should be performed in multi-modal settings in order to enhance the reliability of the correspondence and the voxel-wise comparison across subjects Hellier et al. [2002], Lemoine et al. [1991]. We also aim at checking whether using specifically some reliable neural fibers can guide the registration to not only map functional regions together, but also to characterize the internal organization of the white matter. Anatomical images are uniformly white in white matter regions, and do not contain diffusion information. As a result, the estimated deformations do not ensure the alignment of white matter. Likewise, diffusion images are not adequate for cortex analysis, as they provide no relevant information for analyzing sulcal folding and gray matter. For these reasons, diffusion based registration is mostly used for white matter analysis.

Naturally, both images provide useful information for brain analysis, and in this thesis we proposed a technique to simultaneously combine anatomical and diffusion information to enhance registration. We propose to represent white matter as geometrical structures such as curves, or point clouds, and to combine them with the T_1 anatomical image. We first propose methods to deal with the tractography outputs, to make it easier to use them in a registration context.

3.2 White Matter Representation

With current diffusion tools, we can estimate millions of fibers tracts in the white matter. For a registration framework to be efficient and accurate, we propose to extract the most relevant fiber tracts and incorporate them to the registration. We analyse and propose different techniques to group white matter tracts that share similar shape and space distances. While the relevance of a bundle can be differently defined for example by its anatomical meaning, we focus on technical aspects such as the capacity of detecting them across subjects.

In Chapter 8 we analyse three different clustering algorithms for grouping white matter tracts:

1. KMeans: a simple but widely used and known clustering algorithm. Thanks to its simplicity we propose and test different metrics to enhance intrinsic curves features.
2. Two Level Average-linkage clustering: a two level agglomerative clustering pipeline developed by Guevara et al. [2012] was applied based on segmentations priors obtained by registering subjects to the Talaraich space. In Talaraich space we obtain a segmentation of the subjects, which allows to apply the clustering algorithm on each sub-region. The second level clustering finds correspondences across subjects by applying the method to the cluster representatives obtained in the previous step.
3. QuickBundles: a fast clustering algorithm developed by Garyfallidis et al. [2012], that creates clusters on demand based on a distance threashold. Each time a new fiber is added, if no cluster is close enough to the fiber, a new cluster is created.

Each of the clustering algorithms analysed differs greatly by its features and goals. *Two Level Average-Linkage Clustering* is multi-step pipeline consisting of registration, segmentation and

multiple clustering steps. As a result we obtain corresponding bundles across subjects, nevertheless errors can be made at each of the stages, and reliability of a one-bundle to one-bundle correspondence across subjects is tightened to the reliability and priors included in previous steps. *Quickbundles* on the contrary includes no priors on the clustering, and it serves for a fast high level white matter representation compression. *KMeans* allows us to analyse the impact of different metrics when clustering fiber tracts.

The strongest white matter analysis pipeline was developed in Guevara et al. [2012] and it is based on average linkage clustering, where the tractography dataset is first divided based on previous segmentations performed on the cortex based on T_1 images, and then the algorithm is applied in each subgroup. A second level of clustering groups fibers from multiple subjects together to detect corresponding fibers across subjects. This methodology is robust, and it builds on many preprocessing steps to enhance results: T_1 based cortex segmentation is used to infer a rough initial segmentation of the white matter tracts, and registration needs to be performed before clustering multiple subjects together.

In contrast with the latter technique, QuickBundles was developed in Garyfallidis et al. [2012], and is a fast algorithm, capable of clustering a massive tractography database in a matter of seconds. Although QuickBundles has not showed to perform well on metric comparisons to other algorithms and metrics, it is very handy for fast preprocessing, and we have found that in average the main white matter tracts are finely detected.

With the aim to compare the impact of different metrics on white matter analysis, we chose K-Means algorithm and extended its metric to better suit our needs. We showed how simple metrics such as Euclidean distances, the most widely used in clustering algorithms, can be improved. Specifically, we focus on metrics such as Hausdorff and Measures, where no point to point correspondence is required. This is relevant in white matter analysis not only because fibers can have different lengths, but also, as a consequence of poor image quality, a fiber can end earlier or be split. Our results show that the Measure metric outperformed other metrics. We have also introduced different metrics to evaluate the clustering, which are widely known in the machine learning literature, but hardly used on the diffusion neuroimaging community.

We are aware that distances such as Hausdorff or Measure are computationally more expensive than a point-wise distance such as Euclidean, and as a consequence of the high-dimensionality of the diffusion data, we found ourselves forced to explore other options. We introduced Multi-dimensional scaling to embed tracts into a new featured spaced defined by the desired metric, to then cluster the embedded tracts with the regular K-Means algorithm. This is performed by selecting a percentage of random tracts as sampled, and we show that while computation time dramatically changes, accuracy remains stable when varying this percentage.

3.3 Multi-modal Registration: T_1 and Fiber Tracts

The heart of this thesis is on the multi modal registration of T_1 images and the geometric descriptors of fiber tract. We explore different representations of the white matter architecture, each of them being associated with different priors to the registration. We build on a well-known T_1 registration algorithm, the *Demons Algorithm* that estimates a diffeomorphic deformation that minimizes the sum of squared distances between a target and a source image. The new approach jointly minimizes both image and geometric descriptor distances between the source and target images and fibers respectively.

In Chapter 9 we develop and analyse a multi-modal algorithm with the following geometry distances:

1. Closest Point Distance (CPD): the fibers are represented as as a sequence of points. For this distance a one-to-one fiber correspondences are assumed a priori, and each point in the moving fibers will move towards to closest point on the corresponding fixed fiber. This restriction comes from its high computational cost. This direction will also be restricted by the image forces and the regularization constraints to hold for diffeomorphic properties.

2. Currents: This distances uses the notion of tangents across the curves (fibers). Fibers are represented as the integral of the vector fields defined by its tangents. Thus, a consistent orientation across fibers is necessary for a proper comparison, as opposites direction may mislead the registration. As a consequence, this metric requires as a prior some bundle-to-bundle correspondences, a previous segmentation of fibers consistently oriented across individuals.

3. Weighted Measures: This builds on a simplification of the currents distance, with a weaker geometrical meaning. Tangents are replaced by weights representing the importance of bundles, e.g. size. Each bundle is represented by the centroid of the cluster, weighted by its importance on the subject. This metric allows registering two subjects without strong priors and preprocessing steps.

Different approaches have been explored during this thesis. The first proof of concept was using the Closest Point Distance, where results have shown that T_1 registration could be widely improved, as T_1 alignment was maintained by the new algorithm, but white matter alignment was greatly improved. Some subjects have even shown improvements on the T_1 alignment, verifying that indeed white matter information can lead to better overall inter-subject registration.

When using the CPD metric, a fiber-to-fiber correspondence is convenient for computational reasons. This was obtained by using the two-level pipeline of average-linkage clustering developed in Guevara et al. [2012]. The resulting bundles were further simplified to only one representative fiber, the centroid.

To avoid this fiber-to-fiber requirement which is mostly unrealistic, we upgrade the registration algorithm by representing fiber bundles with Currents. Instead of a cloud of points, each bundle is represented by a sum of dirac deltas centered at fiber points associated with the tangents following the curve direction. Although this new representation does not require fiber-to-fiber inter-subject correspondences, it does requires bundle-to-bundle correspondence as orientation needs to be consistent across subjects for a proper registration. Results have once again shown to hold T_1 alignment while dramatically improving tractography alignment in comparison with the original algorithm.

In this last stage we remove the requirements of bundle-to-bundle correspondences. The reason why this dependency is undesirable is usability. First, obtaining corresponding bundles across subjects takes lots of preprocessing time, but second, it is not always plausible to define correspondences across subjects. The latter holds especially in neurodegenerative diseases, and longitudinal studies for analyzing brain development. But we were still interested in the white matter simplification, and a new metric was defined on that basis. We represented the whole tractography dataset as a sum of dirac delta centered at each point of each cluster representative. The clustering can be performed with any method, but we have used QuickBundles. Each dirac delta is weighted by the amount of fibers there was in the cluster of the representative. By doing

so, the registration is lead mostly by the larger clusters, which are expected to be the main white matter tracts. With this reasoning, small bundles are taken as noise, and have low impact on the alignment. Once again, results have shown a dramatic improvement of white matter alignment, while holding accurate results for T_1 image alignment.

3.4 Conclusion

Population analysis for detecting disease biomarkers and for understanding normal growth is nowadays a standard technique linked to the wide availability of scanners in hospitals and the new interest of sharing research purpose databases. The wide range of imaging techniques measuring different features of the brain leads to a natural evolution path of the analysis. Multi-modal analysis has received more and more attention in the neuroimaging field at every stage of analysis: white matter clustering, functional region activation detection, cortex segmentation, registration, etc.

Within this thesis we have mainly explored the simplification of white matter structure, and how white matter can be incorporated into a registration framework to improve inter-subject analysis.

In Chapter 8 we have performed an extensive analysis of common techniques to simplify intra-subject fiber tractography analysis. With the interest of further performing inter-subject studies, we focus only on the main tracts, which are expected to be large and easily detectable across subjects. We have compared different clustering algorithms for the simplification of white matter, from the most famous and widely known K-Means, to hierarchical average linkage, and a new proposed algorithm in the community, QuickBundles. The latter was specially designed for the fast analysis of massive white matter datasets.

We have chosen K-Means for the analysis of the different metrics on clustering, and we have proven that metric better suited for curves can enhance clustering results. However further work could be the implementation of Measures with Multi-dimensional scaling on QuickBundles or on average linkage clustering and one can hope that it will enhance clustering accuracy.

Given that tractography outputs are large, containing possible few million tracts, and registration algorithms are computationally expensive to compute, prior simplifications of the white matter is mandatory.

In Chapter 9 we have extended a well-known method for T_1 image registration, the Demon's Framework, and incorporated into it the geometrical information coming from fibers tracts by using different metric well suited for curves.

We have compared our registration methodology to a tensor-based and a muti-modal T_1+FA registration using the ANTs software. For tensor-based registration results were as expected, as white matter alignment was improved but the registration was useless for T_1 analysis, and therefore for most multi-modal approaches that go beyond white matter analysis. The comparison with the multi-modal $T_1 + FA$ was more interesting, as for the Currents representation improvements where mostly in white matter, but ANTs showed slightly better results on image criteria. On the other hand, with the Weighted Measures representation, results showed improvement in white matter but also regarding the imaging criterion. As we believe that Currents give a better representation of shape than Measures, we intuitively conclude that the improvement was related to enforcing bundle correspondences across subjects.

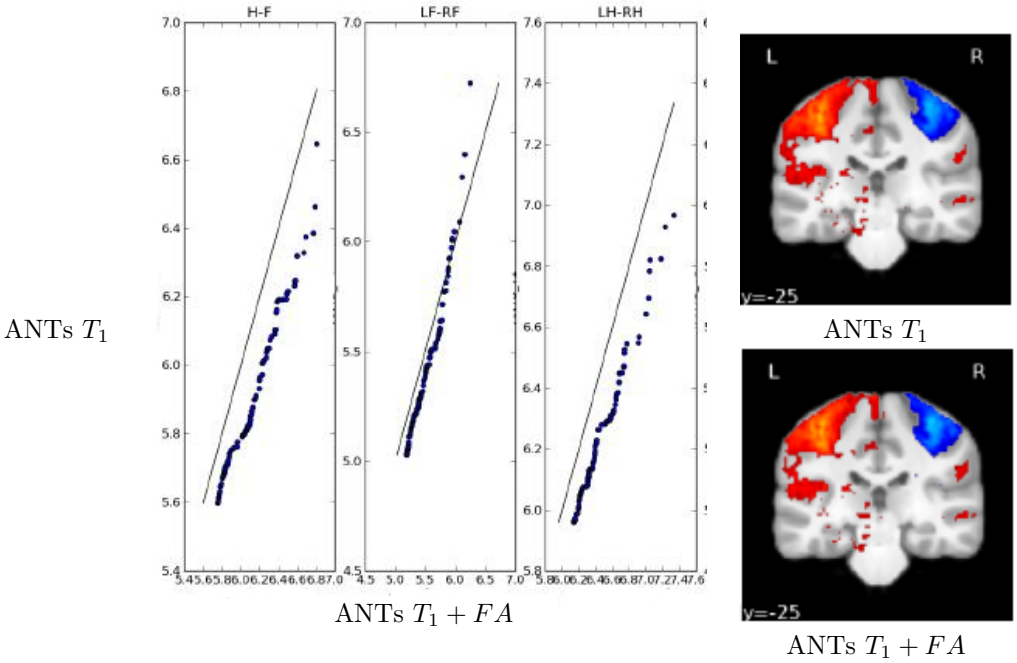

Figure 3.4: Comparison between a group analysis registration of 20 subjects from the HCP database, using ANTs with purely T_1 images, and ANTs with $T_1 + FA$. Results shows that higher values are obtained with the incorporation of information coming from diffusion imaging, hinting at reduced functional variability across subjects.

As future work on registration, it is worth investigating the use of non-oriented versions of currents, such as with Varifold.

Meanwhile, the proposed registration methods will be used to analyze the impact of including white matter connections for normalization on fMRI analysis, such as activation zones detection. A proof of concept of adding diffusion information such as FA to the registration in a group analysis of activation detection zones is shown in Fig. 10.1, indicating that indeed, connection information might improve sensitivity. This first results motivates the use of the methods developed in this thesis to potentially improve the accuracy on fMRI activation detection. A proof of concept of adding diffusion information such as FA to the registration in a group analysis of activation detection zones is shown for both registrations on Fig. 10.1 (right images), indicating that indeed, connection information might improve accuracy. This first results motivates the use of the methods developed in this thesis to potentially improve the accuracy of fmri activation detection.

Chapter 4

Abstract

"Find what you love and let it kill you."

—Charles Bukowski

Since the late 90's many computational methods for the statistical analysis of brain Magnetic Resonance Imaging across populations have been proposed in order to better understand normal development as well as analyzing diseases and finding biomarkers at early stage of neurodegenerative deseases.

Brain image registration consists in aligning corresponding structures to ease the comparison between different brain images. Images are taken to the same coordinate system where voxel-based morphometric methods are used to detect changes across different studies Leporé et al. [2010], Lepore et al. [2008a], Mani et al. [2010a]. The deformations applied to achieve the alignment are further analyzed in order to measure the amount of deformations between a given image and a template. The latter is useful in longitudinal studies of neurodegenerative deseases such as Alzheimer, where brain changes over time are characterized across subjects, such as decrease of white matter volume and the increase of cerebral-spinal fluid in ventricules.

Anatomical MRI (T_1) is the reference in research and radiology, however since the late 90's other image modalities such as diffusion MRI and functional MRI have been gaining attention Filler

[2009], Bandettini [2012], Oishi et al. [2008]. Diffusion MRI yields information on the underlying organization of the brain white matter, the connections inside the brain. Neural fibers are the pathways of brain interactions, but they also make up the connection to the rest of the body, and the medium used by the brain to transmit information. Lots of efforts have been applied to unveil the architecture of the brain white matter, from the estimation of each single fiber connection, to a bundle level analysis. At the latter, a higher level of abstraction is sought where the effors are not on the microstructure of the white matter, but rather at a functional level Faria et al. [2012], Oishi et al. [2008].

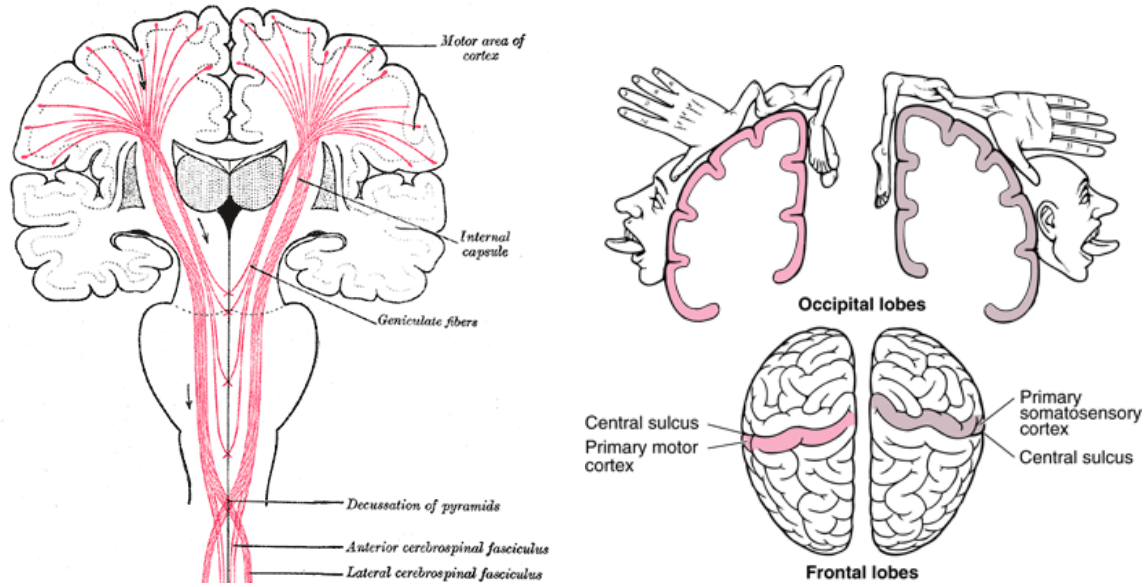

Figure 4.1: On the right the somatosensory illustration of the primary motor cortex and its topography, while on the left the white matter connections involved. Images taken from *teachmeanatomy.info* and *www.merckmanuals.com*

When we hold a glass of water and direct it to our mouth, many regions of the brain are interacting to fulfill this task: the posterior frontal lobe in charge of the motor movements, the posterior parietal lobe to analyze the space, and the occipital lobe to visualize the object, these meta-roles are illustrated in Fig. 4.1. In order to understand how the brain is organized, and how it works, we need to understand how it is connected, and for this reason white matter fibers are generally classified together when connecting the same functional regions. This is crucial to understand and follow normal brain development.

For example, early symptoms of Alzheimer (AD) are loss of short time memory, gradually followed up by language troubles and the loss of body functions. On the other hand, brain regions associated with those task are considered to develop high physical atrophy as shown in Fig. 4.2, where a comparison between a normal brain and an Alzheimer diseased brain are shown. Research has shown that in its early stages, AD is associated with microstructural abnormalities in white matter (WM) Alves et al. [2012], and this changes can also analyzed in functional and anatomical images Cash et al. [2012], Lorenzi et al. [2012], Li et al. [2012], Wagner [2000]. Nevertheless, studies in diseases such as Dyslexia have shown no differences in T_1 images between

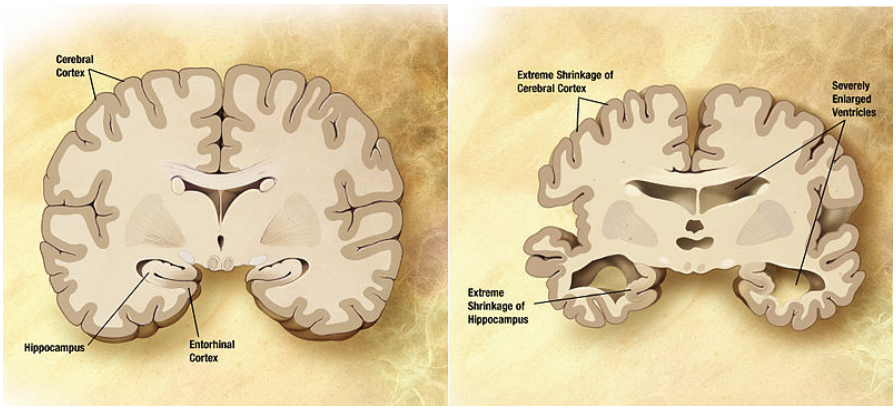

Figure 4.2: Combination of two brain diagrams to illustrate pathological brain variability. In the left normal brain, in the right brain of a person with Alzheimer's disease. Image provided by *The Alzheimer's Disease Education and Referral Center, a service of the National Institute on Aging.*

poor readers and control subjects, while anisotropy in diffusion images reflected a decrease in the microstructure of the white matter tracts as shown in Carter et al. [2009], Klingberg et al. [2000]. In a later study, changes were found in both gray and white matter, and a potential correlation to defects in speech-in-noise deficits Dole et al. [2013]. Another example is the Gerstmann syndrome, that is characterized by the tetrad of four cognitive faculties. Gerstmann claimed in 1920s, that this resulted from the damage of a common functional denominator essential for those four regions, However no direct evidence has yet been found from the cognitive perspective, and a recent study suggests a detriment on the internal white matter structures connecting those four regions Rusconi et al. [2009].

Brain image registration is the basis of population comparison, nevertheless most registration techniques today rely purely on anatomical features such as sulcal lines, that are good landmarks for some functional regions and are the main information that can be extracted from anatomical T_1 images 4.3 Goualher et al. [1997, 1998], Corouge and Barillot [2002]. However, besides the most common sulci, sulci detection and classification is hard to perform on the whole brain surface, as they largely vary from one subject to another in size and location. Other registration techniques use diffusion MRI imaging, and try to map together the regions of high diffusion by using different diffusion representations such as Tensor based images and Fractional Anisotropy images. Although this technique can be good at detecting regions with an unexpected diffusion level in comparison to normal subjects, registration contains no information about connected regions. The later can be estimated following the paths of high diffusivity to obtain the underlying white matter structures, the fiber tracts.

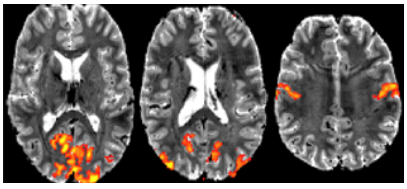

Figure 4.3: High resolution functional images show that activation detection regions are tightly link to sulcal lines. Image provided by *https://humanconnectome.org*

This thesis is based on the hypothesis that registration should be performed in multi-modal settings in order to enhance the reliability of the correspondence and the voxel-wise comparison

across subjects Hellier et al. [2002], Lemoine et al. [1991]. We also aim at checking whether using specifically some reliable neural fibers can guide the registration to not only map functional regions together, but also to characterize the internal organization of the white matter. Anatomical images are uniformly white in white matter regions, and do not contain diffusion information. As a result, the estimated deformations do not ensure the alignment of white matter. Likewise, diffusion images are not adequate for cortex analysis, as they provide no relevant information for analyzing sulcal folding and gray matter. For these reasons, diffusion based registration is mostly used for white matter analysis.

Naturally, both images provide useful information for brain analysis, and in this thesis we proposed a technique to simultaneously combine anatomical and diffusion information to enhance registration. We propose to represent white matter as geometrical structures such as curves, or point clouds, and to combine them with the T_1 anatomical image. We show that T_1 image jointly with geometric descriptors from diffusion image can be used to align subjects with the same accuracy as solely T_1 image registration. Nevertheless, with joint information we can concurrently ensure to align gray matter seen in T_1 images and white matter structures.

With current diffusion tools, we can estimate millions of neural fibers in the white matter. For a registration framework to be efficient and accurate, we propose to extract the most relevant fiber tracts, and incorporate them to the registration. We show that few featured fibers can help to better guide the white matter registration. Following this line, an exploration of the white matter architecture has been performed, and we show different techniques for analyzing white matter and possible ways of organizing them by their similarity in space and shape. The relevance of bundles has been defined by our capacity of detecting them across subjects, or the single subject importance (the size of the bundle).

Chapter 5

Contributions

"Science must not he a selfish pleasure; those who have the opportunity to devote themselves to scientific goals ought equally to be the first to put their knowledge at the service of humanity."

—Karl Marxs, Economics: Critical Assessments

5.1 Publications

In peer reviewed conference proceedings – Full lenght papers [* Oral Presentation]

– 2013

- Unsupervised Fiber Bundles Registration using Weighted Measures Geometric Demons

Viviana Siless; Sergio Medina; Pierre Fillard; Bertrand Thirion

Workshop on Multi Modal Brain Image Analysis, Sep 2013, Nagoya, Japan. Springer Lecture Notes in Computer Science

- A Comparison of Metrics and Algorithms for Fiber Clustering

  Viviana Siless; Sergio Medina; Gaël Varoquaux; Bertrand Thirion

  Pattern Recognition in NeuroImaging, Jun 2013, Philadelphia, United States.

– 2012

- Joint T1 and Brain Fiber Log-Demons Registration Using Currents to Model Geometry

  Viviana Siless; Joan Glaunès; Pamela Guevara; Jean-François Mangin; Cyril Poupon; Denis Le Bihan; Bertrand Thirion; Pierre Fillard

  Medical Image Computing and Computer Assisted Intervention, Oct 2012, Nice, France, France.

- Connectivity-informed Sparse Classifiers for fMRI Brain Decoding [*]

  Bernard Ng ; Viviana Siless; Gaël Varoquaux; Jean-Baptiste Poline; Bertrand Thirion; Rafeef Abugharbieh

  Pattern Recognition in Neuroimaging, Jul 2012, London, United Kingdom.

– 2011

- Joint T1 and Brain Fiber Diffeomorphic Registration Using the Demons [*]

  Viviana Siless; Pamela Guevara; Xavier Pennec; Pierre Fillard

  Multimodal Brain Image Analysis, 7012, Springer Berlin / Heidelberg, pp. 10-18, 2011, Lecture Notes in Computer Science, 978-3-642-24445-2

5.2 Abstracts

In peer reviewed conference – abstract [* Oral Presentation; $ awarded]

– 2013

- Brain Image and Fiber Log-demons Registration with Currents [*, $]

  Viviana Siless; Joan Glaunès; Pamela Guevara; Jean-François Mangin; Cyril Poupon; Denis Le Bihan; Bertrand Thirion; Pierre Fillard

  Organization for the Human Brain Mapping, June 2013, Seattle, USA.

  Trainee Abstract Travel Awards: 140 award recipients out of 1281 applications.

– 2012

- Joint T1 and brain fiber diffeomorphic registration using the demons

  Viviana Siless; Pamela Guevara; Xavier Pennec; Pierre Fillard; Bertrand Thirion.

  Organization for the Human Brain Mapping, Jun 2012, Beijing, China

5.3 Invited Talks

– "Joint T1 and Brain Fiber Log-demons Registration using Currents to model Geometry"

The 11th Brain Connectivity Workshop (BCW'2012) will be held on June 6-8, 2012, Beijing, China

5.4 Awards

– Trainee Abstract Travel Award for the 2013 OHBM Annual Meeting in Seattle, WA, USA.

Submitted abstract: Brain Image and Fiber Log-demons Registration with Currents.

140 award recipients out of 1281 applications.

Chapter 6

Introduction

"the only people for me are the mad ones, the ones who are mad to live, mad to talk, mad to be saved, desirous of everything at the same time, the ones who never yawn or say a commonplace thing, but burn, burn, burn like fabulous yellow roman candles exploding like spiders across the stars."

— Jack Kerouac, On the Road

6.1 History of brain knowledge

The heart has long been thought to be the substrate of intelligence. In ancient Egypt, from the late Middle Kingdom onwards, in preparation for mummification the brain was regularly removed, as it was believe to be head stuffing.

Pythagorean Alcmaeon of Croton (6th and 5th centuries BC) believed that the seat of sensations was in the brain, and that storing up perceptions gave memory and belief which when stabilized became knowledge Gross [1987].

In the 4th century BC Hippocrates believed the brain to be the seat of intelligence while Aristotle thought that the heart was the seat of intelligence and the brain was a cooling mechanism for the

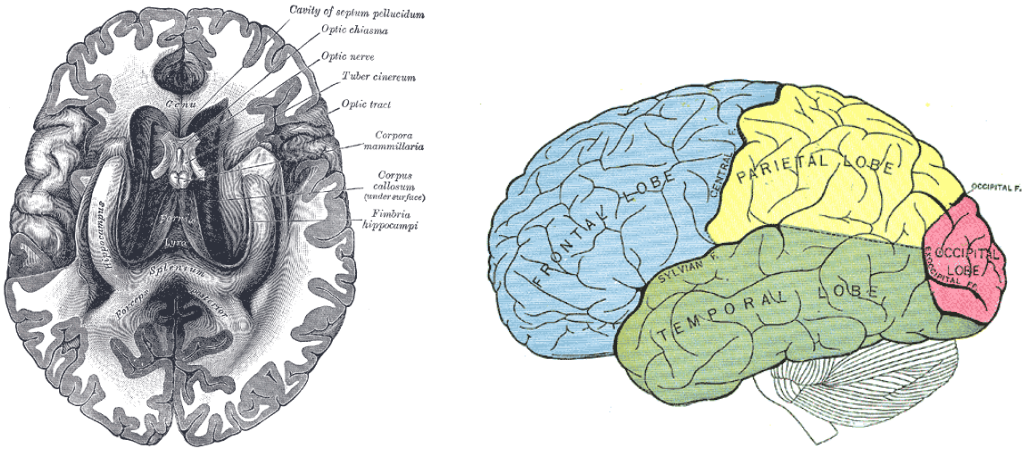

Figure 6.1: Anatomy of the human brain as we know today drawn in Henry Gray book published in 1858. A book widely appreciated as an extraordinary and authoritative book in medicine. Gray and Carter [2002]

blood. He reasoned that humans are more rational than the beasts because they have a larger brain to cool their hot-bloodedness Bear et al. [2002].

During the Hellenistic period, Herophilos of Chalcedon (c.335/330–280/250 BC) proposed that the brain rather than the heart housed, the intellect, and he believed that the calamus scriptorius in the cranium was the seat of the human soul. Erasistratus of Ceos (c. 300–240 BC) concluded that the heart was not the center of sensations, but instead that it functioned as a pump.

Years have passed but with little advance on the brain understanding. Up to 19th century cerebral dissection used to be the only way to access the neural architecture Dejerine [1985, 1901]. The brain as we know today is identical as the one describe in Grays Anatomy book which was published in 1858 Gray and Carter [2002], see Figure 6.1. They knew very little of the complex functioning of the brain but they knew quite a lot about its anatomy.

Up to now only little is known about the brain compared to other organs. During the 1800s, scientists debated whether areas of the brain corresponded to specific functions, or if the brain functioned as a whole. The work of Paul Broca, Carl Wernicke and Korbinian Brodmann eventually helped to show that different areas of the brain have specific functions Broca [1861], Wernicke [1897].

6.2 Anatomy

The brain controls the nervous system and regulates the activity of humans (and many other aspects). Neural tissue uses electrical impulses to send information from one region of the body to another. How the information is carried through the *white matter (WM)* and how the different parts of the brain are connected has not been fully unveil. About 98% of neural tissue is concentrated in the brain and spinal cord.

The white matter is a major component of the

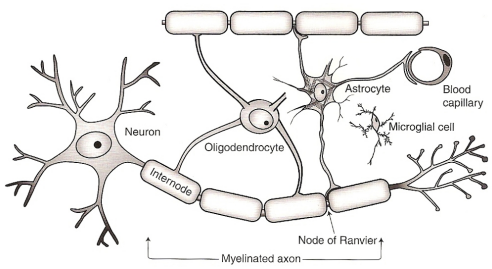

Figure 6.2: Schematic representation of the major cellular elements of neural tissue. A neural cell body in the gray matter extends several short dendritic processes and a single, long axonal process. The axon is in the white mat-

central nervous system (CNS). It is composed of axonal nerve fibers or neurons covered by a myelin sheath giving its distinctive color. White matter axons are often tightly packed and highly organized. *Axons* are often called nerve fibers and bundles of these axons are called fiber tracts, see Fig. 6.2. White matter connects gray matter areas together and carries nerve impulses between neurons.

The *gray matter* is also a major component of the CNS composed of unmyelinated neurons as opposed to white matter. It has gray brown color which comes from the capillary blood vessels and the neural cell bodies. The cerebral cortex is the most important structure of the gray matter and plays a major role in cognitive functions. Gray matter is highly folded to find a larger surface in the limited volume of the skull. This folding process creates grooves on the surface of the brain called *sulci* and ridges called *gyri*. About two thirds of the cortical surface is buried in those sulci.

The introduction of modern imaging techniques such as MRI, fMRI, dMRI, PET and MEG is helping the field of neuroscience to grow rapidly, bringing a new insight into the human brain analysis.

6.3 Magnetic Resonance Imaging (MRI)

Thanks to MRI one can investigate the anatomy in health and disease avoiding exposure to ionizing radiation. Diffusion MRI (dMRI) gives insight into the underlying white matter neural fiber architecture, and functional MRI links anatomical regions to functional tasks with a more accurate spatial resolution than other techniques such as PET or MEG. A difficulty of functional analysis is to isolate a task, as even in resting state multiple brain regions are functioning together at the same time. This can be concluded from fMRI as high correlations are observed in the spontaneous activity of several regions at resting state. To better analyze the correlation between functional regions, fMRI can be complemented with dMRI, but also from T_1-weighted MR images as sulcal line landmarks can be extracted from them Ng et al. [2012], Molko et al. [2003], Mangin et al. [2004] . By combining different modality images with different perspectives from the brain we will hopefully converge to a complete model of the brain, to help us understand it and analyze it.

6.3.1 Structural MRI (T_1)

Magnetic resonance images primarily reflect water and fat concentration that are observed though the signal from the hydrogen nuclei. A magnetic field is used to aligned the hydrogen atoms, which are then excited by the radio-frequency (RF) pulse. MRI images are created by measuring the excitation and refocusing time. Hydrogen atoms are present in any tissue containing water molecules. The contrast between different tissues is determined by the rate at which the atoms return to the equilibrium state.

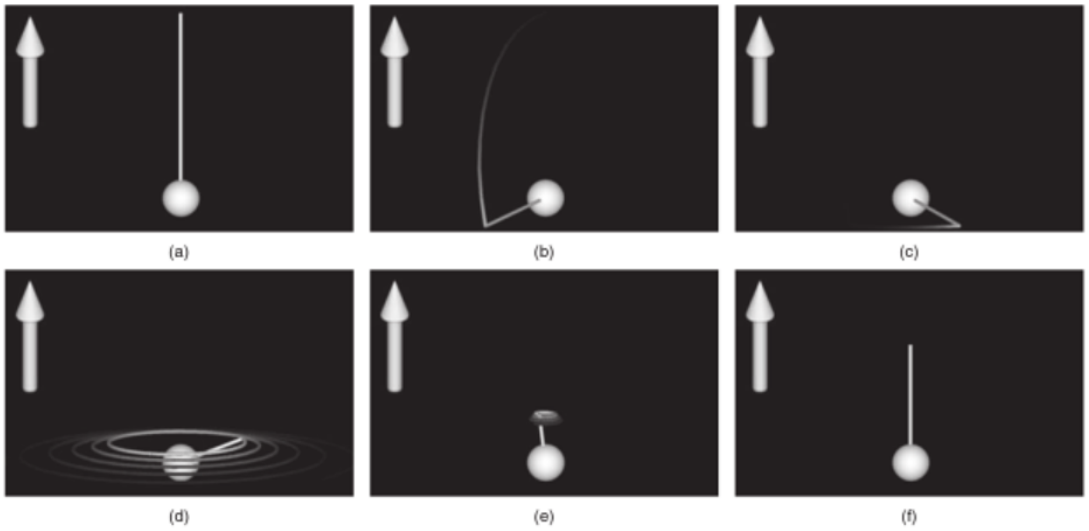

Figure 6.3: Spin behavior during MRI imaging: in (a) the spin is aligned with the magnetic field B_0 (white arrow). After applying an RF pulse, the spin rotates away from B_0 in (b), and in (c) precesses about the axis of B_0. (d) represents the transverse phase decay, and the longitudinal amplitude decay is shown in (e), until is alignment with B_0 again in (f). Image adapted from Pipe [2009].

MRI data is collected by turning certain magnetic field on and off in sequence, referred to as *pulse sequence*. The spins of the hydrogen nuclei can be modeled as a dipole (north and south poles). These spins align themselves with the applied external magnetization. The three magnetic fields generated by an scanner are the B_0, radio-frequency (RF) pulses, and magnetic field gradients. B_0 is known as 'no-gradient' as it is used to align the spins to a reference direction. B_0 is a strong static field of 1.5 to 7 Tesla most commonly, that tends to increase across years. The RF pulses are applied for brief time, and oscillate at radio frequencies. When the RF pulse frequency is applied at the Larmor frequency of the spins (γB, γ being the gyromagnetic ratio, and B the magnetic field strength), it lets them rotate about the z-axis. RF pulses are used for excitation and refocusing. RF-induced excitation rotates spins away from their preferred orientation along B_0. The part of the magnetization that is perpendicular to B_0 decays exponentially with a constant time T_2. The T_2 decay time varies with tissues and is typically on the order of milliseconds. The spins realign themselves exponentially in the direction of B_0 with a time constant T_1 which varies with tissues, but is typically of the order of one second. And example of this process is shown in Fig. 6.3.

MR Image contrast may be weighted to demonstrate different anatomical structures or pathologies. Each tissue returns to its equilibrium state after excitation by the independent processes of T1 (spin-lattice) and T2 (spin-spin) relaxation. Differences in relaxation time across different structures such as gray matter, white matter and CSF (cerebrospinal fluid) are shown in Fig 6.4. These

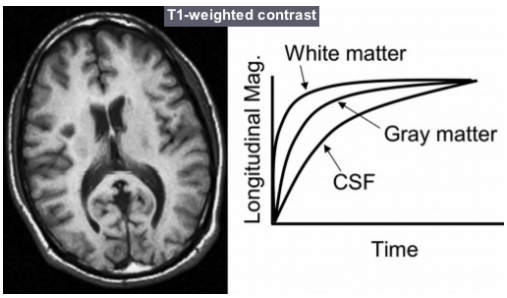

Figure 6.4: Comparison of relaxation T_1 relaxation time across different structures: White Matter, Gray Matter, and Cerebrospinal Fluid (CSF). Image adapted from Pooley [2005]

time differences let us characterize different tissues in the brain using MRI.

T1-weighted images are useful for segmenting cerebral cortex and identifying fatty tissue.

T2-weighted images are useful for detecting edema, revealing white matter lesions and assessing zonal anatomy in the prostate and uterus. The contrast provided between grey and white matter makes it the optimal choice for many conditions of the central nervous system including demyelinating diseases, dementia, cerebrovascular disease, infectious diseases and epilepsy.

6.3.2 Diffusion MRI (dMRI)

6.3.2.1 Principles

Diffusion weighted magnetic resonance imaging was introduced in the middle of the 80's by Lebihan and Breton [1985], Merboldt et al. [1985], Taylor and Bushell [1985], and today is the only non invasive technique capable of describing the geometry of the underlying brain microstructure.

In 1984 diffusion MRI was introduced by Wesbey Wesbey et al. [1984], but their acquisition sequence was not clinically feasible. Later Taylor and Bushell Taylor and Bushell [1985] did the first diffusion acquisition using hen's egg as phantom in a small bore magnet. Lebihan did the first dMRI acquisition in vivo of the human brain using a whole body scanner Lebihan and Breton [1985], Bihan et al. [1986]. At that time dMRI was simply the unprocessed result of a sequence application in only one gradient direction Hagmann et al. [2006].

The first important application of diffusion MRI emerged in early 1990s when it was discovered that dMRI can detect a stroke in its acute phase Moseley et al. [1990a]. Around the same time, scientist had also noticed that there is a peculiar property of water diffusion in highly ordered organs such as brains Moseley et al. [1990b], Doran et al. [1990], Turner et al. [1990] In these organs water does not diffuse equally in all directions but preferentially along axonal fiber directions. This property is known as diffusion anisotropy.

Shortly after the first acquisitions of diffusion weighted images in vivo Moseley et al. [1990a] Basser proposed in Basser [1993] the formalism of Diffusion Tensor (DT) model. Diffusion tensor imaging describes the three dimensional nature of anisotropy in tissues by assuming that the average diffusion of water molecules follows a Gaussian distribution. DTI has been proved to be extremely useful to study the normal and pathological human brain Bihan et al. [2001].

Molecular diffusion or Brownian motion was first formally described by Einstein in 1905 Hagmann et al. [2006]. The term molecular diffusion refers to the notion than any type of molecule in a fluid is randomly displaced as the molecule is agitated by thermal energy. Most of the molecules travel short distances and only a few travel further. Typically the displacement distribution for free water molecules is a Gaussian (bell shaped) function.

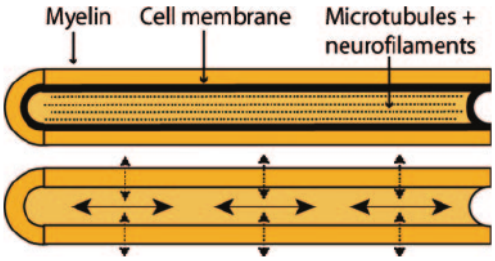

Figure 6.5: Diagram showing the cellular elements that contribute to diffusion anisotropy. Image adapted from Hagmann et al. [2006]

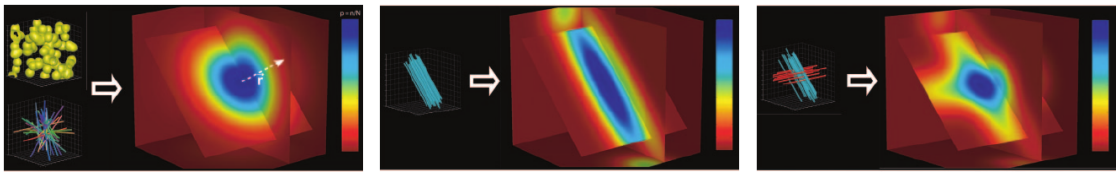

Figure 6.6: Diffusion probability density function within a single voxel: (a) shows randomly tubular oriented structures (top left), such as axons (bottom left) that intersect. The 3D displacement distribution is roughly bell shaped, resulting in a symmetric image with no preferential direction of diffusion. (b) shows the diffusion probability density function withing a voxel which all the axons are aligned in the same direction. The displacement distribution is cigar shaped and aligned withe the axons. (c) shows the diffusion probability density function of two populations of fibers intersecting at 90°. The displacement distribution produced is a cross shape. Image adapted from Hagmann et al. [2006].

When molecules are agitated by thermal energy alone, the displacement distribution is centered. This means that the average displacement of the molecular population is zero. Factors other than heat also may contribute to molecular displacement. The same random diffusion is given to water molecules within impermeable spheres that may be introduced into the glass of water. The water molecules inside each sphere diffuse within the restricted space of that sphere; and the water molecules outside the sphere move randomly around them. Because molecules inside the sphere cannot move beyond its boundaries, and because molecules outside cannot penetrate the sphere, the expected displacement distance is reduced. It is difficult to predict the shape of the resultant displacement distribution, but it will be more or less bell shaped and narrower than that for unrestricted diffusion if the diffusion time interval is sufficiently long. Biological membranes are semipermeable and water molecules can cross them with some resistance.

Biological tissues are highly heterogeneous as they consist of various compartments and barriers with different diffusivity, see Fig 6.5 for layers illustration. Neuronal tissue consists of tightly packed and coherently aligned axons that are surrounded by glial cells and that often are organized in bundles. As a result, movements of water molecules are hindered in a perpendicular direction to the axonal orientation rather than parallel to it. Experimental evidence suggests that the tissue component predominantly responsible for the anisotropy of molecular diffusion observed in white matter is not myelin, as one might expect, but rather the cell membrane Beaulieu [2002]. The degree of myelination of the individual axons and the density of cellular packing seem merely to modulate anisotropy. Furthermore, axonal transport, microtubules, and neurofilaments appear to play only a minor role in anisotropy measured at MR imaging Beaulieu [2002]. An illustration of white matter diffusivity hindered by myelination can be seen in Fig. 6.6.

6.3.2.2 Diffusion MRI(dMRI) acquisition

Using a pulsed gradient spin-echo (SE) sequence, spins are exposed to different magnetic field strengths depending on their position along the gradient axis. A regular diffusion sequence is shown in Fig. 6.7a. The pulsed gradient SE sequence includes two additional diffusion gradient

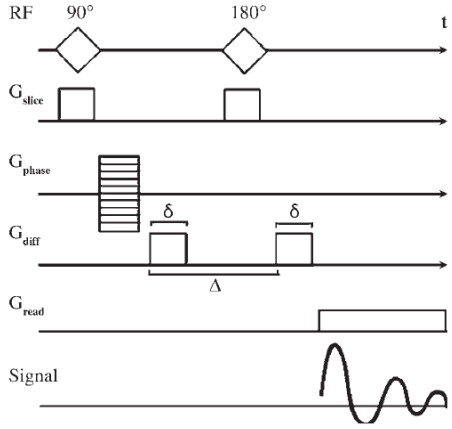

(a) Diagram showing the pulsed gradient SE sequence. δ is the dilation of the diffusion encoding gradient. Δ is the diffusion time interval . G_{phase} is the phase encoding gradient , G_{read} is the readout gradient. G_{slice} section is the selective gradient. RF radiofrequency pulse, t acquisition time.

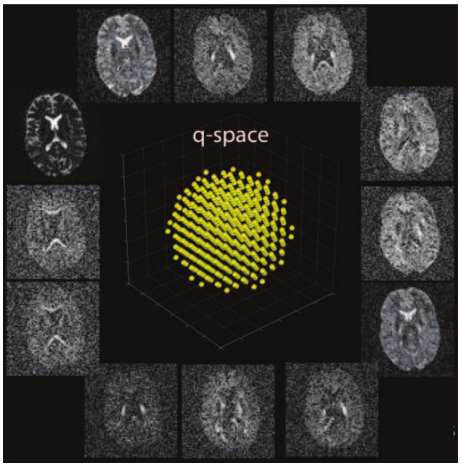

(b) Series of diffusion weighted MR brain images obtained with variations in the direction and strength of the diffusion gradient in the pulsed gradient SE sequence. Each image show the signal sampled at one point in the q space (yellow dots). Every sampling point in the q-space corresponds to a specific direction strength on the diffusion gradient. MR signal generated by the phase and frequency encoding gradients is sampled to fill a q-space (coordinate system used to organize the signal measurements).

Figure 6.7: Images adapted from Hagmann et al. [2006].

pulses. The first of the two gradients pulses in this sequence introduces a phase shift that is dependent on the strength of the gradient at the position of the spin at $t = 0$. Before the application of the second gradient pulse, which induces a phase shift dependent on the spin position at $t = \delta$, a 180° RF pulse is applied to reverse the phase shift induced by the first gradient pulse. Spins that remain at the same location along the gradient axis during the two pulses will return to their initial state. However spins that have moved are subject to a different field strength during the second pulse and therefore do not return to their initial state. Those spins experience a total phase shift that results in decreased intensity of the measured MR spectroscopic signal. A diffusion gradient can be represented as a 3D vector q whose orientation is the direction of diffusion and whose length is proportional to the gradient strength. The application of a single pulsed gradient SE sequence produces one diffusion weighed image that corresponds to one position in q-space or, more precisely, that depicts the diffusion-weighted signal intensity in a specific position q for every brain position.

But the values of the measured signal are most commonly organized in a coordinate system known as k-space. Performing the acquisition enables the filling of the k-space as shown in Fig 6.7b. To transform the raw MR imaging data from k-space into a position-encoded visual image, a Fourier transform is

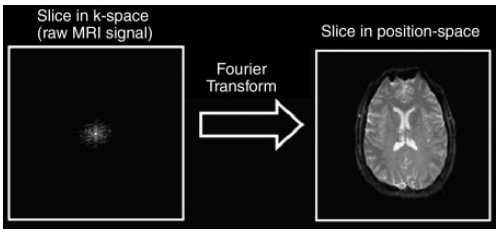

Figure 6.8: A a Fourier transform is applied to the q-space images to reconstruct the image in the standard position space. Image adapted from Hagmann et al. [2006].

applied Glockner et al. [2005].

A single application of the pulsed gradient SE sequence produces one brain image with a given diffusion weighting. Multiple repetitions of the sequence each with a different diffusion weighing are necessary to sample the entirely of the q-space. The q-space is sampled for a specific diffusion time interval δ which is determined by the interval between the two gradient pulses.

Like data from conventional MR imaging in which a Fourier transform is applied to the data in k-space, the q-space data are subject to a Fourier transform in every brain position. An example is shown in Fig 6.8. The result is a displacement distribution in each brain position.

6.3.2.3 Fractional Anisotropy (FA)

The problem of diffusion weighted imaging is that the interpretation of the resultant images is not easy. The average diffusion coefficient (ADC) is derived from the equation $\text{ADC} = -b\ln(\text{DWI}/b_0)$ where DWI is the diffusion weighted image intensity for a specific b value and gradient direction. Thus to obtain and ADC value, two acquisitions are needed. For this reason the ADC is biased to the gradient used. To overcome this the Trace is defined which average three orthogonal measurements to better approximate the diffusion coefficients. This methods is equivalent to the Trace derived from the diffusion tensor that will be discussed in next section. FA (factional anisotropy) images are used to easily identify regions of high and low diffusivity in the brain. Its value is high when the diffusion displacement distribution is cigar shaped, and low when no preferred direction is found. FA quantifies the directional dependence of water diffusion and depends on features such as axonal integrity, myelination, axon diameter and density. FA can help to detect tumors, or strokes. Another useful parameter is the *principal diffusion direction* which corresponds to the underlying fiber direction within a coherent fiber bundles. By following these directional estimates, it is possible to perform *diffusion tractography* and trace the pathways of underlying fiber bundles.

6.3.2.4 Tensors and fODF

Diffusion tensors were introduced to better model the anisotropy in white matter tissues. Scalar value images are a limited medium to represent the 3 dimensional information from the white matter, therefore a tensor model was introduced to model the water direction with an ellipsoid. This ellipsoid can be decomposed in three vectors that are the eigenvectors of a matrix which describes the covariance of diffusion displacements in three dimensions. Each eigenvector is associated to an eigenvalue which gives the intensity of diffusion in the direction guided by the corresponding vector. The larger eigenvalue corresponds to the vector of principal diffusion direction. This model is illustrated in Fig. 6.9. The information that can obtained from this types of images is richer, but it also requires more acquisitions than the previous mentioned images (ADC, Trace). FA is still a scalar-value image but it is obtained from the eigenvalues estimated in this method. These images require at least 6 acquisitions, although 60 acquisitions (or more) are recommended. The tensor representation is still limited: for example, when having fiber crossing at 90°, the tensor representation is an isotropic sphere which gives not relevant information about the principal diffusion orientations as shown in Figure 6.11. For this reason, a new technique called fODF has been developed to overcome this situation as shown in Fig.

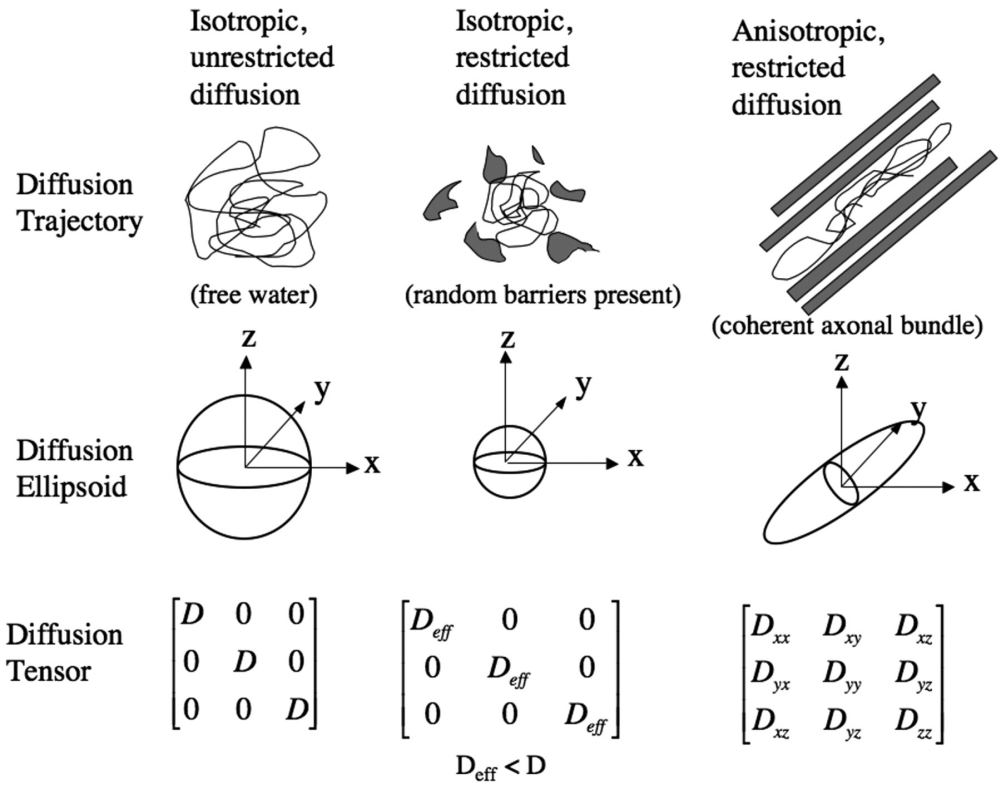

Figure 6.9: Modeling anisotropy with diffusion tensors. Image taken from http://www.ajnr.org/

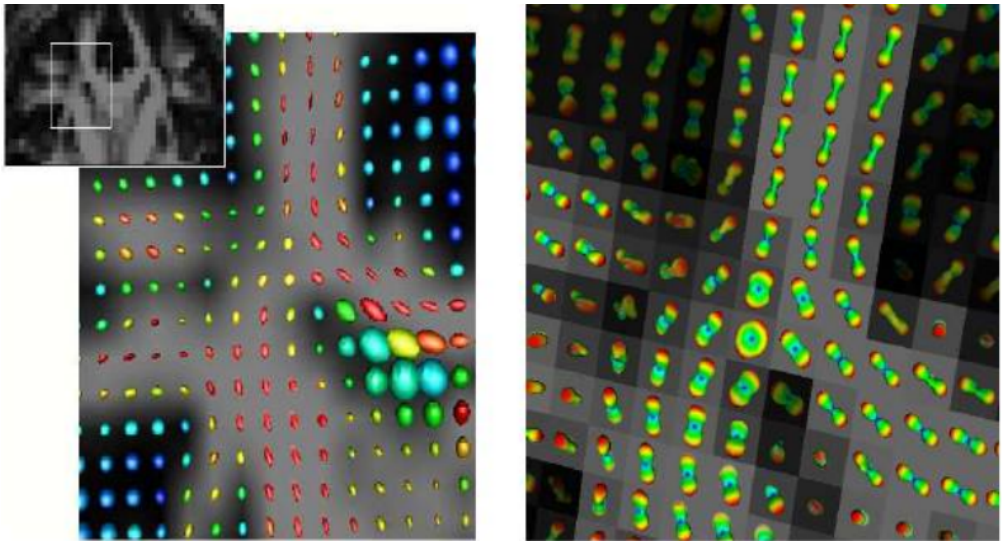

Figure 6.10: Comparison between modeling anisotropy with Tensors and with an ODF. Image taken from Descoteaux Thesis Descoteaux [2008].

6.10. This representation are generally possible on High Angular Resolution Diffusion Imaging (HARDI) acquisitions where more than 200 gradient are needed.

6.3.2.5 Tractography

Tractography is one of the most powerful tools developed to aid image interpretation. The primary purpose of tractography is to clarify the architecture orientation of tissues by integrating pathways of maximum diffusion coherence. Fibers are constructed following the direction of the maximum diffusion from voxel to voxel. The fibers depicted with tractography are often considered to represent individual axons or nerve fibers. Nevertheless, they are more correctly viewed in physical terms as lines of fast diffusion that follow the local diffusion maxima, reflecting only in a general manner the axonal architecture. The connectivity maps obtained with tractography vary according to the diffusion imaging modality used to obtain the diffusion data. If we assume the displacement distribution to be a Gaussian distribution as for diffusion tensors, the representation will be restricted to an ellipsoid. The chosen representation (DTI, fODF,etc) and the assumptions made by the tracking algorithm to estimate the most probably path from one node to another one, will bias the tractography result. Deterministic fiber tracking from diffusion tensor imaging uses the principal direction of diffusion to integrate trajectories over the image Mori and van Zijl [2002]. This technique ignores the fact that fiber orientation is often undetermined in the diffusion tensor imaging data, and for this reason probabilistic approaches have been proposed Hagmann et al. [2003], Parker et al. [2003], Behrens et al. [2003].

6.3.3 Functional MRI (fMRI)

The goal of functional MRI (fMRI) data analysis is to detect brain activity, generally correlations between brain activation while the subject is demanded to perform a task during the acquisition.

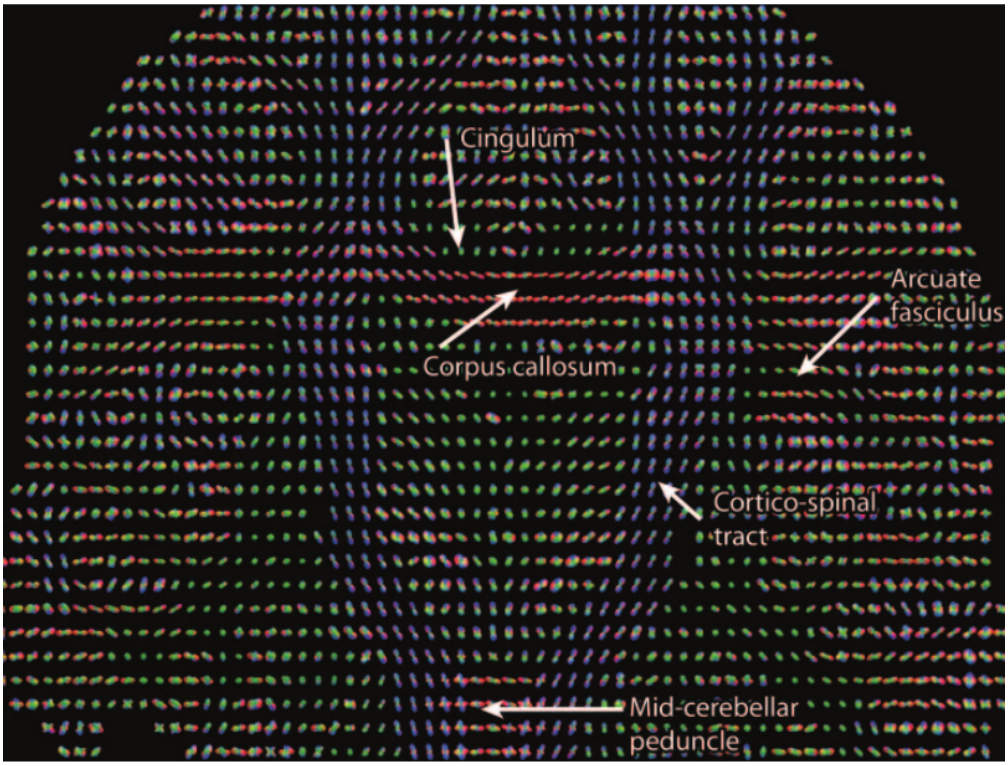

Figure 6.11: Orientation distribution function map of a coronal brain section. The orientation distribution function is plotted at every brain position, showing the local diffusion probability density function. The cortico-spinal tract is easy to see as it is highly anisotropic, however the corpus callosum, cingulum ,arcuate fasciculus and mid cerebellar penducle are harder to detect. Hagmann et al. [2006]

A task can correspond to cognitive states such as memory and recognition, or a motor task such as moving a hand. fMRI relates brain activity to measured changes in blood flow Huettel et al. [2008]. This technique relies on the fact that cerebral blood flow and neuronal activation are coupled, and when an area of the brain is working, blood flow should increase locally. See Fig. 6.12. The fact that the magnetic state of hemoglobin changes with its state of oxygenation was discovered in 1936 by Pauling and Coryell, before the discovery of nuclear magnetic resonance (NMR) itself Raichle et al.. However, only in the late 1990s the potential significance of this effect for functional neuroimaging was realized by Seiji Ogawa .

fMRI uses the Blood-Oxygen-Level Dependent (BOLD) contrast Huettel et al. [2008]. The procedure is similar to MRI but uses the change in magnetization between oxygen-rich and oxygen-poor blood as its basic contrast. This measure is frequently corrupted by noise from various sources, hence statistical procedures are used to extract the underlying signal.

In 1982 Thulborn and colleagues demonstrated relaxation rate (T2) changes in blood samples due to the magnetic susceptibility changes caused by the presence of paramagnetic deoxyhemoglobin.

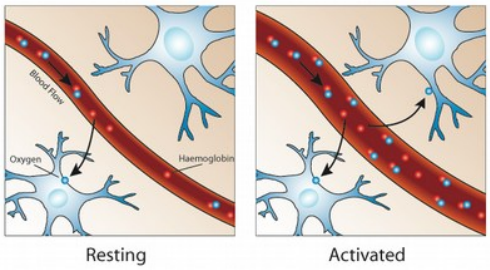

Figure 6.12: Image adapted from FMRIB, oxford webpage

The change in the MR signal from neuronal activity is called the hemodynamic response (HDR). Neuronal events trigger 1 to 2 seconds after, time for the vascular system to respond to brain's need for glucose. The peak rises at about 5 seconds after the stimulus. If the neurons keep firing, say during a continuous stimulation, the peak spreads to a flat plateau while the neurons stay active. After activity stops, the BOLD signal falls below the original level, a phenomenon called the undershoot. Over time the signal recovers to the baseline Huettel et al. [2008] as shown in Fig. 6.13.

6.4 Plasticity

The brain is the source of behavior, but in turn it is modified by its own activity, the experiences: when we regularly practice a sport we increase our motor abilities, which most probably results in a change on the motor cortex. This ability to adapt and develop itself is known as plasticity. This dynamic loop between brain structure and brain function is at the root of neural cognition, learning and plasticity. Recent studies examining inter regional correlations of cortical thickness reveal that gray matter, anatomical networks and functional organizational patterns are modified during development, as they are sensitive to training Zatorre et al. [2012]. The brain is not a static arrangement of circuits but a network of vastly interconnected neurons that are constantly changing their connectivity and sensitivity. To understand the brain we need to understand that it changes over time, from birth until old age. Neuroplasticity is the ability of the brain to change its organizations as a result of experience, including location of functions. Different type of neuroplasticity regarding white matter and gray matter are illustrated in Fig. 6.14. A successful brain model needs to combine the shape of anatomical structures, white matter architecture as a physical network, and functional areas which are not exclusive and interact

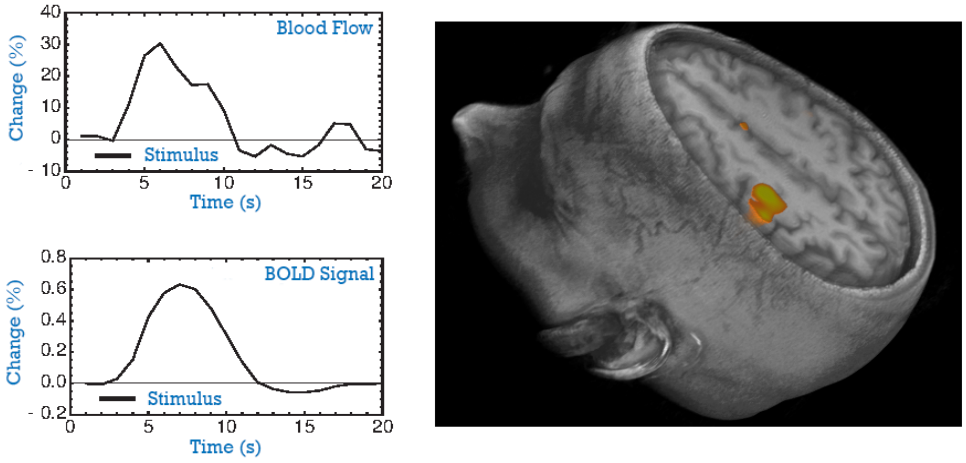

Figure 6.13: The MR signal relates to the changes in blood flow that are followed by the neural activity. Oxygen-rich blood and oxygen-poor blood have different magnetic properties related to the hemoglobin that binds oxygen in blood, so if the blood is more oxygenated the signal is slightly stronger. On the other hand neural activity triggers a much larger change in blood flow than in oxygen metabolism, and this leads to the blood being more oxygenated when neural activity increases. This blood oxygenation level dependent (BOLD) effect is the basis for fMRI. The image is adapted from Richard Buxton at *http://cfmriweb.ucsd.edu*.

with each other through the white matter connections. Neuroplasticity and genetics makes the task harder as each component will be exposed to inter-subject variability.

Many studies have exploited anatomical imaging to reveal group differences that reflect skill knowledge or expertise. Among the first was the demonstration of larger posterior hippocampal volume in expert taxi drivers Maguire et al. [2000]. The obvious implication suggested that experience in spatial navigation resulted in plasticity of the structure involved. This conclusion supported a correlation between years of experience and hippocampal volume in this population. Musicians consistently show greater gray mater volume and cortical thickness in the auditory cortex, and they also show differences in motor regions and in white matter organization of the spinothalamic tract Schneider et al. [2002], Bengtsson et al. [2005]. Juggling, involves rigorous motor coordinations and anatomical changes have been found after as little as 7 days after training it. Changes in occipito-parietal regions involved in visio-motor coordination, reaching and grasping were found regarding gray matter concentration, along with alterations on the white matter organization which were detected on FA. Driemeyer et al. [2008], Scholz et al. [2009]

It is not always clear whether training or ability should be associated with increases or decreases in relevant brain regions because of the complex relationship between anatomical changes and underlying functionality.

6.5 Population Analysis in neuroimaging

To compare different subject in a population we need to find corresponding structures across subjects.

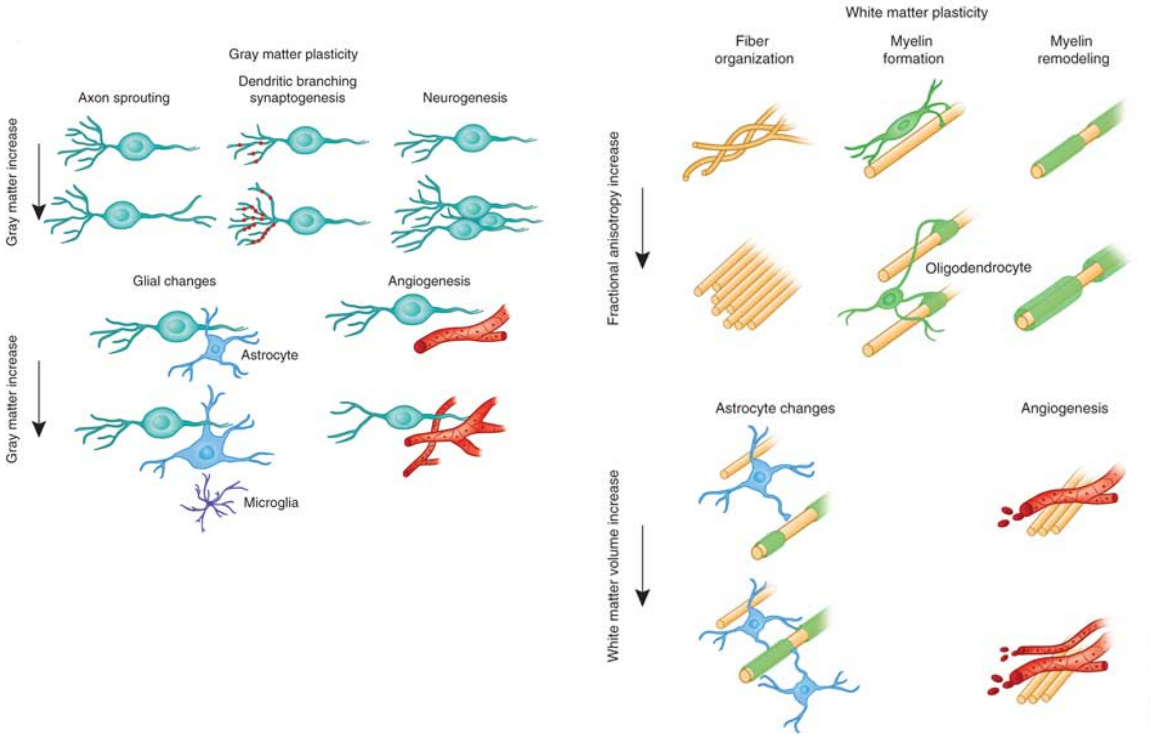

Figure 6.14: This figure shows different anatomical changes that are seen on MRI as changes in gray matter, white matter, and FA. Image adapted from Zatorre et al. [2012]

In the case of the brain one can rely on a wide range of anatomical and functional landmarks including AC-PC which goes from the superior surface of the anterior commissure to the center of the posterior commissure as shown in Figure 6.15 Talairach and Szikla [1980], sulcal lines Mangin et al. [2004], Goualher et al. [1999], sucal ribbons Glaunès et al. [2008], Durrleman et al. [2007], Auzias et al. [2009], Fillard et al. [2007b]. But each brain has a unique configuration of gyri and sulci. In particular, secondary and tertiary sulci are not found in all individuals Ono et al. [1990]. This makes it difficult for software to precisely match sulci between different individuals. Even common sulci and gyri vary drastically in shape and position among subjects, and a point-to-point correspondence between brains of different subjects might not be defined.

Nevertheless, to analyze a population, it is necessary to at least approximate these correspondences. Registration (or normalization) is the process of warping a brain through a transformation or deformation to roughly match a standard template image, an atlas image.

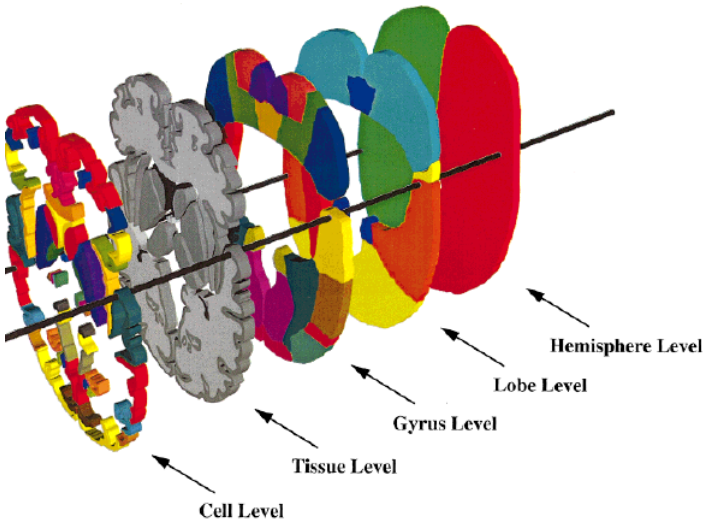

Figure 6.15: A hierarchical atlas scheme is shown in Lancaster et al. [2000] to automatically label the anatomical regions of the Tailarach space.

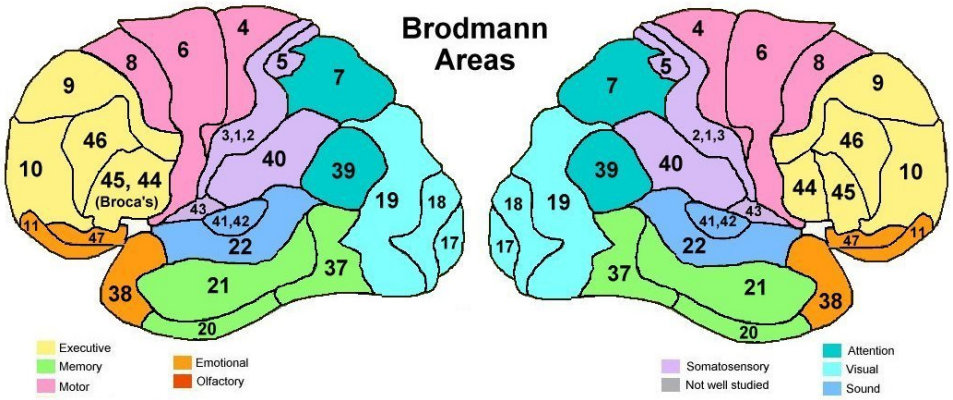

Figure 6.16: Brodmann areas were based on the cytoarchitectural organization of neurons observed in the cerebral cortex. Maps on humans and different species were published in 1905 Brodmann [1905] Image adapted from *http://www.brainm.com*.

To integrate the results across subjects, one adjusts every subject to the atlas and analyze them as a single group. The most famous atlases nowadays are the Talairach and the Montreal Neurological Institute (MNI).

The Tailarach space, is defined by Jean Talairach using stereotaxic ("Talairach") coordinates on a single brain from an elderly woman which was dissected and photographed. This coordinate format uses three numbers (X, Y, Z) to describe the distance from the Anterior Commissure (the *origin* of Talairach space). The X, Y, Z dimensions refer to left-right, posterior-anterior, and ventral-dorsal respectively. i.e. $(38, 64, 58)mm$ refers to a point in right posterior dorsal region of the brain. Landmarks such as the anterior and posterior commissures are detectable in every subject in different modalities such as MRI, PET, etc, making this coordinates system easy to use. Fig. 6.15 show an hierarchical scheme developed in Lancaster et al. [2000] to label structures in Tailarach space.

Stereotaxic coordinates do not necessarily refer to a well defined sulcal location; their anatomical meaning is to some extent "probabilistic" Mazziotta et al. [1995]. However, this level of uncertainty is rather a lack of accuracy of the spatial model. Sulcal location and stereotaxic space may both be probabilistic in terms of functional location. In a study of cortical cytoarchitecture, Zilles et al. [1997] marked that "sulci are not generally valid landmarks of the microstructural organization of the cortex". Unfortunately, the cytoarchitecture can not be directly examined in living humans.

Brodmann, in 1905 classified brain regions based on their cytoarchitecture, the appearance of the cortex under the light of a microscope as shown in Fig 6.16 Brodmann [1905]. According to him a clear link could be drawn between the microscopic appearance of a region and its func-

tion. For example, the *stripe* of the striate cortex delineates the first main cortical area of the visual system, today known as V1, and Brodmann area 17. However, Brodmann's Areas were identified purely based on visual appearance, which is not necessarily related to function. The atlas has Brodmann's areas labeled in a rather approximate way: "The brain presented here was not subject to histological studies and the transfer of the cartography of Brodmann usually pictured in two dimensional projections sometimes possesses uncertainties". Attempting to convert stereotaxic coordinates based on MRI scans to Brodmann areas based on cytoarchitecture raises several problems. First because correspondences can only be drawn in approximation, and secondly because the delineated Broadman areas in atlases are, again, delineated arbitrarily. Delineation of the BAs can be obscure, and in neither case is based on cytoarchitectonic data from the individual brains.

A comparison between Boadmann areas and Tailarach space is shown in Fig. 6.17.

Talairach coordinates map locations of brain structures independent from individual differences in the size and overall shape of the brain. However, alternative methods such as the Montreal Neurological Institute and Hospital (MNI) coordinate system have largely replaced Talairach space Talairach and Szikla [1980].

The MNI atlas aims to define a brain that is more representative of the population. The MNI created a new template that was approximately matched to the Talairach brain in a two-stage procedure. First, they took 250 MRI scans from healthy subjects, and manually defined various landmarks, in order to identify a line very similar to the AC-PC line, and the edges of the brain. Each brain was scaled to match the landmarks to equivalent positions on the Talairach atlas. This resulted in the 250 atlas brain that is very rarely used. An extra 55 images were automatically registered with a linear method Evans et al. [1993], Collins et al. [1994]. The result is a probabilistic map created by combining scans from different individuals after normalization. The MNI template widely used nowadays as a common space for further analyzing populations. A comparison between MNI and Tailarach is shown in Fig. 6.18, where we can see that both representations are extremely different.

The problem with those atlases, is that none of them gives place for the white matter architecture. A complete model of the brain anatomy should also represent behavior, which is intrinsically related to the white matter architecture, as it shapes the network responsible for inter-functional regions communication. Ideally an atlas would represent an averaged population and its variability on anatomical structures, white matter and functional regions. Through this thesis we will go through different methodologies to analyze variation across subjects not only regarding gray matter anatomy but also white matter. The task of finding correspondences across subjects is hard on the cortex, on the white matter, functional regions, and sulci. Nevertheless, the main well-known structures are expected to be consistent across subjects. Tools for automatically detecting those regions are still under development, and we believe that they should all work together, as finding a functional region will be easier if one could use connection information, or an approximate location information from a Tailarach space for example. This thesis is based on the hypothesis that for building a brain model we need to rely on the information coming from different types of images, as none of them is complete, but they are all complementary. Encouraging results will be shown on the combination of multiple modalities. The brain is a complex entity whose fully mechanism has not been yet unveil, but its research that has been actively for centuries, and with the new upcomming technologies and the correct methods to combine different perspectives on the brain, we hopefully will one day understanding is organization and cross-subject variability.

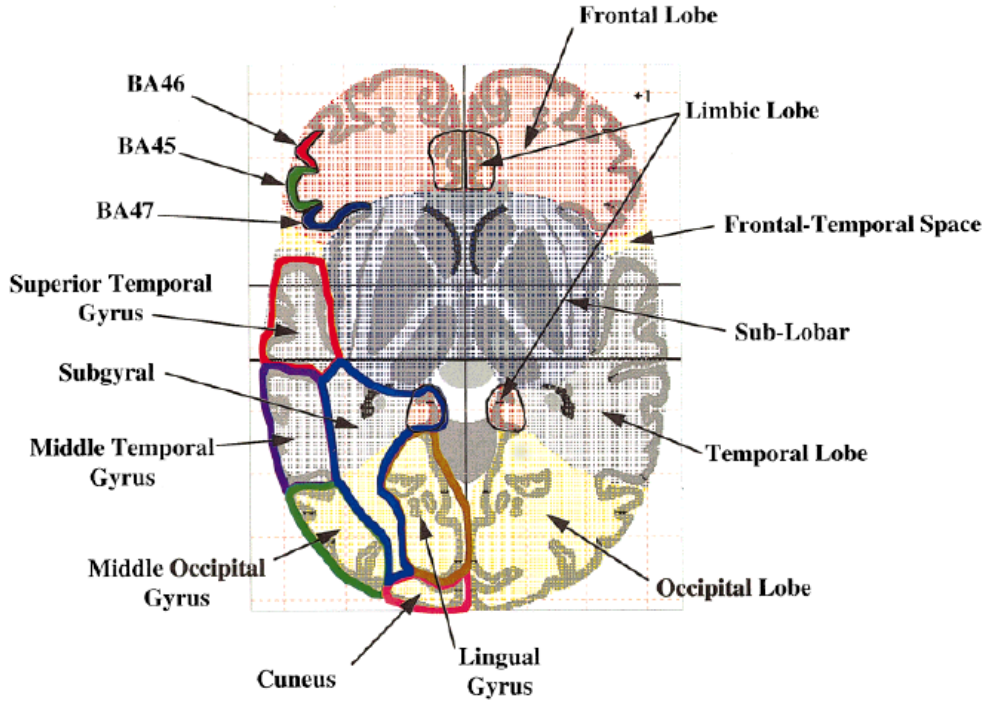

Figure 6.17: Correspondence between Tailarach space and Broadman areas. Tailarach lobe levels are illustrated with patterned color fills. Brodmann areas (cell level) are illustrated on the left using solid color fills, as long as gyral level structures. Image taken from Lancaster et al. [2000]

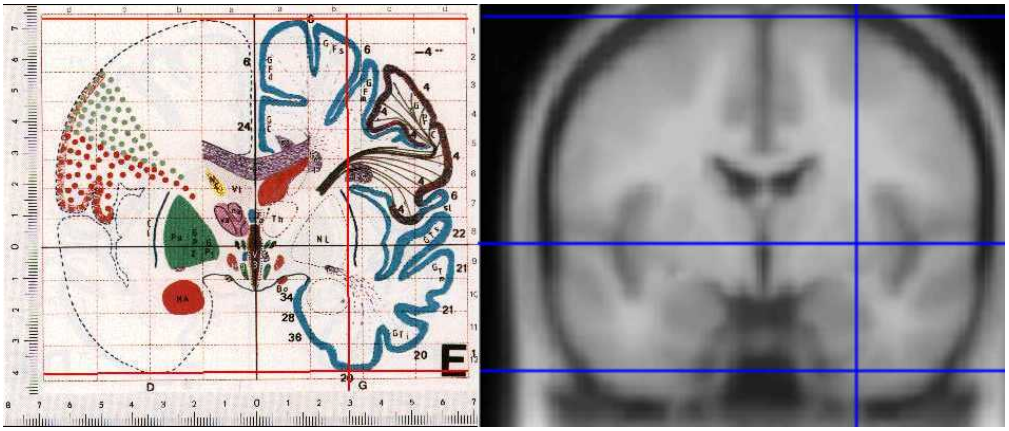

Figure 6.18: Comparison between Tailarach space and MNI. Image adapted from *http://imaging.mrc-cbu.cam.ac.uk*.

Chapter 7

Diffusion MRI

"There are things known and there are things unknown, and in between are the doors of perception."

—Aldous Huxley, The doors of perception.

Diffusion MRI (dMRI) is currently on of the main modalities used to understand the connectivity of cortical brain regions. Revealing brain white matter architecture is expected to improve characterization of neuro-degenerative diseases and understand brain function. Diffusion MRI is a non-invasive in-vivo technique which can also aid surgical planning, as one could previously visualize the patterns of the underlying white matter structure.

7.1 What does dMRI measure?

Diffusion MRI reflects the diffusion properties of water molecules present on brain tissues. If we imagine a drop of color dye falling into a jar of water, initially the drop will appear concentrated at the initial point, and then it will spread radially in a spherically symmetric manner. The physical law that explain this phenomenon is known as Fick's first law Fick [1855], which relates the diffusive particle flux J to any concentration C difference as: $J = -D\nabla C$. Where D is the diffusion coefficient that depends on the medium, the temperature of the environment, and the size of the moving molecule.

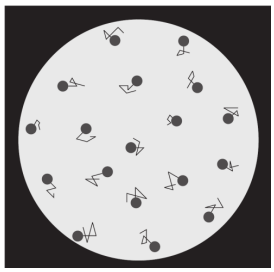

Figure 7.1: Particles moving randomly observed through a microscope. The path traced by the molecules as they travel in a liquid or a gas. Image adapted from Basser and Özarslan [2009]

An interesting feature of diffusion is that it occurs even in thermodynamics equilibrium: although the net flux vanishes, microscopic motions of molecules still persist. This microscopic motions were studied by Brown in 1828, who reported that particles moved randomly without any apparent cause Brown [1828]. In 1905 Einstein concluded that microscopic bodies suspended in liquid perform movements easily seen in a microscope Einstein [1905]. Einstein used a probabilistic model to describe the motion of an ensemble of particles undergoing the diffusion. He introduced the displacement distribution which is Gaussian in the restricted case of free diffusion . Einstein argued that the displacement of a Brownian particle is not proportional to the elapsed time, but rather to its square root Einstein [1956]. The mean squared displacement is defined as :

$$\langle x \rangle^2 = 6D\Delta \tag{7.1}$$

With Δ the elapsed time.

The general diffusion displacement *probability density function* (PDF) also called diffusion propagator of water molecules is extremely complex, and is still unknown today. Hence simple models of diffusion have been historically proposed.

Water diffuses more rapidly in the direction aligned with the internal brain structures, and more slowly as it moves perpendicular to the preferred direction. This also means that the measured rate of diffusion differs depending on the direction from which an observer is looking. dMRI measures the averaged diffusion properties of water molecules inside each voxel. The voxel size is usually small enough to distinguish white matter from gray matter. The white matter in turn consists of densely packed axons (neuronal projections) in addition to various types of neuroglia and other small populations of cells, see Fig. 7.2 and 7.3.

Inside a voxel, water molecules are distributed between these cell types and the extracellular space (80,5 % are intracelular). Thus, even a voxel within a single white matter tract consist of very inhomogeneous environment, and water molecules are likely to experience high anisotropy judging from the architecture of the axon. Inside the axon, water molecules are surrounded by high concentration of neuronal filaments, which are polymers of protein molecules. Both the axonal membrane and the well-aligned protein fibers within an axon restrict water diffusion perpendicular to the fiber orientations, leading to anisotropic diffusion, see Fig. 7.4.

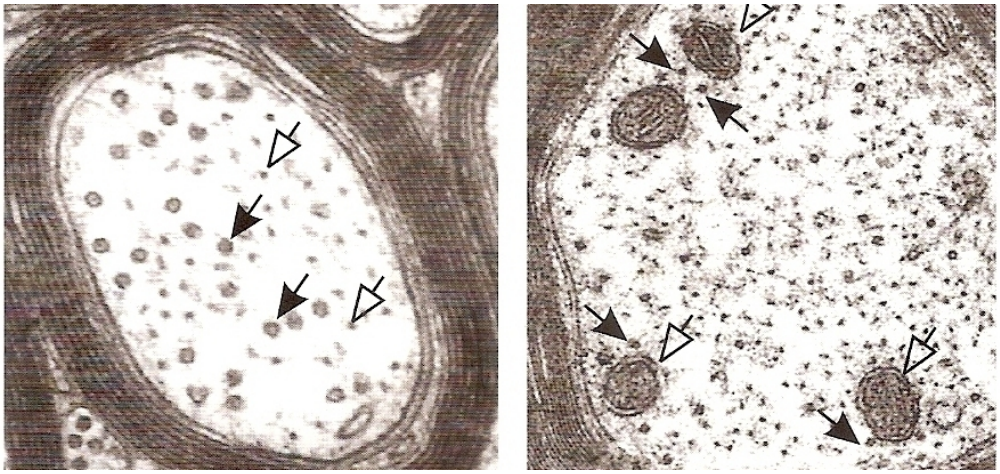

Figure 7.2: Two electromiographs of Central Nervous System (CNS) axons. Cross-section through a myelinated axons. Neurofilaments and microfilaments are elongated structures that appear as small tubes. On the left figure, neurofilaments shown with transparent arrows provide structure and are the main determinants of axonal size (diameter). Microtubules shown with filled arrows provide the tracks upon which materials are transported along the axons. On the right figure, mitochondria shown in transparent arrows are the most frequently encountered axonal organelles. Image adapted from Johansen-Berg and Behrens [2009].

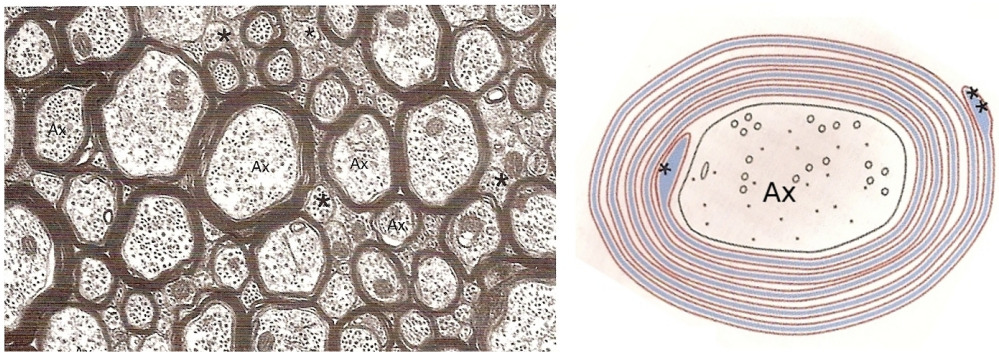

Figure 7.3: On the left an electromiographs of CNS axons through corpus callosal axons. In the CNS, axons over 0.2 μ in diameter are myelinated. Myelin appears as a dark band around the paler axon. Some axons (asterisks) do not attain a myelin sheath. On the right we see and illustration of the arrangement of the myelin sheath and the axon in cross-section. Adapted from Johansen-Berg and Behrens [2009].

Myelin sheaths that surround the axons may also contribute to the anisotropy for both intra and extra cellular water. These contributions have been studied using non-myelinated axons, showing that the contribution of myelin may be significant but that the axonal contribution dominates. It is known that the myelin sheath can modulate the anisotropy of the diffusion while the microtubules and neurofilaments do not modify it Beaulieu [2002].

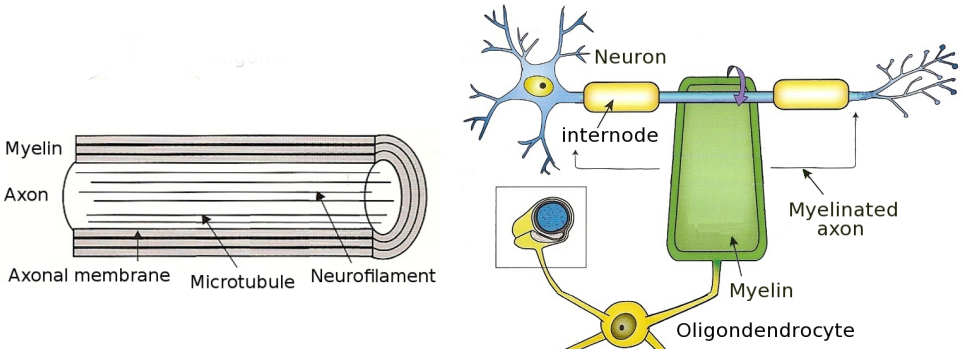

Figure 7.4: Left figure shows the major structural longitudinal elements of the axons. The intra-axonal space contains neurofilaments and microtubules parallel to the direction of the axon. On the left, an schematic illustration shows the oligodendrocyte and the associated axon. Myelin is the membranous structure generated by the tight wrapping of oligodendrocyte processes around the axons. Adapted from Basser and Özarslan [2009].

7.2 Models of dMRI

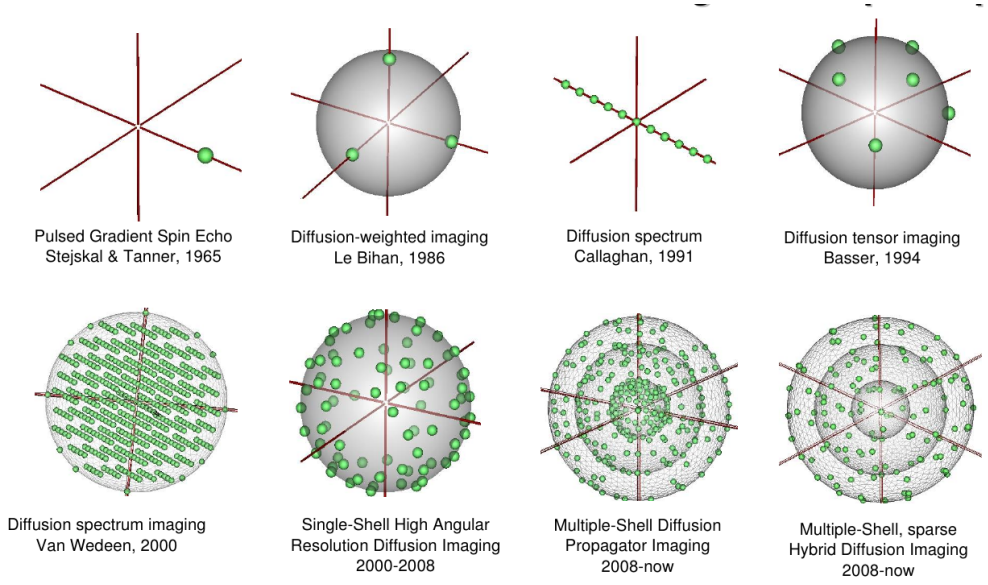

Figure 7.5: Evolution of dMRI acquisition techniques. Starting in 1965 where only one gradient direction was measured. In 1986 a correlation of diffusion to the direction taken was discover, which gave birth to the improvement of acquisitions in gradient directions, strength and representations such as Diffusion Tensor Imaging in 1994. Image adapted from Poupon [2010]

In this section we will explain the basis of diffusion MRI, and the different models that were conceived to analyze the different acquisition techniques and associated models that have evolved through the years as illustrated in Fig. 7.5.

7.2.1 Apparent Diffusion Coefficient

The Apparent Diffusion Coefficient (ADC) concept was introduced to take into account the fact that the diffusion process is complex in biological tissues and reflects several different mechanisms. The *field gradient pulse* method was initially devised for NMR by Stejskal and Tanner Stejskal and Tanner [1965] who derived the reduction in signal due to the application of the pulse gradient related to the amount of diffusion that is occurring through the following equation:

$$\frac{S(TE)}{S_0} = \exp\left[-\gamma^2 G^2 \delta^2 \left(\Delta - \frac{\delta}{3}\right) D\right] \tag{7.2}$$

where S_0 is the signal intensity without the diffusion weighting, S is the signal with the gradient, γ is the gyromagnetic ratio, G is the strength of the gradient pulse, δ is the duration of the pulse, Δ is the time between the two pulses, and finally, D is an scalar representing the diffusion coefficient.

In order to localize this signal attenuation to get images of diffusion, one has to combine the magnetic field gradient pulses used for MRI with additional *motion-probing* gradient pulses. This combination is not trivial, as cross-terms arise between all gradient pulses.

LeBihan suggested to gather all the gradient terms in a "b factor" (which depends only on the acquisition parameters), so that the signal attenuation simply becomes Lebihan and Breton [1985]:

$$\frac{S(TE)}{S_0} = \exp(-b \cdot ADC) \tag{7.3}$$

Also, the diffusion coefficient D is replaced by an Apparent Diffusion Coefficient (ADC). ADC indicates that the diffusion process is not free in tissues but hindered and modulated by many mechanisms such as: restriction in closed spaces, tortuousity around obstacles, and sources of IntraVoxel Incoherent Motion (IVIM). IVIM generally refers to the blood flow in small vessels or cerebrospinal fluid in ventricles which also contribute to the signal attenuation.

At the end, images are *weighted* by the diffusion process. Those diffusion-weighted images are still also sensitive to T1 and T2 relaxivity contrast. It is possible to calculate "pure" diffusion maps by collecting images with at least 2 different values, b_1 and b_2, of the b factor according to:

$$\text{ADC} = \frac{\ln(S_2/S_1)}{b_1 - b_2} \tag{7.4}$$

In Moseley et al. [1990a], measures of ADC were taken along the x and y axis to characterize the level of the tissue anisotropy. At least two acquisitions were required at that moment.

In 1991 Douek suggested that diffusion MRI and measures of the ADC along two directions could be used to determine orientations of fiber bundles in the white matter Douek et al. [1991]. However, the ADC index is very dependent on the direction of the gradient encoding used in the acquisitions. It was starting to be clear that rotationally invariant measures were needed.

The mean diffusivity of the water molecules measured at any direction can be expressed as:

$$d = \frac{1}{2\Delta}\langle R^T, R\rangle \tag{7.5}$$

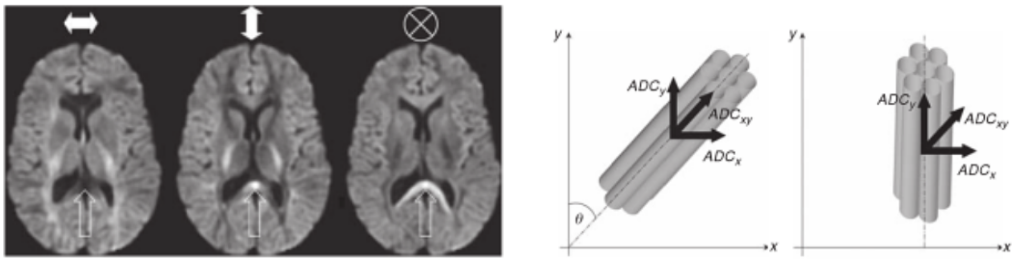

(a) (b)

Figure 7.6: Example of dependency of water diffusion to the gradient direction. In (a) the arrows of the figure represent the orientation of the encoding axis. Measure orientations are longitudinal, transversal and perpendicular to the viewing plane. Dark areas have high apparent diffusivity, and lighter areas lower. (b) illustrates the different orientation encodings behavior given the microtubule configuration. Image adapted from Hagmann et al. [2006]

where Δ is the diffusion time, R is the displacement vector, and $\langle . \rangle$ denotes the average over all particles.

This measures the diffusion of the medium, that depends on the medium and the particles, and does not give any directional information. The scalar constant D known as the diffusion coefficient, measures the molecule's mobility. In the isotropic case, it depends on the molecule type and the medium properties but not on the direction. However Fig 7.6 shows the effect of changing the diffusion encoding gradient on the diffusion weighted signal intensity. In the corpus callosum we can see how the direction of the gradient impacts the measure.

7.2.2 DTI: The Tensors

White matter is composed of myelinated axons, that connect various gray matter areas of the brain to each other, and carry nerve impulses between neurons. The diffusion of water molecules is Brownian under normal conditions but tend to diffuse anisotropically in fibrous structures such as white matter fibers.

Then, as myelin sheaths force water molecules to move in a tangential direction along the fiber rather than orthogonally, we can measure the diffusion of the anisotropic tissue with a covariance matrix of the particles displacement. This covariance matrix will represent the velocity of movement along the different directions, which is more informative that an scalar representing i.e. the average:

$$D = \frac{1}{6\tau}\langle R, R^T \rangle \tag{7.6}$$

where D is a 3×3 symmetric, positive-definite matrix, also called *diffusion tensor*, but in the sequel we refer to it simply as *tensor*.

A symmetric positive definite matrix is a symmetric matrix whose eigenvalues are all strictly greater than zero. The diffusion tensor D can be decomposed into $D = UVU^T$ where U is the matrix of eigenvectors and V is a diagonal matrix of eigenvalues. $\vec{u}_i$ is associated to $v_i \forall_i$.They

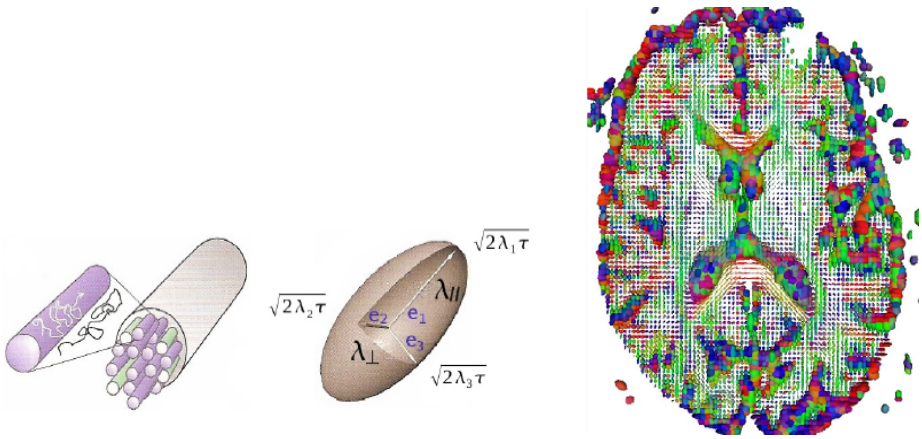

Figure 7.7: Top image illustrates on the left how Brownian motion occurs inside the microtubules, on the center an axon, and on the right its tensor representations with corresponding eigenvalues and eigenvectors. On the bottom image a full brain tensor fitting has been run an is shown in an axial slice. Image taken from Guevara [2008] and Fillard [2008]

are commonly ordered by the magnitude of the eigenvalues, v_1 being the largest eigenvalue, and consequently, $\overrightarrow{u_1}$ is the principal direction of the tensor. As a tensor is a quadratic form, and as we are modeling a diffusion phenomenon, the eigenvalues are positive.

The diffusion tensor is a model of the covariance matrix of the particles displacement. This model assumes a Gaussian distribution of the particle displacement, which can be questioned on crossing fibers regions. Methods such as q-ball and multi-tensor intend to relax such assumptions Descoteaux [2008], Tuch [2004], Stamm et al. [2012] and will be discussed in next section 7.2.3.

The diffusion tensor D is related to the diffusion-weighted images by the Stejskal and Tanner diffusion equation:

$$S_i = S_0 \exp(-b\vec{g_i}^T D\vec{g_i}) \tag{7.7}$$

Where S_i is the diffusion-weighted image, S_0 the baseline image without displacement encoding gradient i.e. T_2; $\vec{g_i}$ the diffusion gradient, and b the b-value in smm^2 which depends on the scanning parameters. Typically a b-value of $1000smm^2$ is used with 7 to 60 gradients directions. $\vec{g_i}$ is the diffusion gradient. S_i is the image returned by the scanner. The gradients can be obtain by linearizing eq 7.7 and solving from least-squares Basser et al. [1994] to more sophisticated Riemannian frameworks Lenglet et al. [2006], Arsigny et al. [2006], Fillard et al. [2007c] that forbid degenerated tensors. Choices should be taken depending on the requirement of speed, robustness to noise, symmetric and positive definite guaranties one must consider when estimating the diffusion tensor. An example is give in Fig 7.7.

Eventhough DT has earned success in many clinical applications, it is limited when imaging voxels with multiple fiber populations crossing, branching, fanning (fibers continuously separating each other, i.e. cortico-spinal tract) or kissing (two fiber populations touching each other without crossing) Basser et al. [2000]. This configurations are shown in Figure 7.8.

The DT model is limited because of the Gaussian-distribution assumption and the limited number of degrees of freedom in the model. To overcome this issue multi-tensor model fitting has been proposed Schultz et al. [2010], Yassine et al. [2006] as well as more sophisticated such as

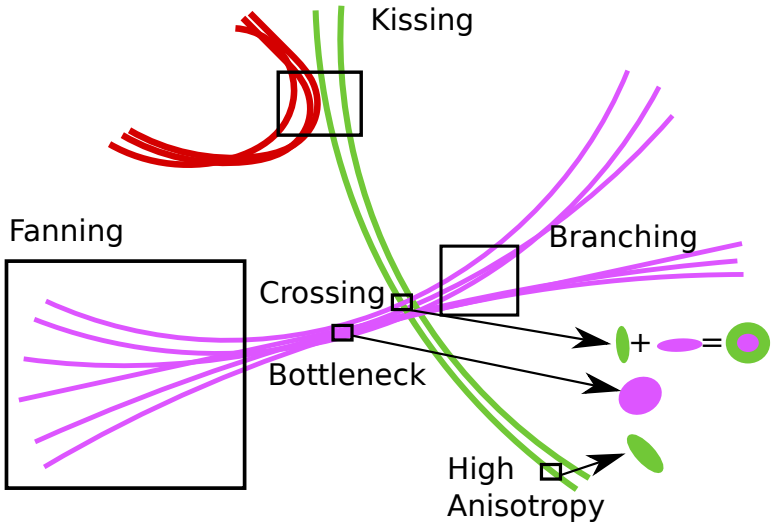

Figure 7.8: We show the different configurations that give problematic situation while using a tensor based representation of white matter: fiber crossing, fanning, branching, kissing, bottleneck. Illustration of tensors are shown for two crossing fibers, and the best and the worst case of a single fiber bundle: high anisotropy and bottleneck.

HARDI models, described in next section.

7.2.3 Q-Ball on High Angular Resolution Diffusion Imaging (HARDI)

The idea is to sample in the q-space along as many directions and q-magnitudes as possible in order to reconstruct the true diffusion PDF. This true diffusion PDF is model free and can recover the diffusion of water molecules in any underlying fiber populations. Instead of having a scalar-valued or tensor-valued image, we now have and image of 3D diffusion distributions.

7.2.3.1 Single and multi-shell imaging

HARDI depends on the number of measurements N and the gradient strength (b-value), which will directly affect acquisitions time and signal to noise ratio in the signal.

There are two strategies to acquire HARDI images:

1) DSI (Diffusion Spectrum Imaging): Sampling on the whole q-space 3D cartesian grid.

2) Single shell spherical sampling

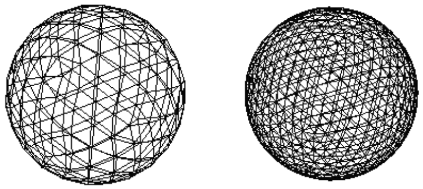

Figure 7.9: Example of amount of sampling points on the sphere for two different single shell HARDI acquisitions. Image adapted from Descoteaux [2008]

In 1) a large number of points are taken over the discrete grid (> 200) and the inverse Fourier transform of the measured DWI signal is taken to obtain an estimate of the diffusion PDF

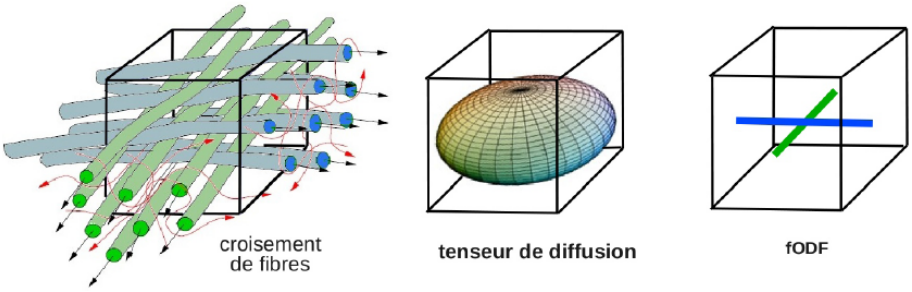

Figure 7.10: The left image illustrates two populations of axons crossing each other at 90°. In the middle figure we can see an isotropic tensor fit, which in turns gives no directional information. Finally on the left figure we see that fODF more accurately represent the crossing of two populations. Image adapted from Poupon [1999]

Wedeen et al. [2005]. This method requires strong imaging gradients ($500 < b < 20000 s/mm^2$). To visualize the PDF, the isosurface of the diffusion PDF is most commonly taken at a certain radius r or the diffusion orientations distribution function (ODF) is computed. The diffusion ODF contains the full angular information of the diffusion PDF and is defined as:

$$\psi(\theta, \phi) \int_0^{\inf} P(r, \theta, \phi) dr, \qquad \theta \in [0, \phi], \phi \in [0, 2\phi] \tag{7.8}$$

In 2) a discrete uniform sampling of the sphere is done for a certain radius in q-space (given by the b-value). The signal attenuation is thus measured on a single shell of q-space Tuch et al. [1999]. The idea is that the radial information of the diffusion PDF can be discarded if one is interested in fiber directions. Most of the single shell HARDI techniques aim at reconstructing the diffusion ODF or variants of this function in order to estimate a function whose maxima are aligned with the underlying fiber structure. More than 60 measurements are desirable and medium gradient strengths are acceptable although stronger gradients give better diffusion ODF reconstructions. An illustration can be seen in Fig. 7.9

7.2.3.2 Q-ball imaging (QBI)

QBI reconstructs a smoothed version of the diffusion ODF directly from single shell or multi-shell HARDI acquisitions with the Func-Rador transform (FRT) Tuch [2004], Khachaturian et al. [2007]. The FRT value at a given spherical point is the great circle integral of the signal on the sphere defined by the plane through the origin perpendicular to the point of evaluation. The ODF is intuitive because it has its maxima aligned with the underlying population of fibers. It is better for tractography, as illustrated in Fig. 7.10. The original version has a closed-form, and spherical harmonic solution reconstructions have been introduced in several works Anderson [2005], Descoteaux and Deriche [2007].

7.2.4 Fractional Anisotropy (FA)

The largest eigenvalue λ_1 gives the principal direction of the DT e_1 and the other two eigenvectors expand the orthogonal plane of it. From this eigenvalue decomposition several rotationally

invariant quantities can be extracted such as trace ($=ADC_x + ADC_y + ADC_z$), the mean diffusivity $\bar{\lambda} = \text{trace}/3$, the fractional anisotropy (FA) Westin et al. [2002]. FA was introduced in Pierpaoli and Basser [1996] as:

$$\text{FA} = \sqrt{\frac{3}{2}}\sqrt{\frac{(\lambda_1 - \bar{\lambda})^2 + (\lambda_2 - \bar{\lambda})^2 + (\lambda_3 - \bar{\lambda})^2}{\lambda_1^2 + \lambda_2^2 + \lambda_3^2}} \tag{7.9}$$

Most often, FA maps are used to visualize regions of anisotropy. It is a scalar-valued image easier to visualize than a tensor one. See Fig. 7.11. It is close to 1 on major white matter tracts and lower in gray matter, while approaching 0 in cerebrospinal fluid. A comparison with ADC can be seen in Fig. 7.12.

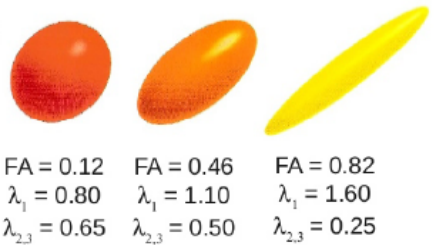

Figure 7.11: Example of variability of FA values and principal eigenvalues in relation with the anisotropy of the tensor. Image adapted from Johansen-Berg and Behrens [2009]

7.2.5 Mean FA Skeleton Analysis

Analyzing tensor images, fibers, and scalar value maps such as FA or ADC can be a very complicated task, especially when performing an inter-subject analysis. Registration methods aim at finding correspondences across structures, but how can one be sure of such an alignment? are FA maps actually aligning corresponding structures? No thorough analysis of these questions have been carried out yet, and everyday tools perform registration mostly by using T_1 images only, giving no guarantee that white matter is correctly aligned.

An attempt to hold a simple scalar-value analysis, especially of fractional anisotropy of images, avoiding introducing alignment errors into morphometry studies, has been achieved by generating an skeleton of the FA images **?**. First, FA images are computed for every subject. Then, it is necessary to define a 'median' subject, or an atlas/target to register to. All FA images are registered to the template by using T_1 information. However, at this step a perfect alignment is not mandatory. Once all FA images are registered to the template space, an average is performed to generate a template FA. From the template a thinning is performed to generate the template skeleton. This thinning is done with non-maximum suppression perpendicular to the local tract structure, which results in an skeletonized mean FA image. An example can be seen in Fig. 7.13.

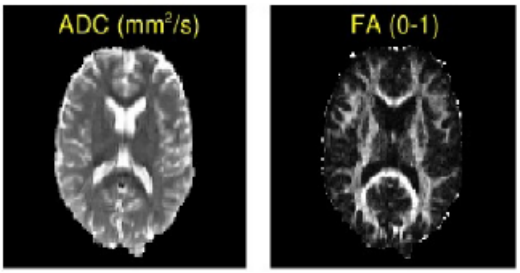

Figure 7.12: Comparison between FA and ADC maps. Because it requires more acquisitions, the level of detail seen in FA maps are higher than in ADC, as it is dependent on the direction measured through acquisition. Image adapted from Johansen-Berg and Behrens [2009]

Each subjects aligned FA image is projected onto the skeleton, by filling the skeleton with FA values from the nearest relevant tract center. This is achieved for each skeleton voxel, by searching the maximum value perpendicular to the local skeleton structure in the subjects FA image. The average of all subjects FA is fed into the tract skeleton generation, which aims to represent all tracts

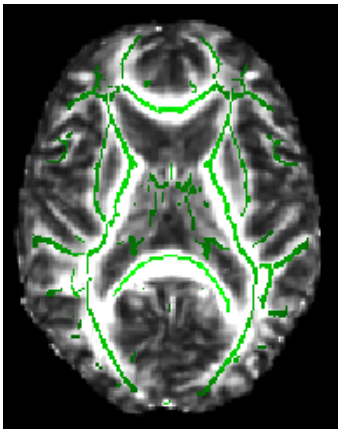

Figure 7.13: Skeleton com-

(FA-based) common to all the subjects. The skeleton represents each tract as a single line or surface running down the center of the sheet. Away from the center surface or line, the FA values fall off gradually becoming very low as one moves out of white matter. To achieve skeletonization the local surface perpendicular direction to all voxels in the image is estimated. Then, non-maximum suppression is performed in this direction. In other words a search is made along all voxels in the local tract perpendicular direction, and the voxel with the highest FA is identified as the center of the tract.

The skeleton tends to be disconnected at many junctions; this is primarily due to the fact that the tract perpendicular direction is not well-defined at junctions, and hence the non-maximum suppression perpendicular to the tract cannot work well.

Then the subjects FA are projected to the skeleton. At each point in the skeleton, the corresponding FA value from each subject is searched along the line, perpendicular to the tract direction to find the maximum FA value, and this value is assigned to the skeleton voxel. This approach achieves a robust alignment across subjects in the perpendicular direction of the tract and not its parallel direction. This is wanted as FA changes fast as one moves perpendicular to the local fiber bundle, so even small misalignments in the direction have great effect on the final FA statistics. Parallel to the tract, FA changes relatively slowly, and the alignment provided by the initial nonlinear registration is sufficient to align the structures of interest across subjects.

7.3 Tractography

Diffusion MRI fiber tractography or *fiber tracking* is the only non-invasive tool to obtain information on the neural architecture of the human brain white matter in vivo.

Fiber reconstruction is mostly known as fiber tracking or tractography. It consists in building a geometric representation of the white matter architecture under the hypothesis that diffusion tensors (or HARDI Q-ball) are aligned with the direction of the oriented tissues. In the case of tensors the hypothesis is wrong for the case of crossing, kissing, fanning, branching or bottleneck fibers. Figure 7.8 illustrates these configurations. Nevertheless we will present tractography algorithms based on tensor imaging, but they can be extrapolated to HARDI Q-ball representation.

There are two different approaches in tractography: Deterministic and probabilistic. The deterministic approach is known as streamline: following the principal diffusion direction, integrates from a seed point the paths expected to belong to the same fiber bundle. In other words, the principal diffusion direction must be consistent from one voxel to an adjacent one, meaning that the angle must not brusquely change, see Figure 7.14. The probabilistic approach simulates many times the diffusion phenomenon from a seed point and simulations are combined to generate a probability map of the fiber bundle. These maps tend to have high probability values along the path of the fibers, and low at the end points connecting the gray matter, as it is naturally where fiber bundles start to split.

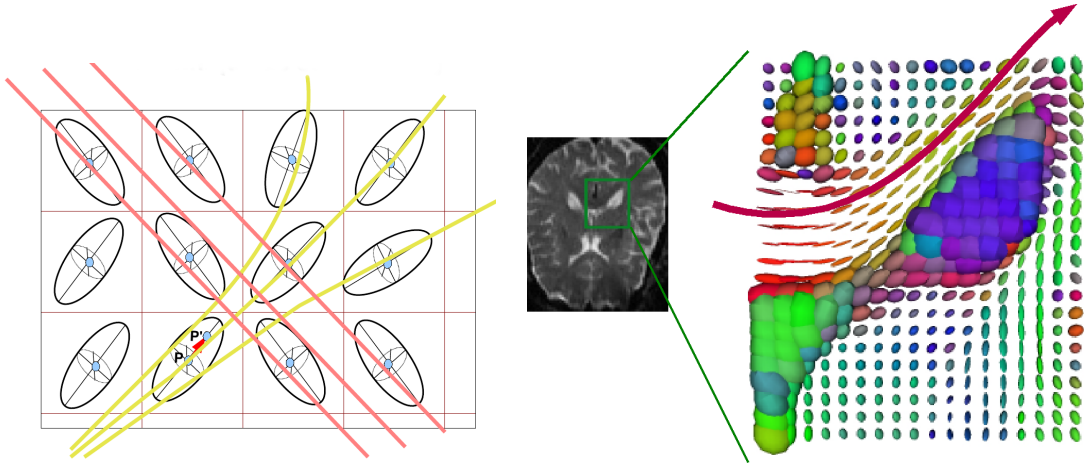

(a) (b)

Figure 7.14: Image (a) show an example of tractography on a crossing fiber setting. Image adapted from Poupon [2010]. Image (b) shows the tractography path following the tensors of high fractional anisotropy on the corpus callosum. Image adapted from Fillard [2008].

7.3.1 Streamline tracking - deterministic

By assuming that the largest principal axis of the diffusion tensor aligns with the predominant fiber orientations in an MRI voxel, we can obtain 2D or 3D vector fields that represent the fiber orientation at each voxel. The 3D reconstruction of tract trajectories, or tractography, is a natural extension of such a vector fields.

Tractography can provide macroscopic neuroanatomical information on white matter structure. Specifically it can parcellate the white matter into fiber structures that contain bundles of axonal tracts that are running largely in the same orientation.

The real advantage of tractography is its ability to quickly characterize the macroscopic white mater structures. It is virtually impossible to generate similar datasets using the single-cell level chemical tracer techniques given that there are 10^{11} neurons in the brain .

Assuming that the orientations of the largest component of the diagonalized diffusion tensor represent the orientation of the dominant axonal tracts, a 3D vector field can be obtained where each vector represents the main local fiber orientation.

Line propagations techniques: The most intuitive way to reconstruct a 3D trajectory from a 3D vector field is to propagate a line from a seed point by following the local vector orientations, as illustrated in Fig. 7.14.

However, if a line is propagated simply by connecting voxels which are discrete entities, the vector information might not be fully reflected in the propagations. When applying a voxel connection approach in a discrete case, connection rules needs to be defined. A simple pixel connection scheme cannot however represent the real tract even in such a simple case. In a continuous representation, a continuous linear propagation approach called FACT (fiber assignment by continuous tracking) is defined. This approach has been successful to tract neural fibers in a fixed rat and showed good agreement with histological knowledge Mori and van Zijl [2002], Mori et al. [1999], Xue et al. [1999]. To be more rigorous one can interpolate diffusion tensors rather

than the vector of the principal axis.

7.3.1.1 Termination

It is not straightforward to know when the line is over. This is related to the resolution, the noise, and the method itself. Heuristics are used, and lines are generally terminated when fractional anisotropy values are low, or similar to gray matter ones. T_1 based cortex mask are used also to determine the end of a fiber as well as possible beginnings.

7.3.1.2 Propagation masks

Propagation masks are used to define the possible seed points, and sometimes also the endpoints. They are generally cortex based masks, which could be inspired from T_1 but also from FA, or their combination. While being interested in a particular region, the propagation mask can define a region of interest (ROI).

7.3.1.3 Favorable conditions

Other reasons to fiber endings are unfavorable conditions. An FA value can be low not only when approaching the cortex, but also in the middle of the path. This can be due to fiber crossing (when no preferred direction is found in DTI), fiber kissing, fanning,branching or bottleneck. All these reasons can lead to ambiguity on the paths, obtaining larger angles than expected within the path of a fiber. Favorable conditions consist in low turning angles through the fiber path, and low FA value on its endpoints only.

7.3.1.4 Fact

The trajectory of a white matter fiber tract can be represented as a 3D space curve, a vector $r(s)$ parametrized by the arc length s at the trajectory. The Frenet equation describing the evolution of $r(s)$ is:

$$\frac{dr(s)}{ds} = t(s) \tag{7.10}$$

where $t(s)$ is the unit tangent vector to $r(s)$ at s. In coherently organized white matter, the normalized eigenvector e_i associated with the largest eigenvalue of the diffusion tensor D, e_1 lies parallel to the local fiber tract direction Tanner [1979], Scollan et al. [1998], Basser et al. [2000].

In Basser et al. [2000] the key idea of the fiber tracking algorithm is to equate the tangent vector t(s), and the unit eigenvector e_i calculated at position r(s).

$$t(s) = e_i(r(s)) \tag{7.11}$$

Combining we end up having

$$\frac{dr(s)}{ds} = e_i(r(s)) \tag{7.12}$$

Which is a system of three implicit (vector) differential equation solved for the fiber tract trajectory tight to the initial condition of $r(0) = r_0$, which specifies the starting point of the fiber

tract. This can be solved by using the Euler method, approximating the position of the nearby point on $r(s)$ using a Taylor series expansion, for which its first order can be approximated with $\epsilon_1(r(s_0))$ since the slope of $r(s_0)$ at $s_0, r'(s_0)$ is assumed to be parallel to it. Then for a small enough λ

$$r(s_1) \approx r(s_0) + \lambda\epsilon_1(r(s_0)) \tag{7.13}$$

However a first order approximation is sensitive to noise and image errors, so it is better to use higher order methods such as Runge-Kutta Ascher and Petzold [1998]. The sign of ϵ_1 should be chosen to point along the integration path consistently.

7.3.1.5 Fast marching techniques

If we imagine ink being dropped on a glass of water, we can visualize a vector field that indicates the direction and velocity in which the ink is currently spreading. As we known propagation is white matter will be restricted by myelin, We can use this analogy to characterize and estimate white matter paths. The speed for the spreading propagation is defined as:

$$F(r) = A\|\epsilon_1(r).n(r)\| \tag{7.14}$$

where A is the anisotropy, ϵ is the eigenvector and n the orientation normal to the front. This equation reflects that the spreading speed is largest when the propagating front line is co-linear with the eigenvector, and minimal when it is perpendicular. The shape of the stain can be calculated from the vector field which is equivalent to a contour line showing the distance traveled within an amount of time. Multiple contour lines can be calculated, each representing a stain shape at a different time point. These multiple contours represent a likelihood of connection map. The most likely path between an arbitrary point to the seed pixel can be found by following the gradient of the steepest path.

It is not straightforward to determine the end of a fiber and heuristics on fiber bending, torsion and endpoints are set. A fiber tracking algorithm can stop for the following reasons:

1. It reached a boundary of the imaging volume: a mask can be estimated using other imaging techniques such as T_1 image.
2. A region with low diffusion anisotropy: due to the fiber endpoint, but it can also happens on the mid-path because of fiber crossing issues.
3. The angle of curvature is larger than an expected threshold value: i.e. a smooth fiber bundle should not make brusque turns (i.e. larger than 70°).
4. The most collinear eigenvector is not the one associated with the large eigenvalues: because of fiber crossing issues the path to follow can be ambiguous.

7.3.2 Probabilistic tracking - non-deterministic

7.3.2.1 Introduction

This technique uses density functions to estimate global connectivity, i.e. the probability of a connection existence through the data field between any two distant points. This permits to quantify the belief of tractography results.

In diffusion imaging, there is uncertainty caused by noise, artifacts present in any MR scan, but also by the incomplete modeling of the diffusion signal. These uncertainties may be represented in the form of probability density functions.

Deterministic techniques that follow the major white matter pathways in the brain Turner et al. [1990], Ordidge et al. [1994], Jezzard et al. [1998] do not attempt to quantify the uncertainty in the resulting white matter connections. Streamline approaches are based only on high anisotropic regions, and they hope for ambiguity to be low. Diffusion anisotropy tends to be low in areas of high uncertain fiber directions, such as crossing fibers, splitting, merging, etc; although the converse is not necessarily true. Thus fibers are only traced where anisotropy is high.

When fitting a parametrized model to data, there are two general approaches to be taken. The first is to look for the set of parameters (ω) which best fit the data. This is called a point estimate of the parameters. A special case of this is Maximum Likelihood estimation, where one looks for the set of parameters which maximizes the probability of seeing this realization of the data given the model and its parameters.

$$\omega_{ML} = \arg\max_{\Omega} \mathcal{P}(Y|\omega, M) \tag{7.15}$$

where Y is the data and M is the model.

The second approach is to associate a PDF with the parameters. In the Bayesian framework this distribution is called the posterior distribution on the parameter given the data:

$$\mathcal{P}(\omega|Y, M) = \frac{\mathcal{P}(Y|\omega, M)\mathcal{P}(\omega|M)}{\mathcal{P}(Y|M)} \tag{7.16}$$

Having an hypervolume $\mathcal{V}$ in parameter space Ω, and a posterior density function, we could know how confident we are that ω lies on $\mathcal{V}$. Unfortunately calculating this PDF is seldom straightforward.

$$\mathcal{P}(Y|M) = \int_{\Omega} \mathcal{P}(Y|\omega, M)\mathcal{P}(\omega|M)d\omega \tag{7.17}$$

This integral is often not tractable analytically. This is a join posterior PDF on all parameter, however we generally want a single parameter or a subset of parameters. Obtaining the marginal distribution involves solving large integrals.

$$\mathcal{P}(\omega_I|Y, M) = \int_{\Omega_{-I}} \mathcal{P}(Y|\omega, M)\mathcal{P}(\omega|Y, M)d\omega_{-I} \tag{7.18}$$

where ω_I are the parameters of interest and ω_{-I} are all the other parameters. To solve this equation is possible to sample the parameter space from the joint posterior distribution, and perform the integrals numerically. This can be done for example with Markov Chain Monte Carlo (MCMC) MacKay [2003].

The parameters of real interest in a tensor representation are the three eigenvalues and the three angles defining the shape and orientations of the tensor. By choosing these parameters in the model we obtain the posterior PDFs of the parameters of real interest, while being free to also introduce constraints, such as forcing the eigenvalues to be positive.

The set of parameters contains rotational parameters to align the principal eigenvector, the eigenvalues, the non diffusion gradient signal, and a standard deviation to account for errors. Then for n number of acquisitions, u_i and μ_i measured and predicted values, the probability of Y given the model M is:

$$\mathcal{P}(Y|\omega, M)\prod_{i=1}^{n}\mathcal{P}(y-i|\omega, M) \tag{7.19}$$

7.3.2.2 Global Connectivity Estimations

Using the previously defined PDFs we can infer a model of global connectivity. We want to know the probability of an existing connection between points A and B given the knowledge of the local fiber direction. In order to solve this, we start a connected path from a seed point A and follow local fiber direction until a stopping criterion is met. If B lies on this path we say that a connection between A and B exist.

In the case where there is uncertainty associated with $(\theta, \phi)_x$ we compute the probability of a connection given the data Y_x. For this we would need to compute $\mathcal{P}(\exists A \rightarrow B|Y_x)$:

$$\mathcal{P}(\exists A \rightarrow B|Y) = \int_0^{2\phi}\int_0^{\phi}...\int_0^{2\phi}\int_0^{\phi}\mathcal{P}(\exists A \rightarrow B|(\theta,\phi)_{x_1})\mathcal{P}((\theta,\phi)_{x_n}|Y)... \\ ...\mathcal{P}((\theta,\phi)_x|Y)d\theta_{x_1}d\phi_{x_1}...d\theta_{x_n}d\phi_{x_n} \tag{7.20}$$

For each possible value of fiber direction at every voxel $(\theta, \phi)_x$ we must incorporate the probability of connection given this $(\theta, \phi)_x$ and also the probability of this$(\theta, \phi)_x$ given the acquired MR data. This process is known as marginalization. When there is no uncertainty in the local fiber direction, this equation reduces to the streamlining using maximum likelihood solution. However when local fiber direction is uncertain, the global connectivity pattern from A will spread to incorporate the known uncertainty in local fiber direction.

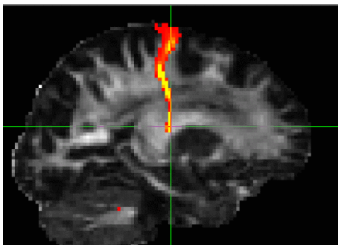

Figure 7.15: Probabilistic tractography example. Image adapted from Behrens et al. [2003]

7.3.2.3 Algorithm:

1. Select a random sample (θ, ϕ) from $\mathcal{P}(\theta, \phi|Y)$ at z.
2. Move z a distance s along (θ, ϕ)
3. Repeat until stopping criterion is met.

This probabilistic streamline is said to connect A to all point B along its path. By drawing many samples we build the spatial PDFs of $\mathcal{P}(\exists A \rightarrow B|Y)$ for all B. We then discretized this distribution into voxels by simply counting the number of probabilistic streamlines that pass through voxel B and normalize, i.e. divide by the maximum value. An example of the probabilities between two different ROIs in the brain is shown in Fig. 7.15.

7.4 Discussion

Altought the probabilistic method is robust, it is sometimes unclear how to deal with uncertain regions, specially within this thesis where neural fiber information are not the end of the analysis but the beginning, the input. For this reason we choose a deterministic setting through the thesis. Nevertheless other methods have been explored and therefore will be mentioned and analyzed. We use MedInria Toussaint et al. [2007] tractography which is performed using a modified version of the advection-diffusion algorithm of Weinstein et al. [1999] with a tri-linear log-Euclidean tensor interpolation and a 4^{th} order Runge-Kutta integration scheme, which was proved to be more accurate numerically Ascher and Petzold [1998].

7.4.1 Probabilistic vs deterministic tractography

Probabilistic algorithms have advantages in regions where fiber direction is uncertain, as whenever it can not progress along a single direction with high confidence, it can progress in many directions. The uncertainty is represented by voxels with lower probabilities associated. Probabilistic algorithms are more robust to noise: it can be difficult to track beyond a noisy voxel with a streamline algorithm, and probabilistic errant paths routes tend to disperse quickly ending up being classified with low probability. Therefore we can be confident up to a probability percentage about the more certain path.

Probabilistic maps can be useful for a final level analysis, group level or subject level Wassermann et al. [2010b]. But it is hard to incorporate them as priors, as two regions with same low probability in different subjects do not necessarily correspond to each other. They can be useful when analyzing a specific regions, the effects of aging or a disease. However, they can be limited if the goal is to make a global analysis of the general white matter architecture. While it is true that streamline tracking can nowadays give spurious fibers, streamline tracking algorithms are always combined with a priori parameter selection of allowed angles, minimum length, low and high FA values. In Guevara et al. [2012] a tractography propagation mask based on T1 data rather than FA was used in order to improve the accuracy of the anatomical connectivity, where dilated sulci, and ventricles were removed from the mask Marrakchi-Kacem et al. [2012]. Figure 7.16 show how results can dramatically change when using one technique or the other one. Unfortunately not much can be concluded from this as using T_1 based propagation mask definitely gives more structural meaning, except when FA values on those regions are low, then there is no guarantee to avoid the creation of spurious fibers.

Another option to increase confidence in the streamline tracking results, is to compress the output, and work with the most representative fibers. This will be better discussed in Chapter 8. Fortunately the research field is evolving fast, resolution is improving HCP [2012], and techniques are constantly evolving.

7.4.2 FA vs Skeleton

Diffusion fractional anisotropy (FA) as been widely used as a marker for white matter tract integrity, for example for disease diagnosis, tracking of disease progression, finding disease subcategories, studying normal development/aging, and as complementary information to investigating normal brain function Horsfield and Jones [2002], Moseley et al. [2002], Neil et al. [2002]. Some researchers have simply summarized diffusion characteristics globally, such as using the

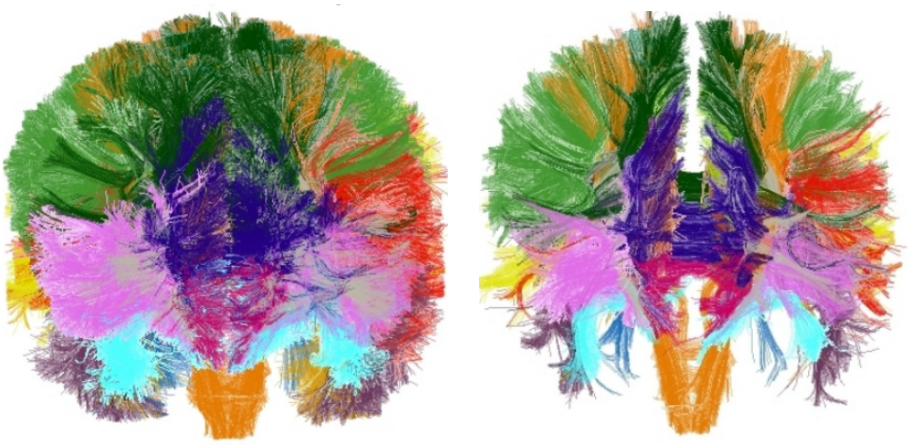

Figure 7.16: On the left we see the propagation mask used in tractography based on T_1 images, while a propagation mask based on FA was used on the right figure. Image adapted from Guevara [2008]

FA histograms in Cercignani et al. [2003] in order to compare different subjects. Other works intend to localize spatially interesting diffusion-related changes, generally using voxel-wise morphometry (Voxel Based Morphometry (VBM) originally developed for finding local changes in gray matter density in T1-weighted structural brain images Ashburner and Friston [2000], Good et al. [2001]. In VBM-FA setting style, registration is performed using FA images, to warp them into a standard space.

Some researchers doubt the general interpretation of the results from this approach primarily because there can be ambiguity as to whether apparent changes are really due to change in grey matter density or simply due to local misalignment, although convincing results can be found in studies using VBM Watkins et al. [2002]. However the limitations of FA in inter-subjects image analysis have not been fully investigated yet. So, how can one guarantee that registration of every subject to a common space has been totally successful? How can one guarantee that any given voxel contains data from the same white mater (WM) tract from each and every subject? There are two main issues to be tackled here: resolving for topological variabilities and the exact alignment of the very fine structures.

A priory we can not guarantee that the voxel-space statistics analysis relies on anatomically corresponding regions.

Some work have already presented reports on alignment issues specific to diffusion tensor data, i.e. Jones et al. [2002] use FA to drive affine alignment across subjects. In Park et al. [2004, 2003] they investigate the registration of DTI tensor component versus FA, or derived information, and noted some improvements by analyzing DTI although the differences were not large. For example, while studying white mater differences in schizophrenics patients, errors in the boundary of narrow tracts were found, and on those cases a VBM approach should be avoided. The registration problem is not necessarily resolved by increasing the degrees of freedom of the deformation model (discussed on Chapter 9), because it is be possible to distort one image to look very much like another one, not necessarily increasing the confidence of aligned structures. The mentioned issue while using DTI registration can suggest that a combination of FA and DTI or even T_1 image registration should be used, as one can not always rely on one image information, i.e.

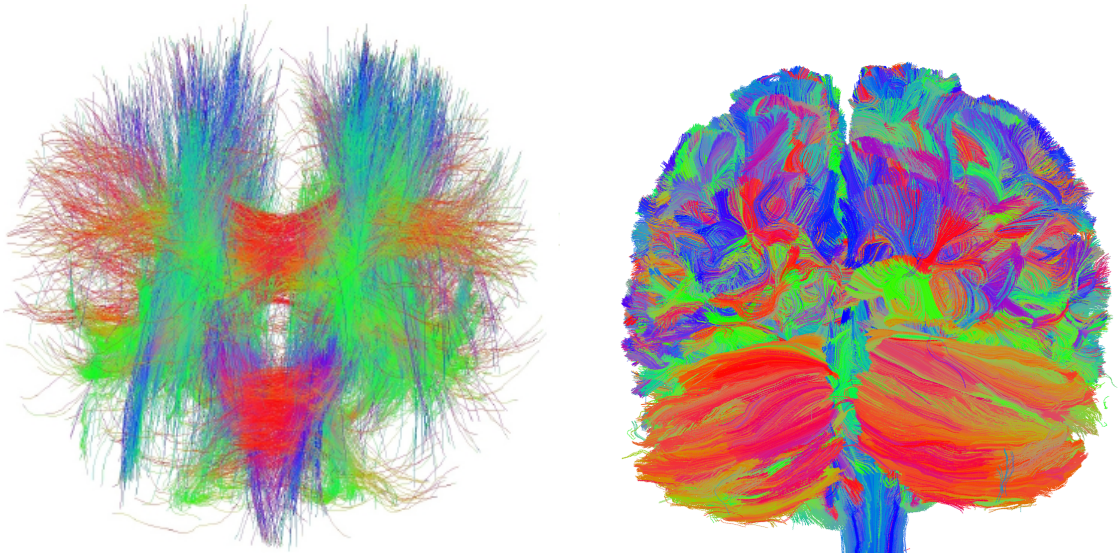

60 gradients 200 gradients

Figure 7.17: Varying amount of fibers depending of image resolution but also tractography parameter. Fibers on the left do not look realistic due to noise and low image resolution: $128 \times 128 \times 30$ spatial resolution: $1.8 \times 1.8 \times 4mm$ 60 gradients, while the image on the right contains higher image resolution: and spatial resolution: $145 \times 145 \times 174$ spatial resolution: $1.25 \times 1.25 \times 1.25mm$ 200 gradients in a 3-shell acquisition. Left image adapted from Fillard [2008] and right image computed from HCP data HCP [2012] and tracktography has been perform on MedInria Toussaint et al. [2007].

where white matter information is not strong enough, T_1 might introduce relevant constraints.

The skeleton based approach intends to solve some of the registration issues, by using a very simplistic version of the white matter structure. While it is useful to align diffusion image primal tracts, or analyzing the main white matter structure across subjects, it discards endpoints information, making it only suitable for a rough FA density analysis, but hardly useful for extrapolating connection information, or specifically analyzing a selected fiber bundle (corpus callosum variability across subjects).

7.4.3 The fairy tale of tractography

Tractography based approaches have fairly complementary advantages and disadvantages. They can overcome alignment problems by working in the space of individual subjects tractography results and for this reason they do not require pre-smoothing to correct for registration errors. However such approaches do not allow the whole brain to be investigated and generally require user intervention in order to define the tracts to be used. Guide by the magnitude that a white matter reconstruction output can achieve, it is intuitive to guess that corresponding fibers across subjects are not easy to find as shown in Figure 7.17:

By simply looking at the fiber tracking result, one can only feel impotent to conclude anything about the subject's white matter architecture, and this indicates how hard it can be to analyze a population. Nevertheless, many studies have confirmed over the years the structure of certain

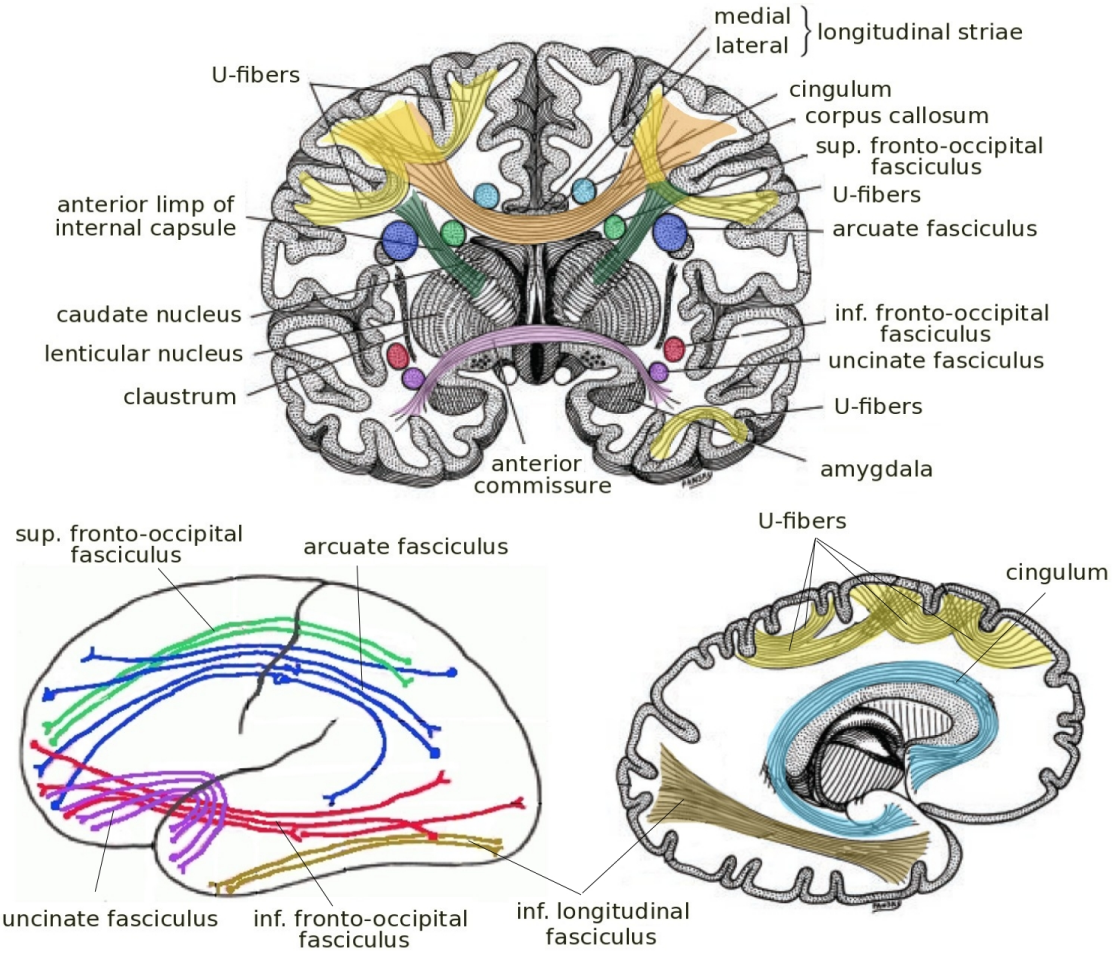

Figure 7.18: Illustration of the anatomic relationships of several WM fiber tracts. Images adapted from Jellison et al. [2004] and Poupon [1999]]

neural fibers connection on the brain such as the ones shown in Figure 7.18 Yendiki et al. [2011], Wassermann et al. [2013]. The question is thus, through which kind of analysis can one approach such representations in a data-driven manner? Nowadays there is no method that gives a ground truth about the white matter architecture segmentation, however, our aim in this thesis is to take advantage of the new technologies such as dMRI and fMRI. These technologies keep on advancing and improving their acquisition techniques, and methods need to evolve to extract the maximum amount of information as possible from the available datasets. We must still remember that no method will provide us with the ground truth, neither a probabilistic one, nor a deterministic one.

Chapter 8

Analysis of brain fiber tracts: Compression of fibers

> "Anyone whose goal is 'something higher' must expect someday to suffer vertigo. What is vertigo? Fear of falling? No, Vertigo is something other than fear of falling. It is the voice of the emptiness below us which tempts and lures us, it is the desire to fall, against which, terrified, we defend ourselves."
>
> —Milan Kundera, The Unbearable Lightness of Being

It is a challenge to analyze the underlying architecture of the human brain white matter as the brain is made up of about 100 billion of neurons. Tractography methods only recover part of the true brain tracts. Moreover, to provide a sufficient sampling of the connectivity structure across all brain regions tens of thousands of tracts are necessary. Working with such an amount of fibers is inconvenient both for clinicians, who need to visualize them, and for research, to perform further analyses.

Anatomical atlases such as Brodmann areas have been proposed for the cortex to delineate functional regions, however no complete atlas of the neural fiber architecture has been defined, and some recent approaches partition them by the regions they connect Wassermann et al. [2013]. However, when analyzing each specific subject, variability is high and ambiguity on delineating regions increases Ashburner and Klöppel [2011], Ardekani et al. [2005]. Another option is to focus on the white matter structure, and to group neural fibers by their shape and closeness. We

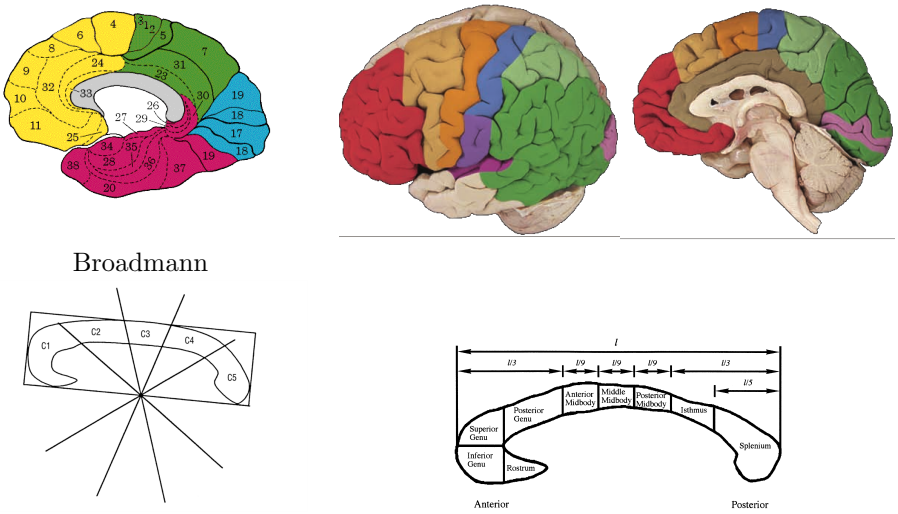

Figure 8.1: Example of different granularities while segmenting. In Broadmann areas the corpus callosum is seen as a whole, while in Hampel a geometric delineation is made and in Highley a segmentation based on a post morten analysis on axons. Image adapted from and from Hampel et al. [1998] Highley et al. [1999]

call *bundle* a group of tracts connecting the same regions in the brain, and that thus share the same features such as shape, size and location.

Clustering algorithm can help us to group tracts with similar features in bundles. Clustering techniques can be divided in supervised and unsupervised methods. In unsupervised methods one solely analyses the set of tracts with no further information about their anatomy. Unsupervised methods can be great tools to simplify the tractography output, and once a cleaner view of the fiber architecture is obtained, further analyses can be performed. Nevertheless, those bundles or clusters obtained through an unsupervised method are not necessarily meaningful from the anatomical point of view, and it should be seen only as a simplification of the underlying white matter structure Wassermann et al. [2010a, 2009]. On the other hand, supervised method can introduce anatomical information before the clustering, and thus the clusters can be considered as anatomically meaningful Mani et al. [2010b].

With supervised methods, brain white matter segmentation can be done manually or automatically based on atlases. The latter generally relies on registration methods which are imperfect, hence can introduce errors. In the context of this thesis, we believe that manual and automatic segmentation could be improved by first simplifying the fiber dataset, and feeding registration methods with richer and cleaner information.

Unsupervised clustering cannot directly create anatomically valid bundles without extensive prior information coming from experts or atlases. This is because anatomical bundles differ in both length and shape, and bundle variance highly changes from one bundle to another: e.g. corpus callosum variance is high while u-shape fiber bundles variance tend to be small, see Fig 8.2. On the other hand, such validation will be highly ambiguous as for a given structure many possible segmentations have been proposed with different granularities through the years, as shown in Fig 8.1.

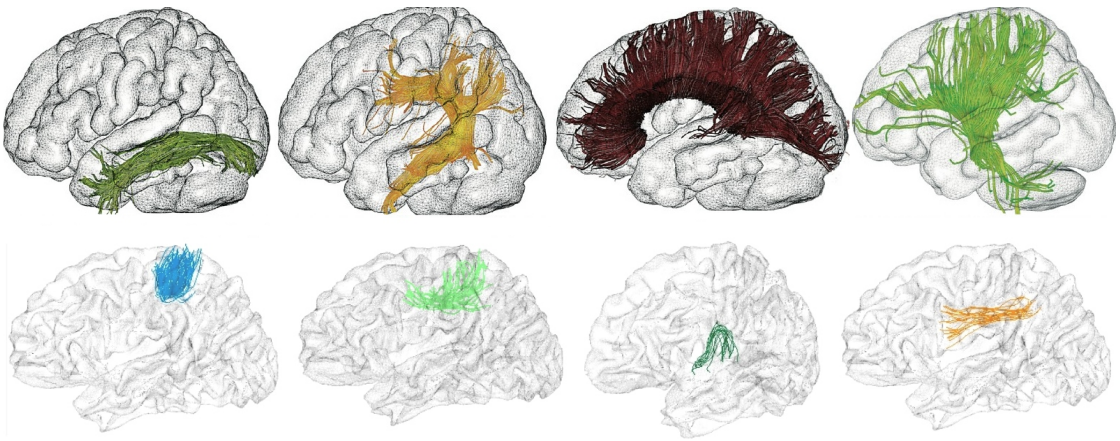

Figure 8.2: The variability that can be found within long fiber bundles (upper images) is bigger than the one we can be in short fiber bundles (bottom images). Image adapted from Guevara [2008]

Some attempts to gather fiber tracts with similar functional activation zones have recently been tried in Ge et al. [2013]. However border regions of functional activation are not well defined, and to solve for these differences, analogously to voxel-based morphometry, the functional images are smoothed. The latter decreases the confidence especially on borders, which can yield unreliable results.

In the following sections we will analyze different clustering algorithms, and some techniques to overcome problems inherent to the high dimensionality of the space under analysis. Another interesting aspect is the question of what defines two neural fibers to be alike: the shape, location, connecting regions, lengths. We will analyze different metrics and different methods to evaluate a problem where no ground truth is known.

8.1 Metrics

A metric is a function that measures object distances in a given space. The most widely used metric is the Euclidean distance, also known as the L2 distance, which on 3D points, is the L2-norm over the coordinates. A tract (or fiber) is a sequence of points in a 3-dimensional space: we define X and Y such that $X = x_1, ...x_N, Y = y_1, ...y_N$ where $x_i, y_i \in \mathcal{R}^3$. The Euclidean distance can equally be applied by seeing these sequences of points as a unique point x,y $\in \mathcal{R}^{3N}$ where coordinates and points are flattened together. However, the Euclidean distance might not be the optimal choice to represent neural brain fibers. We will analyze it drawbacks and the different alternative metrics proposed in the literature to represent brain fiber tracts.

8.1.1 Undirected Euclidean (UE)

The Euclidean distance on vectors of stacked coordinates has been widely used for clustering, yet in the setting of fiber tracts it can yield very different results depending on the chosen fiber orientation. Having a consistent orientation for all fibers across the brain is an extremely difficult

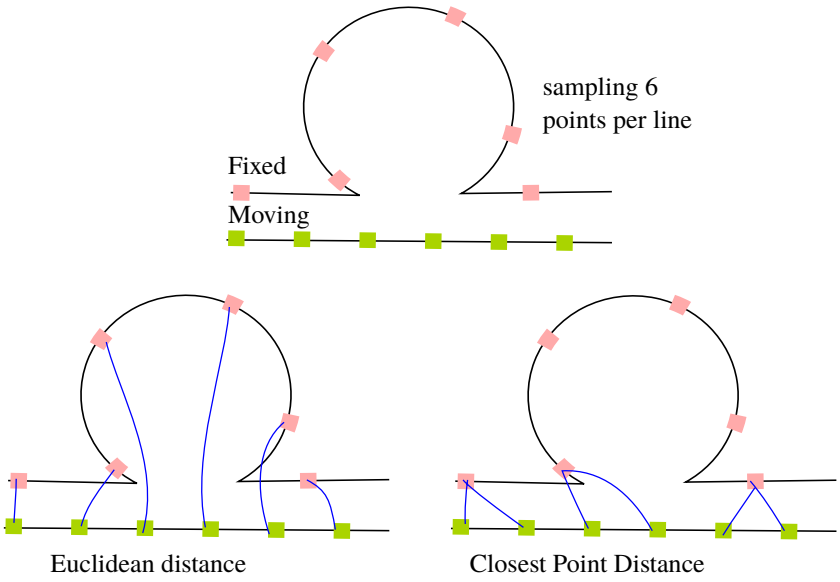

Figure 8.3: Having a fixed number of sampled points, we can see that a point-wise distances such as Euclidean (bottom-left) can have an impact regarding the length of the fibers, while distances that compare all-to-all points such as Hausdorff (maximum of the closest point distances might not). It is straight forward to see also that distances such as Hausdorff are not symmetric.

task without previously segmenting the brain. To overcome this issue we evaluate the distance in both directions, and select the minimum.

Thus each tract is represented as a sequence of ordered points, which is equivalent to its reverse version: $X = \text{reverse}(X)$ with $\text{reverse}(x_1, ...x_N) = \{x_N, ..., x_1\}$

The UE is thus defined as follows:

$$UE(X,Y) = \min(||X - Y||_2, ||X - reverse(Y)||_2) \tag{8.1}$$

where $||X - Y||_2 = \sqrt{\sum_{i=1}^{N} \|x_i - y_i\|^2}$

This metric requires streamlines to have the same number of points. By imposing the number of point per fiber, we force short and long fibers to have different resolution. Although it has been shown that depending on the application few points can be enough to classify the streamlines ?O'Donnell et al. [2012b], Mayer et al. [2011], O'Donnell et al. [2012a], it might not be the optimal setting, as longer tracts will contain more information than shorter ones.

The main advantage of UE, is that being a point-wise distance, it is linear in the number of points: $O(2K) = O(K)$. It is fast to compute, and is sensitive to fiber lengths as shown in Fig 8.3.

8.1.2 Point Density Model (PDM)

We propose the Point Density Model to better capture the shape of the fibers. PDM is sensitive to the form of the fiber, its position and is quite robust to missing fiber segments. This last property is much desired as fibers are often mis-segmented due to noise and crossing fibers (issues). Given a fiber X we represent it as the sum of Dirac concentrated at each fiber point: $\sum_{i=1}^{k} \delta_{x_i}$ (resp. Y). If we let K_σ be a Gaussian kernel with scale parameter σ, we can conveniently define the scalar product between two fibers as follows:

$$\langle X, Y \rangle = \frac{1}{k^2} \sum_{i=1}^{k} \sum_{j=1}^{k} K_\sigma(x_i, y_j)$$

The Point Density Model distance is thus defined as:

$$PDM^2(X, Y) = \langle X, X \rangle + \langle Y, Y \rangle - 2\langle X, Y \rangle \tag{8.2}$$

This distance captures misalignment and shape dissimilarities at the resolution σ. Distances much larger or much smaller than σ do not influence the metric. As it compares every point in one set to every point in the other set, its complexity order is: $O(N \times M)$ N being the number of points in X and M being the number of points in Y. However it can be narrowed by its maximum if we assume for example that $M \leq N$: $O(N \times M) \leq O(N^2)$.

8.1.3 Hausdorff (H)

Informally, two sets are close in the Hausdorff distance if every point of either set is close to some point of the other set. In other words it is the greatest of all distances from a point in one set to the closest point in the other set.

Hausdorff metric can be useful to bring together short and long fibers.

$$H(X, Y) = \max(\max_{i=1..k} \min_{j=1..k} \|x_i - y_j\|, \max_{j=1..k} \min_{i=1..k} \|x_i - y_j\|) \tag{8.3}$$

The Hausdorff metric does not require the tracts to have the same number of points. As it compares every point in one set to every point in the other set, its complexity order is: $O(N \times M)$ N being the number of points in X and M being the number of points in Y. However it can be narrowed by its maximum if we assume for example that $M \leq N$: $O(N \times M) \leq O(N^2)$.

8.1.4 Mean Closest Point

This metric takes the average of the closest points between two curves. As the closest point is asymmetric, it needs to be calculated in both directions. This metric has been conceived to find the representatives of a cluster, to be sure the centroid will lied on the center of the cluster. Its time complexity is analogously to Hausdorff, quadratic.

$$\mathrm{d}_{MCP}(A, B) = \mathrm{mean}(\operatorname*{mean}_i \min_j \|a_i - b_j\|, \operatorname*{mean}_i \min_j \|b_i - a_j\|) \tag{8.4}$$

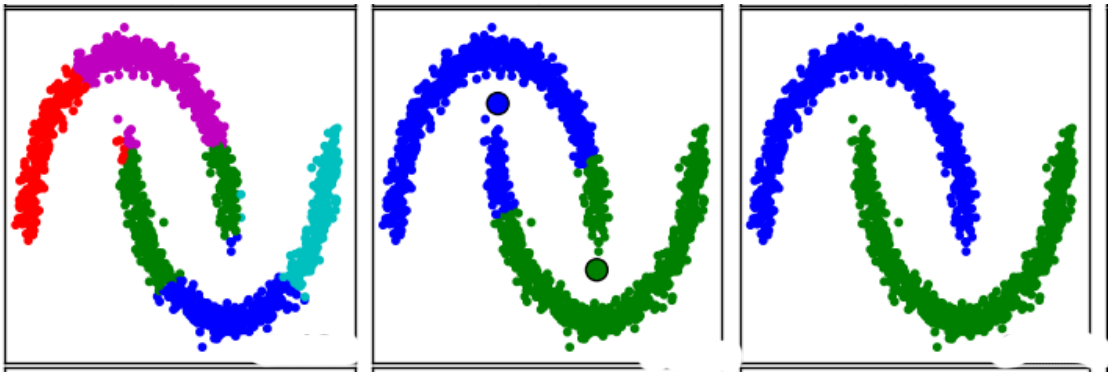

Affinity Propagation Mean Shift Spectral Clustering

Figure 8.4: Different ways to cluster the same data. This behavior can be obtained changing algorithms and metrics. The image illustrates the variability of results, and all of them can be desirable results depending on the problem definition *http://scikit-learn.org* Pedregosa et al. [2011]

8.2 Clustering

As illustrated in Figure 8.1, a combinatorial amount of segmentations can be drawn for a given set of fibers. For a given set of observations $X = x_1, .., x_n$ and a given distance, different levels of granularity give us valid solutions that might be useful or not depending on the use case, see Fig. 8.4.

Clustering algorithms search for homogeneous clusters, with similar variance per clusters. This variance can be parametrized by the number of clusters or by a variance threshold defined by the user.

8.2.1 K-Means

The name K-Means comes from MacQueen in 1967 MacQueen [1967] but it was earlier proposed by Steinhaus in Steinhaus [1956]. K-means is probably the most famous unsupervised clustering algorithm. The procedure follows a clear way to classify a given dataset through k clusters, where k is defined a priori. The main idea is to define a centroid for each cluster, and then associate each element to the cluster whose distance to the centroid is the minimum. K-Means belongs to the family of amalgamation clustering because of this last association step. The algorithm minimizes the within-cluster sum of squares error (WCSS) to the cluster with the closest centroid. This is known as *inertia*, and is defined as:

$$\min_s \sum_{i=1}^{k} \sum_{\mathbf{x}_j \in S_i} \|\mathbf{x}_j - \mu_i\|^2 \tag{8.5}$$

where μ_i is the centroid of S_i. At initialization μ_i is randomly selected from the set, and at each iteration each element evaluate its distance to the centroids, and it is assigned to the cluster with the closest centroid μ.

Once every element has been assigned, the centroids can be recomputed to better represent the cluster: mean element of the cluster. However when every centroid has changed, an element can find itself closer to the centroid of another cluster. For this reason assignment and centroids are recalculated iteratively until convergence, when the centroids do not change anymore.

Although it can be proved that the algorithm always terminate, it does not always find the optimal configuration. The algorithm is sensitive to the initial random selection of cluster centroids. The complexity of the algorithm is $O(I * D)$ I being the number of iterations, and D the distance order. In this case, an Euclidean distance over the points for our setting yields $D = O(N * M * k)$ k being the number of clusters, N the number of fibers and M the number of points per fiber. We will later analyze different metrics to adapt it to our fiber clustering problem, and how to overcome time complexity issues when using expensive metrics.

8.2.2 QuickBundles

QuickBundles is a clustering algorithm that aims to obtain a fast segmentation of the brain fiber tracts. Having a list of clusters $C = [c_1, .., c_M]$ and a list of cluster representatives $R = [r_1, .., r_M]$, each fiber tract is compared to the representatives list sequentially and the fiber is assigned to the first cluster where the distance is lower than a defined threshold and no other comparison is performed. When the distance is larger than the threshold, the tract is compared to the next cluster in the list until the list is empty. If no distance between the representatives in the list and the selected fiber tract is lower than the threshold, a new cluster is created with that fiber tract as representative. Thus, at initialization the first fiber to analyze will create the first cluster, and it will represent it.

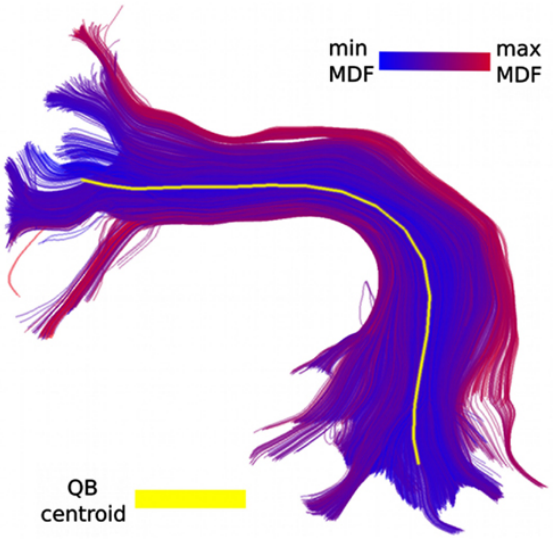

Figure 8.5: Centroid example

The centroid of a cluster is calculated as the average of the fibers in the cluster see Fig 8.5. A variable of the sum of fibers in the cluster is updated at each insertion, and by dividing this sum of fibers by the number of fibers in the cluster we obtain a centroid in $O(1)$.

Unlike amalgamation clustering, there is no reassignment or updating stage, and distances between tracts and existing clusters are computed only once. Nevertheless, the threshold parameter plays a crucial role, as it leads the size and the amount of resulting clusters.

Complexity of QB is in worst case $O(N^2)$ but in average it behaves linear $O(N)$. Nevertheless, the only property that holds on clusters is that the variance is lower than a certain threshold, as different results ca be obtained based on the different ordering of the fibers: fibers are assigned to the first acceptable cluster, but not necessarily to the best one. Additionally, clusters and centroids change as new fibers are processed.

However the presented approach is a good approach for a quick visualization of the organization

of the fiber tracts in the brain. We will analyze other approaches that can provide stronger properties on the resulting clusters at the expense of speed.

8.2.3 Hierarchical Agglomerative Clustering

Hierarchical clustering is a different methodology to analyze massive tractography datasets.

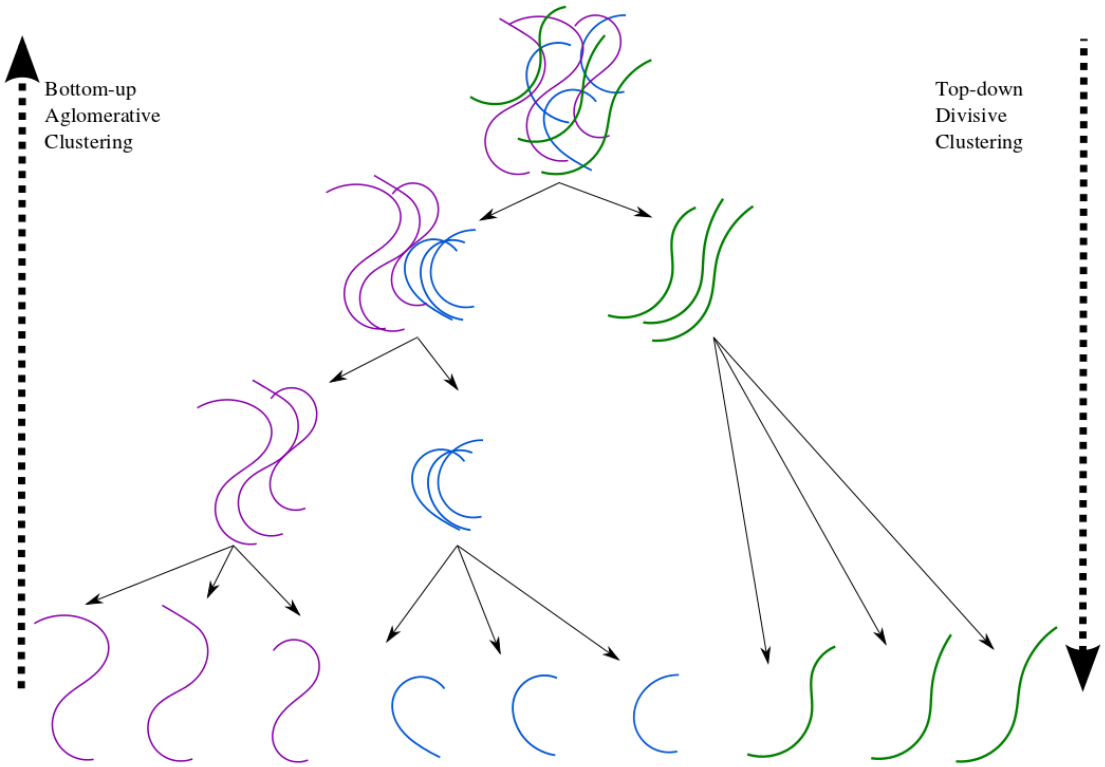

Figure 8.6: Illustration of bottom-up and top-dowm clustering approaches on three population of fibers (violet, blue and green). Different threshold values are held in the intra-cluster variability across the different stages of the algorithms. It can be started from bottom as well as from the top.

Hierarchical clustering can be agglomerative (bottom up) or divisive (top down) as shown in Figure 8.6. In an agglomerative approach, each element starts being a cluster and across iterations clusters are merged to form larger clusters. In the case of divisive clustering, every element start in the same cluster and they are divided across iterations. The intra-cluster variance varies across iterations. In the case of fibers, it is extremely hard to define a variance for the whole tractography, as it will change across bundles (i.e. u-shape, corpus callosum as shown in Fig 8.7), and in Guevara et al. [2011] different thresholds where used on short and long fibers.

Figure 8.7: Variability of fiber bundles between short and long bundles. ON the left fibers, we can see the corticospinal bundle, which variability increases as it get closer to the motor cortex (as it goes up), as the bundle splits between hemispheres, and when reaching the cortex a fanning is produced. This behaviors is hardly found among short bundles. Images adapted from Guevara [2008].

8.2.3.1 Average linkage-clustering

Agglomerative average linkage-clustering would start with every single element as a cluster. Over the iteration the following metric is calculated between clusters A and B:

$$\frac{1}{|\mathcal{A}| \cdot |\mathcal{B}|} \sum_{x \in \mathcal{A}} \sum_{y \in \mathcal{B}} d(x, y). \tag{8.6}$$

At each iteration the closest clusters are merged together. Each agglomeration occurs at a greater distance within clusters than in the previous agglomeration, and one can decide to stop clustering either up to a certain thresholded maximal distance or a number of clusters.

8.2.3.2 Multi-Subject clustering approach

In this section we describe a strategy developed in Guevara et al. [2012] to simultaneously cluster subject bundles. As a result we expect to obtain a labeling of the bundles per subject, meaning that we can map corresponding bundles across subjects.

A two level strategy is applied by first performing an intra-subject hierarchical clustering which results in a compression of the whole tractography into homogeneous bundles. Then a second level clusters together the bundle centroids from the different subjects.

For the second level a normalization is crucial to account for different brain shapes across subjects, which can have a strong impact as distance metrics are often sensitive to location. Therefore, all tractography sets are taken to the Talaraich space.

Intra-Subject Clustering Using information from the Tailarach normalization, the set is divided into right and left hemisphere, inter-hemispheric and cerebellum tracts, and a mask of the thalami was used, see Fig 8.9. Fibers are also divided based on lengths.

A hierarchical decomposition of tracts in the space of white matter voxels (or voxel parcels) is performed. During clustering, white matter voxels are merged when they are connected by several tracts leading to reconstruct the gross mask of the underlying bundles.

To check for homogeneous fascicles, a watershed approach is used to detect 3D regions with high extremity density, and the rest are discarded. The results are thin and regular fiber fascicles composed of fibers with similar length and shape.

An average-link hierarchical clustering can be run on the fascicle centroids to merge fascicles with similar geometry.

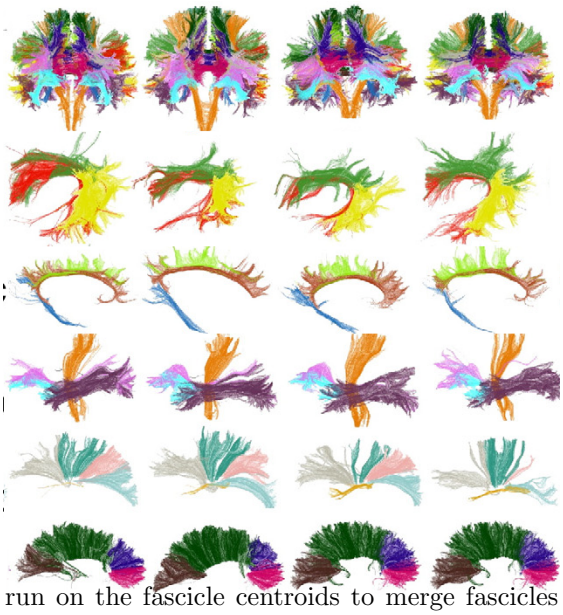

Figure 8.8: Consistent labeling across subject Guevara [2008]

Inter-Subject Clustering Once having a clean clustering for each subject, the aim is to gather similar clusters from different subjects together. The centroid of each cluster is calculated using a symmetric closest point distance defined as the mean of the two directed closest point distances (MCP). The tract that minimizes the sum of distances to the rest of the fascicle fibers represents the geometry and is at the center of the bundle.

Before clustering bundle centroids from different subjects together, it is imperative to normalize them, taking them to the same coordinate system. This normalization can be performed based on T_1 images or dMRI; on affine and on non-rigid deformations to improve accuracy. All these methods on normalization will be further analyzed and discussed in next Chapter 9.

An affinity graph is computed using a pairwise distance between fibers bundle centroids using the Hausdorff distance. Graph vertices are centroids, and edges are affinity weight. Only weights higher than a defined threshold are kept. The threshold is different for short and large fibers, as short fiber bundles tend to be tight, but large fiber bundles tend to have higher variance, e.g. in extremities. This graph is the input the average link hierarchical clustering.

Clusters that contain bundles from less than half of the subjects are discarded, or if their variance is higher than a certain threshold. The pipeline is illustrated in Figure 8.10. Thus the algorithm gives a consistent labeling across subjects as shown in Fig 8.8. Nevertheless, all the stages and parameter that need to be defined make this approach rather complicated, and it can take days to run.

8.3 Multidimensional Scaling

A whole brain tractography with current dMRI technologies can produce a few millions of fiber tracts. A distance matrix, containing distances between elements is sometimes used to avoid

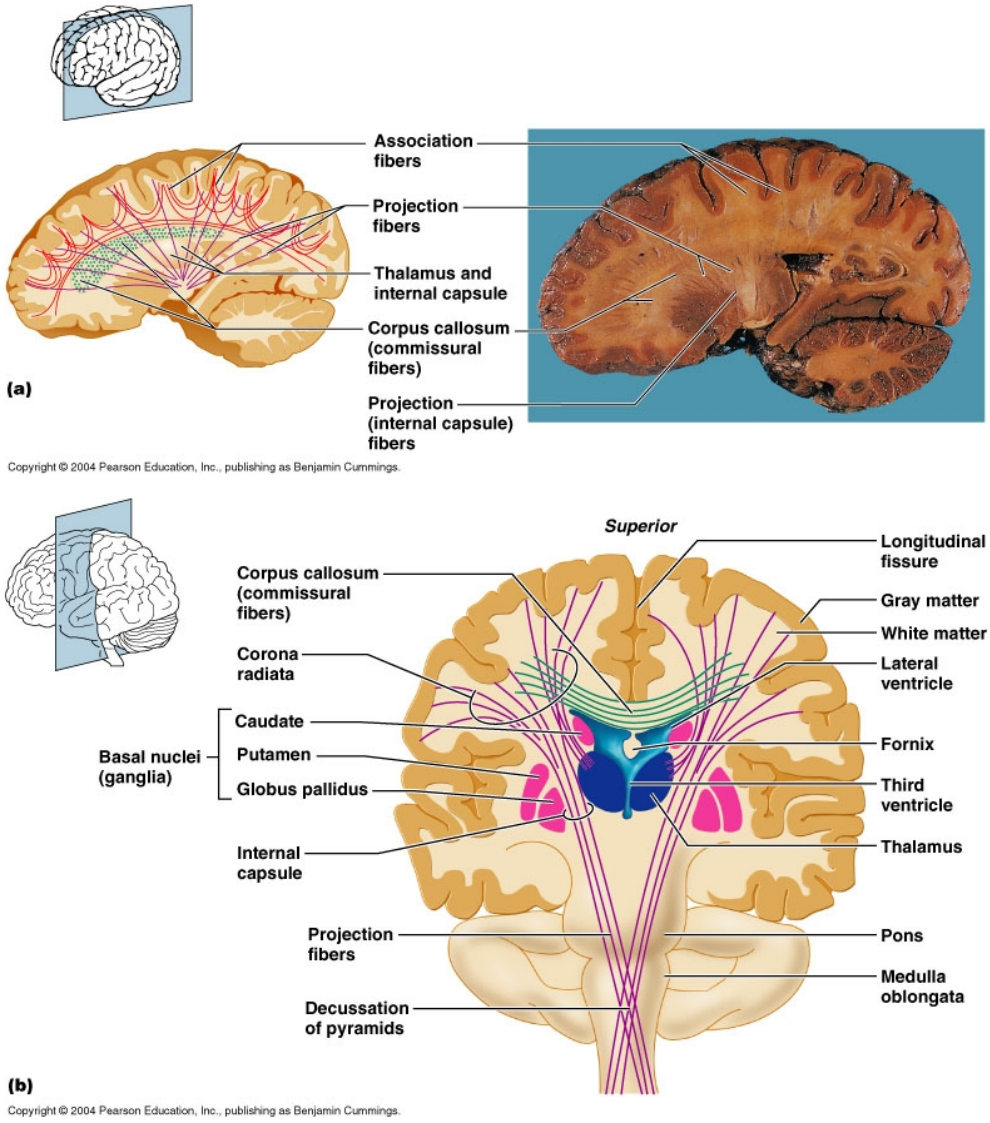

Figure 8.9: Association fibers connects the various gyri and nuclei within a single cerebral hemisphere. Commissural fibers are connections from a single hemisphere to corresponding locations in the opposite hemisphere. Projection fibers connects cerebral hemispheres to other parts of the brain and spinal cord, such as descending tracts of white matter connecting the cerebrum to the rest of the CNS. Image provided by *Pearson education 2004 , Benjamin Cummings*

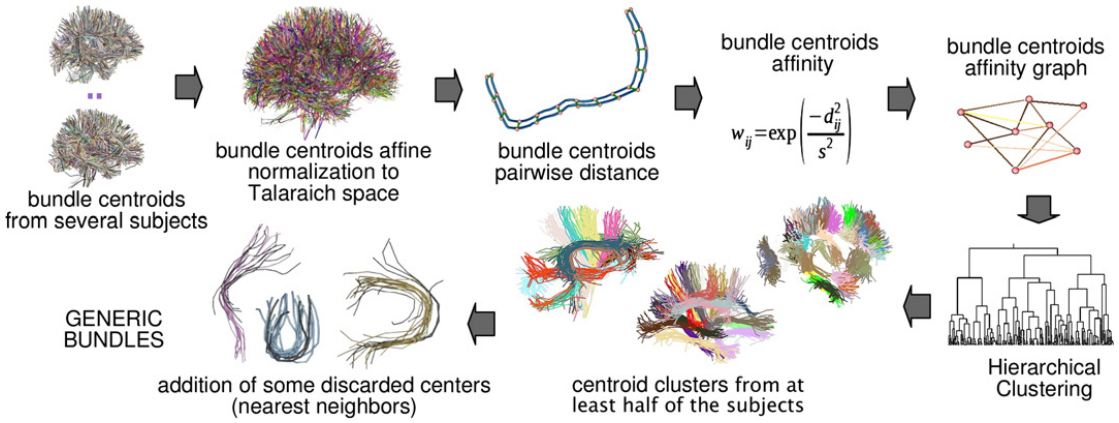

Figure 8.10: Graphic showing the clustering process starting at the intra-clustering level and ending at the inter-subject clustering level. Image taken from Guevara [2008]

recalculating the distances. However, in this case a distance matrix is too big to be stored in memory. To have an idea, on a 64bit machine, where a float uses 8 bytes, a distance matrix on a million fibers will need 500GB of disk. It is impossible to allocate a full matrix in memory, therefore distances will need to be recomputed across iterations. Distance on fiber tracts depend on the number of points per fiber, which can also be computationally expensive. Time complexity for the distance matrix is $O(M^2N)$ M being the number of tracts, N being the number of points per fiber if using a linear distance such as UE as previously presented.

Ideally we would like to evaluate different distances that could better represent white matter geometry on a clustering algorithm. Distances such as Hausdorff and Point Density Model have been widely used in the literature for analyzing neural fiber tracts Siless et al. [2013], Guevara [2008] However, the main drawback of those distances is their high computational cost, which is $O(N^2)$. In compression algorithms inputs are expected to be massive, thus having a costly measure to compare them pairwise is inefficient.

8.3.1 Manifold Learning

High-dimensional data is often represented in a simplified manner using techniques such as manifold learning. The main idea is to assume that the data lies on an embedded (non-linear) manifold within a higher-dimensional space. If the manifold has a lower intrinsic dimension, then it can be represented in that dimension, assuming that the dimensionality of the embedding was high.

The simplest way to accomplish this dimensionality reduction is by taking a random projection of the data. However, it is likely that interesting structures within the data might be lost.

Algorithms such as PCA (unsupervised Principal components analysis), ICA (unsupervised Independent components analysis), and LDA (supervised Linear Discriminant Analysis) address the dimensionality reduction problem, however by using a linear projection. These methods can be powerful but they miss the non-linearity of the structures of interest.

Manifold learning can be seen as a generalization of these linear frameworks to the non-linear case. In the next section we introduce a manifold learning technique Multidimensional scaling

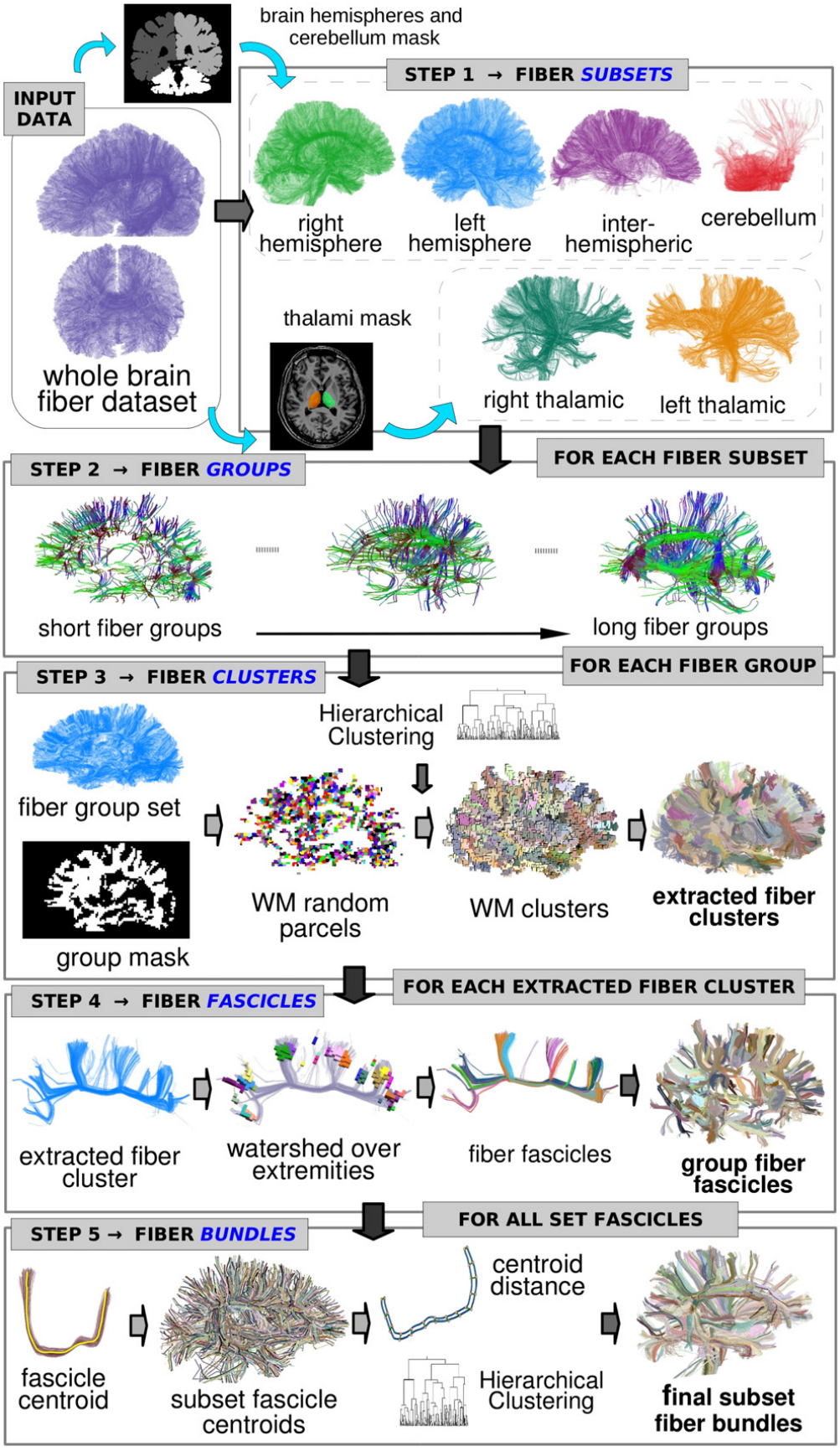

Figure 8.11: Multi-step pipeline for multi subject massive tractography clustering Guevara [2008]

(MDS) used for non-linear cases, however MDS based on Euclidean distances yields a result identical to PCA. Nevertheless, MDS can also be used with more complex distances such as Hausdorff or PDM, which are useful for analyzing fiber tracts.

8.3.2 MDS

Multidimensional scaling is an unsupervised approach, that embeds data from the original high-dimensional space to a low-dimensional space, while holding the subjective distances across elements. Multidimensional Scaling (MDS) needs a distance metric to infer a feature matrix from that information. Given a distance matrix Δ, it tries to find vectors $x_1, ..., x_n \in R^N$ such that

$$\|x_i - x_j\|^2 \approx \Delta_{i,j} \tag{8.7}$$

Thus it tries to find a new embedding of the points while preserving their distances.

This is done by finding a row and column centering matrix H and then applying an SVD decomposition. Since Δ is not symmetric, we need 2 centering matrices $H_{\#s}$ and $H_{\#F}$, and the SVD decomposition is applied on $H_{\#s}\Delta H_{\#F}$. The first N components of the decomposition yield the best-preserving N-dimensional representation of the data. The optimal embedding is then given by $X = U.S_N$, where S_N represents the first N columns of the diagonal S matrix. The solution is given by the singular value decomposition performed on the matrix of cross-samples distances Δ after centering the rows and columns.

With MDS we obtain a new set of transformed samples F' which maps 1-to-1 to the original set F and approximately preserves the input distances.

8.3.3 Clustering pipeline with MDS

To summarize, MDS given a subset of the distances, allows to embed them into a new set of fiber-like points. Then new fibers are characterized by their distance to the fiber-like points in the new embedding.

The algorithm is defined as follows:

1: $s \leftarrow$ take random sample(F)
2: $\Delta \leftarrow$ compute distance matrix($s, F, metric$)
3: $F' \leftarrow$ multidimensional scaling(Δ)
4: $L \leftarrow$ clustering($F', n_{clusters}$)

We first take a random sample s from the full set of fibers F. In step 2, we compute the pairwise distances between fibers in s and fibers in F, creating a distance matrix $\Delta \in R^{\#s \times \#F}$ and $metric$ can be any fiber distance such as UE, Hausdorff or PDM. Note that the size of this matrix depends linearly on $\#s \times \#F$.

Step 3 uses the asymmetric version of MDS. This corresponds to using the classical Nyström's approach for efficient dimension reduction Fowlkes et al. [2004]. We will discuss the accuracy of this approximation and the required sample size for it to yield a good trade-off between accuracy and running time.

Finally, in step 4 we run the traditional K-Means algorithm over the set F' to obtain the clusters of fibers. The clustering algorithm is run on a linear distance, e.g. the Euclidean distance, as the embedding of the input fiber tracts already contained information from the non-linear distances such as Point Density Model or Hausdorff.

The time complexity of the similarity matrix is $O(N^2k^2)$ N being the number of fiber tracts and k being the number of points per fiber. By using MDS the time complexity will be reduce relatively to the random samples p we take, nevertheless $p << N$ as we will later analyze in the results section: $O(Npk^2)$.

8.4 Validation Scheme

The problem of evaluating models in unsupervised settings is notoriously difficult. Ideally, the loss should be task-dependent; here we consider a set of standard criteria: the inertia of the clusters, the silhouette coefficient and some measures that require a ground truth: completeness, homogeneity and adjusted rand index.

8.4.1 Unsupervised Scores

8.4.1.1 Silhouette

The Silhouette Coefficient measures how close a tract is to its own cluster in comparison to the rest of the clusters, e.g. whether there is another cluster that might represent it better.Rousseeuw [1987].

The silhouette score for a given tract is defined as:

$$\text{silhouette} = \frac{a - b}{\max(a, b)} \tag{8.8}$$

where a is the mean intra-cluster distance and b the mean nearest cluster distance. The main drawback of this metric is that it is computationally expensive. However we can approximate it by using MDS, e.g. using only 10% of the fibers, the error compared with the silhouette applied on the full dataset was less than 10^{-2} on a random test.

8.4.1.2 Inertia

The **Inertia** is the variance of the cluster measured by the distance of each fiber of the cluster to the cluster centroid. This is exactly the function minimized by K-Means, see Section 8.5. The cluster centroid may not necessarily be a member of the cluster. Having a set of tracts $C = f_1, ..., f_N$, $f_i = p_1, ...p_K$ N being the number of fibers, and K the number of points, then the centroid of the clusters C is given by $c = \frac{\sum_1^k p_1}{k}, .., \frac{\sum_1^k p_k}{k}$, if we use the Euclidean distance.

The less clusters there are, the bigger the intra cluster variance is, and the larger the inertia is. This holds true for any metric used. Hence the inertia is not a model selection metric, but it is useful when comparing scores across algorithms when fixing the number of clusters. Inertia also assumes clusters to be convex and isotropic, which is not always the case, and it is not a normalized metric.

8.4.2 Supervised Scores

These scores can only we used when a predefined labeling is already known. It is useful for algorithm selection when testing on pre-labeled training data. Thus having a set of fibers $F = \{f_1, .., f_N\}$ of N fiber tracts, partitions of the set of fibers given by a clustering algorithm $C = \{C_1, ...C_K\}$ K being the number of clusters, and a set of labels $L = \{L_1, ..., L_M\}$ the ground truth partitioning of the fiber tracts set, M being the number of ground truth labels. Then the following scores can be defined:

8.4.2.1 Homogeneity

This score penalizes the clustering scheme in which samples from different modes are clustered together Rosenberg and Hirschberg [2007]. Tracts belonging to different anatomical structures should not be clustered together.

8.4.2.2 Completeness

Completeness score measures whether fibers from the same mode are clustered together Rosenberg and Hirschberg [2007]. Tracts belonging to the same anatomical structure should be clustered together, and therefore this metric penalizes situations in which samples from the same class are clustered separately.

8.4.2.3 Rand Index

Named after Willand Rand Rand [1971] is an index of the global consistency of assignments with respect to the reference labeling Moberts et al. [2005]. The **Normalized Adjusted Rand Index (NARI)** is a normalized and corrected for chance index of the global consistency. We will first see the normalized version NRI.

- $a = \#\{(f_i, f_j)/f_i, f_j \in C_k, f_i, f_j \in L_m\}$: The pairs of elements that belongs to the same cluster in both sets C and L.
- $b = \#\{(f_i, f_j)/f_i \in C_{k1}, f_j \in C_{k2}, f_i \in L_{m1}, f_j \in L_{m2}\}$: The pairs of elements that are separated in both clustering sets..
- $c = \#\{(f_i, f_j)/f_i, f_j \in C_k, f_i \in L_{m1}, f_j \in L_{m2}\}$: The pairs of elements that belongs to the same cluster in C and to different clusters in L.
- $d = \#\{(f_i, f_j)/f_i \in C_{k1}, f_j \in C_{k2}, f_i, f_j \in L_m\}$: The pairs of elements that belongs to the same cluster in L and to different clusters in C.

$$RI = \frac{a+b}{a+b+c+d} = \frac{a+b}{\binom{N}{2}} \tag{8.9}$$

where a and b are seen as agreements between C and L, c and d are disagreements on C and L. Rand Index is 1 when both clustering are exactly the same, and 0 when intersection is empty.

A version of Rand Index is defined adjusted by the chance of the element grouping **?**. This version yields values between -1 and 1. It is formulated as follows:

$$ARI = \frac{\mathrm{P(i)} - E(i)}{\max(i) - E(i)} \tag{8.10}$$

$P(\cdot)$ is the probability of the index i, $E(\cdot)$ the expected value, and $\max(i)$ its upper bound which is 1.

The contingency table The contingency table T summarizes the overlap of the partitions. Each entry $T_{i,j}$ denotes the number between objects in common between C_i and L_j :$T_{i,j} = |C_i \cap L_j|$. And we define $a_i = \sum_{j=1}^{K} T_{i,j}$ the sum of agreements for a ground truth partition with all the given clusters, and $b_j = \sum_{i=1}^{M} T_{i,j}$ the sum of agreements between a given cluster to all the ground truth partitions. We now can rewrite the ARI index:

$$ARI = \frac{\sum_{ij}\binom{n_{ij}}{2} - [\sum_i \binom{a_i}{2} \sum_j \binom{b_j}{2}]/\binom{n}{2}}{\frac{1}{2}[\sum_i \binom{a_i}{2} + \sum_j \binom{b_j}{2}] - [\sum_i \binom{a_i}{2} \sum_j \binom{b_j}{2}]/\binom{n}{2}} \tag{8.11}$$

In this metric big clusters have more influence that smaller ones which does not suit completely our needs, and fiber bundles are naturally not of the same size in the brain. For this reason the contingency table is normalized so that each $a_i = G$, with G an arbitrary positive value. Then each $T_{i,j}$ is multiplied by $\frac{G}{a_i}$. Now a new a' is defined where $a'_i = \sum_{j=1}^{K} T_{i,j}\frac{G}{a_i}$ and $b'_j = \sum_{i=1}^{M} T_{i,j}\frac{G}{a_i}$. Thus the NARI score is redefined over the new contingency table Moberts et al. [2005].

8.5 Results

8.5.1 Data description

We use a database of ten healthy volunteers scanned with a 3T Siemens TrioTim scanner. Acquisitions consisted of an MPRAGE T_1-weighted ($240 \times 256 \times 160, 1.09375 \times 1.09375 \times 1.1mm$) and DW-MRI ($128 \times 128 \times 60, 2.4 \times 2.4 \times 2.4mm$) TR = 15000ms, TE = 104 ms, flip angle = 90^o, 36 gradient directions, and b-value = 1300 s/mm2. Eddy currents correction was applied to DTI data using the FSL software. We used the medInria software for tractography and fibers shorter than $40mm$ were discarded **?**. This yielded an average of 25000 fibers per subject.

8.5.2 Experiments

We use the MDS+Nyström's method with 10% of the fibers. The relative error between the true distance matrix and an approximate one was smaller than 10^{-2} on a random fiber set.

8.5.2.1 Manually labeled data

We tested the algorithms on a subset of real fibers previously identified from the corpus callosum, corticospinal tract, u-shape, and fronto-occipital. We compared the clustering solutions to

the ground truth while varying the number of clusters (K-Means) or the threshold parameter (QuickBundles, see below), using the five criteria described previously.

8.5.2.2 Real data

We performed a parameter selection test over one subject to analyze the impact of the kernel size for K-Means with Point Density Model. We vary σ from 10 to 60mm and the number of clusters from 200 to 1200. We noticed that after $\sigma = 42$mm the quality of the clusters stop improving significantly w.r.t. smaller kernel sizes. For the following tests we fixed $\sigma = 42$mm. About 20% of the full set of fibers were used for the random sample, then only 5%, yielding very similar results yet significantly decreasing running time. Results are shown in Fig. 8.13.

We tested K-Means exhaustively over ten subjects with PDM, Hausdorff and UE while varying the number of clusters from 18 to 3200. Additionally we compared their output to the available QuickBundles (QB) clustering algorithm Garyfallidis et al. [2012]. However, in QB the resulting number of clusters is guided by a threshold value. Therefore we ran QB over one subject varying the threshold from 5 to 40mm, and selected threshold values based on the number of clusters obtained to run them over the 10 subjects.

8.5.3 Results and Discussion

8.5.3.1 Manually labeled Data

On the manually labeled data we were able to run the validation criteria that needs a ground truth, such as Homogeneity, Completeness and NARI. We tested each clustering 10 times while randomly removing 1/8 of the fibers, to sample variable configurations.

It can be seen in Fig. 8.12 that QB performs well regarding completeness but not so well on homogeneity, which means that clusters have fibers from different structures but fibers from the same structure are clustered together. QB obtains higher performance with large numbers of fibers.

On the other hand, K-Means+PDM obtained high homogeneity but lower completeness, indicating that clusters contain fibers from the same structure but that they are not complete, which means that some structures are split. For example, cluster A contains mostly fibers from the corpus callosum, therefore its homogeneity is high. Nevertheless, corpus callosum fibers are also found in cluster B, being itself highly homogeneous too. Neither A nor B are complete.

Looking at the inertia criterion, we can effectively confirm that clusters of QB have high variance, and those of K-Means+PDM a lower one. This can also be link to the minimization criteria of K-Means, as we mentioned in Section 8.5, its minimization energy is exactly inertia.

K-Means+UE performs poorly both regarding homogeneity and completeness compared to the other approaches; as could be anticipated, it yields lower inertia. A point-to-point Euclidean distance seems to be a poor representation of the fiber geometric structure.

K-Means+H seems to have a similar behavior as K-Means+PDM except for the silhouette criterion, which means that the resulting clusters are typically not well separated.

Regarding Silhouette and NARI, one can observe that K-Means+PDM plateaus at around 9 clusters and then decreases, while QB reaches a maximal value when more clusters are considered, and then decreases more slowly.

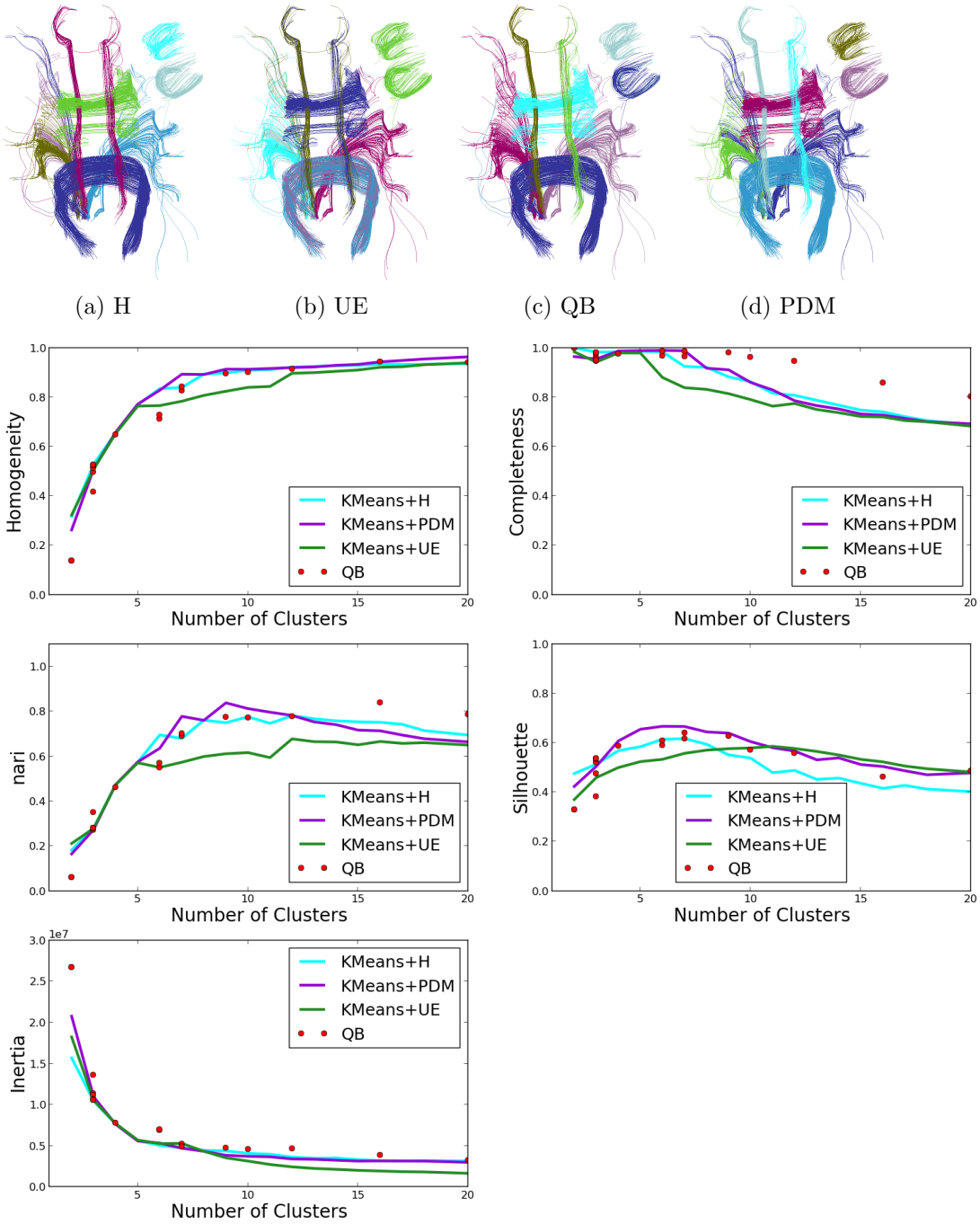

Figure 8.12: **Manually labeled data results**: (top) Example of clusterings obtained with fours methods on the simulation (bottom) Average of the criteria obtained over 10 random samplings of the manually labeled data, as a function of the number of clusters obtained.

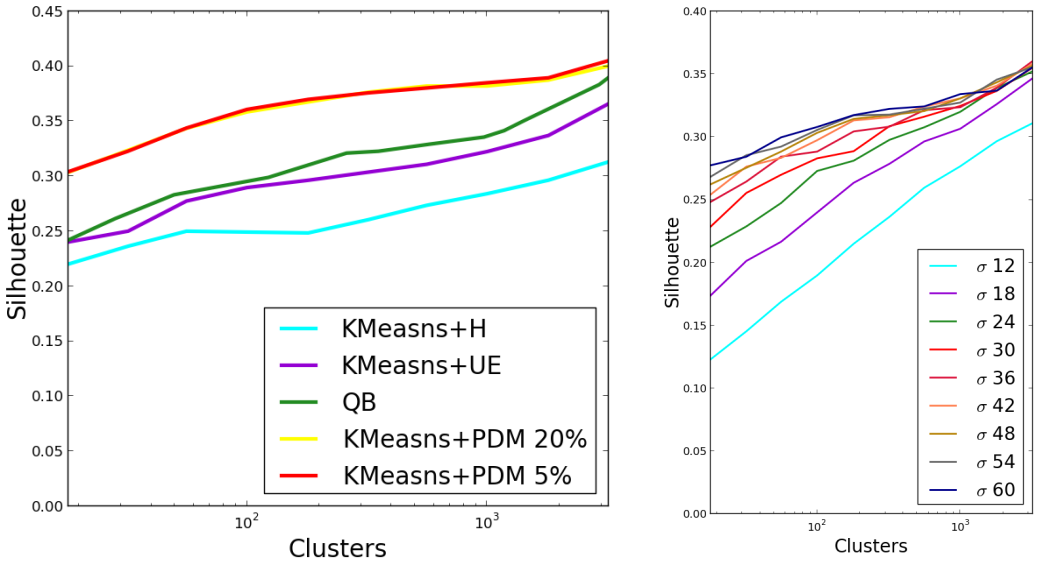

Figure 8.13: **Silhouette score on real data**: (left) Comparison of K-Means with PDM, UE, and Hausdorff metrics, and QuickBundles. Each curve shows the average score of the ten subjects. K-Means+PDM is used with two size of the learning set in Nyström step. (right) Dependence of the results of K-Means+PDM on the parameter σ.

Last, by looking the silhouette criterion K-Means+PDM seems to better assign the clusters to fibers than QB, which is probably related to the algorithm itself that, unlike K-Means, does not systematically update the cluster assignment.

8.5.3.2 Real data

On real data we can only use the fully unsupervised criteria, such as inertia and the silhouette criterion. We focus on the latter. Results are given in Fig. 8.13 for each of the aforementioned criteria and algorithms. We can see that the K-Means+H and K-Means+UE metrics result in a poor silhouette score, meaning that the separation between the clusters is not very clear with these algorithms.

Moreover, K-Means+PDM consistently improved results given by the other algorithms. Nonetheless when going to large number of clusters (over 3000) curves between QB and K-Means+PDM seem to converge in terms of cluster quality, such as measure with Silhouette score.

Note that a given number of clusters can correspond to strikingly different structures in the data, depending on the algorithm and metric: In Figure 8.14 we show the result of the full brain fiber clustering for all algorithms on an arbitrary chosen subject. The number of fibers was set to 560 for all of them. Resulting clusters on (e), (f) and (g) seem to be wider and more heterogeneous than (h), showing that the PDM metric can indeed better capture shape of fibers. Homogeneity of clusters in comparison to (e) (f) and (g) can clearly be seen on the corpus callosum and the corticospinal tract. Below, we can see the histograms on the cluster sizes. We see that QB has the largest amount of small clusters, that likely correspond to outlier fibers, and it also yields very large clusters. K-Means+PDM also seems to generate a few small clusters, unlike K-Means+H

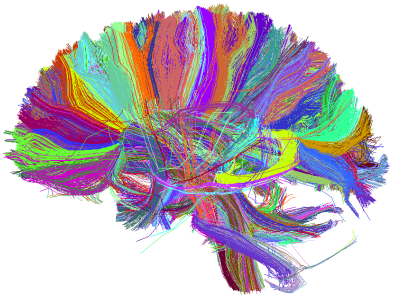

(e) H

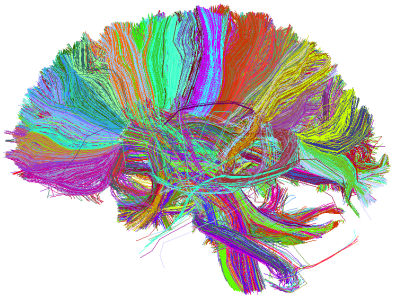

(f) UE

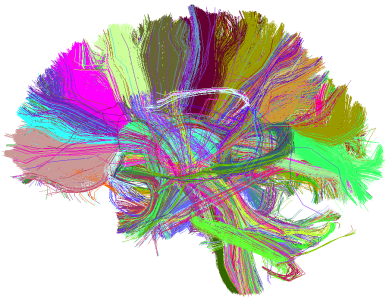

(g) QB

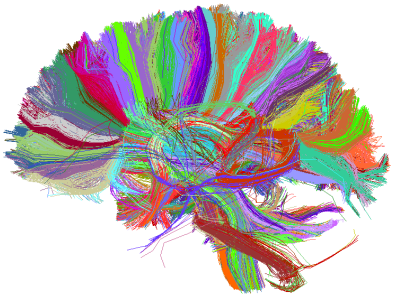

(h) PDM

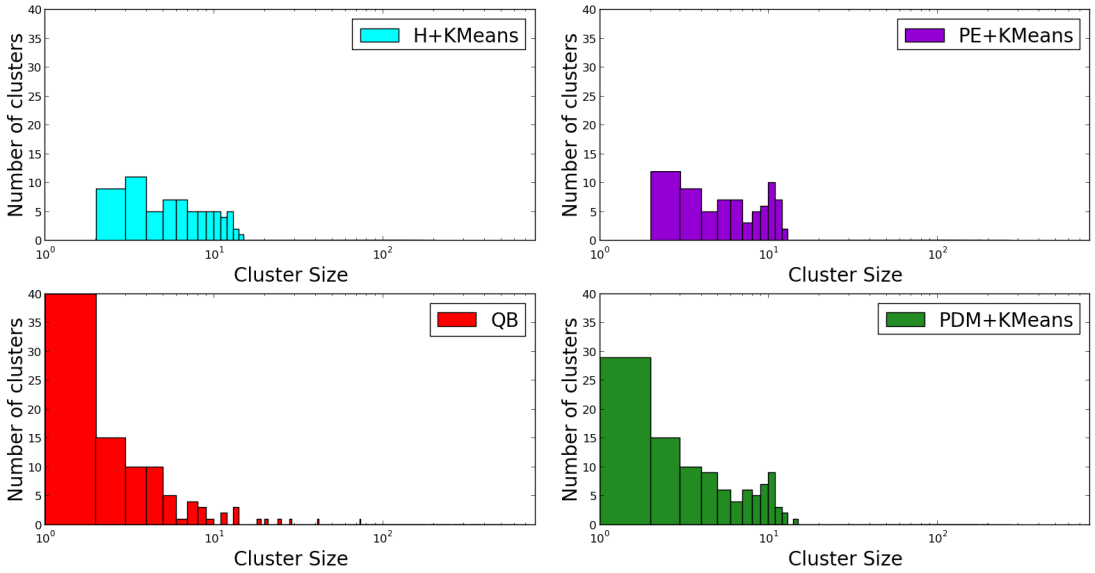

Figure 8.14: (top) **560 clusters on brain**: Qualitative algorithm comparison for the resulting fiber clusters on an arbitrary chosen subject. (below) Histogram of the cluster sizes for the different algorithms.

and K-Means+UE that do not yield small clusters, meaning that spurious fibers are included in clusters, and not rejected as outliers.

Both QB and PDM-K-Means running time are sensitive to the number of clusters, however QuickBundles' time complexity is $O(NCk)$ and K-Means+PDM $O(NSk^2 + NCk)$, where C is the number of clusters, k the fiber resolution and S the sample size. In K-Means+PDM, the creation of the partial distance matrix dominates the time complexity as long as $Sk > C$.

This code has been implemented in Python based on utilities provided by Scikit-Learn Pedregosa et al. [2011].

8.6 Conclusion

We presented an analysis and comparison of some of the techniques most commonly used for fiber clustering.

As our goal is to simplify the complicated structure of brain fibers, we prioritize homogeneous clusters, where centroids can accurately serve as a cluster representative. Thus simplifying the dataset by only their centroids.

Three different methods were proposed, where two are fully unsupervised and one uses previous cortex segmentations to roughly initialize and separate the full tractography (e.g. hemispheres, inter-hemispheres). In the latter the resulting bundles can be mapped to anatomical bundles, while in the fully unsupervised methods we can only expect a compression of the fibers.

Nevertheless pipelines attached to supervised clustering methods, especially for inter-subject analyses are generally long, hard to parametrize and can take days to run, especially with such dataset magnitude. For these reasons other alternatives have to be considered.

We compared the available metrics found in the literature for measuring distances between fibers, incorporating PDM which has been used recently to represent geometric structures in the brain, but never for fiber clustering. We analyze their performance against a fast algorithm called QuickBundles.

QuickBundles is able to return a segmentation of the white matter in minutes, while KMeans takes longer.

We show different behaviors of the methods depending on the number of clusters: while QB is good at isolating outlier fibers in small clusters, it requires a large number of clusters to represent effectively the whole set of fibers. K-Means+PDM has a better compression power, but is less robust against outlier fibers. Nevertheless, it clearly outperforms other metrics for all criteria that we tested.

It is necessary to remind that algorithms that K-Means and QuickBundles, will in general return an homogeneous set of clusters, but that theses clusters cannot be readily identified with anatomical bundles. These algorithms are proposed as tools to simplify the white matter structures, e.g. to represent it with few prototypical ones. By doing so, we not only improve computation time and visualization comfort, but also we remove spurious fibers, as they will end up in small irrelevant clusters.

By simplifying white matter underlying architecture we expect to simplify and improve the accuracy of further analyses methods. In this thesis, we propose to improve accuracy of brain image registration by introducing white matter connection information. White matter fiber datasets are immense, and tractography errors can lead to spurious fibers, therefore it is imperative before a wise pre-selection of stable bundles to perform further analysis.

Chapter 9

Multi-modal Registration of T_1 images and Fiber tracts

"The rule is, jam tomorrow and jam yesterday – but never jam today."
"It must come sometimes to 'jam today'," Alice objected.
"No, it can't," said the Queen. "It's jam every other day: today isn't any other day, you know."

— Lewis Carroll's 1871, Through the Looking Glass and What Alice Found There

As fingerprints, each brain is unique: its shape and size differ among individuals, depending on genetics and learning experience. Statistical atlases of the human brain anatomy are used to model the variability of its shape across populations. These atlases are crucial to understanding the development of the human brain in vivo and most importantly to analyze pathologies in neurological or psychiatric diseases.

Imaging biomarkers can be used to diagnose neurodegenerative and psychiatric diseases, hence

finding relevant biomarkers is the first step to early disease detection. Neurological diseases are known to have an impact on brain anatomy, for instance Alzheimer patients' ventricles are larger Chintamaneni and Bhaskar [2012]. To detect such types of pathologies, it is mandatory to analyze a diseased population and contrast it to a normal one. Manually comparing thousands of images is not only time consuming, but it might also introduce errors, hence it is crucial to develop and improve methods to automatically analyze massive datasets of individual images.

Voxel-based morphometry (VBM) compares populations voxel-wise after aligning all subjects to a reference template. The action of aligning structures together is called Registration, also know as Matching. Registration is routinely used to perform group analysis on populations or to analyze changes over time, such as normal growth or neurological disorders.

Ideally, registration finds the optimal spatial transformation that aligns structures from one subject to another, which should result in an anatomically plausible mapping. Having a fixed image F in the target or reference space, and a moving image M that we want to align, the problem is typically handled by minimizing an energy of the form:

$$\mathcal{E}(\phi) = \mathcal{S}(F, M \circ \phi) + \mathcal{R}(\phi) \tag{9.1}$$

The first term quantifies the level of alignment between the target image F and the source image M, while the second term $\mathcal{R}$ regularizes the transformation. The transformation ϕ should map homologous locations from the brain in the moving image to the fixed one, and at every position $x \in \Omega$ is defined as the addition of an identity with the displacement (or update) field u or $\phi(x) = x + u(x)$ is the so-called small deformation framework. When the transformation is parametrized by a small number of variables and is inherently smooth, regularization introduces prior knowledge by imposing constraints. When the transformation is a non-parametric deformation, regularization dictates the nature of the transformation, imposing properties, and improves the estimation of ϕ given the ill-possessedness of the problem.

An image registration algorithm involves three main components: 1) a deformation model, 2) an objective function and 3) an optimization method Sotiras et al. [2012]. It is key to wisely select the components to solve registration problems, and consequently to obtain accurate results. Ideally the results should be independent from the optimization method, however in a deformable registration scenario a displacement is estimated for each voxel of the image, and is thus an ill-posed problem with more unknowns than constraints. Given the non-linearity and non-convexity of the problem in eq 9.1, it is not possible to have a closed-form or even unique solution, thus the optimization strategy to estimate the registration parameters is crucial to obtain relevant solutions Hadamard [2003].

9.1 Deformation models

The deformation model limits the solution to a class of transformations, hence it results from an inherent compromise between efficiency and power of description. The degrees of freedom or the parameters to estimate vary from 6 in a rigid transformation, 12 in an affine, and thousands or even millions when non-parametric/non-rigid [1] deformations are considered, depending directly on the dimensionality of the space.

[1] We call non-rigid to free-form deformation, where each voxel can freely deform. Although non-rigid formally could stand for affine, in the medical imaging community non-rigid is mostly a synonym of free-form.

The mapping from the source to the target is called forward mapping, while the one from target to source the backward mapping. In the fist case voxel locations of the source image are usually mapped to non-voxel locations on the moving image, and the intensity values of the voxels of the deformed image needs to be calculated. This is shown in Fig 9.1 in red. In the second case when voxel location of the deformed image are mapped to non-voxel locations in the source image, their intensities can be easily calculated by interpolating between neighboring voxels. This is shown in Fig 9.1 in blue.

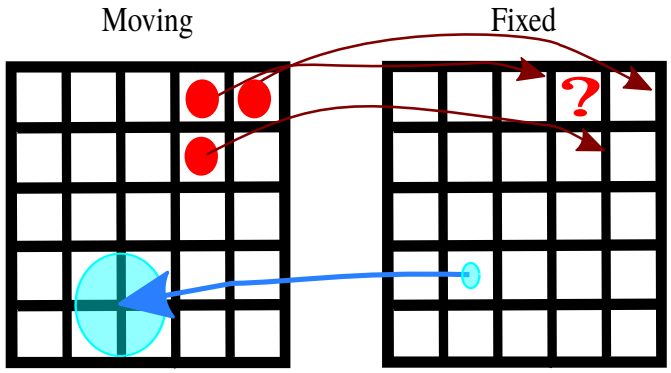

Figure 9.1: A deformation can take voxel locations to non-voxel locations (as shown by arrows mapping from the center of the voxels). The forward mapping (in red) is generally harder to compute as an interpolation is needed to compute with the image values in the target space, which are only tractable after applying the deformation and are not expected to lie on voxel locations. However, in the backward mapping (in blue), from the target desired location, we can easily interpolate the region that surrounds the mapped location from the target to the source image (big blue circle).

We will analyze three groups of deformation models that are used in this thesis; however a deeper analysis on deformation models for medical imaging can be found in Holden [2008], Sotiras et al. [2012].

9.1.1 Geometric Constraints

When analyzing images from the same subject, one is likely to use a rigid transformation, as it only contains translations and rotations, preserving volume, size, and shape. These types of transformations are useful to correct head movement, or roughly align skulls. The situation occurs with images from different modalities such as T_1 and DWI/T_2 obtained from one given subject and also when following normal or disease development over time in longitudinal studies. Affine registration also contains scale and shear factors, which makes it more useful in inter-subjects situations. Non-rigid deformations account for morphological differences across objects, while affine transformations include differences in size, rotation and shear. Affine registration serves as an initialization step for morphological analysis, therefore we first introduce affine transformations and in the next sections we introduce and discuss non-rigid settings.

Original + Rotation + Scaling + Shear + deformable

Given a transformation $A \in \mathbb{R}^{3X3}$ and a translation vector $t \in \mathbb{R}^{3X1}$, affine transformations are defined as $T' = A|t$ then $T' \in \mathbb{R}^{3X4}$, and their extension $T \in \mathbb{R}^{4X4}$ is defined by completing T' on the 4th row: $T' = \left[\begin{array}{c|c} A & t \\ \hline 0 & 1 \end{array}\right]$

Then any array of coordinates in $\mathbb{R}^3$ is fiven a shape in $\mathbb{R}^4$ by filling the last coordinate with 1: $X' = (x_1, x_2, x_3, 1)$.

Given a fixed and moving image, F and M respectively, we would like to find the transformation $\mathcal{T}$ such that : $M(X) = F(\mathcal{T}(X))$. However, given the degrees of freedom of the transformation, and the complexity of aligning two different images, the exact equality will most likely not be achieved. To find the best affine transformation that aligns the moving image onto the fixed image, we define the following energy:

$$\mathcal{E}(\mathcal{T}) = \sum_{x \in \Omega} \text{Sim}(F(x) - M(\mathcal{T}(x))) \tag{9.2}$$

Where Sim can be any loss function over images, and Ω is the image domain. In Section 9.3.1 we will discuss different available options.

In inter-subject image registration, one may opt for a richer model, that gives more accurate solutions such as deformable transformations. With non-parametric deformation, symmetry and topology preservation are important. In medical imaging, anatomical structures should not be split nor fused together, hence the requirement of topology preservation. On the other hand, a transformation should be invertible, and its inverse should be computable. However, this does not ensure us, that the transformation originally computed by minimizing $\text{Sim}(F, M)$ is the same as the one obtained by computing its inverse $\text{Sim}(M, F)$. For this to be true, the energy formulation needs to be symmetric.

Asymmetric algorithms are biased by the choice of the target domain. The solution may vary greatly when choosing one subject as target or source. Inverse consistency algorithms force backward and forward transformations to map one onto the inverse of the other by simultaneously estimating both, and penalizing the difference. Inverse consistent methods can preserve topology but are only asymptotically symmetric, as solutions depend on the energy formulation, the terms and the weights.

Topology preserving algorithms impose transformations and their inverse to be continuous. Diffeomorphisms ensure a deformation and its inverse to be differentiable, thus preserving topology. A diffeomorphism maps a differentiable manifold onto another one, ensuring smoothness of the map and its inverse.

Most algorithms restrict theirs solutions to the set of diffeomorphic transformations with homogeneous boundary conditions, meaning that rigid and affine transformations have already been

applied and that the borders of the images maps onto each other. This can be assumed, as rigid and affine registration are simpler and fast problems that can easily be applied as a pre-processing step.

9.1.2 Physical models

9.1.2.1 Notations

1. $\vec{u}$ is the update or displacement field.
2. $\vec{v}$ is the velocity field.
3. μ, λ are Lamé constants, describing the properties of the material.
4. $\mathcal{E}(\vec{u})$ is the force field, the loss e.g. $\mathcal{E}(\vec{u}) = \|F + \vec{u} - M\|^2$.

9.1.2.2 Elastic bodies

In 1981, Broit modeled the image grid as an elastic membrane, that deforms under the influence of two forces, an external forcing the matching, and an internal enforcing the elastic properties of the material, until an equilibrium is reached Broit [1981]. Elastic bodies are modeled with the Navier-Cauchy partial differential equation (PDE):

$$\mu\nabla^2\vec{u} + (\mu + \lambda)\nabla(\nabla.\vec{u}) + \mathcal{E}(\vec{u}) = 0$$

where $\mathcal{E}(x)$ is the force field that drives the registration. μ accounts for the rigidity of the material and λ the Lamé first coefficients, and $\vec{u}$ is the displacement field. This linear elastic equation assumes small angles of rotation and small linear deformations. As a result, the elastic registration model penalizes large displacements and is not useful in applications when large nonlinear deformations are natural Yonovsky et al. [2006].

9.1.2.3 Viscous Fluid

In 1996 Christensen et al. introduce the Viscous Fluid flows models that can recover large deformations, and were described with the Navier-Strokes equation Christensen et al. [1996]:

$$\lambda\nabla^2\vec{v} + (\mu + \lambda).\nabla.(\nabla.\vec{v}) + \mathcal{E}(\vec{u}) = 0,$$

where the first term constraints neighboring points to deform similarly by spatially smoothing the velocity field. A velocity field is related to the displacement field as $\vec{v} = \frac{\partial u}{\partial t} + \langle\vec{v}, \frac{\partial u}{\partial x}\rangle$. The velocity field is integrated in order to estimate the displacement field. The second term allows the structure to change in mass while μ and λ are the viscosity coefficients.

9.1.2.4 Diffusion Model : Demons Algorithm

In 1998 J.P. Thirion introduced the simple diffusion model into registration as follows Thirion [1998]:

$$\nabla u + \mathcal{E}(\vec{u}) = 0$$

The initial demons algorithm provided an efficient scheme but it was lacking a theoretical ground. Pennec in Pennec et al. [1999] showed that Demons combined with gradient descent was equivalent to a second order minimization over a Euclidean distance, while for the regularization scheme it was shown that the global transformations convolved with a Gaussian Kernel, is a Green function of the diffusion equation under appropriate initial conditions, providing an efficient regularization scheme.

9.1.2.5 Curvature

Curvature registration was introduced by the deformation is modeled with an equilibrium equation:

$$\nabla^2 u + \mathcal{E}(\vec{u}) = 0$$

This regularization scheme does not penalize affine transformations relieving the algorithm from an affine pre-registration initialization step. Fischer and Modersitzki [2003, 2004]

9.1.2.6 Flows of diffeomorphisms: Large Diffeomorphic Deformation Metric Mapping (LDDMM)

Flows of diffeomorphism, also known as LDDMM, was introduced by Beg et al in 2005 Beg et al. [2005]. It models the deformation by considering its velocity over time according to the Lagrange transport equation Christensen et al. [1996], Dupuis and Grenander [1998], Trouvé [1998], Sotiras et al. [2012]. The regularization term $\mathcal{R}(\phi)$ constraints the velocity field v to be smooth: $\mathcal{R} = \int_0^1 \|v_t\|_V^2 dt$, where $\|f\|_V = \|Df\|_{L2}$ with D a differential operator.

The fact that the velocity field varies over time allows for large deformations. The distance between images is defined as the geodesic distance according to a metric that connects them and this can be used to analyze anatomical variability Miller et al. [2002], Younes et al. [2009].

Demons framework and LDDMM have gained popularity and visibility over the last decade. LDDMM mathematical approach is sound as it allows for large deformations. On the other hand, Demons framework is a simple, and fast approach with accurate results, that can be easily extended for multi-modal registration.

9.1.3 Extrapolating control points

In this setting the goal is to approximate the global deformation by fewer parameters than the whole grid. Landmarks or regions of interest might lead to displacements being defined only at restricted domains of the image. For example, in Figure 9.2 landmarks set on the main articulations of the skeletons might be enough to infer the whole deformation Glaunès et al. [2004]. Nevertheless, by using only a landmark set on the hands and foots as shown in the color circles, lead to an sparse grid of vector field defined only on

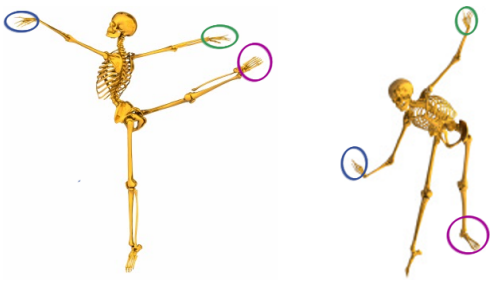

Figure 9.2: Landmark based registration: Few selected landmarks can induce the whole transformation grid, decreasing the number of parameters to estimate.

the landmark regions, which are needed to be extrapolated to the rest of the image domain. By estimating the transformation from a few landmark points, the rest of the image domain smoothly follows the landmark directions. These models are rich enough to describe the needed transformation while having few degrees of freedom and thus facilitating the inference of the parameters.

9.1.4 Interpolation

9.1.4.1 Radial Basis Interpolation

Radial basis function is a well known interpolation function. The value of an interpolated point x is given by a kernel K that depends on the distance to the control points p_i.

$$u(x) = \sum_i w_i K(x, p_i) \tag{9.3}$$

We search for the w_i such that when evaluated at a control point p, $u(p) = p$. Evaluations studies have been presented in Zagorchev and Goshtasby [2006] for non-rigid registration, while the topology preserving properties have been presented in Yang et al. [2011]. Similar approaches inspired by interpolation theory have been presented using B-splines, and cubic B-splines Declerck et al. [1997], Sdika [2008].

9.2 Space of Diffeomorphisms

Diffeomorphic transformations are of particular interest as they preserve topology by definition. Topology preservation is fundamental to make comparisons in the natural world between objects that are known to differ across populations while preserving local neighborhood relations. Cythoarchitectonic brain mapping studies suggest that the layout of cell types in the brain is generally preserved Schleicher et al. [2005], thus calling for topology preserving methods. Additionally, the deformation inverse not only exists but it is also smooth.

A diffeomorphism is a smooth invertible transformation with a smooth inverse. Diffeomorphisms are powerful as by preserving topology, they prevent foldings which are generally physically impossible. A topology preserving example is shown Figure 9.3. For these reason, diffeomorphisms are of special interest in the medical imaging community. The special interest in registration, is to be able to register a subject to an atlas space to further analyze it, and after inference in the common space (i.e. an atrophy in a structure, an activation in fMRI), pull back the results to the original subject space.

The set of diffeomorphism acting upon a given domain have a group structure. More specifically, they form a Lie group.

A Lie Group G is a manifold together with a smooth composition map usually denoted as multiplication ($x \mapsto s \circ x$ for x and s in G) and a smooth inverse map ($x \mapsto x^{-1}$ for x in G), that satisfy the group axioms: closure, associativity, existence of a natural element Id. To any

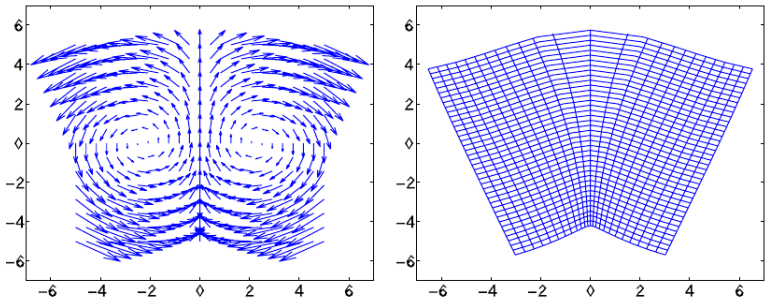

Figure 9.3: Topology preserving deformation example. On the left figure we can see a vector field, and on the right its application to a regular grid. As there is no folding, no overlapping structures have been introduced, no information has been lost, and we can apply the inverse transformation to recover the original grid.

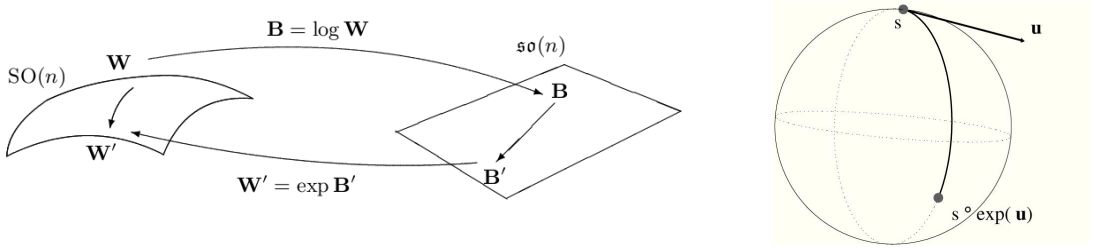

Figure 9.4: In (a) a graphical example shows how using the exponential and logarithm function associate the manifold with a tangent vector space in the case of the SO(n) group. In (b) an unconstrained update u is computed on the Lie Algebra and is projected back onto the Lie group through the exponential map. Image taken from Vercauteren et al. [2009]

Lie Group can be associated a Lie algebra g, whose underlying vector space is the tangent space of G at the neutral element Id. The Lie algebra captures the local structure of G.

The Lie group and the Lie algebra are related through the group of exponential which is a smooth mapping from a neighborhood of 0 in g to a neighborhood of Id in G, shown in Figure 9.4 (a). Canonical coordinates provide local coordinate charts so that for any $x \in G$ in some neighborhood of s, there exists a vector u such that $x = s \circ exp(u)$, and formally this composition of diffeomorphisms is used instead of the addition, to ensure the result is also diffeomorphic. This operation is shown in Figure 9.4.

9.3 Matching Criteria - Similarity Metric

Depending on the application and on the type of images, we can chose between iconic or geometric metrics. In iconic settings the intensity values of the image grid are used, and in geometric metrics, geometric representation of structures are drawn such as surfaces or clouds of points. Given an anatomical T_1 image, accurate and fast results can be obtained by using iconic methods

Thirion [1998], Beg et al. [2005-02-01], Rueckert et al. [2006]. However, from anatomical brain T_1 images we can geometrically represent the brain cortex as a surface to use a geometric approach for registration Yeo et al. [2010], Vaillant and Glaunès [2005], Collins et al. [1996].

Image or voxel-based registration consists in finding a voxel-wise mapping between a source and a target image. These methods evaluate the whole image uniformly, without prioritizing information to drive the registration.

Geometric registration specifically targets the alignment of Structures of Interest (SOI), or landmarks. Landmarks can be placed in salient locations of an image, but can also be inferred as a new representation or model of the image, such as for surfaces or fiber tracts. With higher resolution images we can characterize more details in the images, which facilitates the extraction of landmarks.

While finding reliable landmarks is generally an open problem, geometric registration is robust with respect to the initial conditions. In general, landmarks constraints will be enforced throughout the deformation. Landmarks or geometric models of the image are used to discard irrelevant information from the original image, e.g. putting few landmarks in the ventricles, prefrontal cortex and cerebellum might suffice to perform an affine registration.

Durrleman et al in Durrleman et al. [2011] used a subset of fibers as landmarks to perform a fiber-based registration. While these types of methods clearly improve SOI registration, they are in general not suitable for inferring a volumetric mapping between two subjects and cannot be used for comparing other structures than those used specifically during registration.

Hybrid methods combine both types of information in an effort to get the best of both worlds. For instance, Auzias et al. [2011], Ha et al. [2010] used the mathematical framework of *currents* to simultaneously register images and geometric descriptors, while Sotiras et al. [2010] proposed a Markovian solution to the same problem.

9.3.1 Iconic Methods

The iconic dissimilarity criterion takes into account the intensity information of the image elements. The criterion should be able to account for the different physical principles behind the acquisitions of the two images and thus for the intensity relation between them. The properties of the similarity function (e.g. convexity) may influence the difficulty of the inference and thus the quality of the obtained results. Convexifying the objective function facilitates the solution of the problem, however it may lead to a less realistic problem if this involves a distortion of the time similarity metric.

Let F and M be the fixed and the moving scalar value images, we define the following distances:

9.3.1.1 Sum of Squared Differences (SSD)

In registration this metric is widely used when the same structures are assumed to have the same intensity values, for instance both images should be T_1 or both should be T_2 as white matter appears white in the former, while it appears dark in the later. In addition, if images are from different scanners, intensities can slightly vary, hence it might be relevant to previously normalize images. The dissimilarity between two images with the sum of square distances of the intensity

values is defined as follows:

$$\mathrm{SSD}(F, M) = \sum_p (F(p) - M(p))^2 = \|F - M\|^2 \tag{9.4}$$

This simple metric is the most widely used in medical imaging. In the case of tensor images, that are used to represent the white matter structure, we can analogously define an SSD metric. A tensor being a 3×3 matrix, the SSD can be computed on the coefficients possibly after some transformation to take into account positive definiteness of these matrices Zhang et al. [2006], Yeo et al. [2009], Villalon et al. [2011].

9.3.1.2 Cross Correlation (CC)

Cross-Correlation is a statistic function that also measures the dependency between two measurements. The cross-correlation is zero when the two random variables are independent, however the converse is not true, as CC only measures linear dependency. The population correlation coefficient between two random variables X and Y with expected values μ_X, μ_y and standard deviations σ_x, σ_y is defined as:

$$\mathrm{CC}_{X,Y} = \frac{\mathrm{cov}(X, Y)}{\sigma_X \sigma_Y} = \frac{\mathbb{E}[(X - \mu_X)(Y - \mu_Y)]}{\sigma_X \sigma_Y}, \tag{9.5}$$

where $\mathbb{E}$ is the expected value operator, cov means covariance, and, corr the correlation coefficient. Given two sets of measurements X and Y, the sample correlation coefficient can be used to estimate the population correlation as:

$$\mathrm{CC}_{X,Y} = \frac{\sum_{i=1}^{n}(x_i - \bar{x})(y_i - \bar{y})}{(n-1)s_x s_y} = \frac{\sum_{i=1}^{n}(x_i - \bar{x})(y_i - \bar{y})}{\sqrt{\sum_{i=1}^{n}(x_i - \bar{x})^2 \sum_{i=1}^{n}(y_i - \bar{y})^2}}, \tag{9.6}$$

where $\bar{x}$ and $\bar{y}$ are the sample means of X and Y, and s_x, s_y are their standard deviation. In the setting of medical imaging, computing the sample mean only makes sense locally to capture the local structure intensity. So variance is computed locally on a region around each voxel. Local Cross-correlation, adapts naturally to situations where locally varying intensities occur and is suitable for some multi-modal problems Brown [1992], Avants et al. [2008], Kim and Fessler [2004]. The CC depends only on estimates of the local image average and variance which may be accurately/exactly measured with relatively few samples.

9.3.1.3 Mutual Information (MI)

Inspired by information theory, Mutual Information (MI) measures the mutual dependence between two random variables. MI can be used to estimate the optimal matching between images by inferring how much global information is shared in the image pair, which is estimated from their joint histogram Andronache et al. [2008], Biesdorf et al. [2009], Janssens et al. [2011]. The globality of this approach makes it very useful for robust rigid registration but may limit its

performance in deformable registration, in particular, in cases where non-stationary noise patterns or intensity inhomogeneity require a locally adaptive similarity. Using MI in deformation settings requires a large number of samples for reliable statistics. Therefore, as locality increases its statistical reliability decreases. Given events $e_1, ..., e_m$ occurring with probabilities $p_1, ..., p_m$, the Shannon entropy is defined as:

$$H = \sum_i p_i \log \frac{1}{p_i} = -\sum_i p_i \log p_i \tag{9.7}$$

The Shannon entropy can also be computed for an image based on the histogram of the gray values. A probability distribution of gray values can be estimated by counting the number of occurrences of intensity values, and normalizing by the total number of occurrences. Shannon entropy is a measure of dispersion of a probability distribution. The Shannon entropy for a joint distribution is:

$$H(F, M) = -\sum_{f \in F} \sum_{m \in M} p(f, m) \log p(f, m) \tag{9.8}$$

Mutual information is defined as $I(F, M) = H(M) - H(M|F) = H(F) + H(M) - H(F, M)$. where H(B) is the Shannon entropy of image B, computed on the probability distribution of the gray values, and H(A,B) is the joint entropy of both images. Registration corresponds to maximizing mutual information: the images have to be aligned in such a manner that the amount of information that they contain about each other is maximal.

Then Mutual information is defined as:

$$MI(F, M) = \sum_{f \in F} \sum_{m \in M} p(f, m) \log \left(\frac{p(f, m)}{p(f)\, p(m)} \right) \tag{9.9}$$

9.3.2 Geometric methods

Many methods for extracting landmarks or salients point in scalar value images have been proposed such as using the minimal eigenvalue of the tensor structure or using a Laplacian operator Shi and Tomasi [1994], Lindeberg [1998]. A different approach is to reduce the dimensionality of the problem to keep only relevant information. In Knops et al. [2004] a K-Means on the image was performed, to group voxels with same intensity values, and an histogram was made to be used with MI. A similar approach can be taken over neural fiber tracts, to reduce dimensionality on such a high dimension data. Using clustering algorithms such as K-Means mentioned in Chapter 8 we can simplify the white matter underlying structure, facilitating the registration task by reducing its time complexity but also removing noise introduced by spurious fibers. Otherwise, when a segmentation can be obtained consistently across subjects the registration problem is no longer fully unsupervised as landmark constraints should be matched. Correspondences can be assigned by relying solely on the closeness of the descriptors, or based on structural constraints.

In this thesis we will focus on geometric metrics for fiber tracts. So let us start by defining a representation to be used through the geometric metrics:

Let $\mathcal{G}$ be a set of continuous curves. Having a set of bundles from the fixed fibers C^F (and moving C^M), we define the sequence of points in $\mathcal{G}^{\mathcal{F}}$ as $\mathcal{G}^{\mathcal{F}} = (x_1^F, ..., x_N^F)$, $\mathcal{G}^{\mathcal{M}}$ as $\mathcal{G}^{\mathcal{M}} = (x_1^M, ..., x_L^M)$, N, L being the number of points.

9.3.2.1 Closest Point Distance (CPD)

As the name suggests the Closest Point Distance finds for each point of the fixed structure, the closest one in the moving subject. The metric can be applied to any set of points such as discretized curves for fiber tracts, or surfaces for the brain cortex, however in the sequel we will adapt the problem to curves as our focus is on the registration of fiber tracts. The closest point distance does not need explicit correspondences between points, however it is recommended to have a one-to-one curve correspondence, as it might lead to unwanted results otherwise, as shown in fig 9.5. Let us denote by π_i the point index in $\mathcal{G}^{M,k}$ closest to point i in $\mathcal{G}^{F,k}$, where k is a label assigned consistently to each of the fibers in the moving and fixed subject. We define the similarity measure between point set with the CPD:

$$\text{Sim}_G(\mathcal{G}^{F,k}, \mathcal{G}^{M,k}) = \frac{1}{N}\sum_{i=1}^{N} ||x_i^{F,k} - x_{\pi_i}^{M,k}||_2^2 \tag{9.10}$$

This metric can be a good approach for comparing single fiber bundles representatives. Without a fiber to fiber correspondence the method ends up being a brute force approach as it would need to compare for each point in the fiber set the distance to every other. Assume that we have a dataset of N=3000 fibers (on HARDI data tractography results in few million fibers), and M=20 points per fiber, the numbers of comparisons to be made are $(3000 * 20)^2$, formally $O(N^2 * M^2)$. Computing this metric on the whole dataset is rather expensive, to avoid this corresponding fibers across subjects can be defined, and then the time complexity will be reduce to $O(k * M^2)$,with k ,$0 \leq k \leq N$ the number of correspondences. In practice $k << N$ as corresponding fibers across subjects are hard to define.

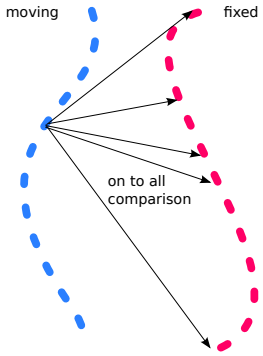

Figure 9.5: Example of how the closest point calculates the distances from each point of the moving curve, to all the points in the fixed one.

9.3.2.2 Currents

Currents can be used to define a metric on oriented curves. By representing geometry in the space of currents, we compare positions and tangents, or oriented vectors, leading to a pose and shape-sensitive measure which permits to define a distance between bundles containing different numbers of fibers Glaunès et al. [2008]. Currents could in theory be used to represent a set of geometric objects without explicit correspondences, but they require an orientation to be chosen for each fiber. A

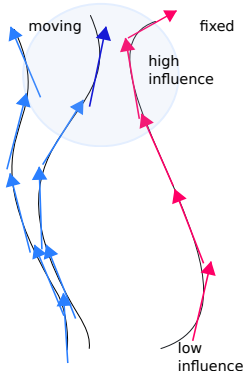

Figure 9.6: Example of currents representation of curves. The light blue circle intends to represent the kernel K, and shows that for the centered blue dirac vector, the bottom part of the fixed (pink) curve will have low influence. The neighbors influence is parametrized by the size of the kernel.

current can be seen as a sum of oriented segments. Therefore it is important to find a consistent orientation, otherwise the same fiber with the opposite orientation cannot be registered properly. Finding a consistent orientation of the whole set of fibers between two subjects without prior information, or a labeled segmentation of the brain is an open problem. An example of its difficulty is shown in fig 9.6. For this reason, we will define it for corresponding bundles, where bundles can contain more than one fiber.

We associate to the sequence of N discretized points in $\mathcal{G}$ a specific measure given by the vector valued Diracs: $\mu_{\mathcal{G}} = \sum_{i=1}^{N-1} \tau_{\mathcal{G},i}\delta_{c_{\mathcal{G},i}}$ where $c_{\mathcal{G},i} = (x_i + x_{i+1})/2$ (center point) and $\tau_{\mathcal{G},i} = x_{i+1} - x_i$ (tangent vector) if x_i and x_{i+1} belong to the same curve.

Following Glaunès et al. [2008], let W be a reproducible kernel Hilbert space (r.k.h.s) of vector fields with kernel K_β^W isotropic and Gaussian of size β. Then, the vector space of currents is a dense span of the set of all the vector valued Diracs currents $\tau\delta_c$ for any $\tau, c \in \mathbb{R}^3$. A Dirac current may be seen as an oriented segment entirely concentrated at point c. Given $\mathcal{G}^F = (x_1, ..., x_N)$ and $\mathcal{G}^M = (y_1, ..., y_L)$, the sequence of discretized points for a fixed and a moving geometric descriptor, with N, L the number of points in the bundle. A vector valued *Dirac Current* can be associated to each $\mathcal{G}^F := \mu^F$ and $\mathcal{G}^M := \mu^M$.

The scalar product between two sums of vector valued Diracs expresses conveniently in terms of the kernel K_β^W:

$$\langle \mu^F, \mu^M \rangle_{W^*} = \langle \sum_{i=1}^{N} \tau_i^F \delta_{c_i^F}, \sum_{j=1}^{L} \tau_j^M \delta_{c^M{}_j} \rangle = \sum_{i=1}^{N}\sum_{j=1}^{L} K_\beta^W(c_i^F, c_j^M)\langle \tau_i^F . \tau_j^M \rangle \tag{9.11}$$

Notice that $\mathcal{G}^F$ and $\mathcal{G}^M$ can contain more than one curve, and N, L are the number of points in each curve, which are not necessarily equal. Then the distance is defined as follows:

$$\begin{aligned} d^2(\mathcal{G}^F, \mathcal{G}^M) &= ||\mu^F - \mu^M||^2_{W^*} = \\ &\langle \mu^F, \mu^F \rangle_{W^*} + \langle \mu^M, \mu^M \rangle_{W^*} - 2\langle \mu^F, \mu^M \rangle_{W^*}, \end{aligned} \tag{9.12}$$

where β defines the kernel size. Points at distances much larger than β have a large distance disregarding the shape. Also, when distances are much smaller than β, they have little impact due to the smoothing effect of the kernel they are not taken into account. So the distance captures misalignment and shape dissimilarities until a difference level smaller than β is reached.

Fiber tracts orientation

As currents requires the tangents along the fibers to be defined, it is mostly adaptable in situations where a previous segmentation is given as prior or fiber bundles correspondences across subjects is introduced. In Fig. 9.7 we show how orientation is crucial for *Currents* model and that a random orientation might force a fiber to be registered to the wrong corresponding structure. In Fig. 9.7 (e) and (f) we show that an orientation may define a segmentation. Last, In (g) and (h) a segmentation is introduced to remove the ambiguity.

Another example is shown in Figure 9.8 where two close Currents take opposite orientation on a close region, and as a consequence their vectors cancel each other, impeding the moving fiber to correctly register as the attraction forces will be close to zero.

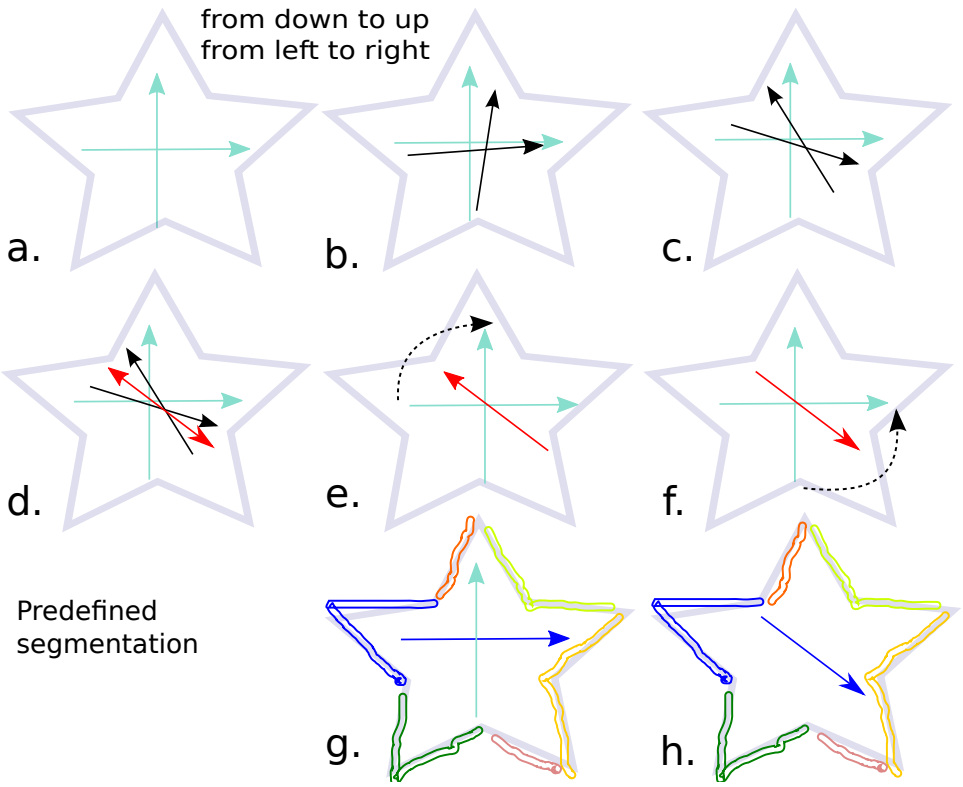

Figure 9.7: In (a) we define an orientation (from down to up, and from let to right) and two lines as example. In (b) and (c) we show how two new lines adapt to the predefined orientation. In (d) we show a new line (in red) inbetween the two possible orientations which are opposite to each other. In (e) we show that by choosing the down-to-up orientation in a registration scheme the line will rotate clockwise to align itself with the vertical on (same orientation), but by choosing the left-to-right orientation as in (f) in a registration scheme the line will rotate anti-clockwise to align to the horizontal one. Finally, if we take (g) as a ground truth segmentation, then the arrow in (h) with undefined direction in the previous examples will be force to go down to connect blue→yellow as in (g).

9.3.2.3 Weighted Measures

Weighted Measures are nothing but a simplified version of currents, where the tangent term is replaced by a scalar value. This loses robustness in the model, but makes it possible to relax a necessary hypothesis. Because of the complexity of orienting neural fibers, and as in a realistic scenario one is unlikely to have corresponding bundles, we now define a metric to compare the whole fiber dataset without requiring critical assumptions on the object. With the new imaging acquisition techniques resolution is improving and datasets are becoming larger, and

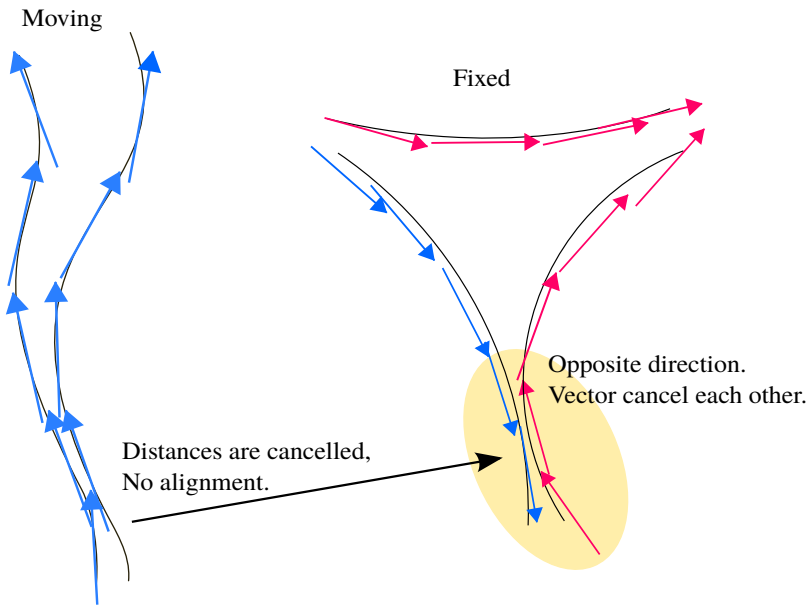

Figure 9.8: Example of a fiber alignment that forces two fibers to take opposite orientations on a close region. Vector around the yellow are will canceled each other, and therefor the Moving fiber will not be able to align itself: forces will be zero.

computationally more expensive to analyze. Clustering and segmentation techniques are used to simplify and compress such datasets, and therefore, this metric will be defined over clusters of fibers. C^F and C^M are the set of clusters in the fixed and moving subject respectively. $C_i^{F,k}$ will denote the i-th fiber of the k-th cluster of the fixed subject, and analogous for the moving subject $C_i^{M,k}$. $|C^F|$ and $|C^M|$ denotes the number of fixed and moving clusters, while $|C^{F,i}|, |C^{M,i}|$ stands for the number of points of the representative bundle of the i-th cluster. The sampling of points are defined as: $x_{i,j}, i \in [1..|C^F|]$, $j \in [1..|C^{F,i}|]$, where $x_{i,j}$ the j-th point of the representative from the i-th cluster in C^F.

We can associate to the sequence of discretized points in $\mathcal{G}$ a specific measure as a sum of weighted Dirac Measures: $\mu^F = \sum_{i=1}^{|C^F|} \sum_{j=1}^{|C_i^F|} w_{i,j}\delta_{x_i}$ where $w_{i,j} = \frac{|C_i^F|}{\sum_{i=0}^{|C^F|} |C_i^F|}$, which weights measures according to the number of fibers that the bundle of $C^{F,i}$ represents. From now on, to simplify notations, we refer to points from the geometry in $\mathcal{G}^F$ as x_i and to points from $\mathcal{G}^M$ as y_i, and we assume that w_i^x (resp. w_i^y) is the weight of the x_i (resp. y_i) given by the corresponding bundle size. Let $\mathcal{G}^F = (x_1, ..., x_N)$ and $\mathcal{G}^M = (y_1, ..., y_L)$ be the fixed and a moving geometric descriptors and N, L being the number of objects. We define the geometry in the fixed subject as $\mathcal{G}^F := \mu^F = \sum_{i=0}^{N} w_i^x \delta_{x_i}$ and for the moving subject as $\mathcal{G}^M := \mu^M = \sum_{j=0}^{L} w_j^y \delta_{y_j}$.

Let K_β be a Gaussian kernel of width β. Then the scalar product between two sums of Weighed Measures can be expressed conveniently with a pre-defined kernel K_β:

$$\langle \mu^F, \mu^M \rangle_\beta = \langle \sum_{i=1}^{N} w_i^x \delta_{x_i}, \sum_{j=1}^{L} w_j^y \delta_{y_j} \rangle_\beta = \sum_{i=1}^{N} \sum_{j=1}^{L} K_\beta(x_i, y_j) w_i^x . w_j^y \tag{9.13}$$

Then the distance between Weighted Measures is defined as follows:

$$d^2_\beta(\mathcal{G}^F, \mathcal{G}^M) = \langle \mu^F, \mu^F \rangle_\beta + \langle \mu^M, \mu^M \rangle_\beta - 2\langle \mu^F, \mu^M \rangle_\beta \tag{9.14}$$

The distance captures misalignment and shape dissimilarities at resolution β. Distances much larger than β do not influence the metric, while smaller ones are considered as noise and thanks to the smoothing effect of the kernel they are not taken into account.

9.4 Optimization Strategy

In this section we will see some of the most classical techniques to find the point x that minimizes the function $\mathcal{E}(.)$. All the previously presented functions are continuous and differentiable at least in the targeted neighborhood, property required for the following minimization techniques.

9.4.1 Gradient descent

$\mathcal{E}$ being defined and differentiable in a neighborhood of a point $\mathbf{a}$, the decreasing direction of $\mathcal{E}(\mathbf{x})$ from $\mathbf{a}$ is in the direction of the negative gradient of $\mathcal{E}$ at $\mathbf{a}$: $-\nabla\mathcal{E}(\mathbf{a})$. If $\mathbf{b} = \mathbf{a} - \varrho\nabla\mathcal{E}(\mathbf{a})$ for ϱ small enough, then $\mathcal{E}(\mathbf{a}) \geq \mathcal{E}(\mathbf{b})$. Therefore, starting from an initial guess $\mathbf{x}_0$ of a local minimum of $\mathcal{E}$, and considers the sequence $\mathbf{x}_0, \mathbf{x}_1, \mathbf{x}_2, \ldots$ such that:

$$\mathbf{x}_{n+1} = \mathbf{x}_n - \varrho_n \nabla\mathcal{E}(\mathbf{x}_n) \tag{9.15}$$

Where ϱ_n is the step size. Hopefully the sequence$(\mathbf{x}_n)$ converges to the desired local minimum.

This solution is easy to compute, however the need of a small enough unknown ϱ can lead to a slow convergence rate with small values of ϱ, or to unstable results with high values of ϱ.

$$\mathcal{E}(x) = \mathcal{E}(x_0) + \frac{1}{2}(\nabla_\mathcal{E}(x_0) + \nabla_\mathcal{E}(x))(x - x_0) + O(\|x - x_0\|^3) \tag{9.16}$$

In general computing $\nabla_\mathcal{E}(x)$ is not possible as x is the optimal unknown position. However, in image registration, one looks for the optimal transformation ϕ_{opt} such that $M \circ \phi_{\text{opt}} = F$, and so the same should hold for its derivative: $\nabla(M \circ \phi_{\text{opt}}) = \nabla\mathcal{E}$.

In other words, we are able to compute $\nabla_\phi(x)$ by using the fixed image, which would be the optimal result.

By defining $\nabla^{\text{ESM}}_\mathcal{E} = \frac{1}{2}(\nabla_\mathcal{E}(x_0) + \nabla_\mathcal{E}(x))$ we rewrite the Taylor expansion as follows:

$$\mathcal{E}(x) = \mathcal{E}(x_0) + \nabla^{\text{ESM}}_\mathcal{E}(x - x_0) + O(\|x - x_0\|)^3 \tag{9.17}$$

We can now use Newton-Raphson formula to compute x:

$$x_{n+1} = x_n + \nabla^{\text{ESM}^{-1}}_\mathcal{E}.\mathcal{E}(x_n) \tag{9.18}$$

9.5 Registration algorithm implementation

When analyzing population variability, affine transformation may only serve for intra-subject registration, and initialization of inter-subject registration. This is because an affine transformation will fail to capture local variability. With deformations we obtain a more detailed mapping, based on a richer model but at the expense of ill-posing the problem by increasing the degrees of freedom.

Having analyzed the most relevant components of registration, we can now select and combine them in order to implement a registration algorithm. A registration algorithm consists in a deformation model, an optimization strategy, and a metric.

The selection of these components to be defined explicitly depends on the aim of the study, the type of input images we have, the required computation speed, and the simplicity of the model. We will start with an example over a multi-modal affine registration that mostly aims to show how components can be combined. We will also present the LDDMM framework and the Demons settings, but our contribution will focus on the extension of the demons framework to include neural fibers to the registration. We chose Demons because of its flexibility and speed. Including geometric descriptors into a registration framework can be a challenge, so multi-modal extensions with image and geometric descriptors within the Demons framework will be emphasized. All non-rigid algorithm will focus on diffeomorphic deformations.

Algorithms settings:

Section	Algorithms	Deformation Model	Image (T_1)		Geometry	Minimization	
			SSD	CC		Grad.	ESM
9.5.2	Affine	Affine			WM	X	
9.5.3	LDDMM	Flows of Diffeo.	X			X	
9.5.4	ANTS (LDDMM)	Flows of Diffeo.		X		X	
9.5.5	Demons	Diffusion	X				X
9.5.6	Tensor Demons	Diffusion			Tensors	X	
9.5.7	Geom. Demons	Diffusion	X		CPD	X	X
		Diffusion	X		Currents	X	X
		Diffusion	X		WM	X	X

9.5.1 Common Notations

Ω is the image domain.
Fixed Image $F \in \Omega_F$, where Ω_F is the fixed image domain.
Moving Image $M \in \Omega_M$, where Ω_M is the moving image domain.
A transformation, generally affine of 12 parameters $\mathcal{T} \in \mathbb{R}^{4\times4}$
A non-rigid deformation ϕ

9.5.2 Weighted Measures Affine Multi-modal Registration

In Chapter 8 we have seen different methods to cluster neural fiber tracts into bundles. While this thesis focuses on non-rigid registration methods, affine registration is widely used for initialization, quick analysis, thus it will serve as an introduction to extending registration methods.

We show how to combine the SSD image metric and the Weighted Measures metric on fiber tracts to find an affine transformation that maps both from the fixed subject to a moving subject via gradient descent.

The goal is to find the affine transformation $\mathcal{T}$ that minimizes the distance of the images and the neural fibers between two different subjects, with $\mathcal{T} \in \mathcal{R}^{4\times4}$ as described in Section 9.1.1.

Let $\mathcal{G}^F$ and $\mathcal{G}^M$ be the fixed and a moving geometric descriptor and N and L the number of objects. We define the geometry in the fixed subject as $\mathcal{G}^F = \sum_{i=0}^{N} w_i^x \delta_{x_i}$ and in the moving subject as $\mathcal{G}^M = \sum_{j=0}^{L} w_j^y \delta_{y_j}$, where x_i, y_j are the points of the representative fibers across the clusters, while w_i^x andw_j^y are their corresponding associated weights.

$$\begin{aligned}\mathcal{E}(\mathcal{T}) &= \sum_{x\in M} (I^F(\mathcal{T}(x)) - I^M(x))^2 \\ &\quad + \sum_{\substack{i=0,L\\ j=0}}^{L,L} w_i^y w_j^y e^{-\frac{\|\mathcal{T}(y_i)-\mathcal{T}(y_j)\|^2}{2\sigma^2}} - 2\sum_{\substack{i=0,N\\ j=0}}^{N,L} w_i^x w_j^y e^{-\frac{\|x_i-\mathcal{T}(y_j)\|^2}{2\sigma^2}}\end{aligned}$$

Note that $\mathcal{T} : \Omega_M \to \Omega_F$ and as for the image term minimization, the iteration is on coordinates of Ω_M we need to apply $\mathcal{T}$ before evaluating I^F.

Hence

$$\begin{aligned}\nabla_{\mathcal{T}}\mathcal{E} &= \sum_{x\in M} x \otimes \nabla I^F(\mathcal{T}(x))(I^F(\mathcal{T}(x)) - I^M(x)) \\ &\quad + \left(-\frac{2}{\sigma^2}\right) \sum_{\substack{i=0,L\\ j=0}}^{L,L} w_i^y w_j^y e^{-\frac{\|\mathcal{T}(y_i)-\mathcal{T}(y_j)\|^2}{2\sigma^2}} y_i \otimes (\mathcal{T}(y_i) - \mathcal{T}(y_j)) \\ &\quad - \left(-\frac{2}{\sigma^2}\right) \sum_{\substack{i=0,N\\ j=0}}^{N,L} w_i^x w_j^y e^{-\frac{\|x_i-\mathcal{T}(y_j)\|^2}{2\sigma^2}} y_j \otimes (x_i - \mathcal{T}(y_j))\end{aligned}$$

Where $\otimes$ is the tensor product. Then we can use gradient descent to estimate $\mathcal{T}$.

9.5.3 Large Diffeomorphic Deformation Mapping Metric (LDDMM)

This framework overcomes the limitation of small deformations model and ensures that the transformations are diffeomorphic. The transformation ϕ of the domain is generated by the transformation $\phi = \phi_1$ of the flow of a time-dependent velocity vector field $v_t : \Omega \to \mathcal{R}^N, t \in [0,1]$ specified by the mapping $\phi_t : \Omega \to \Omega, t \in [0,1]$ in the space of transformations starting with $\phi_0 = Id.\ \forall x \in \Omega$ and terminating at the end-point $t = 1$ of the flow to the particular transformation $\phi = \phi_1 = \phi_0 + \int_0^1 v_t(\phi_t)dt$ matching the given images.

The map ϕ parametrizes over time a family of diffeomorphisms on the image domain Ω, $\phi(x,t) : \Omega \times t \to \Omega$. which can be generated by integrating over time the velocity field $v : \Omega \times t \to \mathbb{R}^d$ trough the ordinary differential equation (o.d.e.).

$$\frac{\partial\phi(x,t)}{\partial t} = v(\phi(x,t),t) \qquad \phi(x,0) = x \tag{9.19}$$

$$\hat{v} = \min_{v} \int_0^1 \|Lv\|^2 dt + \lambda \int_\Omega \text{Sim}(F \circ \phi(x,1), M) d\Omega \tag{9.20}$$

Where Sim is a similarity metric used on the images, $\lambda > 0$ accounts for the precision of the matching, and L is a differential operator chosen to be a Cauchy-Navier type. A discussion on the selection of L can be found in Beg et al. [2005]. This equations is proven to satisfy the following Euler-Lagrange equation:

$$2\hat{v}_t - K(\frac{2}{\sigma^2}|\partial\phi_{t,1}^{\hat{v}}|\nabla(F \circ \phi_{t,0})(F \circ \phi_{t,0} - M \circ \phi_{t,1})) = 0 \tag{9.21}$$

Let K be a green function for the differential operator L, meaning that for any smooth vector field f $K(L^T L)f = f$. After discretization of the time index, the energy becomes Beg et al. [2005]:

$$\mathcal{E}(v^k) = \sum_{j=0}^{N-1} \|v_{t_j}^k\|^2 \delta t + \frac{1}{N} \sum_{x \in \Omega} |F \circ \phi_{t,0}(x) - M \circ \phi_{t,1}(x)|^2 \tag{9.22}$$

Where N is the number of voxels, δt the size of a timestep, and $t_j \in [0,1]$.

9.5.4 Symmetric LDDMM with Cross-Correlation: ANTs

We now explore an extension of the LDDMM framework that is Symmetric and also uses Cross-Correlation metric, that as discussed in Section 9.3.1.2 can have advantages in multi-modal problems (i.e. registering T_1 to a T_2 image) Avants et al. [2008]. With a symmetric diffeomorphism we guarantee that the result is not biased by the selected target image. This is a desirable feature in neuroimaging as when comparing multiple subjects there is no solution today on which one is the best target.

The prior knowledge that this diffeomorphic map should be applied reciprocally to both images can be captured by including the constraint $\text{Sim}(F, \phi_1(x, 0.5)) = \text{Sim}(M, \phi_2(x, 0.5))$ directly to the formulation of the problem, and $\phi_1(x,1) = \phi_2^{-1}(\phi_1(x,0.5),0.5)$

A symmetric alternative to the equation can be constructed by decomposing ϕ into ϕ_1, ϕ_2, where for $t \in [0, 0.5]$, $v(x,t) = v_1(x,t)$ and for $t \in [0.5,1] v(x,t) = v_2(x, 1-t)$ and by using this new definition we obtain:

$$\begin{aligned} v_1^*, v_2^* &= \min_{v_1, v_2} \int_0^{0.5} \|Lv_1\|^2 + \|Lv_2\|^2 dt \\ &+ \lambda \int_\Omega \text{Sim}(F \circ \phi_1(x, 0.5), M \circ \phi_2(x, 0.5)) d\Omega \end{aligned}$$

Where the regularization term is equivalent to eq. 9.20, but the optimization over the split vector fields tries to find an intermediate point of deformation/matching for both images. Thus, gradient based iterative convergence deforms F and M along the geodesic diffeomorphism ϕ to a fixed point midway F and M.

A Greedy SyN (moniker Symmetric Normalization **?**) is defined, which calculates the gradient only at the midpoint of the full diffeomorphism, i.e. at $t = 0.5$. ϕ_1 and ϕ_2 are updated from the previous iterations using gradient descent with step size δ as:

$$\phi_j(x, 0.5) \leftarrow \phi_j(x, 0.5) + (\delta K * \nabla \text{Sim}(x, 0.5)) \circ \phi_j(x, 0.5), \forall j \in \{1, 2\} \tag{9.23}$$

Cross correlation adapts naturally to situations where locally varying intensities occur. Thus, we look for an spatio-temporal diffeomorphic mapping ϕ that minimizes the local cross correlation between an image pair:

$F' = F(\phi_1(x, 0.5)) - \mu_{F(\phi_1(x,0.5))}$ and $M' = M(\phi_1(x, 0.5)) - \mu_{M(\phi_1(x,0.5))}$

$$CC(F', M', x) = \frac{\langle F'(x), M'(x)\rangle}{\sqrt{\langle F'(x), F'(x)\rangle \langle M'(x), M'(x)\rangle}} \tag{9.24}$$

$$\mathcal{E}_{CC}(F', M') = \inf_{\phi_1} \inf_{\phi_2} \int_{i=0}^{0.5} \{\|v_1(x, t)\|_L^2 + \|v_2(x, t)\|_L^2\} dt + \int_\Omega CC(F', M', x) d\Omega \tag{9.25}$$

Which by using Beg's derivation Beg et al. [2005] yields two Euler-Lagrange equations:

$$\nabla_{\phi_1(x,0.5)} E_{CC}(x) = 2Lv_1(x, 0.5) + 2CC(F', M', x) \left(M'(x) - \frac{\langle F'(x), M'(x)\rangle}{\langle F'(x), F'(x)\rangle} F'(x) \right) \|\partial\phi_1\| \nabla_{F'(x)} \tag{9.26}$$

$$\nabla_{\phi_2(x,0.5)} E_{CC}(x) = 2Lv_2(x, 0.5) + 2CC(F', M', x) \left(F'(x) - \frac{\langle F'(x), M'(x)\rangle}{\langle M'(x), M'(x)\rangle} M'(x) \right) \|\partial\phi_1\| \nabla_{F'(x)} \tag{9.27}$$

That velocities v_1, v_2 exist in the space of smooth vector fields given by the linear operator L as well as the determinant of each transformation Jacobian $|\partial\phi|$. The update method for the diffeomorphism comes from discretizing the o.d.e.:

$$\phi(x, t + \delta t) = \phi(x, t) + \ \delta t v(\phi(x, t), t) \tag{9.28}$$

The existence of a solution is guaranteed by the integrability condition established for diffeomorphic image registration Dupuis and Grenander [1998], while uniqueness comes from the uniqueness theorem of o.d.e.s Braun [1980]

Algorithm

1. Initialize $\phi_1 = Id = \phi_1^{-1} = \phi_2 = \phi_2^{-1}$
2. Compute CC
3. v= v*K : Smooth v by convolving with a Green Kernel.
4. update ϕ and approximate ϕ^{-1} by using eq. 9.28
5. Generate solution $t = 1 : \phi_1 = \phi_2^{-1}(\phi_1(x, 0.5), 0.5)$ and $\phi_2 = \phi_1^{-1} = \phi_1^{-1}(\phi_2(x, 0.5), 0.5)$

9.5.5 Iconic Diffeomorphic Demons Registration

The Demons algorithms is based on optical flow methods, and it was introduced by Thirion in Thirion [1998] making an analogy to Maxwell's demons. Maxwell imagines two containers filled with gas at the same temperature. A demons watches out for molecules and opens a door to let pass the faster one to one side, and the slower ones to the other side. As a consequence he manages to have a change of temperature in both containers 9.10.

The algorithm proposed by Thirion imagines demons at the contour of an object, to inform whether it is outside or inside of the boundaries of the target. The moving object diffuses through the contours of the fixed object by the action of the demons. This is illustrated in Figure 9.9

In image matching the basic idea is that, given a moving image M and a fixed image F, the moving image will diffuse through the contours of the image F, assuming one demon per voxel. In Vercauteren et al. [2009] a regularization term was added to the algorithm in order to make it suitable for medical image registration. The goal is to find a deformable displacement field s to align corresponding structures from the moving image to the fixed image as accurately as possible. Ideally the displacement field s minimizes a distance between the fixed and the moving image, while holding some properties such as being diffeomorphic.

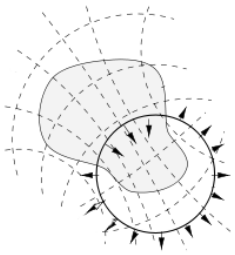

Figure 9.9: Demons at the contour of the fixed image. The demons know when they are inside or outside the target shape, and help the fixed image diffuse through the contours of the target image.

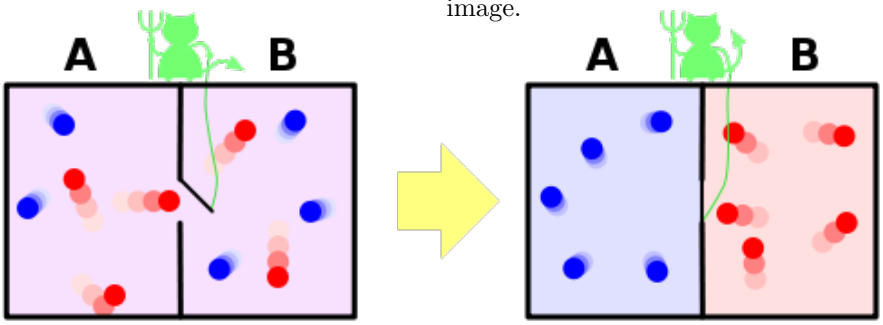

Figure 9.10: Maxwell's demons: A demon watching the door let pass the faster molecules to one side, and the slower ones to the other side. As a result he changes the temperature in both containers, and faster molecules are together, separated from slower ones.

Vercauteren et al. Vercauteren et al. [2009] introduced a correspondence field c to decouple the minimization of the functional energy:

$$\mathcal{E}(c,s) = \frac{1}{\sigma_i^2}\text{Sim}(F, M\circ c) + \frac{1}{\sigma_x^2}\text{dist}(\phi,c)^2 + \frac{1}{\sigma_T^2}\text{Reg}(\phi) \tag{9.29}$$

where Sim is a similarity measure between images defined by the sum of square differences (SSD) and $\text{Reg}(\phi)$ a regularization term chosen to be the harmonic energy $\|\nabla s\|^2$. The amount of regularization is controlled with σ_T while σ_i accounts for the image noise.

The term $\text{dist}(\phi,c)^2$ imposes the displacement field ϕ to be close to the correspondence field c. σ_x weights the spatial uncertainty on the deformation. The c variable accounts for uncertainty of the displacement field. In other words, c is an exact realization of point-to-point correspondences between images while s allows for some errors. In practice, c differs from ϕ by a small displacement field u. The energy minimization is performed by alternating minimization w.r.t. c and s:

1. The first step consists in optimizing eq. 9.29 w.r.t. c, s being fixed:

$$\min_c = \frac{1}{\sigma_i^2}\text{Sim}(F, M\circ c) + \frac{1}{\sigma_x^2}\text{dist}(\phi,c)^2$$

2. The second step consist in minimizing eq. 9.29 w.r.t. ϕ, c being fixed:

$$\min_\phi = \frac{1}{\sigma_x^2}\text{dist}(\phi,c)^2 + \frac{1}{\sigma_T^2}\text{Reg}(\phi)$$

In Vercauteren et al. [2008], small deformations are parametrized by a dense displacement field u: $c \leftarrow \phi\circ\exp(u)$, exp() being the exponential map in the Lie group sense, which ensures that the result is diffeomorphic. In the log-domain demons, ϕ is encoded with the exponential map as $\phi = \exp(v)$ and the inverse of ϕ can be easily computed as $\phi^{-1} = exp(-v)$; then $dist(\phi,c) = \|log(\phi^{-1}\circ c)\|$ and $\text{Reg}(\phi) = \|\nabla log(\phi)\|^2$ where $\log = \exp^{-1}$, so that $\phi\circ\exp(u) = \exp(v)\circ\exp(u)$.

Estimation of the update field

To introduce an optimization strategy into Demons, we first develop the Taylor expansion of $M\circ\phi\circ\exp(u) = f(\phi\circ\exp(u))$

$$\mathcal{E}(\phi\circ\exp(u)) = \mathcal{E}(\phi) + \nabla_\phi^{\mathcal{E}} u + \frac{1}{2}u^T\mathcal{H}_\phi^{\mathcal{E}} u + O(\|u\|^3) \tag{9.30}$$

Where $\nabla_\phi^{\mathcal{E}} = \nabla_{\mathcal{E}}(\phi\circ\exp(u))|_{u=0}$ This approximation is used in Mahony and Manton [2002] to adapt the classical Newton-Rapshon method by using an intrinsic update step:

$$\phi \leftarrow \phi\circ\exp(u) \tag{9.31}$$

where u solves:

$$\mathcal{H}_\phi^{\mathcal{E}} u = -\nabla_\phi^{\mathcal{E}^T}\mathcal{E}(\phi) \tag{9.32}$$

The Hessian matrix is most often difficult and numerically instable to compute, and convergence problems can arise when it is not positive-definite. To address this issue, most of the non-linear least squares optimization such as Levenberg-Marquardt are related to the Gauss-Newton

method Madsen et al. [2004]. Let $\psi(.) = \frac{1}{2}\|\mathcal{E}(.)\|^2$. The Gauss-Newton method is based on a linear approximation of $\mathcal{E}$ in a neighborhood, $\mathcal{E}(\phi \circ \exp(u)) = \mathcal{E}(\phi) + \nabla_\phi^{\mathcal{E}} u + O(\|u\|^2)$. Then a quadratic approximation to derive the Gauss-Newton method on a Lie group will be:

$$\psi(\phi \circ \exp(u)) \approx \frac{1}{2}\|\mathcal{E}(\phi) + \nabla_\phi^{\mathcal{E}^T} u\|^2 \tag{9.33}$$

We know that $\nabla_\phi^{\mathcal{E}}$ has full rank, hence canceling ψ yields:

$$(\nabla_\phi^{\mathcal{E}^T} \nabla_\phi^{\mathcal{E}})u = -\nabla_\phi^{\mathcal{E}^T} \mathcal{E}(\phi) \tag{9.34}$$

By introducing ESM we obtain a second order convergence rate without the need of computing the Hessian. So we can define a first order Taylor expansion of $\nabla_\phi^{\mathcal{E}}(u)$:

$$\nabla_\phi^{\mathcal{E}}(u) = \nabla_\phi^{\mathcal{E}}(x_0) + (x_0 + u)^T \mathcal{H}_\phi^{\mathcal{E}} + O(\|u\|^2)$$
$$(x_0 + u)^T \mathcal{H}_\phi^{\mathcal{E}} = \nabla_\phi^{\mathcal{E}}(x_0) - \nabla_\phi^{\mathcal{E}}(u) + O(\|u\|^2)$$

We can use that equality to remove the Hessian from the second-order Taylor expansion defined at 9.30:

$$\begin{aligned} \mathcal{E}(\phi \circ \exp(u)) &= \mathcal{E}(\phi) + \nabla_\phi^{\mathcal{E}} u + \frac{1}{2}(\nabla_\phi^{\mathcal{E}}(x_0) - \nabla_\phi^{\mathcal{E}}(u))u + O(\|u\|^3) \\ &= f(\phi) + \frac{1}{2}(\nabla_\phi^{\mathcal{E}}(x_0) + \nabla_\phi^{\mathcal{E}}(u))u + O(\|u\|^3) \end{aligned}$$

Thus, in Vercauteren et al. [2008] a new Jacobian is defined $\nabla_\phi^{\mathcal{E}(\text{ESM})}$ which can be incorporated in eq. 9.34 for a Gauss Newton step:

$$\nabla_\phi^{\mathcal{E}(\text{ESM})} = \frac{1}{2}(\nabla_\phi^{\mathcal{E}}(x_0) + \nabla_\phi^{\mathcal{E}}(u)) \tag{9.35}$$

Both, eq. 9.34 and eq. 9.32 can be efficiently solved using a Cholesky or QR decomposition.

Thus let us define ∇_p with the ESM gradient as: $\nabla_p = \nabla_\phi^{\mathcal{E}(\text{ESM})} = \frac{1}{2}(\nabla_\phi^p(F) + \nabla_\phi^p(M \circ \phi))$

So, we can rewrite the functional by using Taylor expansions and approximations:

$$F(p) - M \circ \phi \circ \exp(u)(p) \approx F(p) - M \circ \phi(p) + \nabla_p.u(p)$$

Also $dist(c, \phi) = dist(\phi, \phi \circ \exp(u)) = \|Id - exp(u)\| \approx \|u\|$.

Thus

$$\begin{aligned} E_\phi^{\text{corr}}(u) &= \|F(p) - M \circ \phi \circ \exp(u)(p)\|^2 + \frac{1}{\sigma_x^2} dist(\phi, \phi \circ \exp(u))^2 \\ &\approx \frac{1}{2|\Omega_p|} \sum_{p \in \Omega} \| \begin{bmatrix} F(p) - M \circ \phi(p) \\ 0 \end{bmatrix} + \begin{bmatrix} \nabla_p \\ \frac{1}{\sigma_x^2} I \end{bmatrix} .u(p)\|^2 \end{aligned} \tag{9.36}$$

Which applying Gauss-Newton and Sherman-Morrison formula for the matrix inversion the equations leads to:

$$u_I(p) = -\frac{F(p) - M \circ \phi(p)}{\|\nabla_p\|^2 + \frac{1}{\sigma_x^2}} \nabla_p^T \tag{9.37}$$

The algorithm consists in the following steps:

1. Choose a starting spatial transformation $\phi = Id$ for diffeomorphic demons or for Log-domain diffeomorphic demons.
2. Given ϕ, find the optimal update field u minimizing Eq. 9.37.
3. Let $v \leftarrow \phi \circ \exp(u)$ for diffeomorphic demons or $v \leftarrow \log(\exp(v) \circ \exp(u))$ for Log-domain diffeomorphic demons.
4. let $v \leftarrow K \star v$ where K is a Gaussian convolution kernel
5. Let $\phi \leftarrow \phi \circ \exp(v)$ for diffeomorphic demons or $\phi = \exp(v)$ and $\phi^{-1} = \exp(-v)$ for Log-domain diffeomorphic demons.
6. Go to 2. until convergence

Where ϕ is the diffeomorphism and c are the correspondences obtained from the image. This update has to be small, which implies that small deformations are applied at each iteration, and then it is composed with the previous transformation.

The log-domain demons efficiently compute the deformation on the log-domain space, and the inverse of ϕ parametrized in the log-domain $\phi = exp(v)$ can be easily computed as $\phi^{-1} = exp(-v)$. Having the exponential map: $\phi = \exp(v)$, then $\phi \circ \exp(u) = \exp(v) \circ \exp(u)$ and using the Baker-Campbell-Hausdorff(BCH) formula yields $\log(\exp(v) \circ \exp(u)) \approx v + u + 1/2[v, u] + 1/12[v, [v, u]] + ...$ where $[v, u]$ is the Lie bracket: $[v, u] = Jac(v)(p).u(p) - Jac(u)(p).v(p)$.

9.5.6 Tensor Diffeomorphic Demons: DtRefind

Deforming a tensor image by a transformation ϕ requires a tensor interpolation and a posterior tensor reorientation Yeo et al. [2009]. Tensor reorientation is of high importance as locally consistent orientation will define the white matter structures. Consistent orientations is mandatory for any type of diffusion image analysis, including tractography.

According to the FS tensor reorientations strategy Yeo et al. [2009] for non linear deformation, one first computes the rotations component of the deformation at voxel:

$$R(x) = (J_\phi(x) J_\phi(x)^T)^{-\frac{1}{2}} J_\phi(x) \tag{9.38}$$

$J(x)$ being the jacobian of the transformation ϕ. $R(.)$ is a polar decomposition of the jacobian, and thus a function of the displacement field u in the neighborhood of x. The interpolated tensor $T(.)$ is reoriented as follows:

$$T'(x) = R^T(x) T(x) R(x) \tag{9.39}$$

Therefore the energy can be rewritten as:

$$\mathcal{E}(c, \phi) \quad = \quad \frac{1}{\sigma_i^2} \|F - R^T(M \circ \phi \circ \exp(u))R\|^2 + \frac{1}{\sigma_T} \mathrm{Reg}(\phi) \tag{9.40}$$

A Least-Squares Optimization can be used to solved the Gauss-Nexton method:

$$\mathcal{E}(c, \phi) = \| \begin{bmatrix} \mathrm{Sim}(F, R^T(M \circ \phi \circ \exp(u))R) \\ 0 \end{bmatrix} + \begin{bmatrix} \frac{\partial_\phi}{\partial_x} \\ \frac{1}{\sigma_T} I \end{bmatrix} u \|^2 \tag{9.41}$$

To account for the effect of the displacement field of a neighbor voxel y for the reorientation of a voxel x, the $\frac{\partial_\phi}{\partial_x}$ term is defined as:

$$\frac{\partial_\phi}{\partial_{x,x}} = -\sum_x \nabla(R^T(x)(M \circ \phi)R(x))$$

$$\frac{\partial_\phi}{\partial_{x,y}} = -\sum_x (\frac{\partial_{R^T(x)}}{\partial_y}(M \circ \phi)R(x) + R^T(x)(M \circ \phi)\frac{\partial_{R(x)}}{\partial_y})$$

9.5.7 Iconic and Geometric Difffeomorphic Demons: T_1+ Fiber Tracts

Schematically, iconic registration is mainly driven by the image contours such as boundaries between white and gray matter. Nevertheless, brain white matter appears uniformly white in T_1 images, while being composed of neural fibers connecting cortical areas together. This approach suffers from the aperture problem, as without prior knowledge no distinction can be made between two points from different structures and same intensity. For this reason, surface-based registration discards white matter information, which is uniformly white in T1.

Analogously, diffusion images might not give relevant information in regions where FA is low. FA registration is widely used Avants et al. [2011], Mohammadi et al. [2012], however it discards the directional information of water molecules in contrast to tensor-image model for registration Yeo et al. [2009]. Nevertheless, a fiber representation is richer as it contains priors included in the tractography procedure, and is sparse, as it is only defined to be on the white matter and on reliable fiber tracts.

Auzias in Auzias et al. [2011] shows a misregistration example in an iconic setting, leading to the central sulcus being aligned with the post-central.

Registration should align images as well as cortical and internal structures such as sulcal lines and neural fibers, as their misalignment may have a negative impact on group studies on connection and activation regions. In this section we describe an extension of the demons framework to introduce neural fiber information to the iconic registration.

To include geometric descriptors we extended the demons formulation. The definition of c now carries information coming from both image and geometry. Let $\mathcal{G}^F$ be the fixed geometric descriptors and $\mathcal{G}^M$ the moving one, we aim at minimizing the following energy:

$$\begin{aligned}\mathcal{E}(c,\phi) \quad = \quad & \frac{1}{\sigma_i^2}\left[\mathrm{Sim}_I(F, M \circ c) + \mathrm{Sim}_G(c \star \mathcal{G}^F, \mathcal{G}^M)\right] + \\ & \frac{1}{\sigma_x^2}\mathrm{dist}(\phi, c)^2 + \frac{1}{\sigma_T}\mathrm{Reg}(\phi),\end{aligned} \tag{9.42}$$

where Sim_I is the image similarity criterion, Sim_G the geometric similarity criterion, and $c \star \mathcal{G}^F$ denotes the action of c on the geometry. Then c is parametrized by an update field of image and geometry which is described at the end of this section. Note that ϕ goes from F to M, thus the inverse of ϕ gives the geometric deformation.

Minimization of u_G, the update field for the geometry:

$$u_G^\star = \mathrm{argmin}_{u_G} E_G(\phi, u_G) = \frac{1}{\sigma_i^2}\mathrm{Sim}_G(\phi \circ \exp(u_G) \star \mathcal{G}^F, \mathcal{G}^M) + \frac{1}{\sigma_x^2}\int_{\Omega_G} \|u_G\|^2, \tag{9.43}$$

Where ϕ is the resampling of the deformation field and goes from F to M. Thus, the inverse of ϕ gives the geometric deformation.

9.5.7.1 Metrics

Before moving forward with the algorithm it is necessary to define de similarity metric to be used on the geometry. In the next section, we describe the Closest Point Distance (CPD), Currents and Measures, and the gradients to be used for the chosen optimization strategy.

Let us define the action of the correspondence field c on a point set as: $c \star \mathcal{G} = \{\phi \circ \exp(u_G)(x_i)\}_{i\in[1,N]} \approx \{\phi(x_i) + u_G(x_i)\}_{i\in[1,N]}$.

Closest point distance on Geometry This metric is rather simple but under certain conditions, such as having a fiber-to-fiber correspondence across subjects, it can lead to good results.

Let us consider our geometric descriptors as point sets: $\mathcal{G} = \{x_i\}_{i\in[1,N]}$, N being the number of points. Lets denote by π_i the point index in $\mathcal{G}^M$ closest to point i in $\mathcal{G}^F$. We recall that the similarity of CPD is defined as:

$$\mathrm{Sim}_G(\mathcal{G}^F, \mathcal{G}^M) = \frac{1}{N}\sum_{i=1}^{N} ||x_i^F - x_{\pi_i}^M||_2^2 \tag{9.44}$$

$$\nabla_{CPD}^{G,i} = -2(x_{\pi_i}^M - \phi(x_i^F)) \tag{9.45}$$

Geometry in the Space of Currents

The closest point distance does not need explicit correspondences between points and it can be a good approach for comparing single fiber bundles representatives as in Siless et al.. In contrast, by representing geometry in the space of currents, we have a pose and shape-sensitive measure which permits to define a distance between bundles containing different number of tracts. The analysis of the metric will be performed over a corresponding pair of bundles $\mathcal{G}^{F,k}$ and $\mathcal{G}^{M,k}$

We recall that the current $\mathcal{C}$ over a geometry $\mathcal{G}^{F,k}$, and $\mathcal{G}^{M,k}$ are defined as:

$$\begin{aligned} \mathcal{C}(\mathcal{G}^{F,k}) &= \sum_{i=0}^{N} e^{\,c_i^{F,k}} \tau_i^{F,k} \\ \mathcal{C}(\mathcal{G}^{M,k}) &= \sum_{i=0}^{L} e^{\,c_i^{M,k}} \tau_i^{M,k} \end{aligned}$$

where $c_i^{F,k}$ is the center between two points in the geometry of the fixed subject $\mathcal{G}^{F,k}$, $c_i^{F,k} = \frac{x_i^{F,k}+x_{i+1}^{F,k}}{2}$ and $\tau_i^{F,k}$ the tangent $\tau_i^{F,k} = x_{i+1}^{F,k} - x_i^{F,k}$ and analogously we define for $\mathcal{G}^{M,k}$, $c_i^{M,k} = \frac{x_i^{M,k}+x_{i+1}^{M,k}}{2}$ and $\tau_i^{M,k} = x_{i+1}^{M,k} - x_i^{M,k}$.

For simplicity we define $\chi_{i,j}^{A,B} = e^{\| \, c_i^A - c_j^B \|^2} \langle \tau_i^A, \tau_j^B \rangle$, where the label k is omitted for simplicity

as equal k are only taken into account. And the distance between them

$$\begin{aligned} \|\mathcal{G}^F - \mathcal{G}^M\|_{\mathcal{C}}^{W*} &= \sum_{\substack{i=0,\\ j=0}}^{N,N} \chi_{i,j}^{F,F} \\ + \sum_{\substack{i=0,\\ j=0}}^{L,L} \chi_{i,j}^{M,M} &- 2\sum_{\substack{i=0,\\ j=0}}^{N,L} \chi_{i,j}^{F,M} \end{aligned}$$

Derivation:

$$\begin{aligned} \frac{\partial \|F - M\|_{\mathcal{C}}^{W*}}{\partial x_j^M} &= \frac{\partial \sum_{\substack{i=0,\\ j=0}}^{L,L} \chi_{i,j}^{M,M}}{\partial x_j^M} \\ &- \frac{2\partial \sum_{\substack{i=0,\\ j=0}}^{N,L} \chi_{i,j}^{F,M}}{\partial x_j^M} \end{aligned}$$

$$\begin{aligned} \frac{\partial \|F - M\|_{\mathcal{C}}^{W*}}{\partial x_j^M} &= -2\sum_{\substack{i=0,\\ j=0}}^{L,L} \chi_{i,j}^{M,M}(\, c_i^M - c_j^M) \\ +2\sum_{\substack{i=0,\\ j=0}}^{L,L} e^{\| \, c_i^M - c_j^M \|^2}(\tau_i^M) &+ 2\sum_{\substack{i=0,\\ j=0}}^{N,L} \chi_{i,j}^{F,M}(c_i^F - c_j^M) \\ &+ 2\sum_{\substack{i=0,\\ j=0}}^{N,L} e^{\|c_i^F - c_j^M\|^2}(\tau_i^F) \end{aligned}$$

Geometry in the space of Weighted Measures

Currents could in theory be used to represent a set of geometric objects without explicit correspondences, but they require an orientation to be chosen for each fiber. It is extremely hard to find a consistent orientation on a large number of one-dimensional objects in 3D without a prior segmentation and labeling in each subject. As subject variability is high and –in the absence of complete fiber atlas– correspondence mistakes can lead to poor solutions, we propose to represent the geometry using Weighted Measures.

Given a set of bundles from the fixed fibers C^F (and moving C^M), we define the set of points in $\mathcal{G}^F$ as $x_{i,j}, i \in [1, ..., |C^F|]$, $j \in [1, ..., |C_i^F|]$, where $x_{i,j}$ the j-th point of the representative from the i-th bundle in C^F. Let K_β be a Gaussian kernel of size β.

Then the weighted measures for the fixed and the moving geometry is defined as in Section 9.3.2.3:

$$\begin{aligned} \text{Fixed Geometry} &: \mathcal{G}^F = \sum_{i=0}^{N} w_i^x \delta_{x_i} \\ \text{Moving Geometry} &: \mathcal{G}^M = \sum_{j=0}^{M} w_j^y \delta_{y_j} \end{aligned}$$

where w_i^x (resp. w_i^y) is the weight of the x_i (resp. y_i) given by the corresponding bundle size. With K_β Gaussian kernel of width β. We recall the scalar product between two sums of Weighed Measures from Section 9.3.2.3:

$$\langle \mathcal{G}^F, \mathcal{G}^M \rangle_\beta = \langle \sum_{i=1}^{N} w_i^x \delta_{x_i}, \sum_{j=1}^{M} w_j^y \delta_{y_j} \rangle_\beta = \sum_{i=1}^{N} \sum_{j=1}^{M} K_\beta(x_i, y_j) w_i^x w_j^y \tag{9.46}$$

Thus, the distance between Weighted Measures is defined as follows:

$$d_\beta^2(\mathcal{G}^F, \mathcal{G}^M) = \langle \mu^F, \mu^F \rangle_\beta + \langle \mu^M, \mu^M \rangle_\beta - 2\langle \mu^F, \mu^M \rangle_\beta \tag{9.47}$$

Minimizing $\nabla E_G(\phi, u_G) = 0$ w.r.t. u_G via gradient descent yields to the following update field equation:

$$\begin{aligned} \nabla_{WM}^{G,i} &= -\frac{2}{\beta^2} \sum_{l=0}^{N} w_l^x w_i^x K_\beta(\phi(x_i), \phi(x_l))(\phi(x_i) - \phi(x_l)) \\ &\quad + \frac{2}{\beta^2} \sum_{j=0}^{M} w_i^x w_j^y K_\beta(\phi(x_i), y_j)(\phi(x_i) - y_j) \end{aligned} \tag{9.48}$$

9.5.7.2 Defining Ω_G for Bundles

Since we deal with a discrete set of points, we choose to parametrize the dense update field u_G by a finite set of vectors $u_{G,i}$ using radial basis function extrapolation: $u_G(x) = \sum_{i=1}^{N} \psi(\|x - x_i\|)\lambda_i$, with $\psi(x) = e^{-\frac{x^2}{\gamma^2}}$, where $\gamma > 0$ is the interpolation scale.

λ_i are the interpolation coefficients that are calculated such that $u_G(x_i) = u_{G,i} \forall i$.

Let us define the matrix A such that:

$$[A]_{i,j} = \psi(\|x_i - x_j\|)$$

where $[A]_{i,j}$ denotes the (i,j) entry of A, $\Lambda = [\lambda_1, ..., \lambda_N]$ the vector of λs, $H(x)$ the vector such that $[H(x)]_i = \psi(\|x - x_i\|)$ and $U = [u_{G,1}, ..., u_{G,N}]$.

We can write: $u_G(x) = H(x)A^{-1}U$.

There are two different approaches to combine the image and fiber domain:

1. Non-overlapping domains: Since we want fibers to influence the deformation near the definition domain, we define the domain as the union of $\gamma-$radius balls B centered at each coordinate x_i. We control the influence by varying γ and thus, dilating the domain. We define a binary map $\Omega_G^\gamma = \bigcup_{i=1}^{N} B(x_i, \gamma)$. The domain of the image correspondence field is the complementary of Ω_G^γ: $\Omega_I^\gamma = \Omega \backslash \Omega_G^\gamma$. Extrapolation is used to infer the values inside the balls.

2. Overlapping domains: Extrapolation is used to infer the whole image domain of Ω_G^γ, and then image and fiber vector fields are summed up, as information should be complementary, and better lead the registration. Still γ parametrizes the spread of the fiber vector field influence.

Optimizing Eq. 9.40 w.r.t. to u_G leads to minimizing the following energy:

$$\mathcal{E}_G(\phi, u_G) = \frac{1}{\sigma_i^2}\text{Sim}_G(\phi \circ \exp(u_G) \star \mathcal{G}^F, \mathcal{G}^M) + \frac{1}{\sigma_x^2}\int_{\Omega_G} \|u_G\|^2, \tag{9.49}$$

Where the derivative of Sim w.r.t. u_i has been already discussed specifically for each of the similarity measures, and $\frac{1}{\sigma_x^2}\int_{\Omega_G} \|u_G\|^2$ is the classical demons regularization term.

9.5.7.3 Optimization Method

Along with the different metrics proposed in the previous section we have seen how to compute their gradient. Once we have computed $\nabla_{G,i}$ it is only a matter of choosing the optimization strategy, as with the strategies proposed in this thesis, it is possible to avoid higher order derivatives computation **?**. The simplest optimization strategy will be gradient descent.

$$u_{G,i} = -\varrho \nabla^f_{G,i}(G^M \star \phi) \tag{9.50}$$

with ϱ small. To avoid finding and optimal ϱ, we can use the ESM and perform a Gauss-Newton update step:

$$(\nabla^f_{G,i}(G^M \star \phi) + \nabla^f_{G,i}(G^F))u_{G,i} = -2\nabla^f_{G,i}(G^M \star \phi) \tag{9.51}$$

However, in the case of geometric structures, we derive w.r.t. a point of the fiber, and not w.r.t. a position in the grid as with images. Therefore, the left side of the equation sum will only make sense using an extrapolator to find the corresponding position of the fixed geometry fibers gradient.

9.5.7.4 Iconic + Fibers Demons algorithm

Finally, the Geometric Demons algorithm can be formulated as such:

1. Choose a starting spatial transformation $\phi = Id$ for diffeomorphic demons or for Log-domain diffeomorphic demons.
2. Given ϕ, compute the update field u_I as in Eq. 9.37
3. Given ϕ, compute the update field u_G by minimizing Eq. 9.43
4. Let $u \leftarrow \phi \circ \exp(u_I + u_G)$
5. $v \leftarrow \log(\exp(v) \circ \exp(u))$ using BCH approximation and $\exp(u)$ is efficiently computed with a few compositions, look Vercauteren et al. [2008] for further details.
6. let $v \leftarrow K_\beta \star v$ where K_β is a Gaussian convolution kernel
7. Let $c \leftarrow \phi \circ \exp(u_I + u_G)$ for diffeomorphic demons or $\phi = \exp(v)$ and $\phi^{-1} = \exp(-v)$ for Log-domain diffeomorphic demons.
8. Go to 2. until convergence

9.5.7.5 Parameter Settings

The Demons framework requires various parameters to work in practice. Luckily the classical demons parameters are stable across subjects and datasets, and do not pose us a parameter setting problem. Nevertheless, the incorporation of fibers into the algorithm has brought few more parameter to think about:

1. Deformation smoothing: This parameter applies a convolution with a Gaussian Kernel to the new computed deformation at each iteration. In our experience this parameter works well between 1.5mm and 3mm. On lower values results looks sharps and unrealistic, while higher too smooth and underfitted.

2. Update field smoothing: We have disabled this procedure, although it can be useful when working with unstable optimizations .

3. Iterations and Scales: We work on a 3 scale resolution setting with iterations defined as $15 \times 10 \times 5$. 5 iterations at the original resolution which is the more expensive one, and 15 when resolution is divided by $2^2 = 2^{\#\text{resolutions}}$. We did not find any improvements by increasing these numbers.

4. Gradient descent steps: We fitted these parameters to have an average of update field lengths no bigger than 2mm.

5. Number of points per fiber: We used 20 points per fiber for Weighted Measures and Closest Point Distance, although for Currents we resampled the fibers to be equally distributed in the space.

6. Fiber domain size for splitting domain setting: Experiments performed with Closest Point Distance and Currents defined a splitting domain, where it is necessary to be adapted to the image resolution. At low resolution, the domain radius should be multiply by $2^{\#\text{resolutions}}$, and ideally original resolution radius should be between $1mm$ and $3mm$.

7. Currents and Weighted Measures Kernel width: This parameter might depend on the application, however for most of our test we found that starting at $15mm$ and decreasing it throughout iterations helps avoiding local minima.

9.5.7.6 Implementation

These algorithms previously mentioned were developed using ITK and VTK libraries McCormick et al. [2014], Schroeder et al. [2006]. Implementation has been done purely on C++. Our implementation consist mainly in the following four components:

1. The Registration Component: based on the fixed and the moving images, the fixed and the moving fibers, it outputs the resulting deformation that would align the moving image and fibers onto the fixed subject space.

2. The Metric component: This component combines the metric on the fibers and the image.

3. The Optimizer: this component is in charge of performing the minimization of the defined energy.

4. The Multi-resolution Registration Component: this component calls *registration component* at each of the different resolutions. It changes the input image each time to adapt its resolution according to the current scale.

The Registration Component: Here the metrics between the images and the fibers are computed in order to call the optimizer that will provide us with the update field of the current iteration. The deformation is updated at each iteration, and so the moving fibers are warped and the moving image is deformed and interpolated to match the target space. This is shown in Figure 9.11

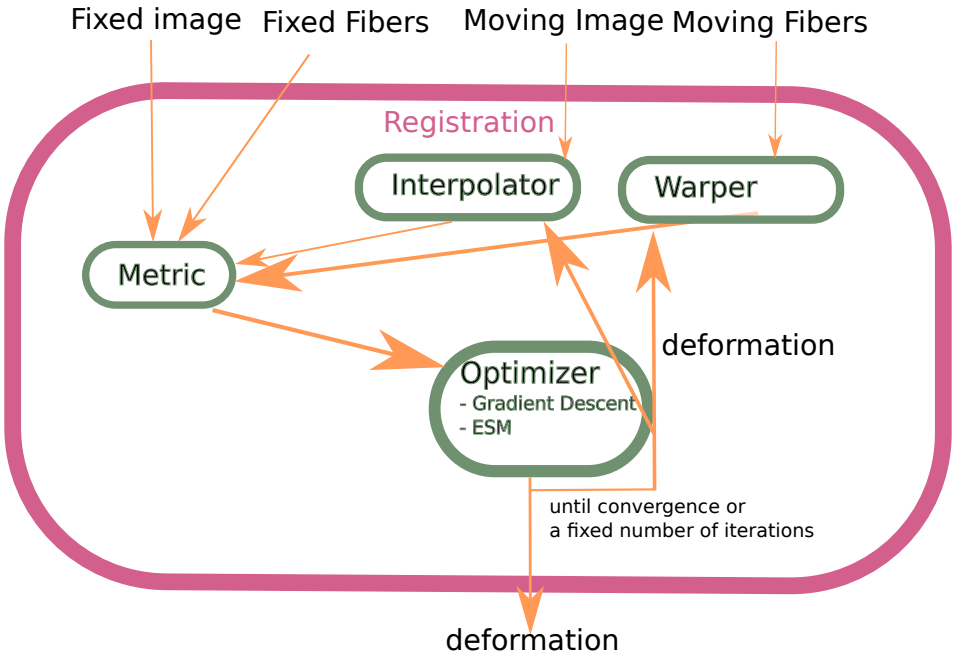

Figure 9.11: *Registration Component*
Input: Fixed image and fibers, moving image and fibers.
The initial deformation is identity, and the deformation is applied to the moving image by interpolation. The warper applies the vector field to each of the points in the Moving Fiber; this results in a sequence of floating points that do not need to fill the whole image grid. The metric is used by the optimizer to infer the new updated deformation field, and the process is repeated until convergence.
Output: deformation.

The Metric Component: Throughout this thesis the combination of the image and fiber metric has been done by an addition. Therefore this component computes the corresponding metric for fibers, and the corresponding metric for the image and both are combined. This is illustrated in Figure 9.12

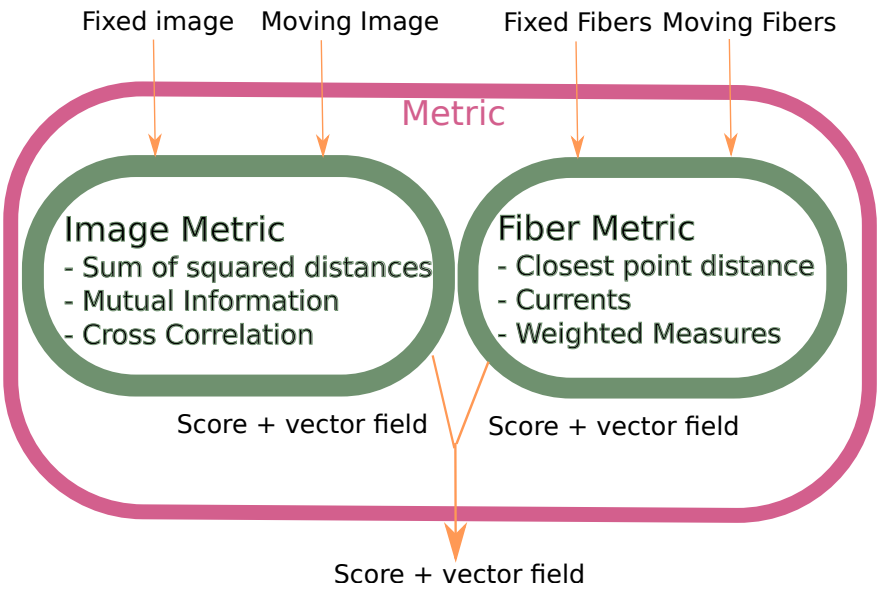

Figure 9.12: *Metric Component*
Input: Fixed image and fibers, moving image and fibers.
This component calls the metric on images and the metric on fibers, to combine them both additively . It metric returns the score and the vector field. The combination depends on the definition of the domains (overlapping, non-overlapping discussed at 9.5.7.2.
Output: It outputs the sum of the scores and a vector field (the derivatives).)

The Multi-Resolution Registration Component This component defines a different resolution at each stage of the registration. We can define different scales, where resolution will be decreased by a factor of two, and we can associate a number of iterations with each scale. Depending on the scale, the fixed and moving images are down-sampled, and the *Registration Component* with the images is evaluated at that resolution, while the fibers are handled at their resolution. The reason why fibers are not also downsampled is because their sampling is sparse originally, and fibers are generally represented by few points. Then the registration is performed along a defined number of iterations. When the *Registration Component* ends, if it is the last stage, the deformation is returned, however, if it is not, the deformation is applied to moving image and fibers, images are resampled according to the deformation, and the registration is performed again. Figure 9.13 shows this process.

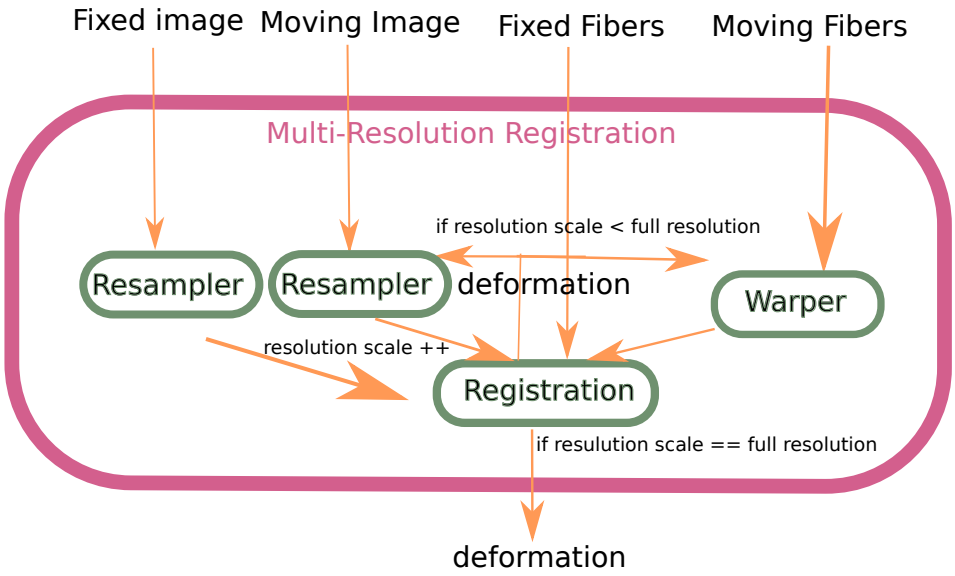

Figure 9.13: *Multi-resolution Component*
Input: Fixed image and fibers, moving image and fibers.
This component is in charge of resampling the images at the required resolution defined by the current scale. Then the Registration Component is called for a fixed number of iteration, and the returned deformation is applied to the moving fibers (by a warping component) and it is used by the resampler to update the moving image. The process is repeated until all resolution scales have been completed.
Output: It outputs the final deformation.

9.6 Experiments: Geometric Demons (GD)

In this section we evaluate the effect of adding fiber constraints into the demons registration algorithm and compare it to different modalities registration algorithms. We selected the Demons's framework because of its simplicity and time complexity. Measuring distances on an unlimited number of geometric curves can be a computational burden, hence one should be careful not to challenge the usability of the method.

We started testing our hypothesis that fiber information can better lead registration, by including the simplest of the presented metrics, the Closest Point Distance (CPD). Throughout all this section, each algorithm is tested in the 3-steps multi-scale approach with 15, 10 and 5 iterations at each scale (from small to large).

9.6.1 Geometric and Iconic Diffeomorphic Demons with Closest Point Distance

We analyze the joint registration of T_1 MRI and brain fibers with the CPD metric. CPD is a quadratic metric, but it can lead to good results under the assumptions of a one-to-one fiber correspondences across subjects which can be obtained using a method such as the one described in Section **??**.

In this experiment, Ω was split into two disjoints domains for geometric and iconic loss functions. The reasons for this were twofold:

1. First we know that fibers are defined on white matter, and T_1 images are uniformly white on those regions, adding no relevant information to the registration.
2. Second, the process of finding a fiber-to-fiber correspondence has been performed in a well-defined and long process framework, followed by visual validation. We expect those fibers to be well defined, thus they will not introduce errors to the gray matter registration.

Therefore a parameter γ measures the spread of the domain, which might be seen as the diameter of a tube along the fiber. As we increase γ the fibers have more influence on the deformation field.

Two experiments were conducted. First, we performed an exhaustive analysis of the parameter γ of Sec. 9.5.7.2 to understand its effect on registration accuracy. Second, we compared the performance between the GD, the Scalar Demons (SD) and the Tensor Demons (TD). For both experiments, 11 subjects were registered onto one, arbitrarily chosen as the target.

9.6.1.1 NMR Database Description

Analysis was performed for 12 subjects of the NMR public database Poupon et al. [2006]. This database provides high quality T1-weighted images and diffusion data acquired with a GE Healthcare Signa 1.5 Tesla Excite II scanner. The diffusion data presents a high angular resolution (HARDI) based on 200 directions and a b-value of 3000 s/mm2 (voxel size of 1.875×1.875×2 mm). Distortion correction and fiber tractography and clustering were performed using the Brainvisa software package (http://brainvisa.info). Using Guevara et al. [2011], we obtained corresponding fiber bundles between several subjects and a single representative fiber for each bundle. About 100 bundles were consistently identified in all subjects. The 50 longest ones (25 in each hemisphere) were retained for the experiments. For each subject we apply affine registration from B_0 to T_1 and use the resulting transformation to align bundles with T_1 images. Bundles were further simplified into point sets, which allows us to use the methodology presented in Sec. **??**.

9.6.1.2 Influence of γ

γ parametrizes the influence of the fiber vector field information when extrapolating the vector field, as defined in Section 9.5.7.2 for non-overlapping domains. We varied γ from 0 (no fiber influence, which is equivalent to Symmetric T_1 Demons (SD)) to 3.0mm. Registration results for three values of γ are shown in Fig. 9.14. Values of the image and fiber similarity measures for increasing values of γ are reported in Fig. 9.14 (d) and (e). As expected, when γ increases, fiber

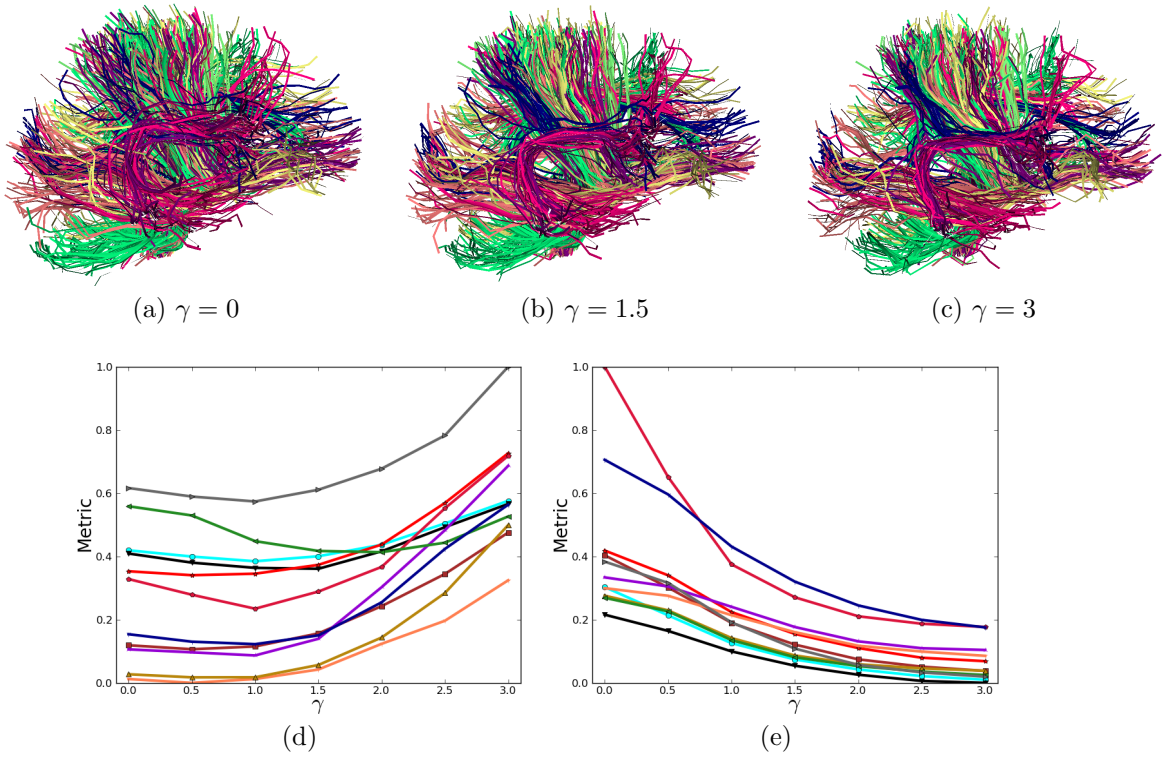

(a) $\gamma = 0$ (b) $\gamma = 1.5$ (c) $\gamma = 3$

(d) (e)

Figure 9.14: **Influence of γ on the registration accuracy. Top**: Tracts of 11 subjects were overlapped after registration with the Geometric Demons for three values of γ. Corresponding fibers in different subjects share colors. **Bottom**: Evolution of the image and tracts similarity measures with varying γ is shown in (d) and (e) (one curve per subject). For each metric, values were scaled using min-max normalization.

matching improves at the expense of image alignment. Indeed, when fibers have a large influence on their neighborhood, image-driven forces are discarded, leading to poor image registration. However, we noticed that a γ value of $1.5mm$ largely improves fiber alignment while keeping a good match between images. Notably, in some cases image matching is improved when using tracts as constraints compared to not using them at all, pointing to the fact that geometry may indeed help image registration to avoid local minima. In the sequel, a γ of $1.5mm$ will be used.

9.6.1.3 Comparison with Scalar (SD) and Tensor Demons (TD)

For Symmetric T_1 Demons, we registered all 11 T_1 images onto the target and applied the inverted deformation field to the bundles. For DtRefind (Tensor Demons Registration (TD)), we extracted tensors as in Fillard et al. [2007a] and registered them onto the target tensor image. Then, inverted deformation fields were applied to each subject's fibers in the DWI space. Finally, the linear transformation calculated between the target B_0 and T_1 images was applied to fibers to carry them to the T_1 space. We evaluated the fiber similarity measure between registered source and target fibers. Results for each method and each subject are reported in Fig. 9.15.

As expected, TD improved fiber registration compared to SD. Similarly, Geometric Demons

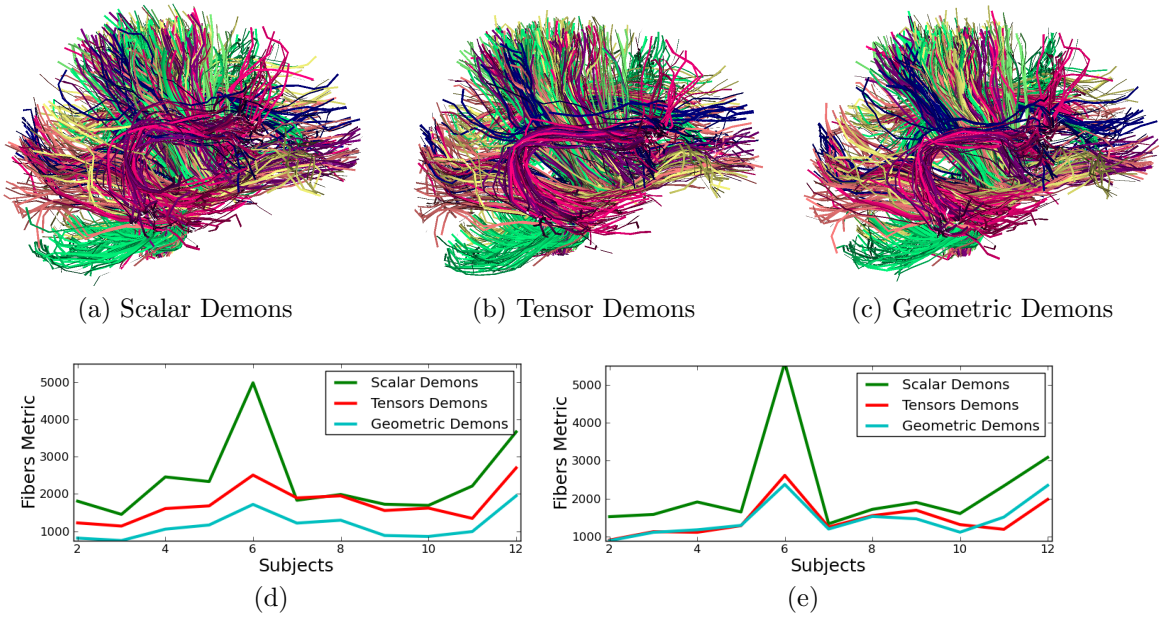

(a) Scalar Demons (b) Tensor Demons (c) Geometric Demons

(d) (e)

Figure 9.15: **Comparison of Scalar, Tensor and Geometric Demons. Top:** Fibers of 11 subjects were overlapped after registering with: (a) Scalar Demons, (b) Tensor Demons, (c) Geometric Demons. Corresponding fibers in subjects share colors. **Bottom:** Fiber similarity metric for each subject and each method evaluated on the fibers set (d) used during registration and (e) left aside.

(GD) further improved fiber alignment consistently for all subjects. However, the same set of fibers used for registration was used for performance evaluation. This favors our method as we explicitly optimize a metric evaluated on these fibers. For a fair evaluation, we measured in another experiment the fiber similarity on the 50 bundles that were left aside (100 bundles were extracted and only 50 were kept). In other words, we perform registration on half of the bundles and evaluate the result quality on the other half. Results are shown in Fig. 9.15 (e). We noticed a similar performance between TD and GD, both improving results obtained by SD. However, GD was only using sparse information from tensors over the set of fibers not being tested: having similar results as TD is thus very promising.

9.6.2 Log Iconic Geometric Diffeomorphic Demons with Current Distance between Fiber Tracts

We have shown that extending the Demons framework to include geometric descriptors of fibers improves the analysis of structures of interest(SOI) while holding, or even improving, the general accuracy on the whole image registration. Aware of the limitation of demanding fiber-wise correspondences, we introduce the Currents metric as it does not require a fiber-wise correspondence across subjects. Nevertheless, it still needs the correspondences between objects where a consistent alignment can be found, as discussed in extend in Section 9.3.2.2. In our experiments, the NMR database described in Section 9.6.1.1 was used, however instead of using the representatives of the thin clusters obtain with Guevara et al. [2011], we used all fibers in the cluster

(average 5 fibers per cluster).

Two experiments were conducted. First, we exhaustively analyzed the impact of the parameter γ in ω_G^γ defined in Sec. 9.5.7.2, to understand its effect on registration accuracy. Second, we compared the performance between Symmetric Log Domain Demons (SLDD), the Symmetric Tensor Demons (STD) and ANTs. The inverted deformation field was applied to the fibers to display the registration. We set the currents kernel size β by using a robust estimator of the maximum distance between bundles thresholded at 20mm. In consequence, when bundles are very close, the kernel size will be small letting the registration account for small details. Nevertheless a threshold is set to avoid aligning bundles at such distances.

9.6.2.1 Influence of γ

γ parametrizes the influence of the fiber vector field information when the vector field is extrapolated, as defined in Section 9.5.7.2 for non-overlapping domains. In the first experiment, the 11 subjects were registered onto one, arbitrary chosen as the target subject. We varied γ from 0 to 4.5mm, where γ is scaled by the smallest dimension of the voxel size. We divided our bundles in 5 sets (13 bundles each, with bundles of ~ 3 tracts, each of 21 points), and used jointly 4 to train, and the left one to test. The following results show the average of the 5 possible permutations for choosing the test set. We show results over training set (a), test set (b), and the image (c) for increasing values of γ in Fig. 9.16. As expected, fiber matching improves as γ increases (a) at the expense of image alignment (c). Indeed, when fibers have a large influence on their neighborhood, image-driven forces are discarded, leading to poor image registration. Also, comparing (a) and (b) we note that $\gamma = 4.5mm$ is overfitting the fibers, misleading the overall registration. $\gamma = 3.0mm$ largely improves fiber alignment, while keeping a good match between images. In the sequel, a $\gamma = 3.0mm$ will be used. In some cases image matching is slightly improved when using $\gamma = 1.5mm$ pointing out that geometry may indeed help image registration to avoid local minima.

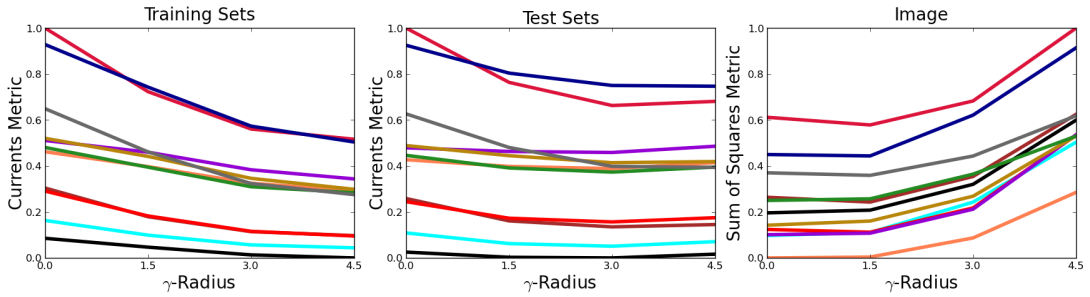

(a) (b) (c)

Figure 9.16: **Influence of γ.** Similarity measure average of the 5 possible training folds of the cross-validation with varying γ. Different color curves represent the 11 subjects.

9.6.2.2 Comparison with SLDD, STD and ANTS

For this experiment we permuted both the test set (of the 5 training sets previously defined), and the target subjects. For each of the 12 subjects the 11 remaining subjects were registered

to it, and for each fold of the cross-validation. This tests also the stability of the algorithm, however, a template subject could have been estimated Lepore et al. [2008b]. For SLDD, we registered 11 T_1 images onto each of the 12 subject (selected as target one at a time) and applied the inverse deformation field to the bundles. For STD, we extracted tensors using Fillard et al. [2007a] and registered each of them onto each of the 12 subject selected as target tensor image, one at a time. Then, inverted deformation fields were applied to each subject's fibers in the DWI space. Finally, the linear transformation calculated between the target B_0 and T_1 images was used to carry fibers to the T_1 space. For ANTs, we extracted the FA from the tensors obtained using Fillard et al. [2007a], and aligned them to their T_1 image. We use the cross correlation setting with equal weight for the image and the FA. Then affine and non-rigid transformation were applied to images, while the inverse of the non-rigid and the affine were applied to the fibers. We show the average metric over training sets (i), test sets (j) and image (k) of registering all subjects to each one with the methods mentioned above in Fig. 9.17. As expected, LGD further

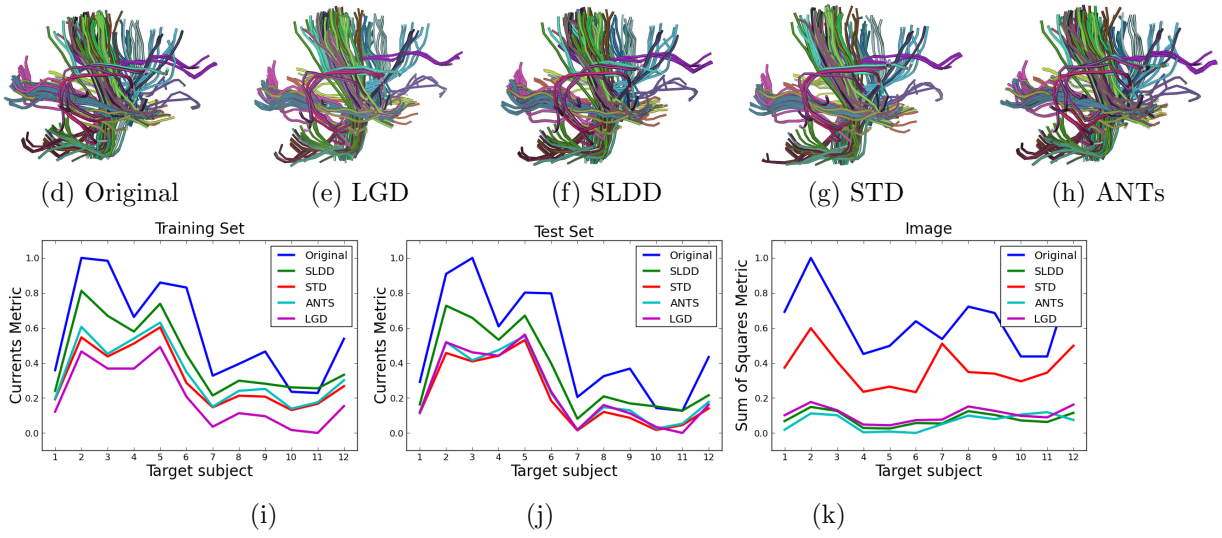

Figure 9.17: **Comparison of SLDD, STD, ANTs and LGD Top:** Source fibers and target fibers overlapped with registered fibers from an arbitrary chosen registration. Corresponding fibers in subjects share colors. **Bottom:** Average of the metric obtained from registering 11 subjects to the target subject.

improved fiber registration in (i) compared to the other algorithms. However, the training set contains the fibers used during registration; we explicitly optimize a metric evaluated on those fibers. Analyzing the results over the test set in (j) we see a similar performance compared to ANTs, and STD, which is remarkable as STD is using information from tensors over the whole dense grid, and ANTs does a cross correlation between the whole FA grid and T_1. By contrast, in LGD the deformation field was obtained using only sparse information coming from selected fibers, which are not defined in the regions tested in (j). Therefore having a similar performance is very promising. We can also see in (k) the image registration for STD was extremely poor.

We time all algorithms with an Intel Xeon 8proc. 2.53GHz, 11.8Gb and obtained: SLDD=19.61min, STD=10.75min, ANTs=25.63min, and LGD=12.51min.

9.6.2.3 Discussion

We compared our algorithm against a scalar (SLDD), a tensor (STD), and a multi-modal (ANTs) registration. Our results show that bundle alignment was improved compared to other algorithms. We get accurate results even for testing set fibers where no information was used from the support regions of the those fibers, and STD and ANTs were using information from the whole grid. This shows that a small set of fibers might be sufficient for a proper registration of the white matter across subjects. Moreover, while fiber alignment is improved, the efficiency of the image alignment is maintained. When evaluating the algorithm for the different γ values, we could see that $\gamma = 1.5mm$ better registers missing structures than $\gamma = 0mm$ and than SLDD. However, we believe there is a trade-off to make between image and fiber alignment, and $\gamma = 3mm$ notably improved fiber alignment while still obtaining good image registration results.

By using labeled bundles instead of purely tensor information, we add relevant features that were previously extracted as prior such as region connection. Nevertheless, consistently labeling fiber bundles across subjects is a hard topic, and it is not always a possible choice. Obstacles can be noise in the image, subjects with degenerated white matter, algorithm not available, or not reliable enough. For this reason in the following section we propose a method for comparing white matter fibers across subjects without the need of any type correspondence. However, when having a consistent labeling of fiber bundles across subjects, using *currents* to model their geometry is an efficient and effective choice. When having corresponding bundles, the computation is reduced to the within correspondences comparisons instead of an all-to-all comparison, and the tangents along the tract curves serve to include shape information into the fiber bundle representation.

9.6.3 Log Iconic and Geometric Diffeomorphic Demons with Measures on fiber tracts

Currents is an appealing similarity metric, as it is pose and shape sensitive; nevertheless the need for bundles correspondences or analogously an orientation of fibers, is a huge limitation. The reason is that by doing so, we are introducing a pre-segmentation in the registration procedure.

This can be featured in examples in which one wants to explicitly define regions of interest, to analyze a disease, the activation of a particular region on fMRI (including only relevant connections). However, when segmentation comes automatically and is intended to perform on the whole brain, it is generally based on a pre-defined atlas, and registration to those atlases, introducing and spreading possible inaccuracy and errors. For these reason, we propose an approach where no explicit correspondence is needed, and the whole brain can be registered using white matter information without such strong assumptions.

For these experiments, Weighted Measures Model was introduced, and the domain of the fiber was defined on the whole grid, meaning that fiber together with image should lead the registration, without prioritizing one over the other based on the intensity of the image.

This method was tested in a different database, and 3 experiments were performed:

1. The Kernel size of the Weighted Measure Model:

    - Different values of kernel size were tested, and were fixed through the iterations of the algorithm.

- An adaptive kernel size, where a starting value is selected, then decreased across iterations, as the distance on the Weighted Measures decreases, the kernel size is shrunk to capture finer details.

2. We analyze the impact of the regularization over fibers, image and the transformation properties

3. We compare the algorithm against the Tensor registration, and the multi-modal of $T_1 + FA$.

9.6.3.1 Data Description

We used ten healthy volunteers from the Imagen database**?** scanned with a 3T Siemens Tim Trio scanner. Acquisitions were MPRAGE for T_1 weighted ($240 \times 256 \times 160, 1.09375 \times 1.09375 \times 1.1mm^3$) and DW-MRI ($128 \times 128 \times 60, 2.4 \times 2.4 \times 2.4mm^3$) with TR = 15000 ms, TE = 104 ms, flip angle = 90^o, 36 gradient directions, and b-value = $1300s/mm^2$.

For each subject we obtained the linear transformation from the non-weighted image B_0 to T_1 to align bundles with T_1 images. Eddy currents correction was applied to DTI data, and skull and neck were removed from T_1 images using the FSL software.

We used MedInria for fiber tractography, and splines to extrapolate for uniformly distributed points. Fibers shorter than $50mm$ were discarded in order to discard U-shape fibers. Within U-shape brain fibers variability is high and mismatch across subjects can be easily introduced during registration. We rather trust the image for those regions around the cortex.

As discussed in section **??** we are not interested in using the whole fiber tractography output, but rather the bundles representatives. We use the QuickBundles algorithm Garyfallidis et al. [2012] to obtain a clustering of the fibers, and used the representatives given by the algorithm for registration. The threshold value for the bundles spread width was set to $10mm$, which gives a trade-off between low cluster variability and number of fibers per cluster. This yielded an average of 600 bundles per subject (range: $[323, 927]$), where a bundle contains at least one fiber. Selecting bundles with more than 50 fibers leads to an average of 63 bundles (range: $[37, 88]$). In the sequel we refer to this subset as the Training Set, and bundles with less than 50 fibers as the Test Set.

Before registering with Weighted Measures Geometric Demons (WMGD) we apply a T_1 affine transformation using the MedInria software to take subjects to the target space, and apply the inverse to the fibers.

After running WMGD we obtained a deformation field that we applied to the moving T_1 and the inverse of the deformation to the fibers.

The rest of this section explains the experiments performed. To assess the sensitivity to parameters we arbitrary choose a subject as target to register the rest of the dataset. Then, for performance comparison with other algorithms, we register the subjects to one another, and average the pairwise distances.

9.6.3.2 Weighted Measures kernel size

To analyze the impact the β parameter defined in Section 9.5.7.1 we register the whole dataset to an arbitrary subject chosen as target by using the Training Set of bundles. Typically large kernels would be able to capture large misalignment and details are discarded.

We run Weighted Measures Geometric Demons with the following parameters fixed $\varrho = 0.3, \gamma = 3mm, \sigma_T = 2mm, \sigma_i = 1mm, \sigma_x = 1mm$ with a 3-steps multi-scale approach with $15, 10$ and 5 iterations at each scale (from small to large). γ parametrizes the influence of the fiber vector field information when extrapolating the vector field, as defined in Section 9.5.7.2 for overlapping domains.

We vary β from 0 to 30mm and show results in Figure 9.18 for fibers (a) and for image (b). However, we believe that decreasing β through iterations might avoid local minima for fiber registration and improve the accuracy of image registration. We decrease it 0.5% at each iteration and results are shown in Figure 9.18 for fibers (c) and for image (d).

9.6.3.3 Regularization

To analyze the smoothness of the deformation field, we run experiments with values of σ_T varying from 0 to 3.0mm and analyze the impact over the results. Analogous to Section 9.6.3.2 we register the dataset to an arbitrary subject chosen as target, and we use the Training Set of fibers for registration. We use the same parameter setting with $\beta = 20mm$. In Figure 9.19 results are shown for fibers (a), image (b) and the regularization term (c).

9.6.3.4 Performance Comparison Experiments

We conducted a cross-validation experiment by performing registration on the Training Set, and validating results over the Test Set (bundles left out for containing less than 50 fibers). To validate the robustness of the results we register subjects dataset to one another and plot the average pairwise distance.

We run Weighted Measures Geometric Demons with the following parameters $\varrho = 0.3, \gamma = 3mm, \beta = 10mm, \sigma_T = 2mm, \sigma_i = 1mm, \sigma_x = 1mm$. β was decreased by 0.5% at each iteration of the algorithm. Symmetric Tensor Demons (STD) was run with its defaults parameters. For ANTS we used recommended parameters from documentation except for the weight of T_1 and FA where different combinations were tested. We finally show results with both parameters equal to 1, which we found to be a fair trade-off. Each algorithm was tested on the 3-steps multi-scale approach with $15, 10$ and 5 iterations at each scale (from small to large).

We recall that for WMGD we first apply a T_1 affine transformation using the MedInria software to take subjects to the target space, and apply the inverse to the fibers. After running WMGD we obtained a deformation field that we applied to the moving T_1 and the inverse of the deformation to the fibers. We compare our results to those of ANTS, a multi-modal image registration combining T_1 image and FA, and Symmetric Tensor Demons, a tensor-based registration algorithm. Before running ANTS, corresponding FA and T_1 were aligned using a linear transformation. The resulting affine transformation and deformation field were applied to the moving T_1 image, and their inverse to the fibers. For tensor-based registration, tensor images were taken to the target T_1 space using an affine transformation for the moving subjects, but preserving the original resolution. The resulting deformation field was up-sampled to the T_1 resolution for application to the image and then inverted for application to the geometry.

9.6.3.5 Weighted Measure: β value

As expected, Figure 9.18 shows that higher β values give better scores for fiber registration while loosing accuracy on the image registration. Each curve in Figure 9.18 has been normalized by its

maximum value in order to analyze the impact of the parameter in each subject. However minimum values across figures are not comparable as they depend on the maximum value achieved. When defining a fixed β though the iteration we quickly lose accuracy for the image registration. When decreasing iteratively β, we can see that with an initial value between 10 and 15, we improve fiber alignment while still holding the image one.

9.6.3.6 Regularization

In Figure 9.19 we can see that as we increase the regularization, the image accuracy decreases. However, low regularization will result in sharp deformations, which are often undesirable for the purpose of registration. As for the fiber accuracy we find that the impact is low, nevertheless, a fair compromise with the harmonic energy can be found for σ_T between 1.5 and 2. The difference of regularization impact over the image and the fibers are related to the resolution differences.

9.6.3.7 Discussion

The aim of WMGD is to align T_1 images and fiber tracts simultaneously by only using a set of bundles that represent well the white matter structure. We compare our results to a tensor-based registration Symmetric Tensor Demons (STD) and a multi-modal registration of $T_1 + \text{FA}$ (ANTS).

Average results for registering the individual datasets to each other are shown in Fig. 9.20 for training set tracts (a), test set (b) and image (c). The WMGD method outperforms the others on the bundles used in the registration as shown in (a), which is expected, given that the minimized energy considered those specific bundles. For a fair comparison we tested our metric on the remaining bundles; the corresponding results are shown in (b). For the left aside bundles, results are similar but generally improved by our method. These results suggest that a sparse bundle selection according to their importance can be sufficient and that there is no need to require datasets to have the same number of bundles. Last, in (c) we compare the methods with respect to image registration accuracy. It is important to mention that diffusion images had a lower resolution than the T_1 images, maybe giving advantage to ANTS and our algorithm in accuracy as the level of details of the images were higher. WMGD yields better performance than ANTS, proving that improvements on bundles registration was not obtained at the expense of image accuracy.

In Fig. 9.21 we can see the result of registering the dataset to an arbitrary chosen as target. In (d) we see the fibers even before applying an affine registration, and in (g) we can see some improvements with respect to (e) and (f) regarding the borders of the image, and a better alignment of the corpus callosum.

We time all algorithms with an Intel Xeon 8proc. 2.53GHz, 11.8Gb and obtained: STD=5.11min, ANTs=29.43min, WMGD=44.0min.

9.7 Conclusion

We have analyzed different metrics to represent information from neural brain fibers tracts as an addition to iconic registration. Each representation was compared to an iconic and a tensor registration.

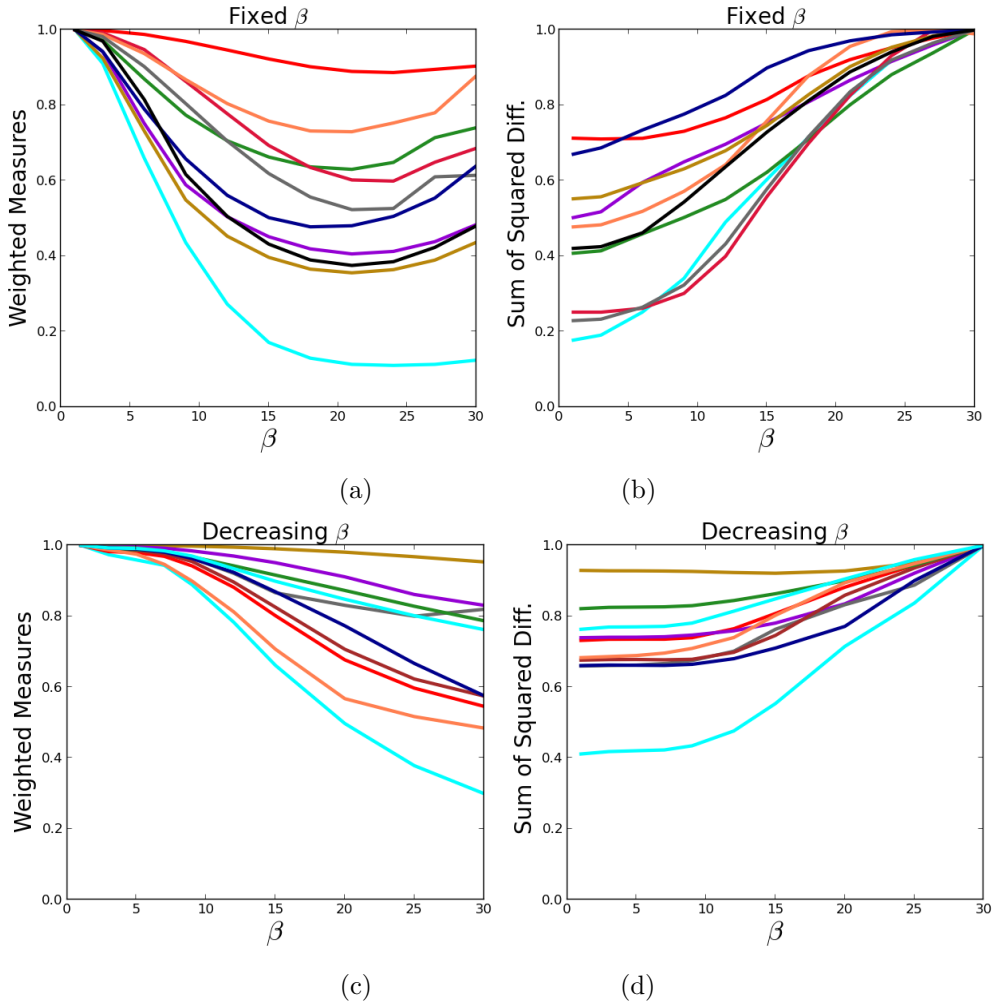

Figure 9.18: Registration of the dataset to an arbitrary subject chosen as target. Each curve encodes one subject registration to the target. β varies in the x-axis. Figures (a) and (b) show the metric for fiber and image respectively at each β value fixed through iterations. Figures (c) and (d) show respectively the metric for fibers and image at each initial value of β, and with a 0.5% decrease at each iteration. Curves were normalized by their maximal value.

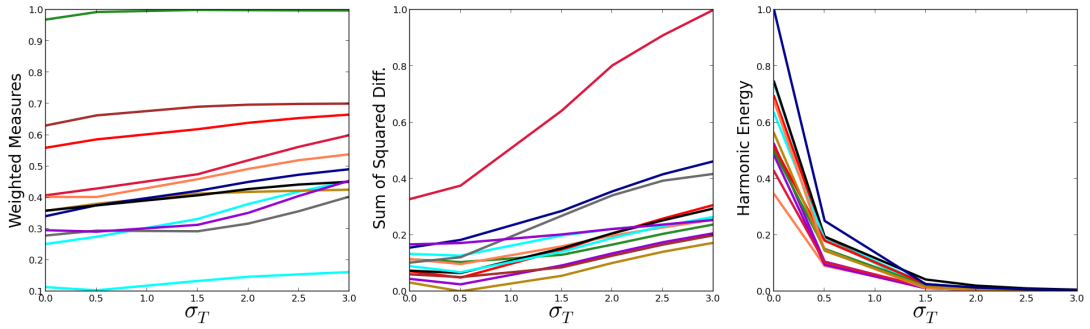

(a) (b) (c)

Figure 9.19: Registration of the dataset to an arbitrary chosen as target with varying σ_T. Each curve encodes one subject registration to the target. Weighted Measures metric is shown in (a) for increasing σ_T, the Sum of Squared Diff. of the image in (b) and in (c) we show the harmonic energy results. Curves were scaled using min-max normalization.

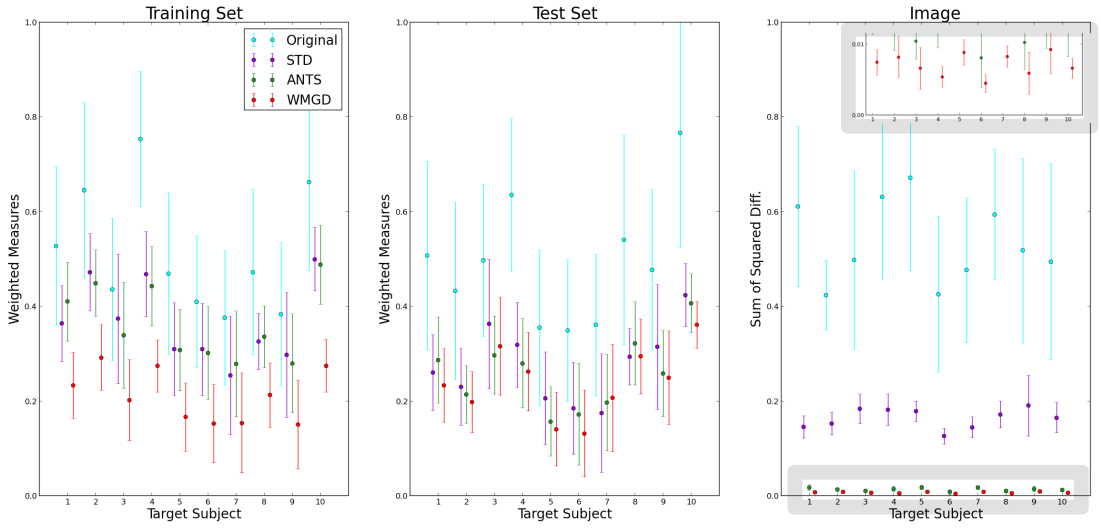

(a) (b) (c)

Figure 9.20: Registration of the dataset to each subject. STD, ANTS, and WMGD show the average accuracy of the registration to each subject for the corresponding method. Original corresponds to the original distances between the dataset and the chosen target subject. Values were scaled using min-max normalization.

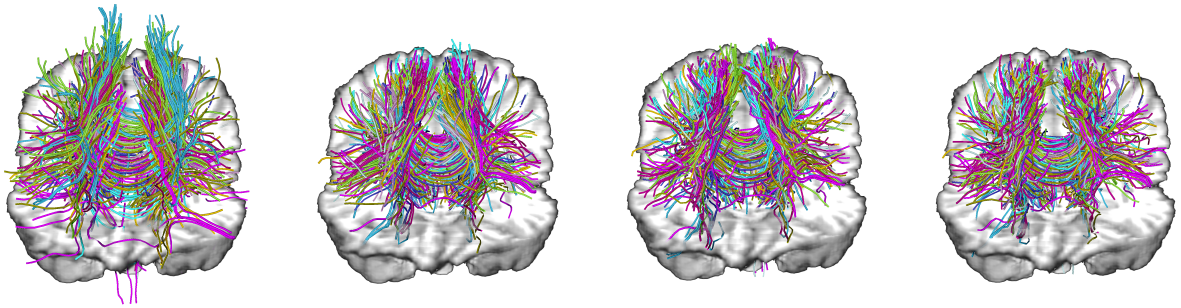

(d) Original (e) STD (f) ANTS (g) WMGD

Figure 9.21: Overlap of fiber bundle representatives from all subjects registered to an arbitrary one chosen as target. Colors encode the different subjects. Behind we see the $3D$ T_1 image of the target subject.

When compared to iconic registration, we significantly improved the registration of fiber tracts, while holding a competitive performance on iconic alignment. Few subjects displayed a better iconic alignment while introducing fibers information, however we believe that this statement can only be proved by analyzing in detail the anatomy of the resulting images, and not the scores of the metric. This is meant to ensure that no overfitting is happening. Nevertheless, the improvement of fiber tracts show that iconic criteria might align perfectly the contours of the image, however without any control of possible misalignment inside regions with uniform intensity, such as white matter.

When fiber-based registration is compared to tensor registration, it is interesting to see that tensor registration is unable to yield an acceptable registration of T_1, leaving us to wonder whether the registration can be useful. Nevertheless, it can serve other types of investigation, such as analyzing the amount of connectivity in a defined region. On the other hand, if tensor registration fails to align T_1 images, it might be hard to extract further features from the resulting population, i.e. while analyzing connectivity patterns, one might be interested in its relation to sulcal lines or functional regions, however if gray matter is misaligned, sulcal folding might also be.

When comparing to a multi-modal algorithms, best results were obtained by using Weighted Measures. This is probably related to the reliability of the corresponding bundles defined.

It is important to decide whether one should use Currents or Weighted Measures. When analyzing one specific region, i.e. the auditory region, and one can accurately label the fibers connecting it, it might be advantageous to use Currents, and define the relevant orientation. However, in more general settings, when one does not have any prior, or any reliable method to introduce them, Weighted Measures are better suited.

Chapter 10

Conclusion

"He had come a long way to this blue lawn, and his dream must have seemed so close that he could hardly fail to grasp it. He did not know that it was already behind him, somewhere back in that vast obscurity beyond the city, where the dark fields of the republic rolled on under the night. Gatsby believed in the green light, the orgastic future that year by year recedes before us. It eluded us then, but that's no matter — to-morrow we will run faster, stretch out our arms farther. . . . And one fine morning —— So we beat on, boats against the current, borne back ceaselessly into the past."

—The Great Gatsby, by F. Scott Fitzgerald

Population analysis for detecting disease biomarkers and for understanding normal growth is nowadays a standard technique linked to the wide availability of scanners in hospitals and the new interest of sharing research purpose databases. The wide range of imaging techniques measuring different features of the brain leads to a natural evolution path of the analysis. Multi-modal analysis has been receiving more and more attention in the neuroimaging field at every stage of analysis: white matter clustering, functional region activation detection, cortex segmentation, registration, etc.

Within this thesis we have mainly explored the simplication of white matter structure, and how white matter can be incorporated into a registration framework to improve inter-subject analysis.

In Chapter 8 we have performed an extensive analysis of common techniques to simplify intra-subject fiber tractography analysis. With the interest of further performing inter-subject studies, we focus only on the main tracts, which are expected to be large and easily detectable across subjects. We have compared different clustering algorithms for the simplification of white matter, from the most famous and widely known K-Means, to hierarchical average linkage, and a new proposed algorithm in the community, QuickBundles. The later was specially designed for the fast analysis of massive white matter datasets.

The strongest white matter analysis pipeline was developed in and it is based on average linkage, where tractography dataset is first divided based on previous segmentations performed on the cortex based on T_1 images, and then the algorithm is applied for each subgroup. A second level of clustering group fibers from multiple subjects together to detect corresponding fibers across subjects. This methodology is robust, and it builds on many preprocessing steps to enhance results: T_1 based cortex segmentation is used to infer a roughly initial segmentation of the white matter tracts, and registration needs to be performed before clustering multiple subjects together.

In contrast with the latter technique, QuickBundles was developed in , and is a fast algorithm, capable of clustering a massive tractography database in a matter of seconds. Although QuickBundles has not showed to perform well on metric comparisons to other algorithms and metrics, it is very handy for fast preprocessing, and we have found that in average the main white matter tracts are finely detected.

With the aim to compare the impact of different metrics over white matter analysis, we chose K-Means algorithm and extended its metric to better suit our needs. We showed how simple metrics such as Euclidean distances, the most widely used on clustering algorithm, can be improved. Specifically, we focus in metrics such as Hausdorff and Measures, where no point to point correspondence is required. This is relevant in white matter analysis not only because fibers can have different lengths, but also, as a consequence of poor image quality, a fiber can end earlier, or be split. Our results show that the Measure metric outperformed other metrics. We have also introduced different metrics to evaluate the clustering, which are widely known in the machine learning literature, but hardly used on the diffusion neuroimaging community.

We are aware that distances such as Hausdorff or Measure are computationally more expensive than a point-wise distance such as Euclidean, and as a consequence of the high-dimensionality of the diffusion data, we found ourselves forced to explore other options. We introduced Multi-dimensional scaling to embed tracts into a new featured spaced defined by the desired metric, to then cluster the embedded tracts with the regular K-Means algorithm. This is performed by selecting a percentage of random tracts as sampled, and we show that while computation time dramatically changes, accuracy remains stable when varying the % of them.

We have chosen K-Means for this analysis, but further work could be the implementation of Measures with Multi-dimensional scaling on QuickBundles or on average linkage clustering and one would hope it can enhance clustering accuracy.

In Chapter 9 we have extended a well-known method for T_1 image registration, the Demon's Framework, and incorporated into it the geometrical information coming from fibers tracts.

Tractography outputs are large, and can contain a few million tracts. Registration algorithms are computationally expensive to compute, therefore a prior simplification of the white matter is mandatory.

Different approaches have been explored during this thesis. The first proof of concept was the representation of the fibers as a sequence of points, and a measure defined by the Closest Point

Distance (CPD). Results have shown that T_1 registration could be widely improved, as T_1 alignment was maintained by the new algorithm, but white matter alignment was greatly improved. Some subjects have even showed improvements on the T_1 alignment, verifying that indeed white matter information can lead to better overall inter-subject registration. A requirement for using the CPD metric was a fiber-to-fiber correspondence. This was obtained by using the 2 levels pipeline of average-linkage clustering developed in . The resulting bundles were further simplified to only one representative fiber, the centroid.

To avoid this fiber-to-fiber requirement which is mostly unrealistic, we upgrade the registration algorithm by representing fiber bundles with Currents. Instead of a cloud of points, each bundle is represented by a sum of dirac deltas centered at fiber points associated with the tangents following the curve direction. Although this new representation does not require fiber-to-fiber inter-subject correspondences, it does requires bundle-to-bundle correspondence as orientation needs to be consistent across subjects for a proper registration. Results have once again shown to hold T_1 alignment while dramatically improving tractography alignment in comparison with the original algorithm.

Naturally, the next step was to remove the requirements of bundle-to-bundle correspondences. The reason why this dependency is undesirable is usability. First, obtaining corresponding bundles across subjects takes lots of preprocessing time, but second, it is not always plausible to define correspondences across subjects. The latter holds especially in neurodegenerative diseases, and longitudinal studies for analyzing brain development. But we were still interested in the white matter simplification, and a new metric was defined on that basis. We represented the whole tractography dataset as a sum of dirac delta centered at each point of each cluster representative. The clustering can be performed with any method, but we have used QuickBundles. Each dirac delta is weighted by the amount of fibers there was in the cluster of the representative. By doing so, the registration is lead mostly by the larger clusters, which are expected to be the main white matter tracts. With this reasoning, small bundles are taken as noise, and have low impact on the alignment. Once again, results have shown a dramatic improvement of white matter alignment, while holding accurate results for T_1 image alignment.

We have compared our registration methodology to a tensor-based and a muti-modal $T_1 + FA$ (ANTS) registration. For tensor-based registration results were as expected, as white matter alignment was improved but the registration was useless for T_1 analysis, and therefore for most multi-modal approaches that go beyond white matter analysis. The comparison with the multi-modal $T_1 + FA$ was more interesting, as for the Currents representation improvements where mostly in white matter, but ANTs showed slightly better results on image criteria. On the other hand, for Weighted Measures representation, results showed improvement in white matter but also regarding the imaging criterion. As we believe Currents give a better representation of shape than Measures, we intuitively conclude that the improvement was related to enforcing bundle correspondences across subjects.

As future work on registration, it is worth investigating the use of non-oriented versions of currents, such as with Varifold.

Meanwhile, the proposed registration methods will be used to analyze the impact of including white matter connections for normalization on fMRI analysis, such as activation zones detection. A proof of concept of adding diffusion information such as FA to the registration in a group analysis of activation detection zones is shown in Fig. 10.1, indicating that indeed, connection information might improve sensitivity. This first results motivates the use of the methods developed in this thesis to potentially improve the accuracy on fMRI activation detection. A proof of concept of adding diffusion information such as FA to the registration in a group analysis of

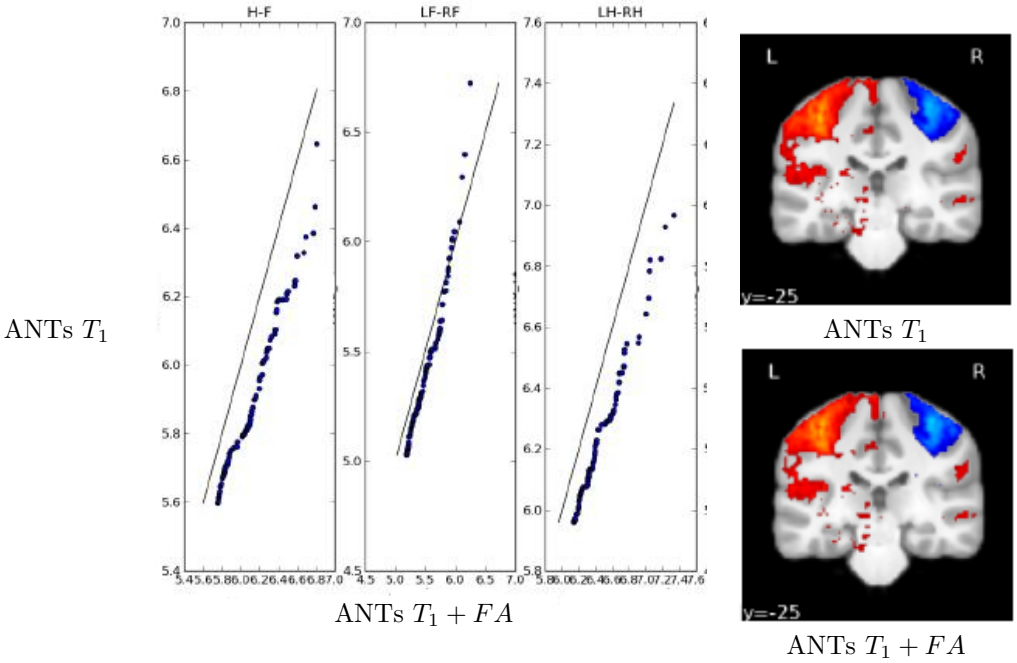

Figure 10.1: Comparison between a group analysis registration of 20 subjects from the HCP database, using ANTs with purely T_1 images, and ANTs with T_1+FA. Results shows that higher values are obtained with the incorporation of information comming from diffusion imaging.

activation detection zones is shown for both registrations on Fig. 10.1 (right images), inciting that indeed, connection information might improve accuracy. This first results motivates the use of the methods developed in this thesis to potentially improve the accuracy on fmri activation detection.

10.1 Acknowledgements

This work was supported by the INRIA CapNeonates Equipe Associée, the ANR (Agence Nationale de la Recherche) "programme blanc" KaraMetria number ANR-09-BLAN-0332-01, the ANR grant (ANR-10-BLAN-0128). The data were acquired within the Imagen project.

Bibliography

Human connectome project, 2012.

Gilberto Sousa Alves, Laurence O'Dwyer, Alina Jurcoane, Viola Oertel-Knöchel, Christian Knöchel, David Prvulovic, Felipe Sudo, Carlos Eduardo Alves, Letice Valente, Denise Moreira, Fabian FuBer, Tarik Karakaya, Johannes Pantel, Eliasz Engelhardt, and Jerson Laks. Different patterns of white matter degeneration using multiple diffusion indices and volumetric data in mild cognitive impairment and alzheimer patients. *PLoS ONE*, 7(12):e52859, 12 2012. doi: 10.1371/journal.pone.0052859. URL http://dx.doi.org/10.1371%2Fjournal.pone.0052859.

Adam W Anderson. Measurement of fiber orientation distributions using high angular resolution diffusion imaging. *Magn Reson Med*, 54(5):1194–1206, Nov 2005. doi: 10.1002/mrm.20667. URL http://dx.doi.org/10.1002/mrm.20667.

A. Andronache, M. von Siebenthal, G. Székely, and Ph Cattin. Non-rigid registration of multi-modal images using both mutual information and cross-correlation. *Med Image Anal*, 12(1): 3–15, Feb 2008. doi: 10.1016/j.media.2007.06.005. URL http://dx.doi.org/10.1016/j.media.2007.06.005.

Babak A Ardekani, Stephen Guckemus, Alvin Bachman, Matthew J Hoptman, Michelle Wojtaszek, and Jay Nierenberg. Quantitative comparison of algorithms for inter-subject registration of 3d volumetric brain mri scans. *J Neurosci Methods*, 142(1):67–76, Mar 2005. doi: 10.1016/j.jneumeth.2004.07.014. URL http://dx.doi.org/10.1016/j.jneumeth.2004.07.014.

Vincent Arsigny, Pierre Fillard, Xavier Pennec, and Nicholas Ayache. Log-euclidean metrics for fast and simple calculus on diffusion tensors. *Magn Reson Med*, 56(2):411–421, Aug 2006. doi: 10.1002/mrm.20965. URL http://dx.doi.org/10.1002/mrm.20965.

Uri M. Ascher and Linda R. Petzold. *Computer Methods for Ordinary Differential Equations and Differential-Algebraic Equations*. SIAM: Society for Industrial and Applied Mathematics, 1998. ISBN 0898714125. URL http://www.amazon.com/Computer-Ordinary-Differential-Equations-Differential-Algebraic/dp/0898714125%3FSubscriptionId%3D0JYN1NVW651KCA56C102%26tag%3Dtechkie-20%26linkCode%3Dxm2%26camp%3D2025%26creative%3D165953%26creativeASIN%3D0898714125.

J. Ashburner and K. J. Friston. Voxel-based morphometry–the methods. *Neuroimage*, 11(6 Pt 1):805–821, Jun 2000. doi: 10.1006/nimg.2000.0582. URL http://dx.doi.org/10.1006/nimg.2000.0582.

John Ashburner and Stefan Klöppel. Multivariate models of inter-subject anatomical variability. *Neuroimage*, 56(2):422–439, May 2011. doi: 10.1016/j.neuroimage.2010.03.059. URL http://dx.doi.org/10.1016/j.neuroimage.2010.03.059.

G. Auzias, O. Colliot, J. Glaunes, M. Perrot, J-F. Mangin, A. Trouve, and S. Baillet. Diffeomorphic brain registration under exhaustive sulcal constraints. *IEEE Trans Med Imaging*, Jan 2011. doi: 10.1109/TMI.2011.2108665.

Guillaume Auzias, Joan Glaunés, Olivier Colliot, Matthieu Perrot, Jean-François Mangin, Alain Trouvé, and Sylvain Baillet. Disco: A coherent diffeomorphic framework for brain registration under exhaustive sulcal constraints. In *LNCS*, volume 5761, pages 730–738. Springer Berlin / Heidelberg, 2009.

Brian B. Avants, Charles L. Epstein, Murray Grossman, and James C. Gee. Symmetric diffeomorphic image registration with cross-correlation: Evaluating automated labeling of elderly and neurodegenerative brain. *Medical Image Analysis*, 12(1):26–41, 2008. URL http://dblp.uni-trier.de/db/journals/mia/mia12.html#AvantsEGG08.

Brian B. Avants, Nicholas J. Tustison, Gang Song, Philip A. Cook, Arno Klein, and James C. Gee. A reproducible evaluation of ants similarity metric performance in brain image registration. *NeuroImage*, 54(3):2033 – 2044, 2011. ISSN 1053-8119. doi: 10.1016/j.neuroimage.2010.09.025.

Peter A. Bandettini. Twenty years of functional mri: the science and the stories. *Neuroimage*, 62(2):575–588, Aug 2012. doi: 10.1016/j.neuroimage.2012.04.026. URL http://dx.doi.org/10.1016/j.neuroimage.2012.04.026.

P. J. Basser. Cable equation for a myelinated axon derived from its microstructure. *Med Biol Eng Comput*, 31 Suppl:S87–S92, Jul 1993.

P. J. Basser, J. Mattiello, and D. LeBihan. Estimation of the effective self-diffusion tensor from the nmr spin echo. *J Magn Reson B*, 103(3):247–254, Mar 1994.

P. J. Basser, S. Pajevic, C. Pierpaoli, J. Duda, and A. Aldroubi. In vivo fiber tractography using dt-mri data. *Magn Reson Med*, 44(4):625–632, Oct 2000.

Peter J Basser and Evren Özarslan. Chapter 1 - Introduction to Diffusion {MR}. In Heidi Johansen-Berg and Timothy E J Behrens, editors, *Diffusion {MRI}*, pages 2–10. Academic Press, San Diego, 2009. ISBN 978-0-12-374709-9. doi: http://dx.doi.org/10.1016/B978-0-12-374709-9.00001-8. URL http://www.sciencedirect.com/science/article/pii/B9780123747099000018.

Mark Bear, Barry Connors, Michael Paradiso, Mark F. Bear, Barry W. Connors, and Michael A. Paradiso. *Neuroscience: Exploring the Brain (Book with CD-ROM)*. Lippincott Williams & Wilkins, 2002. ISBN 0781739446. URL http://www.amazon.com/Neuroscience-Exploring-Brain-Book-CD-ROM/dp/0781739446%3FSubscriptionId%3D0JYN1NVW651KCA56C102%26tag%3Dtechkie-20%26linkCode%3Dxm2%26camp%3D2025%26creative%3D165953%26creativeASIN%3D0781739446.

Christian Beaulieu. The basis of anisotropic water diffusion in the nervous system - a technical review. *NMR Biomed*, 15(7-8):435–455, 2002. doi: 10.1002/nbm.782. URL http://dx.doi.org/10.1002/nbm.782.

M. Faisal Beg, Michael I. Miller, Alain Trouvé, and Laurent Younes. Computing large deformation metric mappings via geodesic flows of diffeomorphisms. *IJCV*, 61(2):139–157, 2005-02-01. ISSN 0920-5691.

M.Faisal Beg, MichaelI. Miller, Alain Trouvé, and Laurent Younes. Computing large deformation metric mappings via geodesic flows of diffeomorphisms. *International Journal of Computer Vision*, 61(2):139–157, 2005. ISSN 0920-5691. doi: 10.1023/B:VISI.0000043755.93987.aa. URL http://dx.doi.org/10.1023/B%3AVISI.0000043755.93987.aa.

T. E J Behrens, M. W. Woolrich, M. Jenkinson, H. Johansen-Berg, R. G. Nunes, S. Clare, P. M. Matthews, J. M. Brady, and S. M. Smith. Characterization and propagation of uncertainty in diffusion-weighted mr imaging. *Magn Reson Med*, 50(5):1077–1088, Nov 2003. doi: 10.1002/mrm.10609. URL http://dx.doi.org/10.1002/mrm.10609.

Sara L Bengtsson, Zoltán Nagy, Stefan Skare, Lea Forsman, Hans Forssberg, and Fredrik Ullén. Extensive piano practicing has regionally specific effects on white matter development. *Nat Neurosci*, 8(9):1148–1150, Sep 2005. doi: 10.1038/nn1516. URL http://dx.doi.org/10.1038/nn1516.

Andreas Biesdorf, Stefan Wörz, Hans-Jürgen Kaiser, Christoph Stippich, and Karl Rohr. Hybrid spline-based multimodal registration using local measures for joint entropy and mutual information. *Med Image Comput Comput Assist Interv*, 12(Pt 1):607–615, 2009.

D. Le Bihan, E. Breton, D. Lallemand, P. Grenier, E. Cabanis, and M. Laval-Jeantet. Mr imaging of intravoxel incoherent motions: application to diffusion and perfusion in neurologic disorders. *Radiology*, 161(2):401–407, Nov 1986. doi: 10.1148/radiology.161.2.3763909. URL http://dx.doi.org/10.1148/radiology.161.2.3763909.

D. Le Bihan, J. F. Mangin, C. Poupon, C. A. Clark, S. Pappata, N. Molko, and H. Chabriat. Diffusion tensor imaging: concepts and applications. *J Magn Reson Imaging*, 13(4):534–546, Apr 2001.

Martin Braun. Review: V. i. arnold, ordinary differential equations. *Bulletin (New Series) of the American Mathematical Society*, 2(3):514–522, 05 1980. URL http://projecteuclid.org/euclid.bams/1183546372.

Paul Broca. Remarks on the seat of the faculty of articulated language,following an observation of aphemia (loss of speech). *Bulletin de la Société Anatomique*, pages 330–357, 1861.

K. Brodmann. Beitrage zur histologischen lokalisation der grosshirnrinde. iii. die rindenfelder der niederen affen. *J. Psychol. Neurol.*, 4:177–226, 1905.

Chaim Broit. *Optimal Registration of Deformed Images*. PhD thesis, Philadelphia, PA, USA, 1981. AAI8207933.

Lisa Gottesfeld Brown. A survey of image registration techniques. *ACM Computing Surveys*, 24:325–376, 1992.

Robert Brown. XXVII. A brief account of microscopical observations made in the months of June, July and August 1827, on the particles contained in the pollen of plants; and on the general existence of active molecules in organic and inorganic bodies. *Philosophical Magazine Series 2*, 4(21):161–173, 1828. doi: 10.1080/14786442808674769. URL http://dx.doi.org/10.1080/14786442808674769.

John C. Carter, Diane C. Lanham, Laurie E. Cutting, Amy M. Clements-Stephens, Xuejing Chen, Muhamed Hadzipasic, Joon Kim, Martha B. Denckla, and Walter E. Kaufmann. A dual dti approach to analyzing white matter in children with dyslexia. *Psychiatry Res*, 172 (3):215–219, Jun 2009. doi: 10.1016/j.pscychresns.2008.09.005. URL http://dx.doi.org/10.1016/j.pscychresns.2008.09.005.

DavidM. Cash, Andrew Melbourne, Marc Modat, M.Jorge Cardoso, MatthewJ. Clarkson, NickC. Fox, and Sebastien Ourselin. Cortical folding analysis on patients with alzheimer's disease and mild cognitive impairment. In Nicholas Ayache, Hervé Delingette, Polina Golland, and Kensaku Mori, editors, *Medical Image Computing and Computer-Assisted Intervention – MICCAI 2012*, volume 7512 of *Lecture Notes in Computer Science*, pages 289–296. Springer Berlin Heidelberg, 2012. ISBN 978-3-642-33453-5. doi: 10.1007/978-3-642-33454-2_36. URL http://dx.doi.org/10.1007/978-3-642-33454-2_36.

Mara Cercignani, Roland Bammer, Maria P Sormani, Franz Fazekas, and Massimo Filippi. Inter-sequence and inter-imaging unit variability of diffusion tensor mr imaging histogram-derived metrics of the brain in healthy volunteers. *AJNR Am J Neuroradiol*, 24(4):638–643, Apr 2003.

Meena Chintamaneni and Manju Bhaskar. Biomarkers in alzheimer's disease: a review. *ISRN Pharmacol*, 2012:984786, 2012. doi: 10.5402/2012/984786. URL http://dx.doi.org/10.5402/2012/984786.

G.E. Christensen, R.D. Rabbitt, and M.I. Miller. Deformable templates using large deformation kinematics. *Image Processing, IEEE Transactions on*, 5(10):1435–1447, 1996. ISSN 1057-7149. doi: 10.1109/83.536892.

D. L. Collins, P. Neelin, T. M. Peters, and A. C. Evans. Automatic 3d intersubject registration of mr volumetric data in standardized talairach space. *J Comput Assist Tomogr*, 18(2):192–205, 1994.

D.L. Collins, G. Goualher, R. Venugopal, A. Caramanos, A.C. Evans, and C. Barillot. Cortical constraints for non-linear cortical registration. In KarlHeinz Höhne and Ron Kikinis, editors, *Visualization in Biomedical Computing*, volume 1131 of *Lecture Notes in Computer Science*, pages 307–316. Springer Berlin Heidelberg, 1996. ISBN 978-3-540-61649-8. doi: 10.1007/BFb0046968. URL http://dx.doi.org/10.1007/BFb0046968.

Isabelle Corouge and Christian Barillot. Statistical modeling of pairs of sulci in the context of neuroimaging probabilistic atlas. In Takeyoshi Dohi and Ron Kikinis, editors, *Medical Image Computing and Computer-Assisted Intervention — MICCAI 2002*, volume 2489 of *Lecture Notes in Computer Science*, pages 655–662. Springer Berlin Heidelberg, 2002. ISBN 978-3-540-44225-7. doi: 10.1007/3-540-45787-9_82. URL http://dx.doi.org/10.1007/3-540-45787-9_82.

Jérôme Declerck, Jacques Feldmar, Michael L. Goris, and Fabienne Betting. Automatic registration and alignment on a template of cardiac stress & rest SPECT reoriented images. *IEEE Transactions on Medical Imaging*, 16(6):727–737, 1997. doi: 10.1109/42.650870. URL http://hal.inria.fr/inria-00615069.

J Dejerine. Anatomie des centres nerveux. *Rueff et Cie, Paris*, page Vol. 1, 1901.

J Dejerine. Anatomie des centres nerveux. *Rueff et Cie, Paris*, page Vol. 1, 1985.

Maxime Descoteaux. *High Angular Resolution Diffusion MRI: From Local Estimation to Segmentation and Tractography*. PhD thesis, Universite de Nice - Sophia Antipolis, 2008.

Maxime Descoteaux and Rachid Deriche. Segmentation of q-ball images using statistical surface evolution. *Med Image Comput Comput Assist Interv*, 10(Pt 2):769–776, 2007.

Marjorie Dole, Fanny Meunier, and Michel Hoen. Gray and white matter distribution in dyslexia: A vbm study of superior temporal gyrus asymmetry. *PLoS ONE*, 8(10):e76823, 10 2013. doi: 10.1371/journal.pone.0076823. URL http://dx.doi.org/10.1371%2Fjournal.pone.0076823.

M. Doran, J. V. Hajnal, N. Van Bruggen, M. D. King, I. R. Young, and G. M. Bydder. Normal and abnormal white matter tracts shown by mr imaging using directional diffusion weighted sequences. *J Comput Assist Tomogr*, 14(6):865–873, 1990.

P. Douek, R. Turner, J. Pekar, N. Patronas, and D. Le Bihan. Mr color mapping of myelin fiber orientation. *J Comput Assist Tomogr*, 15(6):923–929, 1991.

Joenna Driemeyer, Janina Boyke, Christian Gaser, Christian Büchel, and Arne May. Changes in gray matter induced by learning–revisited. *PLoS One*, 3(7):e2669, 2008. doi: 10.1371/journal.pone.0002669. URL http://dx.doi.org/10.1371/journal.pone.0002669.

Paul Dupuis and Ulf Grenander. Variational problems on flows of diffeomorphisms for image matching. *Q. Appl. Math.*, LVI(3):587–600, September 1998. ISSN 0033-569X. URL http://dl.acm.org/citation.cfm?id=298828.298844.

Stanley Durrleman, Xavier Pennec, Alain Trouvé, and Nicholas Ayache. Measuring brain variability via sulcal lines registration: a diffeomorphic approach. In *IN: PROC. MICCAI. VOLUME 4791 OF LNCS*, pages 675–682. Springer, 2007.

Stanley Durrleman, Pierre Fillard, Xavier Pennec, Alain Trouvé, and Nicholas Ayache. Registration, atlas estimation and variability analysis of white matter fiber bundles modeled as currents. *NeuroImage*, 55(3):1073–1090, 2011. ISSN 1053-8119.

A. Einstein. Über die von der molekularkinetischen Theorie der Wärme geforderte Bewegung von in ruhenden Flüssigkeiten suspendierten Teilchen. *Annalen der Physik*, 322:549–560, 1905. doi: 10.1002/andp.19053220806.

A. Einstein. Investigations of the theory of brownian movement. *Dover Publications Inc.*, 1956.

A.C. Evans, D.L. Collins, S. R. Mills, E. D. Brown, R. L. Kelly, and T.M. Peters. 3d statistical neuroanatomical models from 305 mri volumes. In *Nuclear Science Symposium and Medical Imaging Conference, 1993., 1993 IEEE Conference Record.*, pages 1813–1817 vol.3, Oct 1993. doi: 10.1109/NSSMIC.1993.373602.

Andreia V Faria, Suresh E Joel, Yajing Zhang, Kenichi Oishi, Peter C M van Zjil, Michael I Miller, James J Pekar, and Susumu Mori. Atlas-based analysis of resting-state functional connectivity: Evaluation for reproducibility and multi-modal anatomy–function correlation studies. *NeuroImage*, 61(3):613–621, 2012. ISSN 1053-8119. doi: http://dx.doi.org/10.1016/j.neuroimage.2012.03.078. URL http://www.sciencedirect.com/science/article/pii/S1053811912003667.

Adolf Fick. Ueber Diffusion. *Annalen der Physik*, 170(1):59–86, 1855. ISSN 1521-3889. doi: 10.1002/andp.18551700105. URL http://dx.doi.org/10.1002/andp.18551700105.

P. Fillard, X. Pennec, V. Arsigny, and N. Ayache. Clinical DT-MRI estimation, smoothing and fiber tracking with log-Euclidean metrics. *IEEE Trans Med Imaging*, 26(11):1472–1482, 2007a. ISSN 0278-0062.

Pierre Fillard. *Riemannian Processing of Tensors for Diffusion MRI and Computational Anatomy of the Brain*. PhD thesis, University of Nice-Sophia Antipolis, France, 2008.

Pierre Fillard, Vincent Arsigny, Xavier Pennec, Kiralee M Hayashi, Paul M Thompson, and Nicholas Ayache. Measuring brain variability by extrapolating sparse tensor fields measured on sulcal lines. *Neuroimage*, 34(2):639–650, Jan 2007b. doi: 10.1016/j.neuroimage.2006.09.027. URL http://dx.doi.org/10.1016/j.neuroimage.2006.09.027.

Pierre Fillard, Xavier Pennec, Vincent Arsigny, and Nicholas Ayache. Clinical dt-mri estimation, smoothing, and fiber tracking with log-euclidean metrics. *IEEE Trans Med Imaging*, 26(11): 1472–1482, Nov 2007c. doi: 10.1109/TMI.2007.899173. URL http://dx.doi.org/10.1109/TMI.2007.899173.

Aaron Filler. Magnetic resonance neurography and diffusion tensor imaging: origins, history, and clinical impact of the first 50,000 cases with an assessment of efficacy and utility in a prospective 5000-patient study group. *Neurosurgery*, 65(SUPPLEMENT):A29–A43, Oct 2009. ISSN 0148-396X. doi: 10.1227/01.neu.0000351279.78110.00. URL http://dx.doi.org/10.1227/01.NEU.0000351279.78110.00.

Bernd Fischer and Jan Modersitzki. Curvature based image registration. *Journal of Mathematical Imaging and Vision*, 18(1):81–85, 2003. ISSN 0924-9907. doi: 10.1023/A:1021897212261. URL http://dx.doi.org/10.1023/A%3A1021897212261.

Bernd Fischer and Jan Modersitzki. A unified approach to fast image registration and a new curvature based registration technique. *Linear Algebra and its Applications*, 380(0):107 – 124, 2004. ISSN 0024-3795. doi: http://dx.doi.org/10.1016/j.laa.2003.10.021. URL http://www.sciencedirect.com/science/article/pii/S0024379503008115.

C. Fowlkes, S. Belongie, Fan Chung, and J. Malik. Spectral grouping using the nystrom method. *Pattern Analysis and Machine Intelligence, IEEE Transactions on*, 26(2):214–225, 2004. ISSN 0162-8828. doi: 10.1109/TPAMI.2004.1262185.

Eleftherios Garyfallidis, Matthew Brett, Marta Morgado Correia, Guy B. Williams, and Ian Nimmo-Smith. Quickbundles, a method for tractography simplification. *Frontiers in Neuroscience*, 6(175), 2012.

Bao Ge, Lei Guo, Tuo Zhang, Xintao Hu, Junwei Han, and Tianming Liu. Resting state fmri-guided fiber clustering: Methods and applications. *Neuroinformatics*, 11(1):119–133, 2013.

Joan Glaunès, Anqi Qiu, Michael Miller, and Laurent Younes. Large deformation diffeomorphic metric curve mapping. *IJCV*, 80:317–336, 2008. ISSN 0920-5691. 10.1007/s11263-008-0141-9.

Joan Glaunès, Marc Vaillant, and MichaelI. Miller. Landmark matching via large deformation diffeomorphisms on the sphere. *Journal of Mathematical Imaging and Vision*, 20(1-2):179–200, 2004. ISSN 0924-9907. doi: 10.1023/B:JMIV.0000011323.32914.f3. URL http://dx.doi.org/10.1023/B%3AJMIV.0000011323.32914.f3.

James F Glockner, Houchun H Hu, David W Stanley, Lisa Angelos, and Kevin King. Parallel mr imaging: a user's guide. *Radiographics*, 25(5):1279–1297, 2005. doi: 10.1148/rg.255045202. URL http://dx.doi.org/10.1148/rg.255045202.

C. D. Good, I. S. Johnsrude, J. Ashburner, R. N. Henson, K. J. Friston, and R. S. Frackowiak. A voxel-based morphometric study of ageing in 465 normal adult human brains. *Neuroimage*, 14 (1 Pt 1):21–36, Jul 2001. doi: 10.1006/nimg.2001.0786. URL http://dx.doi.org/10.1006/nimg.2001.0786.

G. Le Goualher, E. Procyk, D. L. Collins, R. Venugopal, C. Barillot, and A. C. Evans. Automated extraction and variability analysis of sulcal neuroanatomy. *IEEE Trans Med Imaging*, 18(3): 206–217, Mar 1999. doi: 10.1109/42.764891. URL http://dx.doi.org/10.1109/42.764891.

George Le Goualher, Christian Barillot, and Yves Bizais. Modeling cortical sulci with active ribbons. *International Journal of Pattern Recognition and Artificial Intelligence*, 11(08):1295–1315, 1997. doi: 10.1142/S0218001497000603. URL http://www.worldscientific.com/doi/abs/10.1142/S0218001497000603.

Georges Goualher, D.Louis Collins, Christian Barillot, and AlanC. Evans. Automatic identificaiton of cortical sulci using a 3d probabilistic atlas. In WilliamM. Wells, Alan Colchester, and Scott Delp, editors, *Medical Image Computing and Computer-Assisted Intervention — MICCAI'98*, volume 1496 of *Lecture Notes in Computer Science*, pages 509–518. Springer Berlin Heidelberg, 1998. ISBN 978-3-540-65136-9. doi: 10.1007/BFb0056236. URL http://dx.doi.org/10.1007/BFb0056236.

Henry Gray and Henry Vandyke Carter. *Anatomy Descriptive and Surgical*. London: John W. Parker and Son, 2002.

C.G. Gross. Early history of neuroscience. *Encyclopedia of Neuroscience*, pages 843–846, 1987.

P. Guevara, C. Poupon, D. Riviére, Y. Cointepas, M. Descoteaux, B. Thirion, and J-F. Mangin. Robust clustering of massive tractography datasets. *Neuroimage*, 54(3):1975–1993, 2011.

Pamela Guevara. *Inference of a human brain [U+FB01]ber bundle atlas from high angular resolution diffusion imaging*. PhD thesis, Universite de Paris-Sud, Orsay, France, 2008.

Pamela Guevara et al. Automatic fiber bundle segmentation in massive tractography datasets using a multi-subject bundle atlas. *NeuroImage*, 61(4):1083–1099, 2012.

Linh K. Ha, Marcel Prastawa, Guido Gerig, John H. Gilmore, Cláudio T. Silva, and Sarang C. Joshi. Image registration driven by combined probabilistic and geometric descriptors. In *MICCAI*, pages 602–609, 2010.

Jacques Hadamard. *Lectures on Cauchy's Problem in Linear Partial Differential Equations (Dover Phoenix Editions)*. Dover Publications, 2003. ISBN 0486495493. URL http://www.amazon.com/Lectures-Cauchys-Differential-Equations-Editions/dp/0486495493%3FSubscriptionId%3D0JYN1NVW651KCA56C102%26tag%3Dtechkie-20%26linkCode%3Dxm2%26camp%3D2025%26creative%3D165953%26creativeASIN%3D0486495493.

P. Hagmann, J-P. Thiran, L. Jonasson, P. Vandergheynst, S. Clarke, P. Maeder, and R. Meuli. Dti mapping of human brain connectivity: statistical fibre tracking and virtual dissection. *Neuroimage*, 19(3):545–554, Jul 2003.

Patric Hagmann, Lisa Jonasson, Philippe Maeder, Jean-Philippe Thiran, Van J Wedeen, and Reto Meuli. Understanding diffusion mr imaging techniques: from scalar diffusion-weighted imaging to diffusion tensor imaging and beyond. *Radiographics*, 26 Suppl 1:S205–S223, Oct 2006. doi: 10.1148/rg.26si065510. URL http://dx.doi.org/10.1148/rg.26si065510.

H. Hampel, S. J. Teipel, G. E. Alexander, B. Horwitz, D. Teichberg, M. B. Schapiro, and S. I. Rapoport. Corpus callosum atrophy is a possible indicator of region- and cell type-specific neuronal degeneration in alzheimer disease: a magnetic resonance imaging analysis. *Arch Neurol*, 55(2):193–198, Feb 1998.

P. Hellier, J. Ashburner, I. Corouge, C. Barillot, and K.J. Friston. Inter-subject registration of functional and anatomical data using spm. In Takeyoshi Dohi and Ron Kikinis, editors, *Medical Image Computing and Computer-Assisted Intervention — MICCAI 2002*, volume 2489 of *Lecture Notes in Computer Science*, pages 590–597. Springer Berlin Heidelberg, 2002. ISBN 978-3-540-44225-7. doi: 10.1007/3-540-45787-9_74. URL http://dx.doi.org/10.1007/3-540-45787-9_74.

J. R. Highley, M. M. Esiri, B. McDonald, M. Cortina-Borja, B. M. Herron, and T. J. Crow. The size and fibre composition of the corpus callosum with respect to gender and schizophrenia: a post-mortem study. *Brain*, 122 (Pt 1):99–110, Jan 1999.

M. Holden. A review of geometric transformations for nonrigid body registration. *Medical Imaging, IEEE Transactions on*, 27(1):111–128, 2008. ISSN 0278-0062. doi: 10.1109/TMI.2007.904691.

Mark A Horsfield and Derek K Jones. Applications of diffusion-weighted and diffusion tensor mri to white matter diseases - a review. *NMR Biomed*, 15(7-8):570–577, 2002. doi: 10.1002/nbm.787. URL http://dx.doi.org/10.1002/nbm.787.

Scott A. Huettel, Allen W. Song, and Gregory McCarthy. *Functional Magnetic Resonance Imaging, Second Edition*. Sinauer Associates, 2008. ISBN 0878932860. URL http://www.amazon.com/Functional-Magnetic-Resonance-Imaging-Edition/dp/0878932860%3FSubscriptionId%3D0JYN1NVW651KCA56C102%26tag%3Dtechkie-20%26linkCode%3Dxm2%26camp%3D2025%26creative%3D165953%26creativeASIN%3D0878932860.

Guillaume Janssens, Laurent Jacques, Jonathan Orban de Xivry, Xavier Geets, and Benoit Macq. Diffeomorphic registration of images with variable contrast enhancement. *Int J Biomed Imaging*, 2011:891585, 2011. doi: 10.1155/2011/891585. URL http://dx.doi.org/10.1155/2011/891585.

Brian J. Jellison, Aaron S. Field, Joshua Medow, Mariana Lazar, M Shariar Salamat, and Andrew L. Alexander. Diffusion tensor imaging of cerebral white matter: a pictorial review of physics, fiber tract anatomy, and tumor imaging patterns. *AJNR Am J Neuroradiol*, 25(3):356–369, Mar 2004.

P. Jezzard, A. S. Barnett, and C. Pierpaoli. Characterization of and correction for eddy current artifacts in echo planar diffusion imaging. *Magn Reson Med*, 39(5):801–812, May 1998.

Johansen-Berg and Behrens. Diffusion MRI: From quantitative measurement to in-vivo neuroanatomy. Academic Press, 2009. URL http://www.amazon.com/Diffusion-MRI-quantitative-vivo-neuroanatomy-ebook/dp/B002ZJSVBY%3FSubscriptionId%3D0JYN1NVW651KCA56C102%26tag%3Dtechkie-20%26linkCode%3Dxm2%26camp%3D2025%26creative%3D165953%26creativeASIN%3DB002ZJSVBY.

Derek Kenton Jones, Steve Charles Rees Williams, David Gasston, Mark Andrew Horsfield, Andrew Simmons, and Robert Howard. Isotropic resolution diffusion tensor imaging with whole brain acquisition in a clinically acceptable time. *Hum Brain Mapp*, 15(4):216–230, Apr 2002.

Mark H Khachaturian, Jonathan J Wisco, and David S Tuch. Boosting the sampling efficiency of q-ball imaging using multiple wavevector fusion. *Magn Reson Med*, 57(2):289–296, Feb 2007. doi: 10.1002/mrm.21090. URL http://dx.doi.org/10.1002/mrm.21090.

Jeongtae Kim and J.A. Fessler. Intensity-based image registration using robust correlation coefficients. *Medical Imaging, IEEE Transactions on*, 23(11):1430–1444, 2004. ISSN 0278-0062. doi: 10.1109/TMI.2004.835313.

T. Klingberg, M. Hedehus, E. Temple, T. Salz, J. D. Gabrieli, M. E. Moseley, and R. A. Poldrack. Microstructure of temporo-parietal white matter as a basis for reading ability: evidence from diffusion tensor magnetic resonance imaging. *Neuron*, 25(2):493–500, Feb 2000.

ZegerF. Knops, J.B.A. Maintz, M.A. Viergever, and J.P.W. Pluim. Registration using segment intensity remapping and mutual information. In Christian Barillot, DavidR. Haynor, and Pierre Hellier, editors, *Medical Image Computing and Computer-Assisted Intervention – MICCAI 2004*, volume 3216 of *Lecture Notes in Computer Science*, pages 805–812. Springer Berlin Heidelberg, 2004. ISBN 978-3-540-22976-6. doi: 10.1007/978-3-540-30135-6_98. URL http://dx.doi.org/10.1007/978-3-540-30135-6_98.

J. L. Lancaster, M. G. Woldorff, L. M. Parsons, M. Liotti, C. S. Freitas, L. Rainey, P. V. Kochunov, D. Nickerson, S. A. Mikiten, and P. T. Fox. Automated talairach atlas labels for functional brain mapping. *Hum Brain Mapp*, 10(3):120–131, Jul 2000.

D Lebihan and E Breton. Imagerie de Diffusion In Vivo par Résonance Magnétique Nucléaire. *XXX CR Académie des Sciences de Paris*, 301:1109–1112, 1985.

D. Lemoine, C. Barillot, B. Gibaud, and E. Pasqualini. An anatomical-based 3d registration system of multimodality and atlas data in neurosurgery. In AlanC.F. Colchester and DavidJ. Hawkes, editors, *Information Processing in Medical Imaging*, volume 511 of *Lecture Notes in Computer Science*, pages 154–164. Springer Berlin Heidelberg, 1991. ISBN 978-3-540-54246-9. doi: 10.1007/BFb0033750. URL http://dx.doi.org/10.1007/BFb0033750.

Christophe Lenglet, Mikaël Rousson, Rachid Deriche, and Olivier Faugeras. Statistics on the manifold of multivariate normal distributions: Theory and application to diffusion tensor mri processing. *Journal of Mathematical Imaging and Vision*, 25(3):423–444, 2006. ISSN 0924-9907. doi: 10.1007/s10851-006-6897-z. URL http://dx.doi.org/10.1007/s10851-006-6897-z.

F. Lepore, C. Brun, Yi-Yu Chou, Ming-Chang Chiang, R.A. Dutton, K.M. Hayashi, E. Luders, O.L. Lopez, H.J. Aizenstein, A.W. Toga, J.T. Becker, and P.M. Thompson. Generalized tensor-based morphometry of hiv/aids using multivariate statistics on deformation tensors. *Medical Imaging, IEEE Transactions on*, 27(1):129–141, Jan 2008a. ISSN 0278-0062. doi: 10.1109/TMI.2007.906091.

F. Lepore, C. Brun, Yi-Yu Chou, A.D. Lee, M. Barysheva, X. Pennec, K.L. McMahon, M. Meredith, G.I. de Zubicaray, M.J. Wright, A.W. Toga, and P.M. Thompson. Best individual template selection from deformation tensor minimization. In *Biomedical Imaging: From Nano to Macro, 2008. ISBI 2008. 5th IEEE International Symposium on*, pages 460–463, May 2008b. doi: 10.1109/ISBI.2008.4541032.

Natasha Leporé, Patrice Voss, Franco Lepore, Yi-Yu Chou, Madeleine Fortin, Frédéric Gougoux, Agatha D Lee, Caroline Brun, Maryse Lassonde, Sarah K Madsen, Arthur W Toga, and Paul M Thompson. Brain structure changes visualized in early- and late-onset blind subjects. *NeuroImage*, 49(1):134–140, 2010. ISSN 1053-8119. doi: http://dx.doi.org/10.1016/j.neuroimage.2009.07.048. URL http://www.sciencedirect.com/science/article/pii/S1053811909008167.

Yang Li, Yaping Wang, Guorong Wu, Feng Shi, Luping Zhou, Weili Lin, Dinggang Shen, and Alzheimer's Disease Neuroimaging Initiative . Discriminant analysis of longitudinal cortical thickness changes in alzheimer's disease using dynamic and network features. *Neurobiol Aging*, 33(2):427.e15–427.e30, Feb 2012.

Tony Lindeberg. Feature detection with automatic scale selection. *International Journal of Computer Vision*, 30(2):79–116, 1998. ISSN 0920-5691. doi: 10.1023/A:1008045108935. URL http://dx.doi.org/10.1023/A%3A1008045108935.

Marco Lorenzi, Nicholas Ayache, and Xavier Pennec. Regional flux analysis of longitudinal atrophy in alzheimer's disease. In Nicholas Ayache, Hervé Delingette, Polina Golland, and Kensaku Mori, editors, *MICCAI (1)*, volume 7510 of *Lecture Notes in Computer Science*, pages 739–746. Springer, 2012. ISBN 978-3-642-33414-6.

David J. C. MacKay. *Information Theory, Inference and Learning Algorithms*. Cambridge University Press, 2003. ISBN 0521642981. URL http://www.amazon.com/Information-Theory-Inference-Learning-Algorithms/dp/0521642981%3FSubscriptionId%3D0JYN1NVW651KCA56C102%26tag%3Dtechkie-20%26linkCode%3Dxm2%26camp%3D2025%26creative%3D165953%26creativeASIN%3D0521642981.

J. MacQueen. Some methods for classification and analysis of multivariate observations. pages 281–297, 1967. URL http://projecteuclid.org/euclid.bsmsp/1200512992.

K. Madsen, H. B. Nielsen, and O. Tingleff. Methods for non-linear least squares problems (2nd ed.). page 60, 2004. URL http://f.

E. A. Maguire, D. G. Gadian, I. S. Johnsrude, C. D. Good, J. Ashburner, R. S. Frackowiak, and C. D. Frith. Navigation-related structural change in the hippocampi of taxi drivers. *Proc Natl Acad Sci U S A*, 97(8):4398–4403, Apr 2000. doi: 10.1073/pnas.070039597. URL http://dx.doi.org/10.1073/pnas.070039597.

Robert Mahony and JonathanH. Manton. The geometry of the newton method on non-compact lie groups. *Journal of Global Optimization*, 23(3-4):309–327, 2002. ISSN 0925-5001. doi: 10.1023/A:1016586831090. URL http://dx.doi.org/10.1023/A%3A1016586831090.

J.-F. Mangin, D Rivière, A Cachia, E Duchesnay, Y Cointepas, D Papadopoulos-Orfanos, P Scifo, T Ochiai, F Brunelle, and J Régis. A framework to study the cortical folding patterns. *NeuroImage*, 23, Supplement 1(0):S129 – S138, 2004. ISSN 1053-8119. doi: http://dx.doi.org/10.1016/j.neuroimage.2004.07.019. URL http://www.sciencedirect.com/science/article/pii/S1053811904003854.

M. Mani, S. Kurtek, C. Barillot, and A. Srivastava. A comprehensive riemannian framework for the analysis of white matter fiber tracts. In *Biomedical Imaging: From Nano to Macro, 2010 IEEE International Symposium on*, pages 1101–1104, April 2010a. doi: 10.1109/ISBI.2010.5490185.

Meena Mani, Sebastian Kurtek, Christian Barillot, and Anuj Srivastava. A comprehensive riemannian framework for the analysis of white matter fiber tracts. In *ISBI*, pages 1101–1104. IEEE, 2010b. ISBN 978-1-4244-4125-9.

Linda Marrakchi-Kacem, Cyril Poupon, Jean-Francois Mangin, and Fabrice Poupon. Multi-contrast deep nuclei segmentation using a probabilistic atlas. *2010 IEEE International Symposium on Biomedical Imaging: From Nano to Macro*, 2012. doi: 10.1109/isbi.2010.5490415. URL http://dx.doi.org/10.1109/ISBI.2010.5490415.

Arnaldo Mayer, Gali Zimmerman-Moreno, Ran Shadmi, Amit Batikoff, and Hayit Greenspan. A supervised framework for the registration and segmentation of white matter fiber tracts. *IEEE Trans Med Imaging*, 30(1):131–145, Jan 2011. doi: 10.1109/TMI.2010.2067222. URL http://dx.doi.org/10.1109/TMI.2010.2067222.

J. C. Mazziotta, A. W. Toga, A. Evans, P. Fox, and J. Lancaster. A probabilistic atlas of the human brain: theory and rationale for its development. the international consortium for brain mapping (icbm). *Neuroimage*, 2(2):89–101, Jun 1995.

Matthew McCormick, Xiaoxiao Liu, Julien Jomier, Charles Marion, and Luis Ibanez. Itk: enabling reproducible research and open science. *Front Neuroinform*, 8(13), 02 2014.

K.-D. Merboldt, W. Hanicke, and J. Frahm. Self-diffusion NMR imaging using stimulated echoes. *Journal of Magnetic Resonance*, 64:479–486, 1985. doi: 10.1016/0022-2364(85)90111-8.

Michael I. Miller, Alain Trouve, and Laurent Younes. On the metrics and euler-lagrange equations of computational anatomy. *Annu Rev Biomed Eng*, 4:375–405, 2002. doi: 10.1146/annurev.bioeng.4.092101.125733. URL http://dx.doi.org/10.1146/annurev.bioeng.4.092101.125733.

Bart Moberts et al. Evaluation of fiber clustering methods for diffusion tensor imaging. In *In IEEE Transactions on VCS*, page 9, 2005.

Siawoosh Mohammadi, Simon S Keller, Volkmar Glauche, Harald Kugel, Andreas Jansen, Chloe Hutton, Agnes Flöel, and Michael Deppe. The influence of spatial registration on detection of cerebral asymmetries using voxel-based statistics of fractional anisotropy images and tbss. *PLoS One*, 7(6):e36851, 2012. doi: 10.1371/journal.pone.0036851. URL http://dx.doi.org/10.1371/journal.pone.0036851.

Nicolas Molko, Arnaud Cachia, Denis Rivière, Jean-François Mangin, Marie Bruandet, Denis Le Bihan, Laurent Cohen, and Stanislas Dehaene. Functional and Structural Alterations of the Intraparietal Sulcus in a Developmental Dyscalculia of Genetic Origin. *Neuron*, 40(4):847–858, 2003. ISSN 0896-6273. doi: http://dx.doi.org/10.1016/S0896-6273(03)00670-6. URL http://www.sciencedirect.com/science/article/pii/S0896627303006706.

S. Mori, B. J. Crain, V. P. Chacko, and P. C. van Zijl. Three-dimensional tracking of axonal projections in the brain by magnetic resonance imaging. *Ann Neurol*, 45(2):265–269, Feb 1999.

Susumu Mori and Peter C M van Zijl. Fiber tracking: principles and strategies - a technical review. *NMR Biomed*, 15(7-8):468–480, 2002. doi: 10.1002/nbm.781. URL http://dx.doi.org/10.1002/nbm.781.

J. Bruce Moseley, Kimberly O'Malley, Nancy J Petersen, Terri J Menke, Baruch A Brody, David H Kuykendall, John C Hollingsworth, Carol M Ashton, and Nelda P Wray. A controlled trial of arthroscopic surgery for osteoarthritis of the knee. *N Engl J Med*, 347(2):81–88, Jul 2002. doi: 10.1056/NEJMoa013259. URL http://dx.doi.org/10.1056/NEJMoa013259.

M. E. Moseley, Y. Cohen, J. Kucharczyk, J. Mintorovitch, H. S. Asgari, M. F. Wendland, J. Tsuruda, and D. Norman. Diffusion-weighted mr imaging of anisotropic water diffusion in cat central nervous system. *Radiology*, 176(2):439–445, Aug 1990a. doi: 10.1148/radiology.176.2.2367658. URL http://dx.doi.org/10.1148/radiology.176.2.2367658.

M. E. Moseley, Y. Cohen, J. Kucharczyk, J. Mintorovitch, H. S. Asgari, M. F. Wendland, J. Tsuruda, and D. Norman. Diffusion-weighted mr imaging of anisotropic water diffusion in cat central nervous system. *Radiology*, 176(2):439–445, Aug 1990b. doi: 10.1148/radiology.176.2.2367658. URL http://dx.doi.org/10.1148/radiology.176.2.2367658.

J. Neil, J. Miller, P. Mukherjee, and P. S. Hüppi. Diffusion tensor imaging of normal and injured developing human brain - a technical review. *NMR Biomed*, 15(7-8):543–552, 2002. doi: 10.1002/nbm.784. URL http://dx.doi.org/10.1002/nbm.784.

Bernard Ng, Viviana Siless, Gaël Varoquaux, Jean-Baptiste Poline, Bertrand Thirion, and Rafeef Abugharbieh. Connectivity-informed Sparse Classifiers for fMRI Brain Decoding. In *Pattern Recognition in Neuroimaging*, London, United Kingdom, July 2012. Christos Davatzikos, Moritz Grosse-Wentrup, Janaina Mourao-Miranda, Dimitri Van De Ville. URL http://hal.inria.fr/hal-00726656.

Lauren J O'Donnell, Laura Rigolo, Isaiah Norton, William M Wells, Carl-Fredrik Westin, and Alexandra J Golby. fmri-dti modeling via landmark distance atlases for prediction and detection of fiber tracts. *Neuroimage*, 60(1):456–470, Mar 2012a. doi: 10.1016/j.neuroimage.2011.11.014. URL http://dx.doi.org/10.1016/j.neuroimage.2011.11.014.

Lauren J O'Donnell, William M Wells, Alexandra J Golby, and Carl-Fredrik Westin. Unbiased groupwise registration of white matter tractography. *Med Image Comput Comput Assist Interv*, 15(Pt 3):123–130, 2012b.

Kenichi Oishi, Karl Zilles, Katrin Amunts, Andreia Faria, Hangyi Jiang, Xin Li, Kazi Akhter, Kegang Hua, Roger Woods, Arthur W Toga, G Bruce Pike, Pedro Rosa-Neto, Alan Evans, Jiangyang Zhang, Hao Huang, Michael I Miller, Peter C M van Zijl, John Mazziotta, and Susumu Mori. Human brain white matter atlas: Identification and assignment of common anatomical structures in superficial white matter. *NeuroImage*, 43(3):447–457, 2008. ISSN 1053-8119. doi: http://dx.doi.org/10.1016/j.neuroimage.2008.07.009. URL http://www.sciencedirect.com/science/article/pii/S1053811908008240.

M. Ono, M. Ono, S. Kubik, and C.D. Abernathey. *Atlas of the Cerebral Sulci*. G. Thieme Verlag, 1990. ISBN 9780865773622. URL http://books.google.fr/books?id=xroe986wtkEC.

R. J. Ordidge, J. A. Helpern, Z. X. Qing, R. A. Knight, and V. Nagesh. Correction of motional artifacts in diffusion-weighted mr images using navigator echoes. *Magn Reson Imaging*, 12(3):455–460, 1994.

Hae-Jeong Park, Marek Kubicki, Martha E Shenton, Alexandre Guimond, Robert W McCarley, Stephan E Maier, Ron Kikinis, Ferenc A Jolesz, and Carl-Fredrik Westin. Spatial normalization of diffusion tensor mri using multiple channels. *Neuroimage*, 20(4):1995–2009, Dec 2003.

Hae-Jeong Park, Carl-Fredrik Westin, Marek Kubicki, Stephan E Maier, Margaret Niznikiewicz, Aaron Baer, Melissa Frumin, Ron Kikinis, Ferenc A Jolesz, Robert W McCarley, and Martha E Shenton. White matter hemisphere asymmetries in healthy subjects and in schizophrenia: a diffusion tensor mri study. *Neuroimage*, 23(1):213–223, Sep 2004. doi: 10.1016/j.neuroimage.2004.04.036. URL http://dx.doi.org/10.1016/j.neuroimage.2004.04.036.

Geoffrey J M Parker, Hamied A Haroon, and Claudia A M Wheeler-Kingshott. A framework for a streamline-based probabilistic index of connectivity (pico) using a structural interpretation of mri diffusion measurements. *J Magn Reson Imaging*, 18(2):242–254, Aug 2003. doi: 10.1002/jmri.10350. URL http://dx.doi.org/10.1002/jmri.10350.

F. Pedregosa et al. Scikit-learn: Machine learning in Python. *Journal of Machine Learning Research*, 12:2825–2830, 2011.

Xavier Pennec, Pascal Cachier, and Nicholas Ayache. Understanding the "demon's algorithm": 3d non-rigid registration by gradient descent. In Chris Taylor and Alain Colchester, editors, *Medical Image Computing and Computer-Assisted Intervention – MICCAI'99*, volume 1679 of *Lecture Notes in Computer Science*, pages 597–605. Springer Berlin Heidelberg, 1999. ISBN 978-3-540-66503-8. doi: 10.1007/10704282_64. URL http://dx.doi.org/10.1007/10704282_64.

C. Pierpaoli and P. J. Basser. Toward a quantitative assessment of diffusion anisotropy. *Magn Reson Med*, 36(6):893–906, Dec 1996.

James G. Pipe. Chapter 2 - Pulse Sequences for Diffusion MRI. In Heidi Johansen-Berg and Timothy E J Behrens, editors, *Diffusion {MRI}*. Academic Press, San Diego, 2009. ISBN 978-0-12-374709-9. doi: http://dx.doi.org/10.1016/B978-0-12-374709-9.00001-8.

Robert A. Pooley. Aapm/rsna physics tutorial for residents: fundamental physics of mr imaging. *Radiographics*, 25(4):1087–1099, 2005. doi: 10.1148/rg.254055027. URL http://dx.doi.org/10.1148/rg.254055027.

C. Poupon, Xavier Pennec, Aymeric Perchant, and Nicholas Ayache. A database dedicated to anatomo-functional study of human brain connectivity. In *12th HBM Neuroimage*, number 646, Florence, Italie, 2006.

Cyril Poupon. *Détection des faisceaux de fibres de la substance blanche pour l'étude de la connectivité anatomique cérébrale*. PhD thesis, Ecole Nationale Supérieure des Télécommunications., 1999.

Cyril Poupon. Poupon. Technical report, CEA, NeuroSpin, 2010.

M. E. Raichle, A. W. Toga, and J. C. Mazziotta.

William M Rand. Objective Criteria for the Evaluation of Clustering Methods. *Journal of the American Statistical Association*, 66(336):846–850, 1971. doi: 10.1080/01621459.1971.10482356. URL http://www.tandfonline.com/doi/abs/10.1080/01621459.1971.10482356.

Andrew Rosenberg and Julia Hirschberg. V-measure: A conditional entropy-based external cluster evaluation measure. In *Proceedings of the 2007 Joint Conference on Empirical Methods in Natural Language Processing and Computational Natural Language Learning (EMNLP-CoNLL)*, pages 410–420, 2007. URL http://www.aclweb.org/anthology/D/D07/D07-1043.

Peter J. Rousseeuw. Silhouettes: A graphical aid to the interpretation and validation of cluster analysis. *JCAM*, 20(0):53 – 65, 1987. ISSN 0377-0427.

Daniel Rueckert, Paul Aljabar, Rolf Heckemann, Joseph Hajnal, and Alexander Hammers. Diffeomorphic registration using b-splines. In *LNCS*, volume 4191, pages 702–709. Springer Berlin / Heidelberg, 2006.

Elena Rusconi, Philippe Pinel, Evelyn Eger, Denis LeBihan, Bertrand Thirion, Stanislas Dehaene, and Andreas Kleinschmidt. A disconnection account of gerstmann syndrome: functional neuroanatomy evidence. *Ann Neurol*, 66(5):654–662, Nov 2009. doi: 10.1002/ana.21776. URL http://dx.doi.org/10.1002/ana.21776.

A. Schleicher, N. Palomero-Gallagher, P. Morosan, S.B. Eickhoff, T. Kowalski, K.de Vos, K. Amunts, and K. Zilles. Quantitative architectural analysis: a new approach to cortical mapping. *Anatomy and Embryology*, 210(5-6):373–386, 2005. ISSN 0340-2061. doi: 10.1007/s00429-005-0028-2. URL http://dx.doi.org/10.1007/s00429-005-0028-2.

Peter Schneider, Michael Scherg, H. Günter Dosch, Hans J Specht, Alexander Gutschalk, and André Rupp. Morphology of heschl's gyrus reflects enhanced activation in the auditory cortex of musicians. *Nat Neurosci*, 5(7):688–694, Jul 2002. doi: 10.1038/nn871. URL http://dx.doi.org/10.1038/nn871.

Jan Scholz, Miriam C Klein, Timothy E J Behrens, and Heidi Johansen-Berg. Training induces changes in white-matter architecture. *Nat Neurosci*, 12(11):1370–1371, Nov 2009. doi: 10.1038/nn.2412. URL http://dx.doi.org/10.1038/nn.2412.

Will Schroeder, Ken Martin, and Bill Lorensen. *Visualization Toolkit: An Object-Oriented Approach to 3D Graphics, 4th Edition*. Kitware, 4th edition, 2006. ISBN 193093419X. URL http://www.amazon.com/exec/obidos/redirect?tag=citeulike07-20&path=ASIN/193093419X.

Thomas Schultz, Carl-Fredrik Westin, and Gordon Kindlmann. Multi-diffusion-tensor fitting via spherical deconvolution: a unifying framework. *Med Image Comput Comput Assist Interv*, 13 (Pt 1):674–681, 2010.

D. F. Scollan, A. Holmes, R. Winslow, and J. Forder. Histological validation of myocardial microstructure obtained from diffusion tensor magnetic resonance imaging. *Am J Physiol*, 275 (6 Pt 2):H2308–H2318, Dec 1998.

Michaël Sdika. A fast nonrigid image registration with constraints on the jacobian using large scale constrained optimization. *IEEE Trans. Med. Imaging*, 27(2):271–281, 2008. URL http://dblp.uni-trier.de/db/journals/tmi/tmi27.html#Sdika08.

J. Shi and C. Tomasi. Good features to track. In *Computer Vision and Pattern Recognition, 1994. Proceedings CVPR '94., 1994 IEEE Computer Society Conference on*, pages 593–600, 1994. doi: 10.1109/CVPR.1994.323794.

Viviana Siless, Pamela Guevara, Xavier Pennec, and Pierre Fillard. Joint t1 and brain fiber diffeomorphic registration using the demons. In *MBIA*, LNCS, pages 10–18. Springer. ISBN 978-3-642-24445-2.

Viviana Siless, Sergio Medina, Pierre Fillard, and Bertrand Thirion. Unsupervised fiber bundles registration using weighted measures geometric demons. In Li Shen, Tianming Liu, Pew-Thian Yap, Heng Huang, Dinggang Shen, and Carl-Fredrik Westin, editors, *Multimodal Brain Image Analysis*, volume 8159 of *Lecture Notes in Computer Science*, pages 95–106. Springer International Publishing, 2013. ISBN 978-3-319-02125-6. doi: 10.1007/978-3-319-02126-3_10. URL http://dx.doi.org/10.1007/978-3-319-02126-3_10.

Aristeidis Sotiras, Yangming Ou, Ben Glocker, Christos Davatzikos, and Nikos Paragios. Simultaneous geometric–iconic registration. In *MICCAI*, volume 13, pages 676–683, 2010.

Aristeidis Sotiras, Christos Davatzikos, and Nikos Paragios. Deformable Medical Image Registration: A Survey. Rapport de recherche RR-7919, INRIA, September 2012. URL http://hal.inria.fr/hal-00684715.

A. Stamm, P. Perez, and C. Barillot. A new multi-fiber model for low angular resolution diffusion mri. In *Biomedical Imaging (ISBI), 2012 9th IEEE International Symposium on*, pages 936–939, May 2012. doi: 10.1109/ISBI.2012.6235710.

H Steinhaus. Sur la division des corp materiels en parties. *Bull. Acad. Polon. Sci*, 1:801–804, 1956.

E. O. Stejskal and J. E. Tanner. Spin Diffusion Measurements: Spin Echoes in the Presence of a Time-Dependent Field Gradient. *jcp*, 42:288–292, January 1965. doi: 10.1063/1.1695690.

J. Talairach and G. Szikla. Application of stereotactic concepts to the surgery of epilepsy. In F.John Gillingham, Jan Gybels, Edward Hitchcock, GianFranco Rossi, and Gábor Szikla, editors, *Advances in Stereotactic and Functional Neurosurgery 4*, volume 30 of *Acta Neurochirurgica Supplementum*, pages 35–54. Springer Vienna, 1980. ISBN 978-3-211-81591-5. doi: 10.1007/978-3-7091-8592-6_5. URL http://dx.doi.org/10.1007/978-3-7091-8592-6_5.

J. E. Tanner. Self diffusion of water in frog muscle. *Biophys J*, 28(1):107–116, Oct 1979. doi: 10.1016/S0006-3495(79)85162-0. URL http://dx.doi.org/10.1016/S0006-3495(79)85162-0.

D. G. Taylor and M. C. Bushell. PRELIMINARY COMMUNICATION: The spatial mapping of translational diffusion coefficients by the NMR imaging technique. *Physics in Medicine and Biology*, 30:345–349, April 1985. doi: 10.1088/0031-9155/30/4/009.

J.-P. Thirion. Image matching as a diffusion process: an analogy with Maxwell's demons. *Medical Image Analysis*, 2(3):243–260, September 1998. ISSN 1361-8415.

N Toussaint, J C Souplet, and P Fillard. MedINRIA: Medical Image Navigation and Research Tool by INRIA. In *Proc. of MICCAI'07 Workshop on Interaction in medical image analysis and visualization*, Brisbane, Australia, 2007.

Alain Trouvé. Diffeomorphisms groups and pattern matching in image analysis. *International Journal of Computer Vision*, 28(3):213–221, 1998. ISSN 0920-5691. doi: 10.1023/A:1008001603737. URL http://dx.doi.org/10.1023/A%3A1008001603737.

D. S. Tuch, R. M. Weisskoff, J. W. Belliveau, and V. J. Wedeen. High Angular Resolution Diffusion Imaging of the Human Brain. In *The International Society for Magnetic Resonance in Medicine*, 1999.

David S Tuch. Q-ball imaging. *Magn Reson Med*, 52(6):1358–1372, Dec 2004. doi: 10.1002/mrm.20279. URL http://dx.doi.org/10.1002/mrm.20279.

R. Turner, D. Le Bihan, J. Maier, R. Vavrek, L. K. Hedges, and J. Pekar. Echo-planar imaging of intravoxel incoherent motion. *Radiology*, 177(2):407–414, Nov 1990. doi: 10.1148/radiology.177.2.2217777. URL http://dx.doi.org/10.1148/radiology.177.2.2217777.

Marc Vaillant and Joan Glaunès. Surface matching via currents. In GaryE. Christensen and Milan Sonka, editors, *Information Processing in Medical Imaging*, volume 3565 of *Lecture Notes in Computer Science*, pages 381–392. Springer Berlin Heidelberg, 2005. ISBN 978-3-540-26545-0. doi: 10.1007/11505730_32. URL http://dx.doi.org/10.1007/11505730_32.

Tom Vercauteren, , Xavier Pennec, Aymeric Perchant, and Nicholas Ayache. Symmetric Log-Domain Diffeomorphic Registration: A Demons-Based Approach. In *MICCAI*, volume 5241 of *LNCS*, chapter 90, pages 754–761. 2008. ISBN 978-3-540-85987-1. doi: 10.1007/978-3-540-85988-8_90.

Tom Vercauteren, , Xavier Pennec, Aymeric Perchant, and Nicholas Ayache. Diffeomorphic demons: Efficient non-parametric image registration. *NeuroImage*, 45(1, Sup. 1):S61–S72, 2009. ISSN 1053-8119.

J. Villalon, A.A. Joshi, F. Lepore, C. Brun, A.W. Toga, and P.M. Thompson. Comparison of volumetric registration algorithms for tensor-based morphometry. In *Biomedical Imaging: From Nano to Macro, 2011 IEEE International Symposium on*, pages 1536–1541, March 2011. doi: 10.1109/ISBI.2011.5872694.

A. D. Wagner. Early detection of alzheimer's disease: an fmri marker for people at risk? *Nat Neurosci*, 3(10):973–974, Oct 2000. doi: 10.1038/79904. URL http://dx.doi.org/10.1038/79904.

D. Wassermann, L. Bloy, R. Verma, and R. Deriche. Bayesian framework for white matter fibers similarity measure. In *Biomedical Imaging: From Nano to Macro, 2009. ISBI '09. IEEE International Symposium on*, pages 815–818, June 2009. doi: 10.1109/ISBI.2009.5193174.

D Wassermann, L Bloy, E Kanterakis, R Verma, and R Deriche. Unsupervised white matter fiber clustering and tract probability map generation: Applications of a Gaussian process framework for white matter fibers. *NeuroImage*, 51(1):228–241, 2010a. ISSN 1053-8119. doi: http://dx.doi.org/10.1016/j.neuroimage.2010.01.004. URL http://www.sciencedirect.com/science/article/pii/S1053811910000091.

Demian Wassermann, Efstathios Kanterakis, RubenC. Gur, Rachid Deriche, and Ragini Verma. Diffusion-based population statistics using tract probability maps. In Tianzi Jiang, Nassir Navab, JosienP.W. Pluim, and MaxA. Viergever, editors, *Medical Image Computing and Computer-Assisted Intervention – MICCAI 2010*, volume 6361 of *Lecture Notes in Computer Science*, pages 631–639. Springer Berlin Heidelberg, 2010b. ISBN 978-3-642-15704-2. doi: 10.1007/978-3-642-15705-9_77. URL http://dx.doi.org/10.1007/978-3-642-15705-9_77.

Demian Wassermann, Nikos Makris, Yogesh Rathi, Martha Shenton, Ron Kikinis, Marek Kubicki, and Carl-Fredrik Westin. On describing human white matter anatomy: the white matter query language. *Med Image Comput Comput Assist Interv*, 16(Pt 1):647–654, 2013.

K. E. Watkins, F. Vargha-Khadem, J. Ashburner, R. E. Passingham, A. Connelly, K. J. Friston, R. S J Frackowiak, M. Mishkin, and D. G. Gadian. Mri analysis of an inherited speech and language disorder: structural brain abnormalities. *Brain*, 125(Pt 3):465–478, Mar 2002.

Van J Wedeen, Patric Hagmann, Wen-Yih Isaac Tseng, Timothy G Reese, and Robert M Weisskoff. Mapping complex tissue architecture with diffusion spectrum magnetic resonance imaging. *Magn Reson Med*, 54(6):1377–1386, Dec 2005. doi: 10.1002/mrm.20642. URL http://dx.doi.org/10.1002/mrm.20642.

David Weinstein, Gordon Kindlmann, and Eric Lundberg. Tensorlines: Advection-diffusion based propagation through diffusion tensor fields. In *Proceedings of the Conference on Visualization '99: Celebrating Ten Years*, VIS '99, pages 249–253, Los Alamitos, CA, USA, 1999. IEEE Computer Society Press. ISBN 0-7803-5897-X. URL http://dl.acm.org/citation.cfm?id=319351.319381.

Carl Wernicke. Atlas des gehirns/atlas of the brain; sections of the human brain from photographic originals, following an observation of aphemia (loss of speech). *Schnitte durch das menschliche Gehirn in photographischen Originalen*, 1897.

G. E. Wesbey, M. E. Moseley, and R. L. Ehman. Translational molecular self-diffusion in magnetic resonance imaging. ii. measurement of the self-diffusion coefficient. *Invest Radiol*, 19(6):491–498, 1984.

C-F. Westin, S. E. Maier, H. Mamata, A. Nabavi, F. A. Jolesz, and R. Kikinis. Processing and visualization for diffusion tensor mri. *Med Image Anal*, 6(2):93–108, Jun 2002.

R. Xue, P. C. van Zijl, B. J. Crain, M. Solaiyappan, and S. Mori. In vivo three-dimensional reconstruction of rat brain axonal projections by diffusion tensor imaging. *Magn Reson Med*, 42(6):1123–1127, Dec 1999.

Xuan Yang, Zhong Xue, Xia Liu, and Darong Xiong. Topology preservation evaluation of compact-support radial basis functions for image registration. *Pattern Recognition Letters*, 32 (8):1162 – 1177, 2011. ISSN 0167-8655. doi: http://dx.doi.org/10.1016/j.patrec.2011.03.004. URL http://www.sciencedirect.com/science/article/pii/S0167865511000699.

I.A. Yassine, A.-B.M. Youssef, and Y.M. Kadah. Novel multi-tensor estimation for high-resolution diffusion tensor magnetic resonance imaging. In *Radio Science Conference, 2006. NRSC 2006. Proceedings of the Twenty Third National*, volume 0, pages 1–12, March 2006. doi: 10.1109/NRSC.2006.386386.

Anastasia Yendiki, Patricia Panneck, Priti Srinivasan, Allison Stevens, Lilla Zöllei, Jean Augustinack, Ruopeng Wang, David Salat, Stefan Ehrlich, Tim Behrens, Saad Jbabdi, Randy Gollub, and Bruce Fischl. Automated probabilistic reconstruction of white-matter pathways in health and disease using an atlas of the underlying anatomy. *Frontiers in Neuroinformatics*, 5(23), 2011. ISSN 1662-5196. doi: 10.3389/fninf.2011.00023. URL http://www.frontiersin.org/neuroinformatics/10.3389/fninf.2011.00023/abstract.

B.T.T. Yeo, T. Vercauteren, P. Fillard, J.-M. Peyrat, X. Pennec, P. Golland, N. Ayache, and O. Clatz. Dt-refind: Diffusion tensor registration with exact finite-strain differential. *IEEE Trans Med Imaging*, 28(12):1914–1928, 2009. ISSN 0278-0062.

B.T.T. Yeo, M.R. Sabuncu, T. Vercauteren, N. Ayache, B. Fischl, and P. Golland. Spherical demons: Fast diffeomorphic landmark-free surface registration. *IEEE Trans Med Imaging*, 29 (3):650–668, 2010. ISSN 0278-0062.

Igor Yonovsky, Paul M. Thompson, Stanley Osher, and Alex D. Leow. Large deformation unbiased diffeomorphic nonlinear image registration: Theory and implementation. Technical report, UCLA, 2006.

Laurent Younes, Felipe Arrate, and Michael I. Miller. Evolutions equations in computational anatomy. *NeuroImage*, 45(1, Supplement 1):S40 – S50, 2009. ISSN 1053-8119. doi: http://dx.doi.org/10.1016/j.neuroimage.2008.10.050. URL http://www.sciencedirect.com/science/article/pii/S105381190801166X. ¡ce:title¿Mathematics in Brain Imaging¡/ce:title¿.

L. Zagorchev and A. Goshtasby. A comparative study of transformation functions for nonrigid image registration. *Image Processing, IEEE Transactions on*, 15(3):529–538, 2006. ISSN 1057-7149. doi: 10.1109/TIP.2005.863114.

Robert J. Zatorre, R. Douglas Fields, and Heidi Johansen-Berg. Plasticity in gray and white: neuroimaging changes in brain structure during learning. *Nat Neurosci*, 15(4):528–536, Apr 2012. ISSN 1097-6256. doi: 10.1038/nn.3045. URL http://dx.doi.org/10.1038/nn.3045.

Hui Zhang, Paul A. Yushkevich, Daniel C. Alexander, and James C. Gee. Deformable registration of diffusion tensor mr images with explicit orientation optimization. *Medical Image Analysis*, 10(5):764–785, 2006. ISSN 1361-8415.

K. Zilles, A. Schleicher, C. Langemann, K. Amunts, P. Morosan, N. Palomero-Gallagher, T. Schormann, H. Mohlberg, U. Bürgel, H. Steinmetz, G. Schlaug, and P. E. Roland. Quantitative analysis of sulci in the human cerebral cortex: development, regional heterogeneity, gender difference, asymmetry, intersubject variability and cortical architecture. *Hum Brain Mapp*, 5(4):218–221, 1997. doi: 3.0.CO;2-6. URL http://dx.doi.org/3.0.CO;2-6.